

UC Santa Barbara

UC Santa Barbara Electronic Theses and Dissertations

Title

Constituent Properties and their Effects on Tensile Response of Unidirectional SiC-SiC Composites

Permalink

<https://escholarship.org/uc/item/5tv93598>

Author

Callaway, Evan Benjamin

Publication Date

2019

Peer reviewed|Thesis/dissertation

UNIVERSITY of CALIFORNIA

Santa Barbara

**Constituent Properties and their Effects on Tensile Response of Unidirectional SiC-SiC
Composites**

A dissertation submitted in partial satisfaction

of the requirements for the degree

Doctor of Philosophy

in

Materials

by

Evan Benjamin Callaway

Committee in charge:

Professor Frank W. Zok, Chair

Professor Carlos G. Levi

Professor Matthew R. Begley

Professor Samantha H. Daly

September 2019

The dissertation of Evan Benjamin Callaway is approved.

Professor Carlos G. Levi

Professor Matthew R. Begley

Professor Samantha H. Daly

Professor Frank W. Zok, Committee Chair

August 2019

Constituent Properties and their Effects on Tensile Response of Unidirectional SiC-SiC
Composites

Copyright © 2019

by

Evan Benjamin Callaway

For Karen, Joe, & Tripp Callaway

Acknowledgements

I would like to express my sincere gratitude to my advisor Frank Zok. He has granted me freedom to pursue problems that I find intellectually stimulating, while also providing the expertise needed to refine my ideas into a coherent and publishable form. His continuing guidance and support have been of great value to my professional growth and have afforded me unique opportunities to explore my interests.

I gratefully acknowledge financial support from the Pratt & Whitney Center of Excellence at the University of California, Santa Barbara. In addition, I acknowledge the IHI Turbine Materials Research Center at the University of California, Santa Barbara for providing additional samples and support.

I would also like to thank my colleagues at UCSB for their help, suggestions, feedback and support. In particular, I would like to thank my committee, Matthew Begley, Carlos Levi, and Samantha Daly, for their continued guidance on my research. I also express my gratitude to the members of Zok and Levi groups, past and present, and in particular John Shaw, Natalie Larson, Will Summers, Victoria Christensen, and Ken Kawanishi. Thanks also to Peter Maxwell, Deryck Stave, Kirk Fields, and Aidan Taylor for all their help overcoming obstacles in the lab.

I would also like to thank my friends Neil, Emily, and everyone from the small incoming class of Fall 2014 for their support, both professionally and personally. I am lucky to have such a close-knit group of friends, and it has made even the most stressful times in graduate school manageable.

Finally, I thank my parents, Karen and Joe Callaway, my brother, Tripp, and my partner, Sophia Arabadjis, for their enduring love and for always believing in me.

Curriculum Vitæ

Evan Benjamin Callaway

Education

2019 Ph.D. Materials, University of California, Santa Barbara.

2014 B.S. Materials Science & Engineering, North Carolina State University, Raleigh, NC

Minor in Economics and Physics, Valedictorian

Publications

1. **E. B. Callaway**, P. Christodoulou, and F. W. Zok. "Deformation, Rupture and Sliding of Fiber Coatings in Ceramic Composites". *Journal of the Mechanics and Physics of Solids*, 2019
2. **E. B. Callaway** and F. W. Zok. "Weibull Parameters Obtained from Dependence of Fiber Strength on Fiber Length and Area". *Journal of the American Ceramic Society*, 2018
3. **E. B. Callaway** and F. W. Zok. "Strengths of Ceramic Fiber Bundles: Theory and Practice". *Journal of the American Ceramic Society*, 2017
4. **E. B. Callaway** and F. W. Zok. "Accurate Determination of Fiber Strength Distributions". *Journal of the American Ceramic Society*, 2016
5. R. Kaminker, **E. B. Callaway**, N. D. Dolinski, S. M. Barbon, M. Shibata, H. Wang, J. Hu, and C. J. Hawker. "Solvent-Free Synthesis of High-Performance Polyhexahydrotriazine (PHT) Thermosets". *Chemistry of Materials*, 2018
6. N. D. Dolinski, Z. A. Page, **E. B. Callaway**, F. Eisenreich, R. V. Garcia, R. Chavez, D. P. Bothman, S. Hecht, F. W. Zok, and C. J. Hawker. "Solution Mask Liquid Lithography (SMaLL) for One-Step, Multimaterial 3D Printing". *Advanced Materials*, 2018

7. **E. B. Callaway**, G. Naderi, Q. V. Le, and J. Schwartz. “Statistical Analysis of the Relationship between Electrical Transport and Filament Microstructure in Multifilamentary $\text{Bi}_2\text{Sr}_2\text{CaCu}_2\text{O}_x/\text{Ag}/\text{Ag-Mg}$ Round Wires”. *Superconductor Science and Technology*, 2013

In Preparation

8. **E. B. Callaway** and F. W. Zok. “Tensile Response of Unidirectional Ceramic Minicomposites”. *In Preparation*
9. F. W. Zok, P. Maxwell, K. Kawanishi, and **E. B. Callaway**. “Degradation of a SiC-SiC Composite in Water Vapor Environments”. *Submitted*

Abstract

Constituent Properties and their Effects on Tensile Response of Unidirectional SiC-SiC

Composites

by

Evan Benjamin Callaway

Mechanical response of ceramic matrix composites is critically dependent on properties of fibers and fiber coatings. In this dissertation, testing methods and analysis techniques for obtaining key constituent properties are developed. First, a critical assessment of existing methods used to determine fiber strength distributions is made, through a combination of established theorems in convolution and uncertainty propagation, Monte Carlo simulations of single fiber tension and fiber bundle tests, and experimental measurements on bundles of SiC fibers. The results reveal that fiber Weibull parameters are most reliably obtained by fitting stress-strain data from fiber bundle tests directly to the functional form predicted by fiber bundle theory. Second, fiber push-in tests are used to probe the mechanical properties of BN fiber coatings and their interfaces with the fibers and the matrix in several prototypical SiC-SiC composites. Push-in results reveal two distinct behaviors: one in which coating rupture occurs suddenly, followed by interface sliding, and another in which yielding of the coating occurs first, followed by rupture and sliding. A new micromechanical model for elastic/plastic coating deformation and subsequent rupture and sliding is developed. The model provides a framework for interpreting push-in results, including ways to ascertain the mechanism that governs the stress for push-in initiation and for extracting pertinent coating properties. Finally, effects of constituent properties on tensile response of

unidirectionally-reinforced composites are examined through a combination of analytical models of fiber fragmentation, matrix cracking, and interface debonding and sliding, along with Monte Carlo simulations and experimental measurements on SiC-SiC minicomposites. The results reveal two distinct domains of fiber fragmentation and subsequent pullout; at low stresses, fibers break in a random manner throughout the composite and, at the stress maximum, additional breaks are localized to regions near the eventual fracture plane. Composite rupture occurs when the *local* fiber bundle response in the most heavily strained regions (within matrix crack planes) reaches a load maximum. The failure stress and strain vary considerably with fiber volume fraction, especially when the matrix strength distribution is broad. In many cases of practical interest, the full potential of the fibers is not realized.

Table of Contents

Title Page	i
Curriculum Vitæ	vi
Abstract	viii
Table of Contents	x
List of Figures	xiv
List of Tables	xviii
1 Introduction	1
1.1 Background	1
1.2 Fiber properties	3
1.3 Interface properties	4
1.4 Tensile response of unidirectional composites	6
1.5 Objectives and dissertation outline	7
2 Accurate determination of fiber strength distributions	20
2.1 Introduction	21
2.2 Background on weakest link fracture statistics	24
2.3 Systematic errors	26
2.4 Random uncertainties	29
2.5 Monte Carlo simulations	32
2.6 Applications	35
2.7 Summary and conclusions	37
3 Strengths of ceramic fiber bundles: Theory and practice	49

3.1 Introduction	50
3.2 Fiber bundle theory: Determining Weibull parameters and their uncertainties .	53
3.3 Critical gauge length for stable response.....	56
3.4 Monte Carlo simulations of fiber bundle tensile tests	58
3.4.1 Numerical procedures	58
3.4.2 MCS results	59
3.5 Experimental measurements on SiC fiber bundles	62
3.5.1 Test Procedures	62
3.5.2 Experimental results	65
3.6 Summary and conclusions	69
3.A Appendix: Procedures for fiber bundle heat treatment and tensile testing	70
4 Weibull parameters obtained from dependence of fiber strength on fiber	
length and area	84
4.1 Introduction	85
4.2 Determination of Weibull parameters	87
4.3 Distributions in Weibull parameters: Analytical results.....	89
4.4 Distributions in Weibull parameters: Monte Carlo simulations	92
4.4.1 Numerical procedures	93
4.4.2 MCS results	93
4.5 Experimental measurements on SiC fiber bundles	94
4.6 Discussion	96
4.7 Summary and conclusions	99
4.A Appendix: Random errors of regression analysis	100

4.A.1	Generic results	100
4.A.2	Application to the Weibull modulus	101
4.A.3	Application to the reference strength	104
5	Deformation, rupture and sliding of fiber coatings in ceramic composites	
	composites	117
5.1	Introduction	118
5.2	Basic mechanics, test methods, and experimental measurements	120
5.2.1	The standard model	120
5.2.2	Test methods	123
5.2.3	Data analysis	124
5.2.4	Experimental results	126
5.3	Elastic-plastic deformation and rupture of fiber coatings	127
5.3.1	Analytical model	127
5.3.2	Finite element analysis	132
5.3.3	Assessment of analytical model	134
5.3.4	Initiation of inelastic fiber push-in	135
5.4	Re-examination of experimental data	136
5.5	Discussion	138
5.6	Summary and conclusions	140
5.A	Appendix: Determination of critical rupture load from compliance measurements	143
6	Tensile response of unidirectional ceramic minicomposites	161
6.1	Introduction	162

6.2	Mechanics of tensile response of unidirectional composites.....	164
6.2.1	Overview	164
6.2.2	Onset of matrix cracking	165
6.2.3	Fragmentation and rupture.....	166
6.2.4	Length and strength of pulled-out fibers	171
6.3	Monte Carlo simulations: Methods, results, and analyses.....	171
6.3.1	Simulation methods	171
6.3.2	Stress-strain response, fiber fragmentation, and rupture	174
6.3.3	Lengths and strengths of pulled-out fibers	177
6.3.4	Determining <i>in situ</i> fiber strength distributions.....	178
6.3.5	Tough-to-brittle transition	179
6.4	Exact closed-form solution for unidirectional composite response.....	181
6.5	Experimental study	185
6.5.1	Materials and measurements.....	185
6.5.2	Analysis of test results	187
6.5.3	Discussion	189
6.6	Summary and conclusions	191
6.A	Appendix: Derivation of $\Delta_f(\Delta_m)$	193
7	Conclusion and recommendations	216
7.1	General conclusions and impact	216
7.2	Future work	222

List of Figures

1.1	Specific strength as a function of temperature for refractory materials	18
1.2	CMC overview schematic.....	19
1.3	Effects of fiber and interface properties on composite response.....	19
2.1	Effects of Weibull modulus on mean fiber strength and fiber bundle strength..	43
2.2	Comparisons of Weibull and normal distributions.....	43
2.3	Combined effects of $Z(A)$ and m_t on the CV of the nominal strength	44
2.4	Effects of $Z(A)$ and N on nominal Weibull modulus	45
2.5	Ratio of mean strengths	46
2.6	Estimates of true Weibull modulus.....	47
2.7	Summary of experimental data from literature.....	48
3.1	Schematic of snap-back instability from load train compliance.....	75
3.2	Effects of Weibull modulus and gauge length on the fraction of fibers whose strength is measured up to the point of instability.....	76
3.3	MCS results interpreted using the three fitting methods	77
3.4	Effects of gauge length on mean and CV of the Weibull parameters	78
3.5	Effects of experimental error on apparent Weibull parameters.....	79
3.6	Speckle pattern on the end of a tow before and after tensile testing	80
3.7	Representative test results showing effects of gauge length, sizing and lubrication on measured stress-strain curves	80
3.8	Weibull plot from measurements on a lubricated fiber bundle	81
3.A1	Drawing of furnace setup.....	81

3.A2 Drawing of mounting plate showing steps for mounting	82
3.A3 Drawing of fixture with designs for clamp base and clamp plate	82
4.1 Schematics of test methods to determine Weibull parameters and guidelines for selecting test parameters that yield acceptable random error	112
4.2 Comparisons of analytical solutions and MCS results for distributions in Weibull parameters	113
4.3 MCS results and analytical solutions for median, mode and CV of m obtained from area-dependence of mean strength, length-dependence of mean strength, and length-dependence of fiber bundle strength	114
4.4 MCS results for CV of Weibull modulus obtained from gauge-length dependence of mean fiber strength and fiber bundle strength	115
4.5 Experimental results for fiber bundles.....	116
4.6 Uncertainty of Weibull moduli in the literature obtained from single fiber tests and fiber bundle tests.....	116
5.1 Schematic model of push-in response	149
5.2 Micrographs of the four material systems studied.....	150
5.3 Computed compliance with representative fiber and coating properties.....	151
5.4 Representative load-displacement curves during push-in for the four composite materials	152
5.5 Hysteresis loop widths used to infer sliding stress	153
5.6 Distributions of sliding stress and interface toughness for the four material systems using the standard brittle fracture interpretation of push-in response.....	153
5.7 Experimental compliance curves	154

5.8	Representative curves of load vs. inelastic displacement for the four composite materials	154
5.9	Shear stress profile within the coatings from FEA and the analytical model.....	155
5.10	Push-in responses in the elastic and plastic domains from FEA and from the analytical model.....	156
5.11	Plastic zone length from FEA and from the analytical model.....	157
5.12	Map of domains in which initiation of fiber push-in is governed by frictional sliding, coating rupture or coating yielding.....	157
5.13	Two examples of variations in F^2 with non-Hertzian fiber displacement.....	158
5.14	Comparison of toughness obtained from rigid-brittle model and from elastic-plastic model	158
5.15	Γ tracks linearly with $\tau_y u_c$ for materials in which yielding precedes rupture .	159
5.16	Correlation of toughness with sliding stress and yield stress	159
5.17	Correlation between sliding stress and yield stress	160
5.A1	Calculated compliance curves for representative fiber and coating properties for which rupture does not occur at the compliance minimum	160
6.1	Representative tensile stress-strain curves for SiC/SiC minicomposites	201
6.2	Schematic of concurrent fragmentation of fibers and matrix	202
6.3	Comparison of solutions for <i>in situ</i> bundle tensile response	203
6.4	Results from MC simulations of minicomposite tensile response.....	204
6.5	Survival probability of fibers as a function of position	205
6.6	Coefficient of variation of failure probability of fibers	206
6.7	Strength of pulled out fibers as a function of fracture location	207

6.8	Stress-strain response for composites with finite matrix strength	207
6.9	Effect of crack spacing on location of composite fracture	208
6.10	Distributions in pullout length from solutions and MC simulations	208
6.11	Effect of matrix on distributions in pullout length	209
6.12	Weibull plots of strength of pulled-out fibers from MC simulations	209
6.13	Distribution of <i>in situ</i> Weibull parameters from MC simulations	210
6.14	Effect of fiber volume fraction on composite response	210
6.15	Tough-to-brittle transition	211
6.16	Stress-strain curves for matrix fragmentation	212
6.17	SEM images of minicomposites	213
6.18	Experimental fiber bundle test results	214
6.19	Experimental minicomposite test results	214
6.20	Fit of exact solution to experimental minicomposite test results	215

List of Tables

2.1 Distributions of fiber areas of commercial SiC fibers	42
2.2 Nomenclature.....	42
3.1 Averages and CVs of Weibull parameters from bundle tests.....	75
3.2 Comparison of Weibull parameters obtained from the three fitting methods	75
4.1 List of variables	111
5.1 Summary of distributions of interface properties	149
6.1 List of variables	200
6.2 Summary of fiber properties.....	200
6.3 Summary of interface properties	201

Chapter 1

Introduction

1.1 Background

Ceramic matrix composites (CMCs) comprising SiC-based matrices and SiC-fibers are intended for use in hot sections of aerojet engines. This selection is driven by a combination of their high specific strength to temperatures of 1500°C (Figure 1.1), improved toughness over monolithic ceramics, lower density as compared to competing superalloys, and their ability to withstand severe thermochemical environments.¹ Potential upper use temperatures of SiC/SiC composites are 100-200K higher than those of superalloys.² This can have a large impact on thermal efficiency. Using data on turbine-based, combined-cycle power generation systems, a 30K increase in firing temperature results in about 1% increase in efficiency.³ With U.S. airline carriers spending \$38.4 billion on fuel in 2018⁴ and commercial airline travel making up 2-4% of total greenhouse gas emissions,⁵ the higher operating temperatures enabled by insertion of SiC/SiC composites in engine hot sections will reduce fuel costs and NOx emissions in very significant ways. In 2017, GE introduced SiC/SiC composites in turbine shrouds in their LEAP engine: the first large-scale use of SiC/SiC composites in commercial aeroengines. The expectation of GE and other aeroengine manufacturers is that continued research and development will lead to additional hot-section CMC components with consequent increases in efficiency.

Despite the potential benefits of employing CMCs in hot components in gas turbine engines, achieving microstructural uniformity and preventing internal oxidation and embrittlement in steam-laden environments remain outstanding challenges. Microstructural

uniformity takes many forms. Ideally, it entails uniformly spaced fibers with uniformly produced coatings in a uniform fully-dense matrix. Matrix cracks, pores or other defects, when present, enable rapid ingress of oxidants from the environment, leading potentially to local consumption of fiber coatings and formation of silica that bonds fibers to the matrix. Crack deflection and pullout is thereby inhibited. Silica scale formation generates tensile stress in the fibers.⁶ Additionally, oxidation of the fiber may result in sub-critical cracking. Complexity in both geometry and variety of constituents makes quantifying effects of microstructural non-uniformity and internal oxidation on composite response an arduous task.

Conducting experiments on simplified geometries reduces this complexity. Composite response and ultimate strength depend primarily on mechanical and geometric properties of three key constituents: fibers, interface coatings, and matrix.⁷⁻¹⁰ Constituent properties can be obtained directly from tests on three simplified geometries (Figure 1.2): (i) bare, or uncoated, fibers, (ii) coated fibers, and (iii) minicomposites comprising single tows of coated fibers. Testing of simplified geometries allows for high-throughput examination to determine processing-microstructure-property relationships. Degradation mechanisms can be individually probed and quantified. Obtaining constituent properties with high fidelity and having robust micromechanical models relating constituent properties to composite response are key for this bottom-up approach to be successful. Despite extensive work over the last three decades, some important deficiencies remain in the micromechanical modeling and analysis of experimental data on fiber tows and minicomposites.

The rest of the chapter summarizes existing micromechanical models, testing methods, and analysis techniques for obtaining constituent properties. Important deficiencies

and issues are highlighted. Ceramic fiber properties are covered in Section 1.2. The role of fiber coatings is discussed in Section 1.3. Micromechanical models for relating fiber, matrix, and interface properties to composite response are presented in Section 1.4. Finally, the objectives of the present study and an outline of the dissertation are given in Section 1.5.

1.2 Fiber properties

Tensile strength of fiber-reinforced composites is governed by fiber strength. The strength of ceramic fibers is inherently statistical in nature. Distributions in fiber strength, σ , are typically described by the empirical weakest-link Weibull model with parameters σ_o , the reference strength, and m , the Weibull modulus

$$P_F = 1 - \exp\left[\frac{-V}{V_o}\left(\frac{\sigma}{\sigma_o}\right)^m\right] \quad (1.1)$$

where P_F is failure probability, V is volume of material under stress, and V_o is a reference volume.

The most common method for determining fiber strengths is based on tensile tests on individual filaments. A variety of techniques have been used to obtain Weibull parameters from such tests. Traditionally, Weibull parameters have been obtained from linear regression analyses of Weibull plots, of the form $\ln(-\ln[1 - P_F])$ vs $\ln \sigma$. While ASTM standards call for the use of more precise statistical methods (*i.e.* maximum likelihood method),^{11, 12} Weibull plots remain in common use.¹³⁻²⁶ Regardless of fitting method, testing of single filaments is a tedious task as it requires many measurements (typically at least 30) to obtain accurate Weibull parameters. Often, for expediency, areas of all tested fibers are not measured; instead, the *average* fiber area is combined with the fracture load to compute the

nominal strength.^{19, 22–25, 27, 28} The problem is exacerbated by the common practice by fiber manufacturers of reporting only a mean strength, with no mention of gauge length or variation in strength.^{29, 30} In reality, fiber strength depends strongly on volume.^{15, 18, 31–36} Complicating the issue further is the reported observation that Weibull parameters inferred from dependence of strength on fiber area or length differ from those obtained from tests at constant volume. These discrepancies have served as justification for modifying Eqn. (1.1) in ways that often lack sound mathematical or physical basis.³⁷

Alternatively, fiber strength distributions can be inferred from tensile tests on *bundles* comprising hundreds or thousands of aligned fibers. From this method, the strengths of many fibers are determined in a single test without needing to measure individual fiber areas. Moreover, degradation mechanisms inherent to fiber-fiber interactions (*e.g.* fiber welding due to high temperature sintering or oxidation) are captured from testing of bundles. Such effects go unnoticed in testing of single filaments. An issue with fiber bundle tests is the lack of an ASTM standard. A variety of methods with varying statistical fidelity are used for determining fiber Weibull parameters.^{31, 38–48} Much of the work in the following chapters addresses optimizing testing methods and analysis techniques.

1.3 Interface properties

Design of fiber coatings is of critical importance for achieving high composite toughness and strain to failure via crack deflection and frictional pullout. Mechanical properties of the coatings are typically described by an interface (or interphase) toughness Γ_i and a resistance to sliding τ_s (Figure 1.3). For sufficiently low interface toughness relative to fiber toughness, matrix cracks deflect at one of the interfaces on either side of the coating or

within the coating itself.⁴⁹ If instead interface toughness is high relative to fiber toughness, matrix cracks penetrate through fibers, resulting in a brittle, low-strength composite, comparable to a monolithic ceramic. In the ideal scenario in which crack deflection and debonding can occur, frictional sliding allows for reloading of the matrix around matrix cracks and of the fibers around broken fiber ends. With increasing sliding resistance, the slip lengths needed to reload broken fibers and matrix to their respective far-field values decrease; hence, composite strength increases as a greater fraction of fiber remains intact. The preceding is strictly true for the condition of global load sharing. When the sliding resistance is sufficiently high, stress concentrations near the interface lead to a condition of local load sharing.⁵⁰ With increasing degree of local load sharing, composite strength and toughness decrease. The nature of the transition from global to local load sharing remains poorly understood.

A variety of methods exist for obtaining sliding resistance and interface toughness. These properties can be indirectly estimated from either composite tensile hysteresis loops^{51–54} or matrix crack spacings.⁵⁵ More direct measurements can be made via fiber push-in^{56–58} or push-out tests^{59–61} using an instrumented nanoindenter. Fiber push-out tests are a popular choice for the ease in analyzing data to extract interface properties, but sample preparation and conducting the experiment on small diameter fibers (c.a. 10 μm) is difficult. Push-in tests require less sample preparation and are easier to conduct. Additionally, hysteresis loops obtained from unload-reload cycles in push-in tests provide additional information for cleanly measuring sliding resistance.⁵⁸ For these reasons, push-in tests remain the preferred method for directly measuring interface properties.

Direct methods have the additional benefit of giving *distributions* in interface properties. Push-in and push-out tests probe interface properties around individual fibers whereas the indirect methods yield globally-averaged properties. In CMCs, distributions in properties and extreme values (*e.g.* fiber or matrix strength) may be as important as their respective mean values. Effects of interface property variation on d remain largely unknown. Qualitatively, a large variance in interface toughness may lead to crack penetration through some fibers (*i.e.* those with particularly high interface toughness) and crack deflection and debonding around others. Variations in sliding resistance may lead to non-uniform loading of fibers in the vicinity of matrix cracks. Fibers with higher sliding resistance (*i.e.* those under higher loads) are more likely to fail than those with lower sliding resistance. Overall, variations in interface properties are unlikely to benefit composite response.

1.4 Tensile response of unidirectional composites

Micromechanical models relating fiber and interface properties to composite tensile response were established largely in the 1990s. Solutions originated from analyses of a simpler problem: that of fragmentation of a *single* fiber embedded in a high strain-to-failure matrix. Unidirectional composites are then treated as an array of single-fiber composites.^{7, 9, 62-64} To simplify the problem, the load carried by the matrix is usually neglected and the results are couched in terms of *in situ* bundle stress rather than composite stress. As we show in the present work, the ramifications of matrix strength and matrix cracking can be crucial in obtaining useful information from tensile response of unidirectional composites.

Tensile testing of single-tow minicomposites has become a common practice for determining effects of constituent properties on composite response.^{54, 65-71} Much like the

tests for measuring fiber and interface properties described in the previous two sections, tensile testing and analysis methods for minicomposites vary substantially between researchers. In some cases, only composite strength, with limited mention of fiber content, is reported.^{65, 70} With proper analysis, minicomposite tensile response can yield a wealth of information on constituent properties, their effect on composite response, the degree of global load sharing, and degradation of constituent properties during processing or thermochemical exposure.

1.5 Objectives and dissertation outline

The overarching goal of this research is to (i) develop testing protocols and analysis techniques to obtain pertinent constituent properties with high fidelity and (ii) improve the understanding of how these properties affect composite response. These are necessary first steps before degradation mechanisms operative in CMCs during processing or in-use can be identified and quantified. In this work, the key constituent properties are obtained from three types of tests: (1) fiber bundle tensile tests to obtain fiber Weibull parameters; (2) fiber push-in tests on polished cross-sections of composites to obtain sliding resistance and interface toughness; and (3) minicomposite tensile tests to obtain *in situ* fiber and matrix strength distributions and to relate combined effects of fiber, interface, and matrix properties to composite response. While such tests are not uncommon, there is a severe lack of assessment of the fidelity of test data. Here, issues are addressed through a combination of Monte Carlo (MC) simulations, analytical solutions (based, for example, on uncertainty analysis or micromechanical models) and experimental measurements. Insights gleaned

from this work are expected to help guide future experimentation to study degradation mechanisms.

The dissertation is organized in the following way. Chapters 2-4 focus on methods for obtaining distributions in fiber strength. Chapter 2 discusses some issues with accepted testing procedures of single filaments, especially when the test data involve nominal (rather than true) fiber strengths. A method for deconvoluting and correcting systematic errors from random uncertainties is developed and used to assess the fidelity of data reported in various literature sources.

Chapter 3 addresses issues in the fidelity of results stemming from fiber bundle tests and strategies to optimize outcomes. An assessment of various methods for fitting test data is made through MC simulations of bundle response. Effects of gauge length inter-fiber friction on bundle response and procedures for handling the tows in order to maintain alignment are presented. In the appendix to Chapter 3, a procedure is outlined for heat treating and subsequent tensile testing of fiber bundles.

Chapter 4 provides a critical assessment of the efficacy of inferring Weibull strength parameters of ceramic fibers from variations in strength with fiber diameter or gauge length. The issues are addressed using theorems in regression analysis and uncertainty propagation as well as MC simulations. With the small variation in diameter in commercially available fibers (coefficient of variation of diameter < 0.2), inordinately large sample sizes ($>1,000$) are required to achieve reliable Weibull parameters. More reliable results can be obtained from dependence of strengths of bundles containing many (>500) fibers on gauge length.

Chapter 5 examines the mechanics of shear deformation, rupture and frictional sliding of fiber coatings in ceramic composites through a combination of experiments,

modeling and computational simulations. Distributions in interface properties are obtained from fiber push-in tests on four SiC-BN-SiC composite systems. Test results for two of the systems reveal yielding of BN coatings prior to coating rupture, thereby necessitating the development of a new framework for interpreting fiber push-in results. For this purpose, an analytical model for push-in of fibers with elastic-perfectly plastic coatings is developed and verified with extensive finite element simulations.

With Chapters 2-5 covering methods for obtaining fiber and interface properties, Chapter 6 addresses the effects of constituent properties on composite response. Despite being a problem seemingly solved long ago, several nuanced features with important practical implications are identified here. By extending the exact fiber fragmentation model to fragmentation of the matrix, a numerical solution is developed for the tensile response of unidirectional composites. Improved methods are established for extracting *in situ* Weibull parameters for both fibers and matrix. Differences in coated and *in situ* fiber properties indicate effects of degradation during composite processing and the degree of global load sharing. Additionally, MC simulations reveal new and important features of fiber fragmentation and resulting distributions in length and strength of pulled-out fibers. Finally, conclusions and recommendations for future research are presented in Chapter 7.

References

- ¹ R.R. Naslain, "Design, preparation and properties of non-oxide CMCs for application in engines and nuclear reactors: an overview," *Compos. Sci. Technol.*, **64** [2] 155–170 (2004).
- ² F.W. Zok, "Ceramic-matrix composites enable revolutionary gains in turbine engine

- efficiency,” *Am. Ceram. Soc. Bull.*, **95** [5] 22–28 (2016).
- ³ R. Eldrid, L. Kaufman, and P. Marks, *GER-4194 - The 7FB: The Next Evolution of the F Gas Turbine*. Schenectady, NY, 2001.
- ⁴ *Airline Fuel Cost and Consumption (U.S. Carriers - All)*, (n.d.).
- ⁵ C. Hofer, M.E. Dresner, and R.J. Windle, “The environmental effects of airline carbon emissions taxation in the US,” *Transp. Res. Part D Transp. Environ.*, **15** [1] 37–45 (2010).
- ⁶ W. Xu, F.W. Zok, and R.M. McMeeking, “Model of Oxidation-Induced Fiber Fracture in SiC/SiC Composites,” *J. Am. Ceram. Soc.*, **97** [11] 3676–3683 (2014).
- ⁷ W.A. Curtin, “Theory of mechanical properties of ceramic-matrix composites,” *J. Am. Ceram. Soc.*, **74** [11] 2837–2845 (1991).
- ⁸ M.-Y. He, A.G. Evans, and W.A. Curtin, “The ultimate tensile strength of metal and ceramic-matrix composites,” *Acta Metall. Mater.*, **41** [3] 871–878 (1993).
- ⁹ C.Y. Hui, S.L. Phoenix, M. Ibnabdeljalil, and R.L. Smith, “An exact closed form solution for fragmentation of Weibull fibers in a single filament composite with applications to fiber-reinforced ceramics,” *J. Mech. Phys. Solids*, **43** [10] 1551–1585 (1995).
- ¹⁰ W.A. Curtin, “Ultimate strengths of fibre-reinforced ceramics and metals,” *Composites*, **24** [2] 98–102 (1993).
- ¹¹ ASTM C1557-14, “Standard Test Method for Tensile Strength and Young’s Modulus of Fibers,” (2014).
- ¹² ASTM C1239-13, “Standard Practice for Reporting Uniaxial Strength Data and Estimating Weibull Distribution Parameters for Advanced Ceramics,” (2013).

- ¹³ R.S. Hay, “SiC fiber strength after low pO₂ oxidation,” *J. Am. Ceram. Soc.*, **101** [2] 831–844 (2017).
- ¹⁴ J.J. Sha, T. Hinoki, and A. Kohyama, “Microstructural characterization and fracture properties of SiC-based fibers annealed at elevated temperatures,” *J. Mater. Sci.*, **42** [13] 5046–5056 (2007).
- ¹⁵ D.M. Wilson and L.R. Visser, “High performance oxide fibers for metal and ceramic composites,” *Compos. - Part A Appl. Sci. Manuf.*, **32** [8] 1143–1153 (2001).
- ¹⁶ J.J. Sha, J.S. Park, T. Hinoki, and A. Kohyama, “Strength and fracture properties of advanced SiC-based fibers,” *Mech. Compos. Mater.*, **42** [6] 527–534 (2006).
- ¹⁷ J.J. Sha, T. Nozawa, J.S. Park, Y. Katoh, and A. Kohyama, “Effect of heat treatment on the tensile strength and creep resistance of advanced SiC fibers,” *J. Nucl. Mater.*, **329** [A] 592–596 (2004).
- ¹⁸ D.M. Wilson, “Statistical tensile strength of Nextel™ 610 and Nextel™ 720 fibres,” *J. Mater. Sci.*, **32** [10] 2535–2542 (1997).
- ¹⁹ M.K. Cinibulk, G.E. Fair, and R.J. Kerans, “High-temperature stability of lanthanum orthophosphate (monazite) on silicon carbide at low oxygen partial pressures,” *J. Am. Ceram. Soc.*, **91** [7] 2290–2297 (2008).
- ²⁰ R.S. Hay and R.J. Chater, “Oxidation kinetics strength of Hi-Nicalon TM -S SiC fiber after oxidation in dry and wet air,” *J. Am. Ceram. Soc.*, **100** [9] 4110–4130 (2017).
- ²¹ R.S. Hay, G.E. Fair, and T. Tidball, “Fiber Strength After Grain Growth in Nextel™ 610 Alumina Fiber,” *J. Am. Ceram. Soc.*, **98** [6] 1907–1914 (2015).
- ²² R.S. Hay, G.E. Fair, R. Bouffieux, E. Urban, J. Morrow, A. Hart, and M. Wilson, “Relationships Between Fiber Strength, Passive Oxidation and Scale Crystallization

- Kinetics of Hi-NicalonTM-S SiC Fibers,” *Ceram. Eng. Sci. Proc.*, **32** 39–51 (2011).
- ²³ R.S. Hay, G.E. Fair, A. Hart, S. Potticary, and R. Bouffioux, “Kinetics of Passive Oxidation of Hi-Nicalon-S SiC Fibers in Wet Air: Relationships between SiO₂ Scale Thickness, Crystallization, and Fiber Strength”; pp. 253–260 in *Mech. Prop. Perform. Eng. Ceram. Compos. VII*. 2012.
- ²⁴ E.E. Boakye, P. Mogilevsky, T.A. Parthasarathy, R.S. Hay, J. Welter, and R.J. Kerans, “Monazite Coatings on SiC Fibers I: Fiber Strength and Thermal Stability,” *J. Am. Ceram. Soc.*, **89** [11] 3475–3480 (2006).
- ²⁵ R.S. Hay and E.E. Boakye, “Monazite Coatings on Fibers: I, Effect of Temperature and Alumina Doping on Coated-Fiber Tensile Strength,” *J. Am. Ceram. Soc.*, **84** [12] 2783–2792 (2001).
- ²⁶ T.A. Parthasarathy, “Extraction of Weibull parameters of fiber strength from means and standard deviations of failure loads and fiber diameters,” *J. Am. Ceram. Soc.*, **84** [3] 588–592 (2001).
- ²⁷ E.E. Boakye and P. Mogilevsky, “Fiber Strength Retention of Lanthanum- and Cerium Monazite-Coated NextelTM 720,” *J. Am. Ceram. Soc.*, **87** [2] 314–316 (2004).
- ²⁸ M.D. Petry, T.I. Mah, and R.J. Kerans, “Validity of using average diameter for determination of tensile strength and Weibull modulus of ceramic filaments,” *J. Am. Ceram. Soc.*, **80** [10] 2741–2744 (1997).
- ²⁹ J. Lamon, “Ceramic reinforcements for composites;” pp. 51–85 in *Compos. Reinf. Optim. Perform.* 2011.
- ³⁰ H. Ichikawa, “Polymer-derived ceramic fibers,” *Annu. Rev. Mater. Res.*, [46] 335–356 (2016).

- 31 J. Andersons, R. Joffe, M. Hojo, and S. Ochiai, "Glass fibre strength distribution determined by common experimental methods," *Compos. Sci. Technol.*, **62** [1] 131–145 (2002).
- 32 D.M. Kotchick, R.C. Hink, and R.E. Tressler, "Gauge Length and Surface Damage Effects on the Strength Distributions of Silicon Carbide and Sapphire Filaments," *J. Compos. Mater.*, **9** [4] 327–336 (1975).
- 33 H.F. Wu and L.L. Wu, "Strength variability and size effect of Nicalon fibre bundles," *J. Mater. Sci.*, **29** [16] 4232–4237 (1994).
- 34 G. Simon and A.R. Bunsell, "Mechanical and structural characterization of the Nicalon silicon carbide fibre," *J. Mater. Sci.*, **19** [11] 3649–3657 (1984).
- 35 W. Yu and J. Yao, "Tensile strength and its variation of PAN-based carbon fibers. I. Statistical distribution and volume dependence," *J. Appl. Polym. Sci.*, **101** [5] 3175–3182 (2006).
- 36 T. Morimoto, K. Yamamoto, and S. Ogihara, "Dependence of Weibull parameters on the diameter and the internal defects of Tyranno ZMI fiber in the strength analysis," *Adv. Compos. Mater.*, **16** [3] 245–258 (2007).
- 37 F.W. Zok, "On weakest link theory and Weibull statistics," *J. Am. Ceram. Soc.*, **100** [4] 1265–1268 (2017).
- 38 R. Hill and E.U. Okoroafor, "Weibull statistics of fibre bundle failure using mechanical and acoustic emission testing: the influence of interfibre friction," *Composites*, **26** [10] 699–705 (1995).
- 39 K.E. Evans, B.D. Caddock, and K.L. Ainsworth, "Statistical changes during the corrosion of glass fibre bundles," *J. Mater. Sci.*, **23** [8] 2926–2930 (1988).

- 40 M. R'Mili, T. Bouchaour, and P. Merle, "Estimation of Weibull parameters from loose-bundle tests," *Compos. Sci. Technol.*, **56** [7] 831–834 (1996).
- 41 Z. Chi, T.W. Chou, and G. Shen, "Determination of single fibre strength distribution from fibre bundle testings," *J. Mater. Sci.*, **19** [10] 3319–3324 (1984).
- 42 A. Cowking, A. Attou, A.M. Siddiqui, M.A.S. Sweet, and R. Hill, "Testing E-glass fibre bundles using acoustic emission," *J. Mater. Sci.*, **26** [5] 1301–1310 (1991).
- 43 E.N. Brown, A.K. Davis, K.D. Jonnalagadda, and N.R. Sottos, "Effect of surface treatment on the hydrolytic stability of E-glass fiber bundle tensile strength," *Compos. Sci. Technol.*, **65** [1] 129–136 (2005).
- 44 V. Calard and J. Lamon, "Failure of fiber bundles," *Compos. Sci. Technol.*, **64** [5] 701–710 (2004).
- 45 J. Lamon, M. R'Mili, and H. Reveron, "Investigation of statistical distributions of fracture strengths for flax fibre using the tow-based approach," *J. Mater. Sci.*, **51** [18] 8687–8698 (2016).
- 46 K.G. Dassios, M. Steen, and C. Filiou, "Mechanical properties of alumina Nextel™ 720 fibres at room and elevated temperatures: Tensile bundle testing," *Mater. Sci. Eng. A*, **349** [1] 63–72 (2003).
- 47 M. R'Mili, N. Godin, and J. Lamon, "Flaw strength distributions and statistical parameters for ceramic fibers: The normal distribution," *Phys. Rev. E - Stat. Nonlinear, Soft Matter Phys.*, **85** [5] 1–6 (2012).
- 48 M. R'Mili, M. Moevus, and N. Godin, "Statistical fracture of E-glass fibres using a bundle tensile test and acoustic emission monitoring," *Compos. Sci. Technol.*, **68** [7–8] 1800–1808 (2008).

- 49 M.-Y. He and J.W. Hutchinson, "Crack deflection at the interface between dissimilar materials," *Int. J. Solids Struct.*, **25** [9] 1053–1067 (1989).
- 50 W.A. Curtin, "The 'tough' to brittle transition in brittle matrix composites," *J. Mech. Phys. Solids*, **41** [2] 217–245 (1993).
- 51 E. Vagaggini, J.-M.M. Domergue, and A.G. Evans, "Relationships between hysteresis measurements and the constituent properties of ceramic matrix composites: I, Theory," *J. Am. Ceram. Soc.*, **78** [10] 2709–2720 (1995).
- 52 J.-M. Domergue, E. Vagaggini, and A.G. Evans, "Relationships between hysteresis measurements and the constituent properties of ceramic matrix composites: II, Experimental studies on unidirectional materials," *J. Am. Ceram. Soc.*, **78** [10] 2721–2731 (1995).
- 53 J. Lamon, F. Rebillat, and A.G. Evans, "Microcomposite Test Procedure for Evaluating the Interface Properties of Ceramic Matrix Composites," *J. Am. Ceram. Soc.*, **78** [2] 401–405 (1995).
- 54 G.N. Morscher and J. Martinez-Fernandez, "Fiber effects on minicomposite mechanical properties for several silicon carbide fiber-chemically vapor-infiltrated silicon carbide matrix systems," *J. Am. Ceram. Soc.*, **82** [1] 145–155 (1999).
- 55 W.A. Curtin, "Multiple matrix cracking in brittle matrix composites," *Acta Metall. Mater.*, **41** [5] 1369–1377 (1993).
- 56 D.B. Marshall, "An Indentation Method for Measuring Matrix-Fiber Frictional Stresses in Ceramic Composites," *J. Am. Ceram. Soc.*, **67** [12] 259–260 (1984).
- 57 D.B. Marshall and W.C. Oliver, "Measurement of interface mechanical properties in fiber-reinforced ceramic composites," *J. Am. Ceram. Soc.*, **70** [8] 542–548 (1987).

- 58 J.H. Weaver, J. Rannou, M.A. Mattoni, and F.W. Zok, “Interface properties in a porous-matrix oxide composite,” *J. Am. Ceram. Soc.*, **89** [9] 2869–2873 (2006).
- 59 T.A. Parthasarathy, P.D. Jero, and R.J. Kerans, “Extraction of interface properties from a fiber push-out test,” *Scr. Met. Mater.*, **25** [11] 2457–2462 (1991).
- 60 R.J. Kerans and T.A. Parthasarathy, “Theoretical analysis of the fiber pullout and pushout tests,” *J. Am. Ceram. Soc.*, **74** [7] 1585–1596 (1991).
- 61 D.B. Marshall, “Analysis of fiber debonding and sliding experiments in brittle matrix composites,” *Acta Metall. Mater.*, **40** [3] 427–441 (1992).
- 62 W.A. Curtin, “Exact theory of fiber fragmentation in a single-filament composite,” *J. Mater. Sci.*, **26** [19] 5239–5253 (1991).
- 63 W.A. Curtin, “Fiber fragmentation in a single-filament composite,” *Appl. Phys. Lett.*, **58** [11] 1155–1157 (1991).
- 64 S.L. Phoenix, “Statistical issues in the fracture of brittle-matrix fibrous composites,” *Compos. Sci. Technol.*, **48** [1–4] 65–80 (1993).
- 65 F. Rebillat, A. Guette, L. Espitalier, C. Debieuvre, and R. Naslain, “Oxidation resistance of SiC/SiC micro and minicomposites with a highly crystallised BN interphase,” *J. Eur. Ceram. Soc.*, **18** [13] 1809–1819 (1998).
- 66 A.S. Almansour, E. Maillet, S. Ramasamy, and G.N. Morscher, “Effect of fiber content on single tow SiC minicomposite mechanical and damage properties using acoustic emission,” *J. Eur. Ceram. Soc.*, **35** [13] 3389–3399 (2015).
- 67 C. Sauder, A. Brusson, and J. Lamon, “Influence of interface characteristics on the mechanical properties of Hi-Nicalon type-S or Tyranno-SA3 fiber-reinforced SiC/SiC minicomposites,” *Int. J. Appl. Ceram. Technol.*, **7** [3] 291–303 (2010).

- 68 E. Buet, C. Sauder, D. Sornin, S. Poissonnet, J. Rouzaud, and C. Vix-guterl, “Influence of surface fibre properties and textural organization of a pyrocarbon interphase on the interface shear stress of SiC / SiC minicomposites reinforced with Hi-Nicalon S and Tyranno SA3 fibres,” *J. Eur. Ceram. Soc.*, **34** [2] 179–188 (2014).
- 69 C. Chateau, L. Gélébart, M. Bornert, J. Crépin, E. Boller, C. Sauder, and W. Ludwig, “In situ X-ray microtomography characterization of damage in SiC f / SiC minicomposites,” *Compos. Sci. Technol.*, **71** [6] 916–924 (2011).
- 70 G.N. Morscher, “Tensile stress rupture of SiCf/SiCm minicomposites with carbon and boron nitride interphases at elevated temperatures in air,” *J. Am. Ceram. Soc.*, **42** [8] 2029–2042 (1997).
- 71 J. Martínez-Fernández and G.N. Morscher, “Room and elevated temperature tensile properties of single tow Hi-Nicalon, carbon interphase, CVI SiC matrix minicomposites,” *J. Eur. Ceram. Soc.*, **20** [14–15] 2627–2636 (2000).
- 72 D.B. Marshall and B.N. Cox, “Integral Textile Ceramic Structures,” *Annu. Rev. Mater. Res.*, **38** 425–443 (2008).

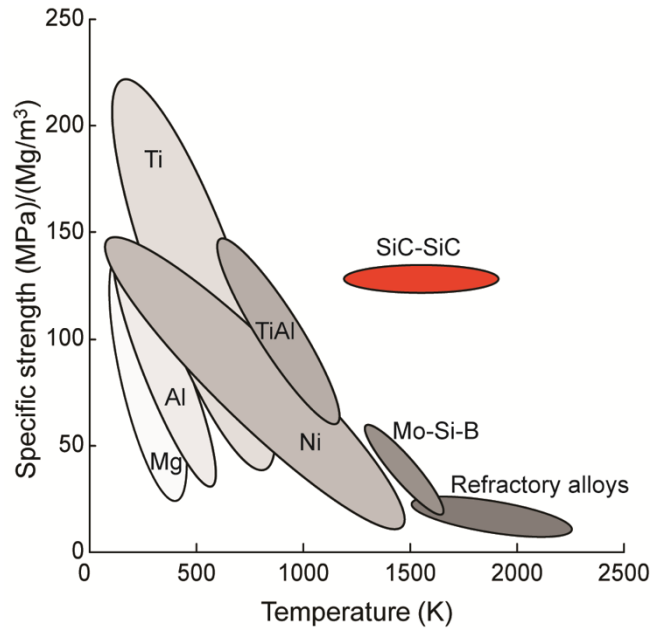


Figure 1.1: Specific strength as a function of temperature for a variety of refractory materials. Figure reprinted from Marshall & Cox with permission from Annual Reviews.⁷²

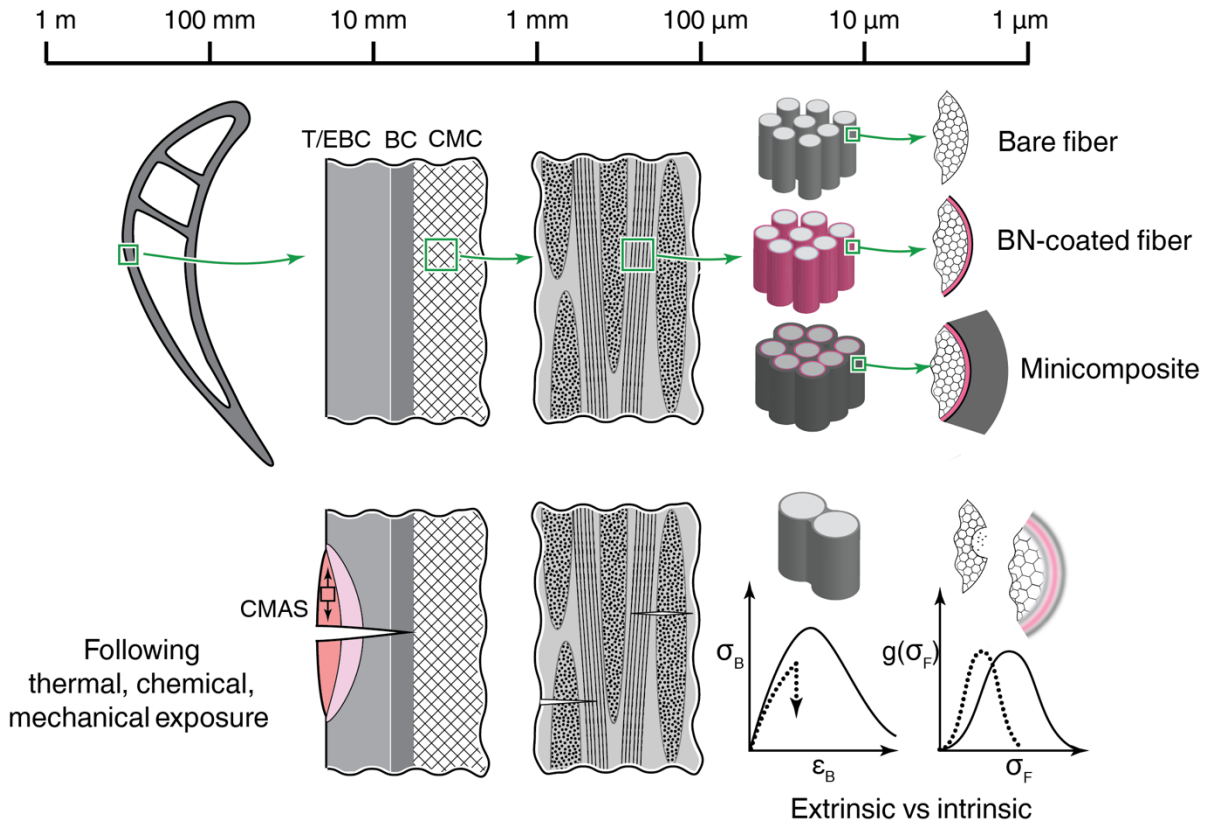


Figure 1.2: Schematics showing the range of length scales associated with CMCs. Testing of the simple geometries on the right are useful for determining constituent properties and identifying and quantifying various degradation mechanisms.

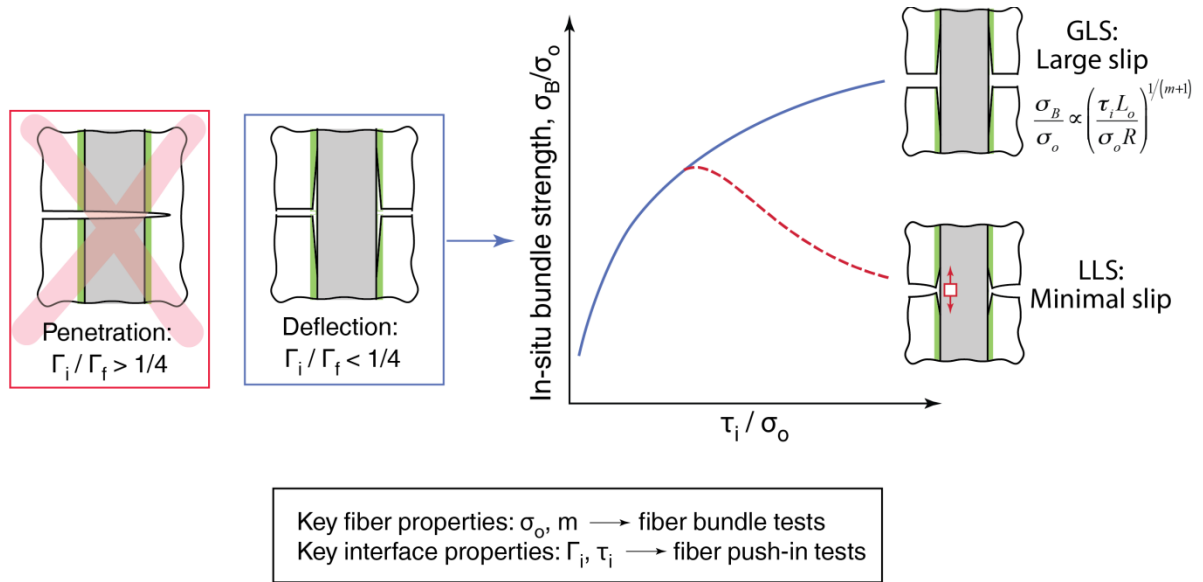


Figure 1.3: Schematic illustrating effects of fiber and interface properties on composite response.

Chapter 2

Accurate determination of fiber strength distributions †

Abstract

Tensile strengths of small-diameter ceramic fibers are commonly obtained from measured fracture loads on individual fibers and the average cross-sectional area of the entire fiber population. The goal of the present chapter is to provide a critical assessment of the consequences of using the average fiber area in the inferred strength distribution. The issues are addressed through established theorems in convolution and uncertainty propagation as well as Monte Carlo simulations. *Systematic* errors introduced by using the average area are well-represented by simple analytical formulae. The formulae are couched in terms of the coefficient of variation of fiber area and the dispersion in fiber strengths, characterized by the Weibull modulus. In turn, the formulae are used to determine the true values of Weibull modulus and reference strength from their nominal values. *Random* uncertainties associated with a finite number of tests decay slowly with number, in accordance with an inverse root scaling. When systematic errors are conflated with random uncertainties, accurate determination of the true Weibull modulus becomes increasingly challenging, even for seemingly large numbers of strength measurements. The results are used to assess the fidelity of previously-reported experimental results based on nominal strength data.

† The content of this chapter has previously appeared in the Journal of the American Ceramic Society (**Evan Benjamin Callaway** and Frank W. Zok, “Accurate determination of fiber strength distributions,” *J. Am. Ceram. Soc.*, **100** [3] 1202–1211 (2017)). It is reproduced here with the permission of John Wiley and Sons.

2.1 Introduction

A tedious task in determining strength distributions of small-diameter (ca. 10 μm) ceramic fibers is measurement of the cross-sectional area of each tested fiber. With the recommended resolution in diameter measurement being 1% of the fiber diameter [ASTM C1557]¹, measurements are usually made by laser diffraction² or by scanning electron microscopy (SEM)³: both laborious and time-consuming techniques. The measurements are further complicated by the common experience that strong fibers shatter upon failure and thus identification of their principal fracture location is a difficult task (even if all fragments are recovered).

The argument has been made that strength distributions can be determined adequately from fracture loads of individual fibers and the *average* cross-sectional area of the entire fiber population, thereby precluding the need to measure the areas of individual broken fibers.⁴ The genesis of the argument was an experimental study by Petry *et al.*⁴ in which strength distributions for numerous lots of SiC and alumina/yttrium aluminum garnet eutectic (AYE) fibers were measured using both individual and average fiber areas. Comparisons of results from the two methods led to the conclusion that the Weibull modulus m obtained using nominal strengths is the same as that obtained using true strengths. That study has since served as the principal basis for justifying continued use of nominal fiber strengths.⁵⁻¹¹

In some cases, the use of nominal fiber strength measurements is justifiable. When, for example, the fiber diameter distribution is narrow – as it for the NextelTM 610 fibers³ – differences between nominal and true strengths are small. In other cases, where fiber strength measurements are used to investigate effects of application of fiber coatings or

introduction of a ceramic matrix, the number of test variables may be inordinately high, making diameter measurements on every tested fiber a formidable task. As one specific example, a recent study by Hay *et al.*¹⁰ examined effects of oxidizing treatments on fiber properties; 20 different treatments were examined, each being assessed by at least 30 individual fiber tests. With the principal objective being assessment of fiber property changes, the expectation that the diameters of some 600 individual fibers be measured becomes unrealistic. The outstanding issue with these measurements is not whether nominal strength measurements are justifiable but rather whether the measurements can be used to obtain reliable estimates of *both* the mean fiber strength *and* the dispersion in strengths. The present chapter addresses this issue.

Studies subsequent to that of Petry *et al.*⁴ have shown that, although the mean nominal strength (obtained using the average fiber area) is the same as the mean true strength^{4, 12}, the inferred Weibull modulus and reference strength differ¹²⁻¹⁴. Lara-Curzio and Russ¹³ used Monte Carlo simulations (MCS) to demonstrate these effects. But the simulations were restricted to one assumed Weibull modulus ($m=5$), one sample size ($N=500$) and only 10 repeats of each simulation. From this narrow set of results, they found that m is underestimated by a factor of up to 4 and the reference strength in the Weibull distribution is overestimated by as much as 25%. Their main conclusion was that measurement of all fiber diameters is necessary in order to obtain reasonable estimates of the Weibull parameters. As we show in the present chapter, this conclusion is not generally true. Indeed, there are many cases of practical interest in which the Weibull parameters can be accurately estimated from nominal strengths.

Parthasarathy¹² built upon the work of Lara-Curzio and Russ¹³, using both experimental data and MCS to address errors in Weibull modulus inferred from nominal strength measurements. The simulations covered a slightly broader parameter space, including two values of m (4 and 8) and a range of sample sizes ($N=20-400$), but with apparently only one simulation for each parameter set. Parthasarathy also developed an iterative numerical procedure for inferring the true Weibull parameters from nominal strength distributions. The numerical procedure was shown to converge to the correct (unbiased) value of m when $N \geq 200$; otherwise, for smaller sample sizes, it overestimated m by a factor of 1.5 to 2, depending on the true value of m and the coefficient of variation (CoV) of fiber area. Attempts at using the procedure to infer m from several experimental data sets, each comprising 30 points, proved unsuccessful, presumably a result of the relatively small number of measurements. Random errors were not considered by either Parthasarathy¹² or Lara-Curzio and Russ¹³.

To provide perspective on the magnitude of fiber area variations, fiber areas of three commercial SiC fibers – Nicalon™, Hi-Nicalon™ and Hi-Nicalon™ Type S – were measured from scanning electron microscope images of transverse cross-sections of either bare fiber tows or of composites containing these fibers. The results are summarized in Table 2.1. The CoV $Z(A)$ of fiber area falls in the range of 0.2–0.3. Comparable values have been reported previously.^{4, 15, 16} By comparison, fiber strength distributions typically exhibit a CoV of about 0.1–0.2.

The present chapter addresses the theory underpinning the fidelity of data from tensile tests in which the average fiber area is employed in computing fiber strengths. The focus is specifically on the breadth of the strength distribution, characterized by the Weibull

modulus. An analytical framework based on established theorems in convolution and uncertainty propagation is developed and its veracity is assessed by exhaustive Monte Carlo simulations. Both *systematic errors* introduced by the use of the average fiber area and *random errors* due to finite numbers of measurements are addressed. The analytical framework provides a straightforward method for estimating the true Weibull modulus and its uncertainty.

The chapter is organized in the following way. First, in Section 2.1, a brief review and key results of weakest link fracture statistics are presented. Next, in Section 2.3, systematic errors introduced by use of the average fiber area in determining fiber strengths are analyzed. The latter include exact solutions from convolution theory and accurate approximations based on uncertainty propagation analysis. These solutions, in turn, are used to estimate the true Weibull parameters from their nominal values. This is followed, in Section 2.4, by an assessment of the effects of finite numbers of strength measurements on random uncertainties in both the Weibull modulus and the reference strength. Thereafter, the analytical results are assessed through exhaustive MC simulations, presented in Section 2.5. Finally, in Section 2.6, the theory and the simulation results are discussed in the context of previously-reported experimental measurements of fiber strength distributions.

2.2 Background on weakest link fracture statistics

The tensile strengths of cylindrical fibers, with radius R and length L and with flaws distributed randomly throughout the fiber volume, can be described by the Weibull distribution:

$$P_f = 1 - \exp \left\{ - \left(\frac{L}{L_o} \right) \left(\frac{R}{R_o} \right)^2 \left(\frac{\sigma}{\sigma_o} \right)^m \right\} \quad (2.1)$$

where P_f is the cumulative failure probability; L_o and R_o are reference values of length and radius; σ is tensile stress; and σ_o is reference strength.

The relationship between the tensile stress-strain response of a fiber bundle and the distribution in strengths of the constituent fibers is readily derived from bundle theory. The resulting *bundle strength* σ_B (*i.e.* the peak in the stress-strain curve) is given by¹⁷

$$(\sigma_B/\sigma_o)(L/L_o)^{1/m} = (me)^{-1/m} \quad (2.2)$$

where e is the base of the natural logarithm (≈ 2.718). The *mean* fiber strength $\bar{\sigma}$ is¹⁸

$$(\bar{\sigma}/\sigma_o)(L/L_o)^{1/m} = \Gamma(1+1/m) \quad (2.3)$$

where Γ is the gamma function (Figure 2.1). Its *coefficient of variation*, defined as $Z(\sigma) = S(\sigma)/\bar{\sigma}$ (S being the standard deviation), is¹⁸

$$Z(\sigma) = \frac{[\Gamma(1+2/m) - \Gamma^2(1+1/m)]^{1/2}}{\Gamma(1+1/m)} \quad (2.4)$$

The latter can be well-approximated by a power law, $Z(\sigma) = m^{-0.92}$, within $\pm 2\%$ over the range $2 \leq m \leq 20$.

Analytical solutions presented here are based on the presumption that a Weibull distribution can be approximated adequately by a normal (Gaussian) distribution with the same mean and standard deviation. With this approximation, established uncertainty propagation theorems can be used to combine uncertainties stemming from multiple sources. To this end, Figure 2.2 shows comparisons of Weibull probability density functions for

representative values of m and corresponding normal distributions with equivalent mean strengths and CoVs. The distributions are deemed sufficiently close to warrant use of this approximation.

2.3 Systematic errors

Hereafter, *nominal* values of reference strength and Weibull modulus (obtained using average fiber areas) are denoted with a subscript n and their *true* values (obtained from actual fiber areas) are denoted with a subscript t . Further distinctions are made between exact values (obtained, in principle, from an infinite number of measurements) and point estimates (obtained from a finite number of measurements); the latter are denoted with a prime superscript. Finally, mean values are denoted with an over-bar. For example, $\bar{\sigma}_t$ is the true mean fiber strength and $\bar{\sigma}_t'$ is the estimate of $\bar{\sigma}_t$ obtained from a finite sample population. The nomenclature is summarized in Table 2.2.

The distribution in nominal fiber strength is obtained through a convolution of the distributions of true fiber strength and of fiber area. Accordingly, the cumulative probability $Q_f(\sigma_n)$ of nominal strength σ_n is given by

$$Q_f(\sigma_n) = \int_0^\infty P_f(\sigma_t) h(A) dA \quad (2.5)$$

where $P_f(\sigma_t)$ is the cumulative failure probability up to a true fiber stress σ_t (described by the Weibull function) and $h(A)$ is the probability density of A . Here A is taken to follow a normal distribution with average \bar{A} , standard deviation $S(A)$, and coefficient of variation $Z(A) = S(A)/\bar{A}$. Numerical solutions of this convolution integral are plotted in Figure 2.3.

They are presented as contours of constant coefficient of variation $Z(\sigma_n)$ of the *nominal* strength distribution in coordinates of $Z(A)$ and m_t . The limiting values are $Z(\sigma_n) = m_t^{-0.92}$ as $Z(A) \rightarrow 0$ and $Z(\sigma_n) = Z(A)$ as $m_t \rightarrow \infty$.

An approximate solution to the convolution integral is obtained from an analysis based on uncertainty propagation. When a function is a quotient or a product of two variables that each follow a normal distribution, the CoV of the function is the root sum of the squares of the CoVs of the two variables. Recognizing that the true and nominal strengths are related by $\sigma_n = \sigma_t A / \bar{A}$ and presuming that the fiber strength distribution at a fixed gauge length can be approximated by a normal distribution with equivalent mean strength and CoV, it follows from uncertainty propagation that $Z(\sigma_n)$ is:

$$Z(\sigma_n) = \left(Z(A)^2 + Z(\sigma_t)^2 \right)^{1/2} = \left(Z(A)^2 + m_t^{-1.84} \right)^{1/2} \quad (2.6)$$

The accuracy of Eqn. (2.6) was assessed by comparing it to the exact results from the convolution integral in Eqn. (2.5); both sets of results are plotted in Figure 2.3. For all realistic values of m_t (≥ 2) and for even moderately high values of $Z(A)$ (up to 0.4), the analytical model is highly accurate.

In turn, the resulting *nominal* Weibull modulus, $m_n = Z(\sigma_n)^{-1/0.92}$, is given approximately by

$$\frac{m_n}{m_t} = \left(1 + \left(Z(A) m_t^{0.92} \right)^2 \right)^{-1/1.84} \quad (2.7)$$

This is a key result; it represents a universal relationship between the normalized nominal Weibull modulus m_n/m_t and the ratio of CoVs: $Z(A)/Z(\sigma_t) = Z(A) m_t^{0.92}$. It proves to be

highly robust. The result is plotted and compared with subsequent MCS results in Figures 2.4(a-b). The effects of $Z(A)$ on the inferred Weibull modulus are particularly large when $Z(A)m_t^{0.92} \geq 1$.

In contrast to the systematic errors in Weibull modulus that arise from use of the average fiber area, the average nominal strength $\bar{\sigma}_n$ is equal to the average true strength $\bar{\sigma}_t$. This conclusion had been reached previously by others^{4, 12} and is borne out by subsequent MCS results in the present study. Thus, from Eqn. (2.3), the nominal reference strength $\sigma_{n,o}$ is predicted to be:

$$\frac{\sigma_{n,o}}{\sigma_{t,o}} = \frac{\Gamma(1+1/m_t)}{\Gamma(1+1/m_n)} \left(\frac{L}{L_o} \right)^{1/m_t - 1/m_n} \quad (2.8)$$

where $\sigma_{t,o}$ is the true reference stress and m_n is given by Eqn. (2.7).

Effects of systematic errors in Weibull modulus and reference strength on the predicted bundle strength (from Eqns. (2.2), (2.7) and (2.8)) are plotted on Figure 2.1. The errors lead to significant under-estimates of the bundle strength, *e.g.*, for $m_t = 10$ and $Z(A) = 0.2$, the bundle strength is under-estimated by more than 20%. Since the errors are systematic in nature, the true Weibull parameters can be estimated from their nominal values. To this end, Eqns. (2.6) and (2.7) are combined to obtain the true Weibull modulus, m_t , from m_n and $Z(A)$:

$$\frac{m_t}{m_n} = \left(1 - \left(Z(A)m_n^{0.92} \right)^2 \right)^{-1/1.84} \quad (2.9)$$

The true reference strength, obtained from Eqn. (2.3) and the measured mean strength, $\bar{\sigma}_n = \bar{\sigma}_t$, is:

$$\frac{\sigma_{t,o}}{\bar{\sigma}_n} = \left(\frac{L}{L_o} \right)^{1/m_t} \left(\Gamma(1+1/m_t) \right)^{-1} \quad (2.10)$$

where m_t is given by Eqn. (2.9). The combination of Eqns. (2.9) and (2.10) is the second key result of this analysis; it provides a straightforward route for estimating the Weibull parameters when the number of measurements is sufficiently large to yield accurate estimates of m_n and $Z(A)$. Affirmation of the fidelity of these results is obtained from the MCS results presented in Section 2.5.

2.4 Random uncertainties

Random uncertainties arise when only a finite number of strength measurements is available. Their magnitudes are obtained from uncertainty propagation analysis, again presuming that the strength distributions are approximately normally distributed. The analytical results are assessed through MCS presented in the subsequent section. The analysis focuses mainly on CoVs; these emerge naturally from uncertainty analysis and are linked directly to the Weibull modulus via Eqn. (2.4).

The quantities of principal interest are: (i) the CoV of the true Weibull modulus (based on true strength data); (ii) the CoV of the nominal Weibull modulus (based on nominal strength data); and (iii) the CoV of the estimated true Weibull modulus obtained from Eqn. (2.9). The first two of these are unambiguous and readily computed from experimental or MCS data. The third, however, is ill-defined in some circumstances. The problems arise when the CoV of nominal strength is less than the CoV of fiber area, *i.e.* $Z(A)m_n^{0.92} \geq 1$. In these cases, the Weibull modulus predicted by Eqn. (2.9) is a complex number. This result is a natural (occasional) outcome of the random selection process when

the fiber strength and the fiber area are each statistically distributed; the same effects are obtained from the MCS results. Each of these quantities is addressed in turn.

If N strength measurements are made, the estimated CoV of the *true* strength is $Z'(\sigma_t) = S'(\sigma_t) / \bar{\sigma}_t'$ where $\bar{\sigma}_t'$ and $S'(\sigma_t)$ are the mean and the standard deviation of the sample population. The estimated standard deviation of the mean strength is $S'(\bar{\sigma}_t') = S'(\sigma_t) / \sqrt{N}$ and the standard deviation $S'(S'(\sigma_t))$ of the standard deviation $S'(\sigma_t)$ is $S'(S'(\sigma_t)) = S'(\sigma_t) / \sqrt{2(N-1)}$. Then, from uncertainty propagation, the coefficient of variation of $Z'(\sigma_t)$ becomes:

$$\frac{S'(Z'(\sigma_t))}{Z'(\sigma_t)} = \sqrt{\left(\frac{S'(S'(\sigma_t))}{S'(\sigma_t)}\right)^2 + \left(\frac{S'(\bar{\sigma}_t')}{\bar{\sigma}_t'}\right)^2} = \sqrt{\frac{1}{2(N-1)} + \frac{Z'(\bar{\sigma}_t')^2}{N}} \quad (2.11)$$

Combining this result with the power law approximation for m yields the CoV of the Weibull modulus:

$$\frac{S'(m_t)}{m_t'} = \frac{S'(Z'(\sigma_t))}{0.92 Z'(\sigma_t)} = \frac{1}{0.92} \sqrt{\frac{1}{2(N-1)} + \frac{1}{m_t'^{1.84} N}} \quad (2.12)$$

For even moderately high values of N (say 10), the second term within the square root of Eqn. (2.12) becomes negligible. The equation then reduces to:

$$\frac{S'(m_t)}{m_t'} = \frac{0.77}{\sqrt{N-1}} \quad (2.13)$$

The same analysis applies to the *nominal* strength distribution. The estimated CoV of the nominal strength is $Z'(\sigma_n') = S'(\sigma_n) / \bar{\sigma}_n'$ where $\bar{\sigma}_n'$ and $S'(\sigma_n)$ are the mean and the standard deviation of the sample population. The estimated standard deviation of the mean

nominal strength is $S'(\bar{\sigma}_n') = S'(\sigma_n) / \sqrt{N}$ and the standard deviation $S'(S'(\sigma_n))$ of the standard deviation $S'(\sigma_n)$ is $S'(S'(\sigma_n)) = S'(\sigma_n) / \sqrt{2(N-1)}$. The coefficient of variation of $Z'(\sigma_n)$ is:

$$\frac{S'(Z'(\sigma_n))}{Z'(\sigma_n)} = \sqrt{\frac{1}{2(N-1)} + \frac{Z'(\bar{\sigma}_n')^2}{N}} \quad (2.14)$$

and, for $N \geq 10$, the CoV of the nominal Weibull modulus is:

$$\frac{S'(m_n)}{m_n'} = \frac{0.77}{\sqrt{N-1}} \quad (2.15)$$

This result can be re-expressed in terms of m_t' (rather than m_n'), yielding:

$$\frac{S'(m_n)}{m_t'} = \frac{0.77 \left[1 + \left(Z(A) m_t'^{0.92} \right)^2 \right]^{-1/1.84}}{\sqrt{N-1}} \quad (2.16)$$

Finally, the CoV of the estimated true Weibull modulus m_t' , obtained from Eqn. (2.9), is given by:

$$\frac{S'(m_t')}{m_t'} = \frac{0.77 \left[1 + \left(Z(A) m_t'^{0.92} \right)^2 \right]}{\sqrt{N-1}} \quad (2.17)$$

This result only has physical meaning for real values of m_t' ; complex values cannot be used.

As a result, in order for the result to be useful, the fraction f_c of the distribution of m_t' that is complex must be small. Indeed, as we show later, a criterion based on a critical value of f_c is useful in delineating the domain in which the analytical model provides meaningful results.

2.5 Monte Carlo simulations

Monte Carlo simulations were performed to probe the combined effects of distributions in fiber strength and fiber area and number of tested fibers. The simulations were performed by first generating two sets of N random numbers between 0 and 1, one set each representing cumulative probability of normalized true strength, $\sigma_t/\sigma_{t,o}$, and normalized fiber area, A/\bar{A} . Fiber strengths and fiber areas were taken to follow Weibull and normal distributions, respectively. The corresponding nominal strengths are given by $\sigma_n/\sigma_{t,o} = (\sigma_t/\sigma_{t,o})(A/\bar{A})$. The (biased) nominal Weibull parameters were computed using the maximum likelihood method and the average Weibull modulus was then corrected using appropriate unbiasing factors, in accordance with current test standards (ASTM C1239¹⁹ and EN 843-5²⁰). The estimated true Weibull modulus for each simulation set was calculated from Eqn. (2.9). The ranges of parameter values in the simulations were: $10 \leq N \leq 1000$; $0 \leq Z(A) \leq 0.3$, and $3 \leq m \leq 20$. Each set of simulations was performed 100,000 times; the results that follow represent averages and standard deviations from these 100,000 simulations.

The results are plotted and compared with analytical predictions in Figures 2.1 and 2.4–6. The key observations follow.

- (i) In all cases, the average value of nominal Weibull modulus m_n obtained from MCS is virtually identical to the prediction of Eqn. (2.7) (Figures 2.4(a-b)). This correlation affirms the universality of the analytical model for prediction of systematic errors.
- (ii) The mean nominal strength is essentially equivalent to the mean true average (Figure 2.5). This conclusion is consistent with that drawn from previous studies.^{4, 12}

- (iii) The predicted fiber bundle strength, from Eqns. (2.2), (2.7) and (2.8), agrees well with that obtained from MCS (Figure 2.1).
- (iv) Analytical estimates of the standard deviations of nominal and true Weibull moduli, given by Eqns. (2.13), (2.15) and (2.16), agree well with the MC simulations when $N > 20$. Discrepancies at small sample sizes are consistent with those reported by others.^{21, 22}
- (v) Analytical estimates of the true Weibull modulus obtained by applying Eqn. (2.9) to the nominal Weibull moduli resulting from the MCS generally agree with the true values that had been used as input to the simulations (Figures 2.6(a-b)). But, at some point, the agreement breaks down, as described below.

As suggested by the analytical model, there is a finite probability that, when choosing a random sample of fibers from an infinite population, the resulting CoV of nominal strength will be less than the CoV of fiber area and thus the estimated true Weibull modulus (via Eqn. (2.9)) will be a complex number. This feature is borne out by the MC simulations. The fraction f_c of instances that yield complex values of m_t' from MCS are plotted against $Z(A)m_n'^{0.92}$ in Figure 2.6(d). In this form, results for each sample size N collapse onto a single curve.

An analytical description of f_c is obtained in the following way. It is based on the presumption that m_n' follows a gamma distribution with a cumulative probability given by:

$$F(m_n'; k, \bar{m}_n) = \frac{\int_0^{km_n'/\bar{m}_n} t^{k-1} e^{-t} dt}{\Gamma(k)} = \frac{\gamma\left(k, km_n'/\bar{m}_n\right)}{\Gamma(k)} \quad (2.18)$$

where k is a shape parameter (dependent on sample size N), \bar{m}_n is the mean value of m_n' , and γ is the incomplete gamma function. The fraction f_c of complex results obtained from Eqn. (2.9) is given by the cumulative probability for which $Z(A)m_n'^{0.92} \geq 1$ or equivalently $m_n' \geq Z(A)^{-1/0.92}$. Combining this with Eqn. (2.18) yields:

$$f_c = 1 - \frac{\gamma\left(k, \left[\frac{k}{\bar{m}_n} Z(A)^{1/0.92}\right]\right)}{\Gamma(k)} \quad (2.19)$$

Eqn. (2.19) was fit to the MCS data in Figure 2.6(d). The shape parameter k was found to follow a power law of the form $k = \alpha N^\beta$, with $\alpha = 0.393$ and $\beta = 1.22$. The resulting analytical description of f_c is:

$$f_c = 1 - \frac{\gamma\left(0.393N^{1.22}, \left[\frac{0.393N^{1.22}}{\bar{m}_n} Z(A)^{1/0.92}\right]\right)}{\Gamma(0.393N^{1.22})} \quad (2.20)$$

This equation agrees well with the MCS results; both are shown in Figure 2.6(d).

The point of divergence of the analytical model for the CoV of m_t' and the MCS results in Figure 2.6(c) can be correlated with a critical value of f_c . Thus, a criterion based on the critical value f_c^* can be used to delineate the domain in which the analytical model for m_t' is expected to be accurate and, in turn, the domain in which the CoV of m_t' is unacceptably high (≥ 1). The predicted critical points are indicated by the vertical lines in Figure 2.6(c), for values of $f_c^* = 10^{-3}$ and 10^{-2} . The pair of lines corresponding to each value of N fall close to one another and correlate closely with the point at which the CoV of m_t'

begins to rise very rapidly. This supports the notion that a criterion based on a critical value of f_c can be used to delineate the two domains.

2.6 Applications

The preceding results were used to assess numerous experimental data sets from previous studies. The experimental data are presented in Figure 2.7 in coordinates of $Z(A)m_n'^{0.92}$ and N , as suggested by the analytical model. Also shown in the figure are the critical combinations of $Z(A)m_n'^{0.92}$ and N that delineate the domains in which the Weibull modulus can and cannot be reliably estimated; the two are denoted “valid” and “not valid”. The critical combinations are given by Eqn. (2.20) using $f_c^* = 10^{-2}$ and 10^{-3} . Over this range, the boundary is insensitive to the exact choice of f_c^* .

Data sets for Nextel™ 610 fibers and most AYE fibers fall within the valid domain, due mainly to the low variability in the fiber areas. But many others – including those for Nicalon™ fibers – do not. Indeed, almost all data sets on Nicalon™ fibers reported by Petry *et al.*⁴ fall in the invalid domain. The results reported by Hay *et al.* on Hi-Nicalon™ Type S fibers span across the boundary: about a quarter lying in the valid domain. In the latter case, the spread in data is due mainly to large changes in Weibull modulus following certain types of fiber treatments. The implication is that, although the test results lying above the boundary may have utility in comparative studies of *mean* fiber strengths, they are not predicted to yield sufficiently accurate results for estimating true Weibull moduli.

The current analytical framework is superior to the iterative numerical procedure that had been developed by Parthasarathy¹² to achieve similar goals. As noted previously, the

numerical procedure converges to the correct (unbiased) value of m_t only when $N \geq 200$. For sample sizes typically used for fiber strength characterization (say $N=50$), the numerical procedure significantly over-estimates m_t . In contrast, for the same sample size ($N=50$), the analytical method presented here would yield an average value of m_t' that lies within 10% of the true value, provided $Z(A)m_t'^{0.92} \leq 1$; the resulting random error would be $S'(m_t')/m_t' \approx 0.2$.

The range of parameter values over which Parthasarathy's iterative numerical procedure yielded reasonably accurate estimates of the true Weibull modulus (presented in his Figure 2.7(a)) are superimposed on the current Figure 2.7. (For this purpose, nominal Weibull moduli were computed using Eqn. (2.7) and combined with the reported CoVs of fiber area to obtain the quantity $Z(A)m_n'^{0.92}$.) The entire range falls well within the valid domain. That is, the present analytical framework could accurately estimate Weibull moduli for the entire parameter range probed by Parthasarathy, obviating the need for the iterative numerical procedure. Furthermore, the minimum number of tests required to accomplish this goal would be significantly less than 200. For example, for the highest point in Parthasarathy's range (corresponding to $Z(A)m_n'^{0.92} = 0.77$), the minimum number would be about 60; random errors would yield $S'(m_t')/m_t' \approx 0.2$. At the low end ($Z(A)m_n'^{0.92} = 0.29$), as few as 20 tests would be adequate to compute the true Weibull modulus with a random error of $S'(m_t')/m_t' \approx 0.2$.

2.7 Summary and conclusions

An analytical framework to address both systematic and random errors in Weibull moduli inferred from nominal strength measurements on individual fibers has been developed. The framework is based on uncertainty propagation analysis and supported by exhaustive MC simulations. In summary, the key results include:

- (i) the expected value of the *nominal* Weibull modulus and its statistical variation (Eqns. (2.7) and (2.16));
- (ii) estimates of the true Weibull modulus and reference strength from data on nominal strengths that account for *systematic* errors (Eqns. (2.9) and (2.10));
- (iii) the uncertainty in the inferred Weibull modulus that arises from *random* errors (Eqn. (2.17)); and
- (iv) critical combinations of $Z(A)m_n'^{0.92}$ and N within which the estimated Weibull modulus should have reasonable accuracy (Eqn. (2.20) with $f_c^* \approx 10^{-3} - 10^{-2}$).

The possibility of obtaining complex values of m_t' had not been identified previously through the MCS results presented by Parthasarathy¹² or Lara-Curzio and Russ¹³. This oversight was almost certainly a consequence of the small number of simulations that had been performed for each parameter set (1 and 10, respectively). Because the probability of obtaining a complex result is generally very small, the result usually emerges only from a very large number of simulations. Indeed, having repeated each simulation 100,000 times, we occasionally encountered such events, even in cases in which the events are very scarce. Complex values of m_t' are also obtained from our analytical model (evident in Eqn. (2.9)) and can be readily understood in terms of the CoVs of fiber strength and fiber area. That is,

complex values are obtained when the CoV of nominal strength of a sample population is less than the CoV of fiber area.

Finally, with estimates of CoVs of fiber area and fiber strength, the analytical framework can be used to estimate the minimum number of tests that would yield high-fidelity results without having to resort to measuring individual fiber areas. Three examples are used to provide broad guidelines. (i) When the CoV ratio is small, *e.g.* $Z(A)m_t'^{0.92} \leq 0.5$, as few as 20 tests would yield adequate estimates of m_t , with a random error of $S'(m_t')/m_t' \approx 0.2$. (ii) For higher values, say $Z(A)m_t'^{0.92} \approx 1$, about 50 tests would be required to obtain results with comparable fidelity. (iii) For even higher values, say $Z(A)m_t'^{0.92} \geq 2$, the minimum number exceeds 1000. In this case, the time benefit derived from using only average fiber areas would be outweighed by the need for an excessively large number of tests. That is, the additional effort required to measure individual fiber areas would be offset by the reduced number of required tests: the latter dropping from over 1000 to about 30.

Acknowledgements

This work was supported by the Pratt & Whitney Center of Excellence in Composites at the University of California, Santa Barbara.

References

- ¹ ASTM C1557-14, “Standard Test Method for Tensile Strength and Young’s Modulus of Fibers,” (2014).

- 2 C.T. Li and J. V. Tietz, “Improved accuracy of the laser diffraction technique for
diameter measurement of small fibres,” *J. Mater. Sci.*, **25** [11] 4694–4698 (1990).
- 3 D.M. Wilson, “Statistical tensile strength of Nextel™ 610 and Nextel™ 720 fibres,”
J. Mater. Sci., **32** [10] 2535–2542 (1997).
- 4 M.D. Petry, T.I. Mah, and R.J. Kerans, “Validity of using average diameter for
determination of tensile strength and Weibull modulus of ceramic filaments,” *J. Am.
Ceram. Soc.*, **80** [10] 2741–2744 (1997).
- 5 R.S. Hay and E.E. Boakye, “Monazite Coatings on Fibers: I, Effect of Temperature
and Alumina Doping on Coated-Fiber Tensile Strength,” *J. Am. Ceram. Soc.*, **84** [12]
2783–2792 (2001).
- 6 E.E. Boakye and P. Mogilevsky, “Fiber Strength Retention of Lanthanum- and
Cerium Monazite-Coated Nextel™ 720,” *J. Am. Ceram. Soc.*, **87** [2] 314–316 (2004).
- 7 E.E. Boakye, P. Mogilevsky, T.A. Parthasarathy, R.S. Hay, J. Welter, and R.J.
Kerans, “Monazite Coatings on SiC Fibers I: Fiber Strength and Thermal Stability,”
J. Am. Ceram. Soc., **89** [11] 3475–3480 (2006).
- 8 M.K. Cinibulk, G.E. Fair, and R.J. Kerans, “High-temperature stability of lanthanum
orthophosphate (monazite) on silicon carbide at low oxygen partial pressures,” *J. Am.
Ceram. Soc.*, **91** [7] 2290–2297 (2008).
- 9 R.S. Hay, G.E. Fair, R. Bouffieux, E. Urban, J. Morrow, A. Hart, and M. Wilson,
“Relationships Between Fiber Strength, Passive Oxidation and Scale Crystallization
Kinetics of Hi-Nicalon™-S SiC Fibers,” *Ceram. Eng. Sci. Proc.*, **32** 39–51 (2011).
- 10 R.S. Hay, G.E. Fair, A. Hart, S. Potticary, and R. Bouffieux, “Kinetics of Passive
Oxidation of Hi-Nicalon-S SiC Fibers in Wet Air: Relationships between SiO₂ Scale

- Thickness, Crystallization, and Fiber Strength”; pp. 253–260 in *Mech. Prop. Perform. Eng. Ceram. Compos. VII*. 2012.
- ¹¹ R.S. Hay, G.E. Fair, and T. Tidball, “Fiber Strength After Grain Growth in Nextel™ 610 Alumina Fiber,” *J. Am. Ceram. Soc.*, **98** [6] 1907–1914 (2015).
- ¹² T.A. Parthasarathy, “Extraction of Weibull parameters of fiber strength from means and standard deviations of failure loads and fiber diameters,” *J. Am. Ceram. Soc.*, **84** [3] 588–592 (2001).
- ¹³ E. Lara-Curzio and C.M. Russ, “On the relationship between the parameters of the distributions of fiber diameters, breaking loads, and fiber strengths,” *J. Mater. Sci. Lett.*, **18** [24] 2041–2044 (1999).
- ¹⁴ D.M. Wilson and L.R. Visser, “High performance oxide fibers for metal and ceramic composites,” *Compos. - Part A Appl. Sci. Manuf.*, **32** [8] 1143–1153 (2001).
- ¹⁵ A.R. Bunsell and A. Piant, “A review of the development of three generations of small diameter silicon carbide fibres,” *J. Mater. Sci.*, **41** [3] 823–839 (2006).
- ¹⁶ T. Morimoto and T. Ogasawara, “Potential strength of Nicalon™, Hi Nicalon™, and Hi Nicalon Type S™ monofilaments of variable diameters,” *Compos. Part A Appl. Sci. Manuf.*, **37** [3] 405–412 (2006).
- ¹⁷ H.E. Daniels, “The Statistical Theory of the Strength of Bundles of Threads. I,” *Proc. R. Soc. A Math. Phys. Eng. Sci.*, **183** [995] 405–435 (1945).
- ¹⁸ W. Weibull, “A statistical theory of the strength of materials,” *R. Swedish Inst. Eng. Res.*, **151** 1–45 (1939).
- ¹⁹ ASTM C1239-13, “Standard Practice for Reporting Uniaxial Strength Data and Estimating Weibull Distribution Parameters for Advanced Ceramics,” (2013).

- ²⁰ EN 843-5, “Advanced technical ceramics. Mechanical properties of monolithic ceramics at room temperature. Statistical analysis,” (2006).
- ²¹ K. Trustrum and A. de S. Jayatilaka, “On estimating the Weibull modulus for a brittle material,” *J. Mater. Sci.*, **14** 1080–1084 (1979).
- ²² A. Khalili and K. Kromp, “Statistical properties of Weibull estimators,” *J. Mater. Sci.*, **26** 6741–6752 (1991).

Table 2.1 Distributions of fiber areas of commercial SiC fibers

Fiber type	Number of measurements	\bar{A} (μm^2)	$S(A)$ (μm^2)	$Z(A)$
Nicalon™	427	143	34	0.24
Hi-Nicalon™	385	140	26	0.19
Hi-Nicalon™-S	295	117	25	0.21

Table 2.2 Nomenclature

σ_t	– true strength	σ_n	– nominal strength
$\sigma_{t,o}$	– true reference strength	$\sigma_{n,o}$	– nominal reference strength
$\bar{\sigma}_t$	– mean true strength	$\bar{\sigma}_n$	– mean nominal strength
$S(\sigma_t)$	– standard deviation of σ_t	$S(\sigma_n)$	– standard deviation of σ_n
$S'(\bar{\sigma}_t')$	– standard deviation of $\bar{\sigma}_t'$	$S'(\bar{\sigma}_n')$	– standard deviation of $\bar{\sigma}_n'$
$S'(S'(\sigma_t))$	– standard deviation of $S'(\sigma_t)$	$S'(S'(\sigma_n))$	– standard deviation of $S'(\sigma_n)$
$Z'(\sigma_t)$	– CoV of σ_t ($= S'(\sigma_t)/\bar{\sigma}_t'$)	$Z'(\sigma_n)$	– CoV of σ_n ($= S'(\sigma_n)/\bar{\sigma}_n'$)
$S'(Z'(\sigma_t))$	– standard deviation of $Z'(\sigma_t)$	$S'(Z'(\sigma_n))$	– standard deviation of $Z'(\sigma_n)$
m_t	– true Weibull modulus	m_n	– nominal Weibull modulus
$S'(m_t)$	– standard deviation of m_t'	$S'(m_n)$	– standard deviation of m_n'
$P_f(\sigma_t)$	– failure probability	$Q_f(\sigma_n)$	– failure probability
R	– fiber radius	R_o	– reference radius
L	– fiber length	L_o	– reference length
A	– fiber area	\bar{A}	– average fiber area
$S(A)$	– standard deviation of A	$Z(A)$	– CoV of A ($= S(A)/\bar{A}$)
N	– number of fibers	$h(A)$	– probability density of A

The symbol ' denotes an estimated quantity obtained from a finite sample size

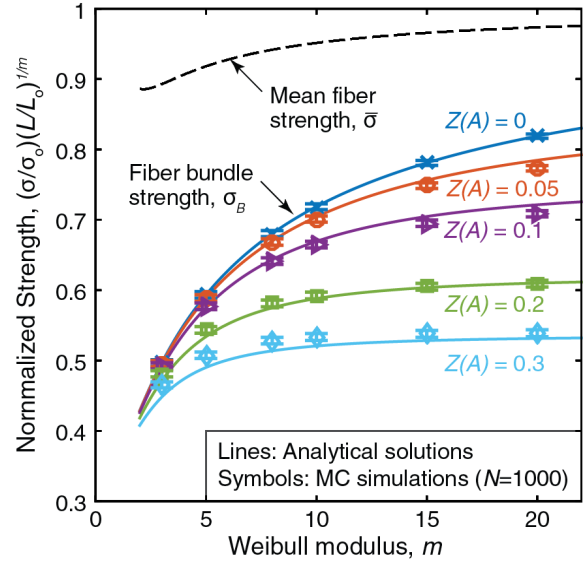


Figure 2.1: Effects of Weibull modulus on mean fiber strength (Eqn. (2.3)) and fiber bundle strength (Eqn. (2.2)). Solid lines are bundle strength predictions based on nominal Weibull moduli obtained using average fiber areas (from Eqns. (2.2) and (2.7)).

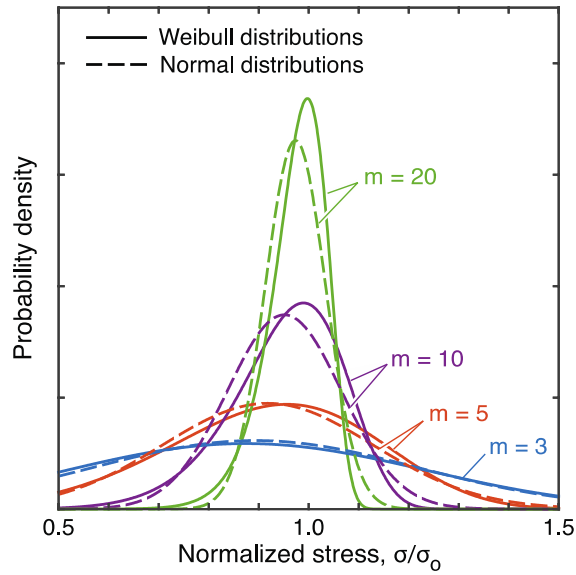


Figure 2.2: Comparisons of Weibull and normal distributions with equivalent mean strengths and CoVs.

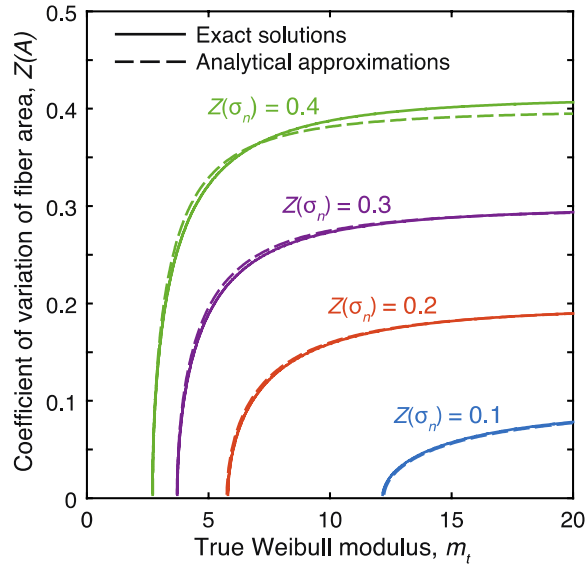


Figure 2.3: Combined effects of fiber area distribution (characterized by $Z(A)$) and true fiber Weibull modulus m_t on the CoV of the nominal strength distribution. Solid lines are from numerical solutions to the convolution integral in Eqn. (2.5) and dashed lines are based on the approximation in Eqn. (2.6).

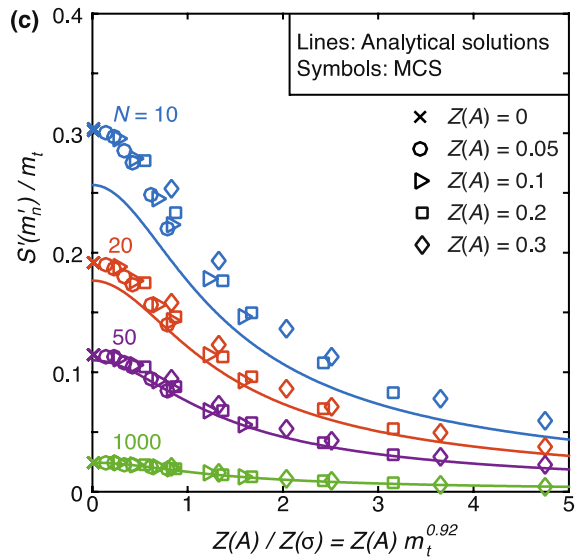
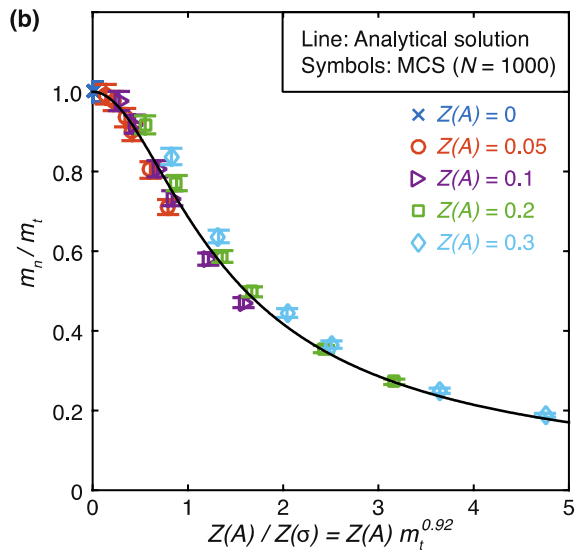
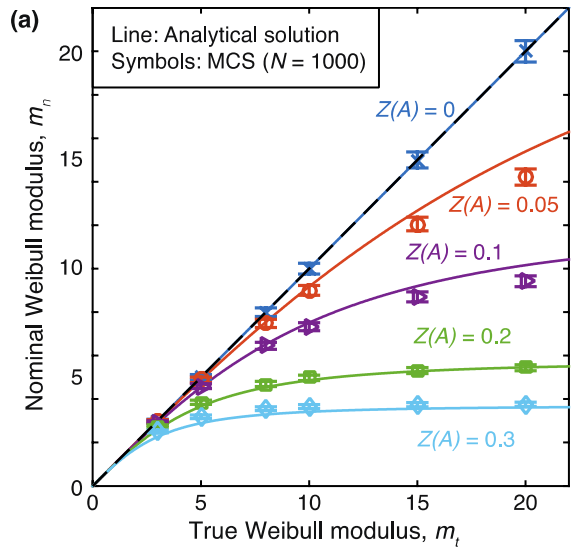


Figure 2.4: (a) Effects of $Z(A)$ on nominal Weibull modulus, from MCS (symbols) and predictions of Eqn. (2.7) (solid lines). (b) Results in (a) re-plotted as m_n/m_t vs. $Z(A)m_t^{0.92}$, showing collapse of all data onto a single curve. Error bars represent \pm one standard deviation from the mean. (c) Effects of sample size on standard deviation of nominal Weibull modulus. Solid lines are predictions of Eqn. (2.16) and symbols are from MCS.

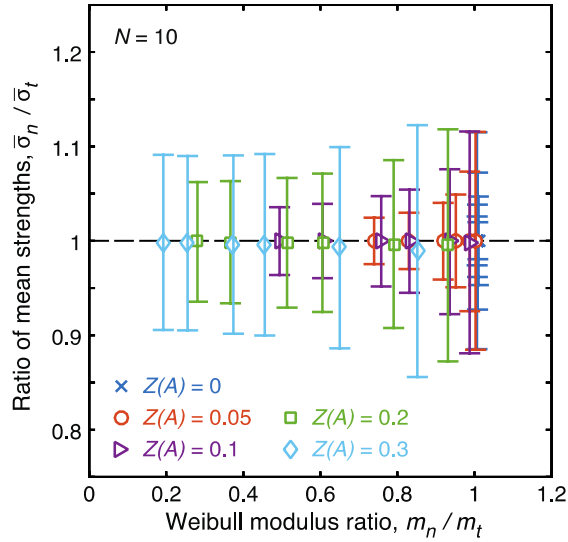


Figure 2.5: MCS results for $N = 10$, re-affirming that the average nominal fiber strength $\bar{\sigma}_n$ is the same as the true value $\bar{\sigma}_t$. Similar results are obtained for larger values of N , but with progressively decreasing standard deviation.

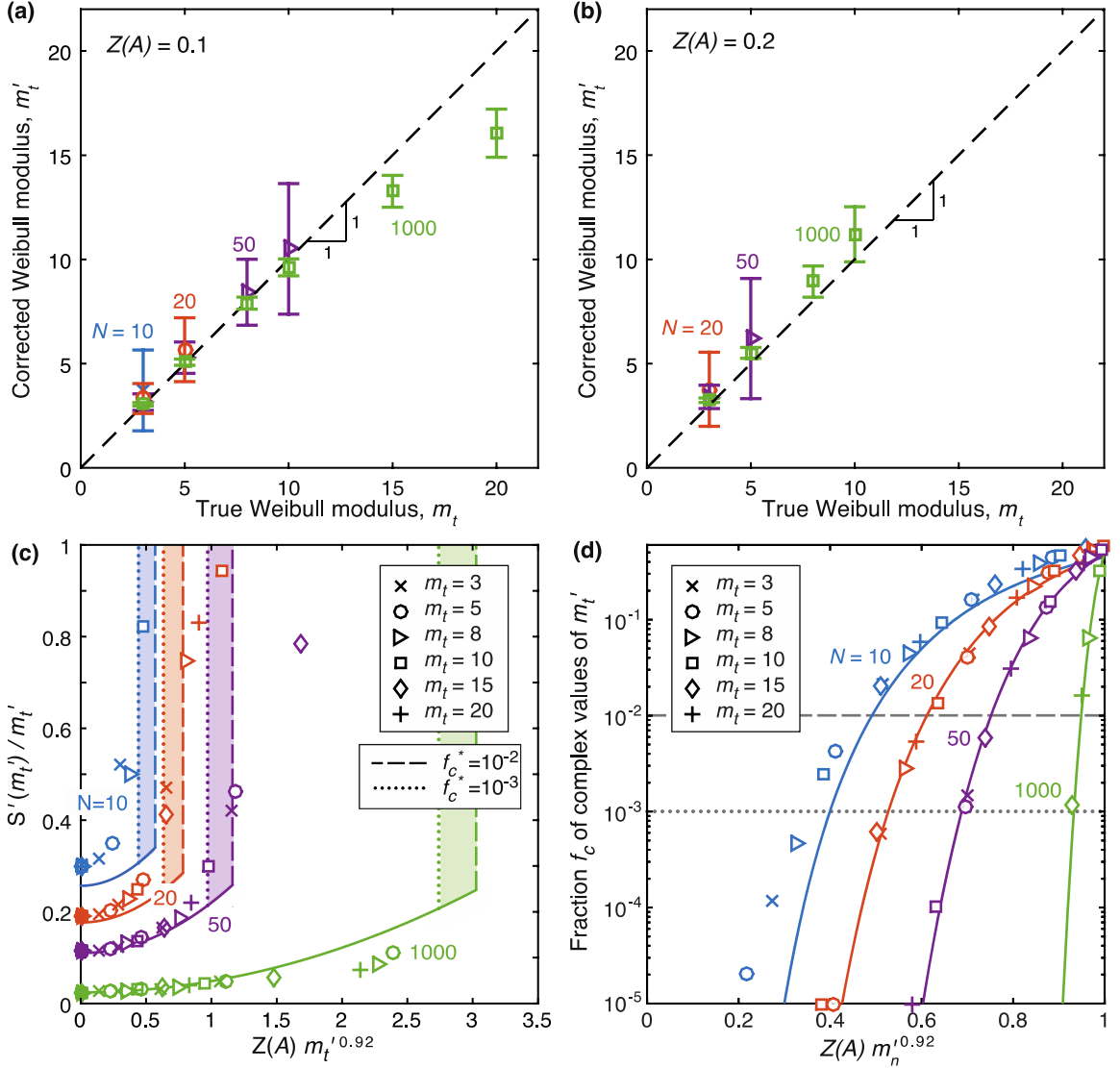


Figure 2.6: Estimates of true Weibull modulus obtained by combining MCS results with Eqn. (2.9), for (a) $Z(A) = 0.1$ and (b) $Z(A) = 0.2$. Error bars represent \pm one standard deviation from the mean. (c) Standard deviation of estimated true Weibull modulus, plotted against $Z(A)m_t^{0.92}$. Only real values of m_t' from MCS were used to calculate standard deviations. Solid lines are from Eqn. (2.17). These lines are terminated at a critical value of f_c^* : either 10^{-2} or 10^{-3} . Beyond these points, the fraction of complex values of m_t' becomes significant and the CoV of m_t' increases rapidly beyond acceptable limits (≥ 1). (d) Fraction of cases that lead to complex values of m_t' . Solid lines are from Eqn. (2.20). Critical values of f_c^* (10^{-2} and 10^{-3}) used in (c) are also indicated by horizontal lines.

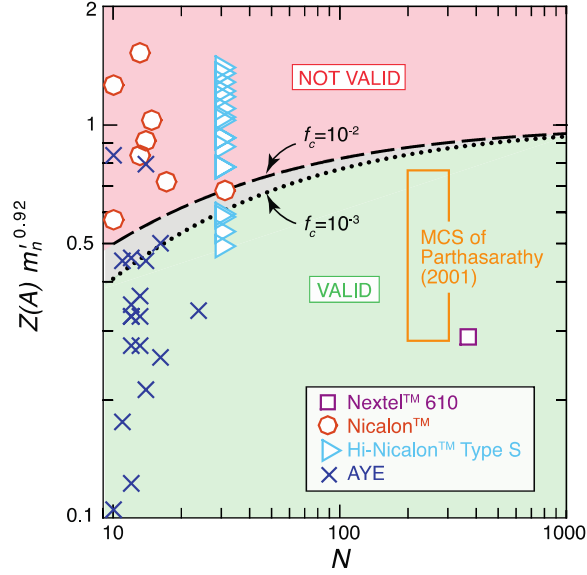


Figure 2.7: Summary of experimental data obtained from studies in which nominal strength distributions were used to estimate Weibull moduli and in which CoVs of fiber area had been reported. Curves represent combinations of $Z(A)m_n'^{0.92}$ and N for which $f_c^* = 10^{-2}$ or 10^{-3} (from Eqn. (2.20)). Only data points that reside below this curve are predicted to yield valid estimates of m_t . Experimental data include those for Nicalon^{TM4}, Hi-NicalonTM Type S¹⁰, AYE⁴, and NextelTM 610¹⁴. The parameter range examined by Parthasarathy¹² with MCS is also indicated.

Chapter 3

Strengths of ceramic fiber bundles: Theory and practice^{*}

Abstract

The Weibull modulus and reference strength of ceramic fibers can be inferred from measurements of the tensile stress-strain response of a bundle of such fibers. The goal of the present chapter is to address issues in the fidelity of results stemming from fiber bundle tests and strategies to optimize outcomes. The issues are addressed through established theorems in uncertainty propagation, Monte Carlo simulations of fiber bundle fracture, and experimental measurements on bundles of SiC fibers of various length and surface condition. The study shows that optimal results are obtained when: (i) tests are performed on fiber bundles with a gauge length that exceeds a critical value (specifically, that needed to prevent mechanical instabilities in the post-load-maximum domain); (ii) bundles are lubricated with a low-viscosity oil, to mitigate both inter-fiber friction and dynamic coupling associated with release waves following fiber fracture; and (iii) the Weibull parameters are obtained by directly fitting the measured stress-strain curves with the function predicted by fiber bundle theory, rather than using methods based on either linear regression analysis of Weibull probability plots or fitting of the peak stress and strain alone.

^{*} The content of this chapter has previously appeared in the Journal of the American Ceramic Society (**Evan Benjamin Callaway** and Frank W. Zok, “Strengths of ceramic fiber bundles: Theory and practice,” *J. Am. Ceram. Soc.*, **100** [11] 5306–5317 (2017)). It is reproduced here with the permission of John Wiley and Sons.

3.1 Introduction

Determining strengths of high-performance ceramic fibers is challenging because of the small diameter of such fibers (ca. 10 μm) and the inherent variability in their strength. Strength measurements are typically made in one of two ways. In the first, tensile tests are performed on individual fibers. The parameters that characterize the strength distribution – typically the Weibull modulus and the reference strength – are obtained from the measurements using the maximum likelihood method.^{1, 2} Although in principle the method is straightforward, it requires a large number of tests (≥ 30) and involves the tedious task of measuring areas of individual tested fibers. Commonly, for expediency, the areas of tested fibers are not measured; instead, the *average* fiber area (measured from a polished cross-section of a representative fiber bundle) is used in combination with failure loads to compute *nominal* strengths.³ The nominal strengths are then used to obtain the Weibull parameters. But, being a convolution of the true fiber strength and fiber cross-sectional area, the nominal strength distribution is inherently broader than the true strength distribution. In turn, the apparent Weibull modulus obtained from nominal strengths is lower than the true Weibull modulus.^{4, 5}

Alternatively, fiber strength distributions can be inferred from tensile tests on bundles comprising hundreds or thousands of aligned fibers. The principal advantage of this method is that strengths of many fibers are determined in a single test. Moreover, bundle tests obviate the selection bias that is inherent to single fiber tests. That is, when performing single fiber tests, weaker fibers are more likely to break during extraction from the bundles; these fibers are naturally excluded from the sample population. Additionally, fibers with the

smallest diameters are probably less likely to be selected for testing, because of the increased difficulty in handling and testing them.^{6,7}

Measured stress-strain curves from bundle tests can be interpreted using classical fiber bundle theory.^{6,8,9} The theory is predicated on two key assumptions: (i) that all fibers are loaded uniformly and equally, and (ii) that the fibers do not interact mechanically with one another either before or after they break. The first condition requires exceptionally well-aligned fibers and a scheme for gripping and loading that ensures equal displacement of all fiber ends. The second condition can be facilitated through the use of fluid lubricants that minimize friction between broken and intact fibers.¹⁰⁻¹⁷ Lubricants may also dampen dynamic release waves resulting from fiber failure.¹

In order to fully exploit information about each fiber failure event in a bundle test, the loading system must be sufficiently stiff to allow for stable fiber bundle rupture, including the softening, post-load-maximum part of the stress-strain response. Otherwise the test results represent only the low end of the strength distribution and are therefore biased. Mechanical instabilities at or near the load maximum are common, even under displacement-controlled loading conditions.^{7, 14} Such instabilities may be exacerbated by inter-fiber friction. That is, if friction leads to cooperative fiber failure, the local softening rate may be anomalously high and the conditions for further stable fiber fracture may be difficult to attain.¹² Dynamic coupling due to release waves may yield analogous effects. One of the goals of the present study is to assess such effects experimentally.

An additional challenge in performing fiber bundle tests involves strain measurement. Fracture strains of high modulus ceramic fibers are typically about 0.5%. Thus, to adequately capture the entire stress-strain curve, the strains must be resolved at a

level of about 0.01%. Although extensometers and strain gauges can achieve this resolution, neither can be used directly on fiber bundles. Non-contacting measurements based, for example, on optical imaging and digital image correlation (DIC) are preferred. But even these methods are problematic when applied directly on fiber bundles, because fiber breaks are not manifested as uniform strains on the bundle surface.

Several methods have been used in the past to infer the Weibull parameters from test data on fiber bundles. Most commonly it has been accomplished by (i) fitting the peak stress and corresponding strain to the values predicted by bundle theory^{6, 11–13, 18, 19}, (ii) constructing a Weibull-like plot from the stress-strain data and performing a linear regression analysis of the data^{6, 7, 20, 21, 11–17, 19}, or (iii) fitting the stress-strain data directly to the functional form predicted by fiber bundle theory^{15–17}. The efficacy of these methods in inferring the Weibull parameters have not been addressed. Indeed, presently there are no established standards for analyzing and interpreting fiber bundle tensile tests.

The present chapter addresses the theory and the practice of fiber bundle testing. The focus is on development of reliable experimental test methods, interpretation of experimental measurements, and assessment of accuracy and precision of inferred Weibull parameters. The latter issues are addressed through established theorems in uncertainty propagation as well as Monte Carlo simulations of fiber bundle fracture, incorporating effects of intrinsic strength variability of the constituent fibers, number of fibers in the bundle, and random errors in stress and strain measurements. The theoretical aspects are complemented by experimental measurements on bundles of SiC fibers of various length and surface condition.

The remainder of the chapter is organized in the following way. First, in Section 3.2, a brief review and key results of fiber bundle theory and weakest link fracture statistics are presented. Next, in Section 3.3, an analysis of the effects of system compliance is presented. A key result is the identification of a critical gauge length needed to prevent mechanical instability during a fiber bundle test. The analytical results of Sections 3.2 and 3.3 are assessed in Section 3.4 through exhaustive Monte Carlo simulations (MCS). Finally, in Section 3.5, results of an experimental study on SiC fiber bundles are presented and discussed in the context of the underpinning theory.

3.2 Fiber bundle theory: Determining Weibull parameters and their uncertainties

Fiber bundle theory relates the load P to the corresponding strain ε during tensile loading. It is based on the assumptions that all fibers are loaded uniformly and that the fibers do not interact mechanically with one another. The *nominal* bundle stress is defined as $\sigma_{nom} = P/\hat{A}N_o$ where N_o is the number of fibers in the bundle and \hat{A} is the average fiber area. If the fibers are elastic to fracture, the nominal stress becomes $\sigma_{nom} = \varepsilon E N_i/N_o$ where E is Young's modulus and N_i is the current number of intact fibers. Here N_i/N_o is the fraction of intact fibers which, when N_o is sufficiently large, represents the survival probability, P_s . For a Weibull distribution, the general form of P_s is:

$$P_s = 1 - P_f = \exp \left\{ - \left(\frac{L}{L_o} \right) \left(\frac{R}{R_o} \right)^\beta \left(\frac{\sigma}{\sigma_o} \right)^m \right\} \quad (3.1)$$

where P_f is cumulative failure probability; L_o and R_o are reference values of length and radius; σ is the tensile stress; σ_o is the reference strength; m is the Weibull modulus; and

β is a coefficient that depends on the distribution of strength-controlling flaws. Specifically, $\beta = 2$ when the flaws are distributed randomly throughout the fiber volume and $\beta = 1$ when the flaws are distributed randomly over the fiber surface. Assuming all fibers have the same radius ($R = R_o$), the nominal stress-strain response of the fiber bundle becomes:

$$\sigma_{nom} = \varepsilon E \exp \left[-\frac{L}{L_o} \left(\frac{\varepsilon E}{\sigma_o} \right)^m \right] \quad (3.2)$$

The maximum nominal stress, defined as the bundle strength σ_B , and the corresponding bundle strain ε_B are obtained by setting $d\sigma_{nom}/d\varepsilon = 0$. The results are⁸

$$\frac{\sigma_B}{\sigma_o} = \left(\frac{Lme}{L_o} \right)^{-1/m} \quad \text{and} \quad \varepsilon_B = \frac{\sigma_o}{E} \left(\frac{Lm}{L_o} \right)^{-1/m} \quad (3.3)$$

where e is the base of the natural logarithm (≈ 2.718).

The Weibull parameters for the constituent fibers can be inferred from bundle tests by one of three methods. (i) The simplest is to combine σ_B and ε_B with Eqn. (3.3) to compute m and σ_o .^{6, 11–13, 18, 19} As we show later, this method is inherently the least precise; most of the data are neglected and hence random errors are high. (ii) The data can be more fully exploited by constructing a Weibull plot, couched in terms of $\ln[\ln(\varepsilon E/\sigma_{nom})]$ vs. $\ln(\varepsilon)$, and performing a linear regression analysis on the results.^{6, 7, 20, 21, 11–17, 19} Although in principle this method is more reliable than the first, it is prone to both systematic and random errors associated with strain measurements (detailed below).^{16, 17} (iii) The most direct method is to perform a least-squares fit (LSF) of the entire stress-strain data with the

function predicted by fiber bundle theory, notably Eqn. (3.2).¹⁵⁻¹⁷ As we show, this method is less prone to the bias produced by the data in the low strain domain in a Weibull plot.

The magnitudes of random errors in the Weibull parameters inferred from a test on a bundle with a *finite* number N of fibers are obtained from uncertainty propagation analysis. The analysis is predicated on the assumptions that the parameters of interest are approximately normally distributed and that their coefficients of variation (CoV) are sufficiently small (say, ≤ 0.3). The strengths in a Weibull distribution satisfy these requirements for realistic Weibull moduli ($3 \leq m \leq 20$). Some basic results were derived previously.²² The CoV of the mean fiber strength, $\hat{\sigma}$, is $Z(\hat{\sigma}) = Z(\sigma)/\sqrt{N}$ where $Z(\sigma)$ is the CoV of the strength distribution, given by $Z(\sigma) = m^{-0.92}$. In turn, the CoV of $Z(\sigma)$ is $Z(Z(\sigma)) = 1/\sqrt{2N}$ and the CoV of m is $Z(m) = 0.77/\sqrt{N}$.

The CoV of σ_o is derived in the following way. First, σ_o is related to $\hat{\sigma}$ and m by:²³

$$\sigma_o = \hat{\sigma} (L/L_o)^{1/m} / \Gamma(1+1/m) \quad (3.4)$$

where Γ is the gamma function. The variance of σ_o , denoted $S^2(\sigma_o)$, is given by:

$$S^2(\sigma_o) = S^2(\hat{\sigma}) \left(\frac{\partial \sigma_o}{\partial \hat{\sigma}} \right)^2 + S^2(m) \left(\frac{\partial \sigma_o}{\partial m} \right)^2 + S^2(m, \hat{\sigma}) \frac{\partial \sigma_o}{\partial \hat{\sigma}} \frac{\partial \sigma_o}{\partial m} \quad (3.5)$$

where $S^2(\hat{\sigma})$ and $S^2(m)$ are the variance of $\hat{\sigma}$ and m and $S^2(m, \hat{\sigma})$ is the covariance between m and $\hat{\sigma}$. For realistic Weibull moduli ($m > 3$), the first term on the right side of Eqn. (3.5) dominates, because σ_o is a much stronger function of $\hat{\sigma}$ than of m . Dropping the last two terms yields $Z(\sigma_o) \approx Z(\hat{\sigma}) = m^{-0.92}/\sqrt{N}$. This result indicates that the random

error in σ_o is significantly lower than that of m : the ratio of their CoVs scaling roughly as $1/m$. The validity of these results is assessed by MCS in Section 3.4.

3.3 Critical gauge length for stable response

The tensile stability of a fiber bundle under ideal loading conditions (with uniform fiber loading and without misalignment) can be addressed through a rudimentary mechanics analysis. To this end, the remote displacement δ is partitioned into two components: one, δ_f , due to extension of the fiber bundle, and the other, δ_m , due to elastic extension of the load train (grips, load cell, etc.) (Figure 3.1a). The latter is $\delta_m = CP$ where C is the compliance of the load train and the load P is obtained from the nominal stress in Eqn. (3.2):

$$P = \frac{A\delta_f E}{L} \exp \left\{ - \left(\frac{L}{L_o} \right) \left(\frac{\delta_f E}{L\sigma_o} \right)^m \right\} \quad (3.6)$$

Load-displacement curves for three combinations of bundle gauge length and load-train compliance are shown in Figure 3.1b. When the compliance is high and/or the gauge length is small, the curve exhibits a snap-back instability shortly beyond the peak (blue curve). In practice, under displacement-controlled conditions, the load would drop unstably to zero at the first point at which $dP/d\delta = -\infty$. Conversely, when the compliance is low and/or the gauge length is high, the entire load-displacement curve, including the softening portion, would be obtained without instability (green curve). There exists a critical combination of properties at which the response transitions from one to the other (red curve). This combination is obtained when $dP/d\delta = -\infty$ and $d^2P/d\delta^2 = 0$, *i.e.* when the point of maximum displacement is also an inflection point.

The first of these two conditions, $dP/d\delta = -\infty$, is met when

$$dP/d\delta_f = -dP/d\delta_s = -1/C \quad (3.7)$$

Differentiating Eqn. (3.6) and combining the result with Eqn. (3.7) yields:

$$\left(\frac{EAC}{L}\right) \left[m \left(\frac{\delta_f E}{L\sigma_o}\right)^m - 1 \right] \exp \left\{ - \left(\frac{\delta_f E}{L\sigma_o}\right)^m \right\} = 1 \quad (3.8)$$

The second condition, $d^2P/d\delta^2 = 0$, is satisfied when (from Eqn. (3.6))

$$\frac{\delta_f E}{L\sigma_o} = \left(\frac{1}{m} + 1\right)^{1/m} \quad (3.9)$$

In turn, combining Eqns. (3.8) and (3.9) yields a critical gauge length:

$$L^* = mEAC e^{-(1+1/m)} \quad (3.10)$$

The response is predicted to be stable throughout when $L > L^*$.

When $L < L^*$, stress-strain data can only be obtained up to the point of instability.

From Eqns. (3.8) and (3.9), the fraction P_f^* of fibers whose strength is measured before the instability is given by the implicit equation:

$$\frac{L}{L^*} \equiv \tilde{L} = (1 - P_f^*) \left[\ln \left(\frac{1}{1 - P_f^*} \right) - \frac{1}{m} \right] e^{(1+1/m)} \quad (3.11)$$

Eqn. (3.11) is plotted in Figure 3.2 for $3 \leq m \leq 20$. There are two limits of interest. First, when $\tilde{L} \ll 1$, the instability occurs essentially at the peak load and P_f^* approaches $P_f^* = 1 - e^{-1/m}$. In the other limit, wherein $\tilde{L} > 1$, there is no instability and thus $P_f^* = 1$.

When $\tilde{L} < 1$, the number of fibers probed by the test is $N^* = NP_f^*$. The reduced number of represented fibers increases the uncertainty in m , since $Z(m) \propto 1/\sqrt{N}$.²² Furthermore, the N^* fibers that comprise the measured distribution are not a random

sampling of the entire population; instead, they represent the weakest of the population. This bias in sampling is expected to further increase errors in both m and σ_o . The effects on $Z(m)$ are assessed through Monte Carlo simulations presented in the following section.

3.4 Monte Carlo simulations of fiber bundle tensile tests

3.4.1 Numerical procedures

MCS of fiber bundle tests were performed to probe the combined effects of distributions in fiber strength, distributions in fiber area, number of fibers in the bundle and random errors in stress and strain measurements. First, two sets of N random numbers between 0 and 1 were generated: one set each representing the cumulative probability of normalized fiber area, A/\hat{A} , and the strength, σ/σ_o . Fiber areas and fiber strengths were taken to follow normal and Weibull distributions, respectively. The simulations were performed by progressively increasing the applied normalized strain in increments of $\varepsilon/\varepsilon_o = 2 \cdot 10^{-3}$ (where $\varepsilon_o \equiv \sigma_o/E$) until all fibers had failed. At each simulation step, the applied strain was compared to the fracture strain of each surviving fiber. Fractured fibers were subsequently assigned an area of 0. The ranges of parameter values in the simulations were: $100 \leq N \leq 2000$, $3 \leq m \leq 20$, $0 \leq Z(A) \leq 0.3$, and $\beta = 1, 2$.

In some cases, random load and strain errors were introduced after the stresses had been computed (but before the data were analyzed to get σ_o and m). The errors were taken to be normally distributed with root-mean-squared averages $\delta\varepsilon_{RMS}$ and δP_{RMS} . In normalized form, the errors in strain and stress are $\delta\tilde{\varepsilon}_{RMS} = \delta\varepsilon_{RMS}/\varepsilon_o$ and $\delta\tilde{\sigma}_{RMS} = \delta P_{RMS}/A_B\sigma_o$. These normalized errors were varied over the range 10^{-4} to $3 \cdot 10^{-2}$.

Each of the three methods described in Section 3.2 was used to compute the Weibull parameters for each simulation. Each set of simulations was performed 10,000 times; the results that follow represent averages and standard deviations from these 10,000 simulations.

3.4.2 MCS results

The first set of simulations focused on effects of number of fibers in the bundle, fiber area distribution, and fitting method on the inferred Weibull parameters, all for $\tilde{L} > 1$ and without random stress or strain errors. Results are shown in Figure 3.3. Three general conclusions are drawn, all applicable to the three methods employed to infer the Weibull parameters, hereafter denoted \bar{m} and $\bar{\sigma}_o$.

1. The inferred mean values of \bar{m} and $Z(\bar{m})$ are independent of $Z(A)$. This result differs from that obtained from single fiber tests. Notably, when using the average fiber area to compute strengths of individual fibers, the computed value of \bar{m} decreases significantly with increasing $Z(A)$.^{4, 5} The implication is that, to obtain the true Weibull parameters from fiber bundle tests, only the total fiber area (or, equivalently, the average area of individual fibers and the number of fibers in the bundle) is needed.
2. The CoVs of \bar{m} and $\bar{\sigma}_o$ follow the expected scalings with N , notably $Z(\bar{m}) \propto 1/\sqrt{N}$ and $Z(\bar{\sigma}_o)\bar{m}^{0.92} \propto 1/\sqrt{N}$. The same scalings are obtained for individual fiber tests, provided the actual fiber areas are used to compute fiber strengths.²² Herein lies the advantage of fiber bundle tests; since bundles typically contain many hundreds or thousands of fibers, the errors in the Weibull parameters inferred from a single, well-

executed bundle test should be lower than those obtained from even the most exhaustive study on individual fibers.

3. Results for $\beta = 1$ and $\beta = 2$ are almost indistinguishable. The insensitivity to β has also been demonstrated for individual fiber tests.²² The implication is that the flaw type (*i.e.* surface vs. bulk) does not significantly affect interpretation of the bundle tests.

The results in Figure 3.3 also provide an assessment of the accuracy and precision of each of the three methods used for computing $\bar{\sigma}_o$ and \bar{m} . The LSF of the stress-strain curves and the linear regression fit of the Weibull plot give average values of $\bar{\sigma}_o$ and \bar{m} that agree well with their true values. In contrast, the method based on the peak in the stress-strain curve consistently slightly overestimates m . Additionally, the CoVs of $\bar{\sigma}_o$ and \bar{m} from the latter method are significantly higher than those from the other two methods, by factors of about 5 to 10. The high CoV values reflect the fact that the method relies on only one datum point on the stress-strain curve. Although $Z(\bar{m})$ from both the LSF and the linear regression methods follows a $1/\sqrt{N}$ scaling (Figure 3.3b), the proportionality constant for the LSF method is about 25% lower (0.89 vs. 1.20). $Z(\bar{\sigma}_o)$ is also lower for the LSF method (Figure 3.3d), by about 13%. A key conclusion is that the LSF method is preferred for computing $\bar{\sigma}_o$ and \bar{m} from fiber bundle tests.

In a second set of MCS, effects of bundle gauge length, \tilde{L} , on the inferred Weibull parameters and their variations were explored. Here, \tilde{L} was taken to be either 0.25, 0.5, 0.75 or 0.99. The simulations were terminated once the number of broken fibers reached the critical number N^* given by Eqn. (3.11). The Weibull parameters were then computed

using a LSF of the stress-strain data up to the point of instability. The results are shown in Figure 3.4.

Although the values of \bar{m} are in agreement with their true values, the random errors, characterized by $Z(\bar{m})$, increase as \tilde{L} decreases below unity. Here $Z(\bar{m})$ follows a $1/\sqrt{N^*}$ scaling: closely analogous to the $1/\sqrt{N}$ scaling of $Z(\bar{m})$ when $\tilde{L} > 1$ (Figure 3.4b). Nevertheless, the proportionality constant for cases in which $\tilde{L} < 1$ is about 15% greater than that for $\tilde{L} > 1$ (1.05 vs. 0.89). The difference is attributable to the biased nature of the measured sample population when $\tilde{L} < 1$. Similar results are shown for the uncertainty in $\bar{\sigma}_o$ in Figures 3.4c-d. The implication is that, since $N^* \ll N$, errors in the inferred values of $\bar{\sigma}_o$ and \bar{m} are reduced significantly (by as much as a factor of 2–3) when the entire stress-strain curve is obtained in the bundle test without instability.

Effects of random stress and strain errors are shown in Figures 3.5a-b. Results from the LSF method are not affected by the large range of errors investigated in this work. That is, for all combinations of $\delta\tilde{\epsilon}_{RMS}$ and $\delta\tilde{\sigma}_{RMS}$, \bar{m} and $\bar{\sigma}_o$ are equivalent to their true values and the uncertainties remain constant at $Z(\bar{m}) \approx 0.04$ and $Z(\bar{\sigma}_o) \approx 0.01$. In contrast, the results from linear regression fits of Weibull plots are highly sensitive to the errors. For either $\delta\tilde{\epsilon}_{RMS} = 3 \cdot 10^{-3}$ or $\delta\tilde{\sigma}_{RMS} = 3 \cdot 10^{-3}$, \bar{m} is about 20% lower than m . $\bar{\sigma}_o$ is less dependent on the errors; it is only about 1% greater than σ_o when $\delta\tilde{\sigma}_{RMS} = 3 \cdot 10^{-3}$. The origin of this effect is evident upon examination of a typical Weibull plot (Figure 3.5c). Since the data at low strains have a disproportionately large influence on these curves, the strain errors are magnified many-fold when computing the Weibull parameters.

As a practical matter, the latter effects can be mitigated by excluding data in the low strain domain, below a cut-off probability P_f^c , from the linear regression fit. Figure 3.5d shows results for $P_f^c = 0.01, 0.05,$ and 0.10 . The best results are obtained for $P_f^c = 0.1$, although m remains slightly under-predicted when $\delta\tilde{\sigma}_{RMS} = 0.03$.

3.5 Experimental measurements on SiC fiber bundles

3.5.1 Test Procedures

The strength distributions of Hi-Nicalon™ Type S fibers were measured through a series of tensile tests on bundles containing 500 fibers. The cross-sectional area of the bundle was determined from measurements of mass density using a Micromeritics AccuPyc 1340 Pycnometer and the linear density from the mass of a 100 mm length of de-sized bundle. The mass and linear densities were 3.05 g/cm^3 and 195 tex. These values correspond to a cross-sectional area of $6.4 \cdot 10^{-8} \text{ m}^2$. By comparison, the manufacturer's reported values are 3.10 g/cm^3 and 195 tex, virtually identical to those measured here²⁴ (<http://www.ngs-advanced-fibers.com/eng/item/index.html>). The bundles were received with polyvinyl alcohol (PVA) sizing on the fibers.

The first set of tests was performed on bundles with a gauge length of 25 mm. These tests exhibited unstable fracture shortly beyond the load maximum. (Indeed, these tests motivated the stability analysis presented in Section 3.2.) Following further analysis of load-train compliance, the critical gauge length L^* was determined to be about 65 mm. All subsequent tests were performed on bundles with a gauge length of 110 mm.

The bundles were tested in four conditions: (i) as-received, with sizing intact and without additional lubrication, (ii) after de-sizing, without lubrication, (iii) sized, with

additional lubrication, and (iv) after de-sizing, with lubrication. De-sizing was achieved through two sequential dissolution treatments in boiling deionized water for one hour each.²⁵ Special precautions were taken to ensure that the fibers remained bundled and aligned during this process. This goal was achieved in part by placing a drop of cyanoacrylate adhesive on each end of the bundle prior to de-sizing. The bundles were mounted between two pairs of flat fiberglass tabs with epoxy and subsequently mounted in a fiber tensile testing machine. For lubricated samples, a few drops of oil (3-IN-ONE® Multi-Purpose Oil) were applied to the bundle immediately before testing. (Extended soaks of sized fibers in the oil did not reveal any changes in the sizing.) Additional details are found in Appendix 3.A.

Strains were measured by digital image correlation (DIC), using Vic-2D software (Correlated Solutions, Inc., Columbia, SC, USA). In preliminary tests, measurements were made on the tabs in regions close to the gauge section. But even when the measurements were made right at the tab edges (nominally coincident with the ends of the gauge section), the measured strains proved to be slightly anomalously high. The additional apparent strain was found to be caused by the elastic displacement within the adhesive that had been used to attach the bundles to the tabs. This deficiency led to the development of a method in which strains were measured directly on the fibers. To this end, a fine speckle pattern was applied with spray paint onto the fibers at the very ends of the gauge section. To prevent paint from covering the entire bundle surface and potentially infiltrating into the bundle, a mask with narrow slits at each of the two ends of the gauge section was placed over the bundle during painting. An example of a speckle pattern on a tow before and after bundle rupture is shown in Figure 3.6. With only a very small number of fiber breaks in the near-surface region

within the speckled section, the speckle pattern remains intact through to complete bundle rupture.

For tests on bundles with the longer gauge length, two digital cameras (Point Grey Research Grasshopper, Richmond, BC, Canada), each with a CCD resolution of 2448 x 2048 pixels and a 70–180 mm lens (Nikon ED AF Micro Nikkor), were used for imaging: one focused on each of the two ends of the bundle. The magnification of these images was 7.5 $\mu\text{m}/\text{pixel}$. For the shorter gauge length bundles, only one camera could be used for DIC measurements. The corresponding magnification was 12 $\mu\text{m}/\text{pixel}$. This magnification is necessarily lower than that for the larger gauge length, because of the need to capture both ends of the bundle in one field of view. The resolution of the measurements was determined by comparing sequential pairs of DIC images prior to testing. The root-mean-squared errors of the displacement on each half of the sample were found to range from 0.3 to 0.7 μm for both gauge lengths. The corresponding strain resolutions are $2 \cdot 10^{-5}$ and $5 \cdot 10^{-6}$ for 25 mm and 110 mm gauge lengths, respectively. In normalized form, they are $\delta\tilde{\sigma}_{RMS} = 4 \cdot 10^{-4}$ and $9 \cdot 10^{-4}$. The normalized stress errors were estimated to be $\delta\tilde{\sigma}_{RMS} = 8 \cdot 10^{-3}$.

Tests were performed at a nominal strain rate of $2 \cdot 10^{-5} \text{ s}^{-1}$. Images were taken at two frames per second, yielding about 1000 images per test. The stress and strain data were subsequently averaged in bins of five, thereby reducing the stress and strain errors by a factor of $\sqrt{5}$. Thus, the normalized errors for bins of five are $\delta\tilde{\sigma}_{RMS,5} \approx 4 \cdot 10^{-3}$ and $\delta\tilde{\epsilon}_{RMS,5} \approx 4 \cdot 10^{-4}$ for $L = 110 \text{ mm}$. Based on the MCS results, these errors fall in a domain in which the linear regression method is expected to underestimate m by about 10-20% (see

arrows in Figure 3.5a) and in which the LSF method should yield accurate estimates of m . All three methods of computing the Weibull parameters were used to analyze the data.

3.5.2 *Experimental results*

Representative stress-strain curves for the as-received sized fibers (without lubrication) at the two gauge lengths are plotted on Figure 3.7. In all cases, the curves are initially linear, without perceptible curvature. This linearity indicates that the vast majority of fibers are loaded uniformly. Moreover, the measured Young's modulus, from about 20 tow tests, is virtually identical to that reported by the fiber manufacturer: 385 ± 19 GPa vs. 380 GPa²⁴.

As noted previously, bundles with a 25 mm gauge length invariably exhibit unstable fracture shortly after the load maximum. Based on the ratio of the final secant modulus to the initial elastic modulus, $P_f^* \approx 0.24$ (based on five tests). This value agrees well with the expected result of $P_f^* = 0.25$ (from Eqn. 3.11). Such instabilities were not obtained in bundles with a 110 mm gauge length.

The Weibull parameters for these and other tests are summarized in Table 3.1. Although the mean values of \bar{m} and $\bar{\sigma}_o$ for the sized fibers are similar for the two gauge lengths of interest, significantly larger variations are evident for the smaller gauge length. For bundles with a gauge length of 110 mm, the measured variation of \bar{m} is $Z(\bar{m}) = 0.082$. The predicted value (from Figure 3.3b) is similar: $Z(\bar{m}) = 0.040$. The predicted value for $L = 25$ mm is $Z(\bar{m}) = 0.1$ (Figure 3.4b); the measured value is significantly higher ($Z(\bar{m}) = 0.34$). The latter discrepancy is attributed to one outlying datum point (wherein

$\bar{m} \approx 14$) and the small number of bundle tests. Excluding the outlier, $\bar{m} = 7.4$ and $Z(\bar{m}) = 0.049$.

Desizing has three effects. First, it leads to unstable fracture very near the peak, despite the fact that $L > L^*$. Instabilities of this kind have been reported previously for other fiber types and have been attributed to inter-fiber friction.¹² That is, friction is postulated to cause coupled fiber fracture, with weak fibers leading to premature fracture of neighboring strong fibers. Second, the range of strains over which fibers break is unusually narrow. This leads to an anomalously high Weibull modulus: about twice that obtained from other tests. Third, the bundle strength is seemingly reduced by an average of 0.25 GPa. The latter two effects are consistent with the coupling of fiber fractures, which decreases the breadth of the inferred strength distribution and the apparent bundle strength. Evidently the sizing is more effective than bare fiber surfaces in mitigating these effects.

Further insights into the effects of friction were gleaned from tests on sized and de-sized bundles that had been lubricated with oil prior to testing (Table 3.1, Figure 3.7). First, no instabilities were obtained in the de-sized bundles, in sharp contrast to the dry bundles. This result indicates that the oil is effective in mitigating inter-fiber friction. Second, the stress-strain curves of lubricated sized and de-sized fibers are indistinguishable from one another. The implication is that the de-sizing process itself does not affect the intrinsic fiber strength distribution. Finally, the Weibull modulus and the bundle strength of the unlubricated sized bundles are slightly higher (by about 10%) than those of the lubricated bundles. This suggests that, although the sizing is more effective than the bare surfaces in mitigating friction, the oil is more effective than the sizing alone.

Dynamic coupling between fibers during fracture may also affect the experimental results. It is well known that strong fibers often fracture in multiple locations;²⁶ indeed, the ASTM standard for testing monofilaments suggests that vacuum grease be used to dampen the energy of the first fiber fracture event and prevent secondary fractures associated with the release wave.¹ The oil used in the present experiments appears to serve the same function, demonstrated in the following way. After testing, the bundles were gently extruded between two fingers, starting at the tab and proceeding through to the other end of the bundle. For the unlubricated bundles, about half of the fibers were extracted from the bundle through this procedure, indicating that about half of the fibers had broken in at least two locations. Performing this operation on the lubricated bundles (sized or de-sized) did not produce any noticeable fiber debris, indicating that each fiber had broken in only one location.

The Weibull parameters obtained from each of the three fitting methods for the lubricated bundles are shown in Table 3.2. Among the three methods, that based on LSF yields the lowest CoVs of both \bar{m} and $\bar{\sigma}_o$ and, based on the MCS results, is expected to produce the best estimates of the Weibull parameters. Furthermore, the experimental value of $Z(\bar{m})=0.051$ for the LSF method is close to the value obtained from MCS: $Z(\bar{m})=0.040$ for $N=500$.

Although the average value of the Weibull modulus obtained in the current study ($m=6.4\pm 0.3$) is consistent with the range of values obtained in previous studies based on single filament tests ($m\approx 6$)²⁷, the reference strength from the bundle tests is somewhat higher: $\sigma_o=1.98\pm 0.06$ GPa vs. $\sigma_o\approx 1.63$ GPa (both for a reference length $L_0=1$ m). (For a reference length $L_0=25.4$ mm, the reference stress from the present study is

$\sigma_o = 3.52 \pm 0.11$ GPa.) In contrast, both the reference stress and the bundle strength obtained here are somewhat lower than those measured previously on similar fiber bundles ($m = 7.08$ and $\sigma_o = 2.47$ GPa).²⁸ Batch-to-batch variations in properties may contribute somewhat. But other differences, especially those associated with the test methodologies, likely play a role. This issue remains unresolved.

As predicted by the results from the MCS, \bar{m} obtained the peak fit method was larger than that from LSF and had a significantly higher CoV. Similarly, the linear regression method on lubricated bundles yields lower values of \bar{m} , similar values of $\bar{\sigma}_o$ and larger CoVs of both as compared to LSF. As shown through MCS, the linear regression method is the most prone to being influenced by experimental strain and load errors. The effects are evident from examination of the Weibull plots. One such example for a test on a lubricated bundle is shown in Figure 3.8. This plot closely resembles the Weibull plot from MCS in Figure 3.5c.

The Weibull parameters obtained from the linear regression method can be corrected to a large extent by excluding data at low strains. Using a failure probability cut-off $P_f = 0.10$ has three effects on the results. (i) The average Weibull modulus ($\bar{m} = 6.4$) becomes virtually the same as that from LSF ($\bar{m} = 6.4$). (ii) $Z(\bar{m})$ is reduced from 0.20 to 0.037: comparable to the value obtained from LSF (0.051) and to the value obtained from MCS (0.052). (iii) $\bar{\sigma}_o$ remains nearly constant and virtually identical to that from LSF ($\bar{\sigma}_o = 1.98$ GPa).

The small discrepancies between the CoVs obtained from experiments and from MCS are attributable to the relatively small experimental sample population. The CoVs of

the CoVs are expected to scale as $1/\sqrt{2(c-1)}$ where c is number of bundle tests. Thus, for $c = 5$, the CoV of CoVs is about 0.35. Relative differences that fall below this value are not deemed to be statistically significant.

3.6 Summary and conclusions

A combination of theory, MCS and experiments has been used to identify test procedures and analysis protocols for determining the Weibull parameters and their uncertainties from fiber bundle tensile tests. In summary, the key results are:

- (i) Neither small variations in fiber area, characterized by $Z(A)$, nor the nature of flaws (surface vs. bulk, characterized by $\beta = 1$ and 2) have a significant impact on the Weibull parameters obtained from fiber bundle tests.
- (ii) In order to stably capture the entire stress-strain curve, the gauge length must be greater than a critical value (dependent on the fiber properties and the system compliance (Eqn. (3.10)) and the bundles must be properly lubricated, to minimize friction and to dampen stress waves.
- (iii) A least-squared fit of Eqn. (3.2) to the stress-strain data is the preferred method of inferring the Weibull parameters from bundle tests.
- (iv) Because the errors in the inferred Weibull parameters for both single fiber and fiber bundle tests scale as $1/\sqrt{N}$ – with N being either the number of single fiber tests or the number of fibers within a bundle – the bundle tests have the potential for yielding far more precise estimates of m and σ_o .

Acknowledgements

This work was supported by the Pratt & Whitney Center of Excellence in Composites at the University of California, Santa Barbara.

3.A Appendix: Procedures for fiber bundle heat treatment and tensile testing

Careful handling of the tows is necessary in order to maintain good alignment of the fibers. The fibers are generally well aligned within the tows on the spool, but if the fibers become misaligned at any point during the mounting procedure, re-alignment becomes problematic. The following procedure describes a method for maintaining this alignment during the mounting and tensile testing of tows.

A length of tow that is 100 mm longer than the gauge length is cut from the spool. (We typically use a gauge length of 110 mm and therefore cut a length of 210 mm from the spool.) A drop of superglue is placed on each end of the tow. The glue keeps the fibers bundled and aligned during subsequent handling and mounting. The as-received fibers come sized with polyvinyl alcohol (PVA). Tows are de-sized by two sequential dissolutions in boiling deionized water for one hour each.²⁵ The desized bundle may now be heat-treated.

The furnace setup is shown schematically in Figure 3A.1. Two SiC blocks (roughly 2 mm × 2 mm × 0.5 mm) are placed on an alumina Dee tube 125 mm apart from each other (this distance is necessarily larger than the gauge length). The tow is placed on top of these blocks such that it is suspended above the alumina Dee tube. The suspended section of the tow is the gauge length section for the tensile test. Two additional SiC blocks are placed on top of the tow; these blocks hold the tow in place during heat treatment. The glued ends of the tow are cut off in order to prevent deleterious chemical reactions between the

decomposed residue from the glue with the fibers. After heat treatment, a drop of superglue is once again placed on each tow end.

The tow is then mounted between two windowed cardboard tabs with epoxy (Figure 3.A2). The cardboard tabs have a small groove which helps to guide the placement of the tow during mounting. One cardboard tab is placed on the mounting fixture and is held in place by two pins at each end. Strips of double-sided tape are placed on the mounting plate adjacent to the top and bottom of the cardboard tab. The tow is placed on the tab and temporarily held in place by the strips of tape adhered to the mounting plate. Epoxy is placed on the tab and the tow at the two ends and a second tab is laid on top. A weight (~1 kg) is placed on top of the tabs and left for about 12 hours in order for the epoxy to fully set. For accurate strain measurement, digital image correlation (DIC) on the fiber bundle is recommended. For this purpose, spray-paint is used to create a speckle pattern on the bundle at the top and bottom of the gauge length. A mask with 2 mm slits near the edges of the gauge covers the sample during spray-painting. Strain measured via remote displacement may be adequate if one only needs the bundle strength, but not the Weibull parameters or the elastic modulus. To lessen the effects of inter-fiber friction, a few drops of oil (3-IN-ONE® Multi-Purpose Oil) are applied to the bundle immediately before testing. The window-type specimen is then mounted in the tensile fixture (Figure 3.A3). A typical crosshead displacement rate is 0.15 mm/min for samples with a 110 mm gauge length; other rates can be used, provided the DIC data acquisition system is capable of capturing a suitable number of images over the duration of the test (about 100).

References

- 1 ASTM C1557-14, “Standard Test Method for Tensile Strength and Young’s Modulus
of Fibers,” (2014).
- 2 ASTM C1239-13, “Standard Practice for Reporting Uniaxial Strength Data and
Estimating Weibull Distribution Parameters for Advanced Ceramics,” (2013).
- 3 M.D. Petry, T.I. Mah, and R.J. Kerans, “Validity of using average diameter for
determination of tensile strength and Weibull modulus of ceramic filaments,” *J. Am.
Ceram. Soc.*, **80** [10] 2741–2744 (1997).
- 4 E. Lara-Curzio and C.M. Russ, “On the relationship between the parameters of the
distributions of fiber diameters, breaking loads, and fiber strengths,” *J. Mater. Sci.
Lett.*, **18** [24] 2041–2044 (1999).
- 5 T.A. Parthasarathy, “Extraction of Weibull parameters of fiber strength from means
and standard deviations of failure loads and fiber diameters,” *J. Am. Ceram. Soc.*, **84**
[3] 588–592 (2001).
- 6 Z. Chi, T.W. Chou, and G. Shen, “Determination of single fibre strength distribution
from fibre bundle testings,” *J. Mater. Sci.*, **19** [10] 3319–3324 (1984).
- 7 K.G. Dassios, M. Steen, and C. Filiou, “Mechanical properties of alumina Nextel™
720 fibres at room and elevated temperatures: Tensile bundle testing,” *Mater. Sci.
Eng. A*, **349** [1] 63–72 (2003).
- 8 H.E. Daniels, “The Statistical Theory of the Strength of Bundles of Threads. I,” *Proc.
R. Soc. A Math. Phys. Eng. Sci.*, **183** [995] 405–435 (1945).
- 9 B.D. Coleman, “On the Strength of Classical Fibres and Fibre Bundles,” *J. Mech.
Phys. Solids*, **7** 60–70 (1958).
- 10 M.A. Hamstad and R.L. Moore, “Acoustic Emission from Single and Multiple Kevlar

- 49 Filament Breaks,” *J. Compos. Mater.*, **20** [1] 46–66 (1986).
- ¹¹ A. Cowking, A. Attou, A.M. Siddiqui, M.A.S. Sweet, and R. Hill, “Testing E-glass fibre bundles using acoustic emission,” *J. Mater. Sci.*, **26** [5] 1301–1310 (1991).
- ¹² R. Hill and E.U. Okoroafor, “Weibull statistics of fibre bundle failure using mechanical and acoustic emission testing: the influence of interfibre friction,” *Composites*, **26** [10] 699–705 (1995).
- ¹³ J. Andersons, R. Joffe, M. Hojo, and S. Ochiai, “Glass fibre strength distribution determined by common experimental methods,” *Compos. Sci. Technol.*, **62** [1] 131–145 (2002).
- ¹⁴ V. Calard and J. Lamon, “Failure of fiber bundles,” *Compos. Sci. Technol.*, **64** [5] 701–710 (2004).
- ¹⁵ M. R’Mili, M. Moevus, and N. Godin, “Statistical fracture of E-glass fibres using a bundle tensile test and acoustic emission monitoring,” *Compos. Sci. Technol.*, **68** [7–8] 1800–1808 (2008).
- ¹⁶ M. R’Mili, N. Godin, and J. Lamon, “Flaw strength distributions and statistical parameters for ceramic fibers: The normal distribution,” *Phys. Rev. E - Stat. Nonlinear, Soft Matter Phys.*, **85** [5] 1–6 (2012).
- ¹⁷ J. Lamon, M. R’Mili, and H. Reveron, “Investigation of statistical distributions of fracture strengths for flax fibre using the tow-based approach,” *J. Mater. Sci.*, **51** [18] 8687–8698 (2016).
- ¹⁸ K.E. Evans, B.D. Caddock, and K.L. Ainsworth, “Statistical changes during the corrosion of glass fibre bundles,” *J. Mater. Sci.*, **23** [8] 2926–2930 (1988).
- ¹⁹ M. R’Mili, T. Bouchaour, and P. Merle, “Estimation of Weibull parameters from

- loose-bundle tests,” *Compos. Sci. Technol.*, **56** [7] 831–834 (1996).
- 20 E.N. Brown, A.K. Davis, K.D. Jonnalagadda, and N.R. Sottos, “Effect of surface treatment on the hydrolytic stability of E-glass fiber bundle tensile strength,” *Compos. Sci. Technol.*, **65** [1] 129–136 (2005).
- 21 EN 1007-5, “Determination of distribution of tensile strengths and of tensile strains to failure of filaments within a multifilament tow at ambient temperature,” (2010).
- 22 E.B. Callaway and F.W. Zok, “Accurate determination of fiber strength distributions,” *J. Am. Ceram. Soc.*, **100** [3] 1202–1211 (2017).
- 23 W. Weibull, “A statistical theory of the strength of materials,” *R. Swedish Inst. Eng. Res.*, **151** 1–45 (1939).
- 24 H. Ichikawa, “Polymer-derived ceramic fibers,” *Annu. Rev. Mater. Res.*, [46] 335–356 (2016).
- 25 R.S. Hay, G.E. Fair, R. Bouffieux, E. Urban, J. Morrow, A. Hart, and M. Wilson, “Hi-NicalonTM-S SiC Fiber Oxidation and Scale Crystallization Kinetics,” *J. Am. Ceram. Soc.*, **94** [11] 3983–3991 (2011).
- 26 J.J. Petrovic, J. V. Milewski, D.L. Rohr, and F.D. Gac, “Tensile mechanical properties of SiC whiskers,” *J. Mater. Sci.*, **20** [4] 1167–1177 (1985).
- 27 R.S. Hay, G.E. Fair, R. Bouffieux, E. Urban, J. Morrow, A. Hart, and M. Wilson, “Relationships Between Fiber Strength, Passive Oxidation and Scale Crystallization Kinetics of Hi-NicalonTM-S SiC Fibers,” *Ceram. Eng. Sci. Proc.*, **32** 39–51 (2011).
- 28 W. Gauthier and J. Lamon, “Delayed failure of hi-nicalon and hi-nicalon s multifilament tows and single filaments at intermediate temperatures (500°-800°C),” *J. Am. Ceram. Soc.*, **92** [3] 702–709 (2009).

Table 3.1 Averages and CoVs of Weibull parameters from bundle tests

Tow conditions	L (mm)	Number of tests, c	Average \bar{m}	$Z(\bar{m})$	Average $\bar{\sigma}_o$ (GPa) (for $L_0 = 1$)	$Z(\bar{\sigma}_o)$
Dry, sized	25	5	8.7	0.34	2.20	0.067
Dry, sized	110	4	7.3	0.081	2.27	0.012
Dry, desized	110	5	13.3	0.28	1.97	0.063
Lubricated	110	5	6.4	0.051	1.98	0.031

Table 3.2 Comparison of Weibull parameters obtained from the three fitting methods (all for lubricated bundles). Values of $\bar{\sigma}_o$ correspond to a reference length $L_0 = 1$ m.

	Weibull modulus, \bar{m}				Reference strength, $\bar{\sigma}_o$ (GPa) (for $L_0 = 1$)			
	Linear regression		Peak fit	LSF	Linear regression		Peak fit	LSF
	$P_f^c = 0.01$	$P_f^c = 0.1$			$P_f^c = 0.01$	$P_f^c = 0.1$		
	7.0	6.7	10.4	6.8	2.04	1.97	2.04	1.98
	6.2	6.0	7.2	5.9	1.96	1.94	1.99	1.93
	5.8	6.5	5.0	6.5	1.87	1.91	1.88	1.92
	4.8	6.4	6.8	6.4	2.08	2.06	2.10	2.05
	5.1	6.4	6.7	6.3	2.10	2.07	2.09	2.04
Average	5.8	6.4	7.2	6.4	2.01	1.99	2.02	1.98
CoV	0.15	0.037	0.27	0.051	0.047	0.034	0.045	0.031

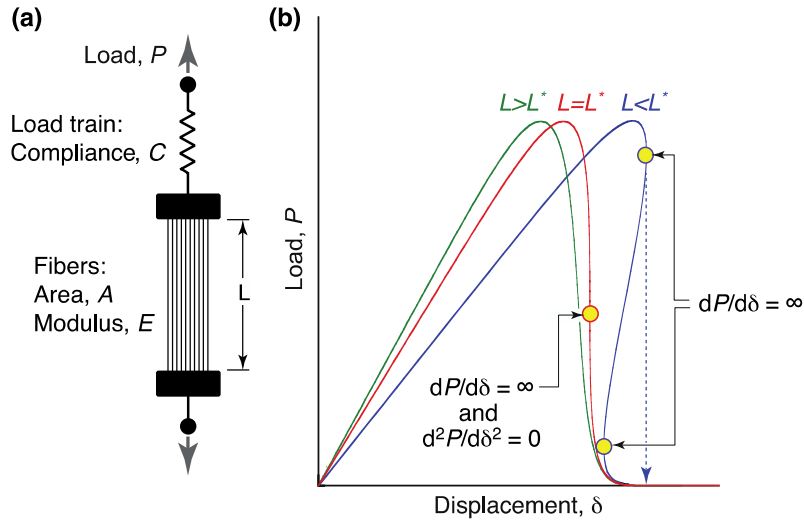


Figure 3.1: Schematics showing (a) a mechanical model of a fiber bundle and the load train, and (b) three types of load-displacement curves, obtained by varying load-train compliance and bundle gauge length.

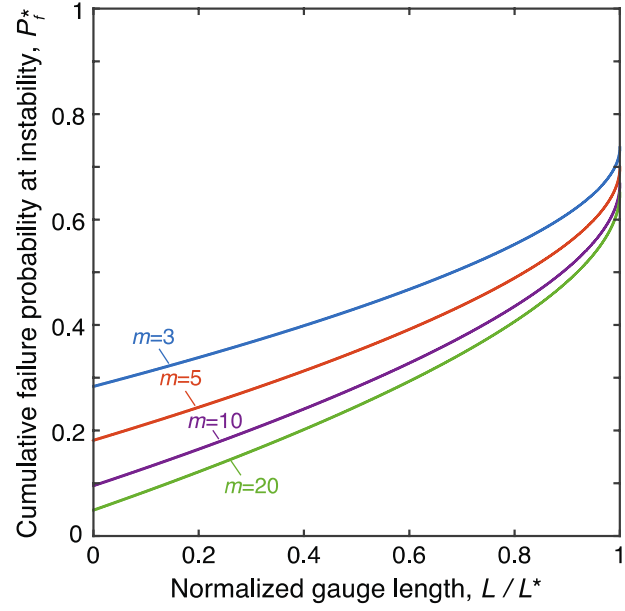


Figure 3.2: Effects of Weibull modulus and gauge length on the fraction P_f^* of fibers whose strength is measured up to the point of instability. When $L/L^* > 1$, no instability is obtained and hence $P_f^* = 1$.

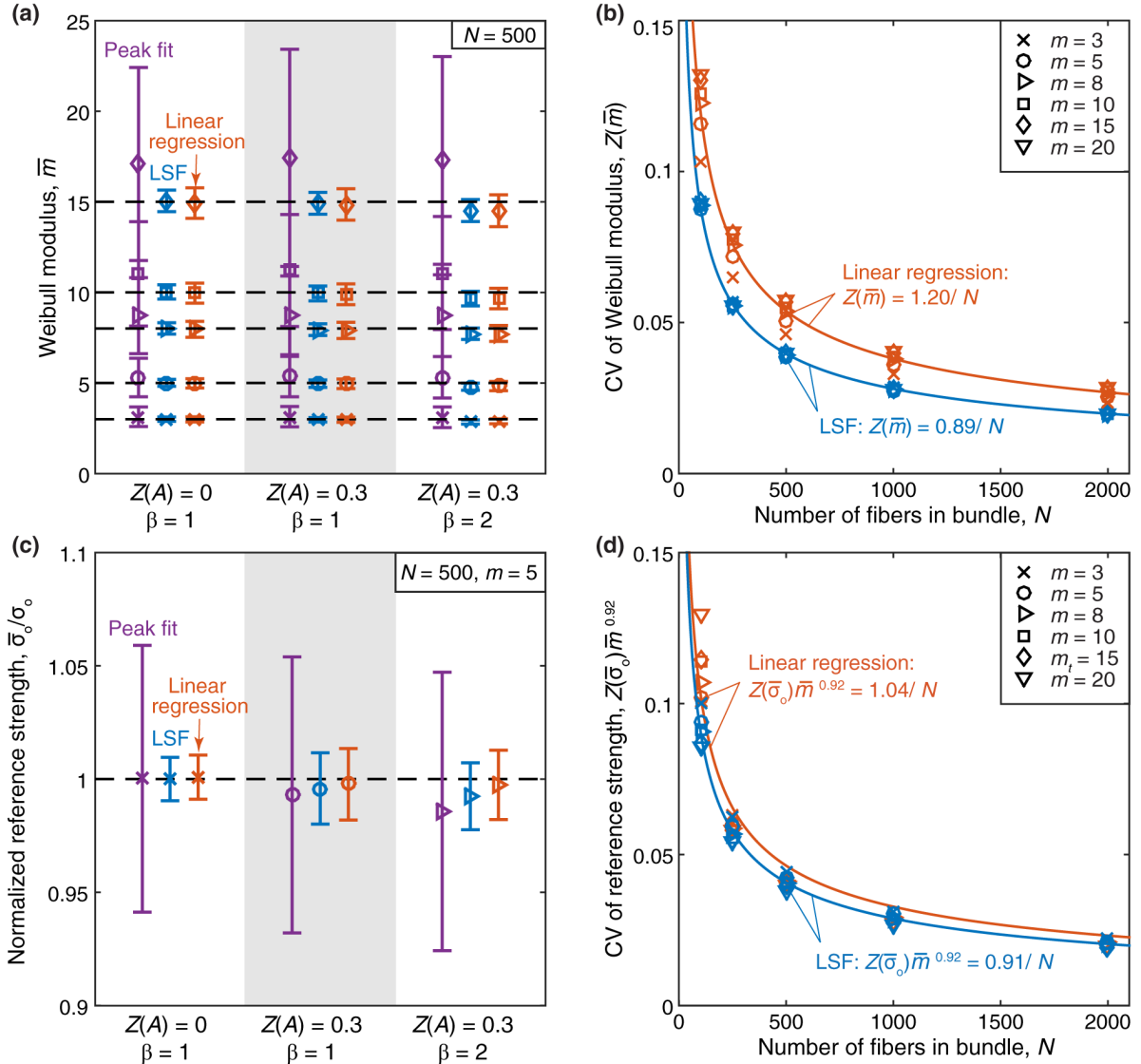


Figure 3.3: MCS results, interpreted using the three fitting methods. (a) Mean and standard deviation of the Weibull modulus for representative values of $Z(A)$ and β . (b) Effects of number of fibers on CoV of the Weibull modulus, obtained from LSF and linear regression methods. Data obtained from peak fit follow the same $1/\sqrt{N}$ scaling but are much larger in magnitude and fall outside the range shown here. (c) Mean and standard deviation of the inferred reference strength normalized by the true value for representative values of $Z(A)$ and β . (d) Effects of number of fibers on CoV of the reference strength. Here, again, data obtained from the peak fit follow the same scaling but are much larger in magnitude.

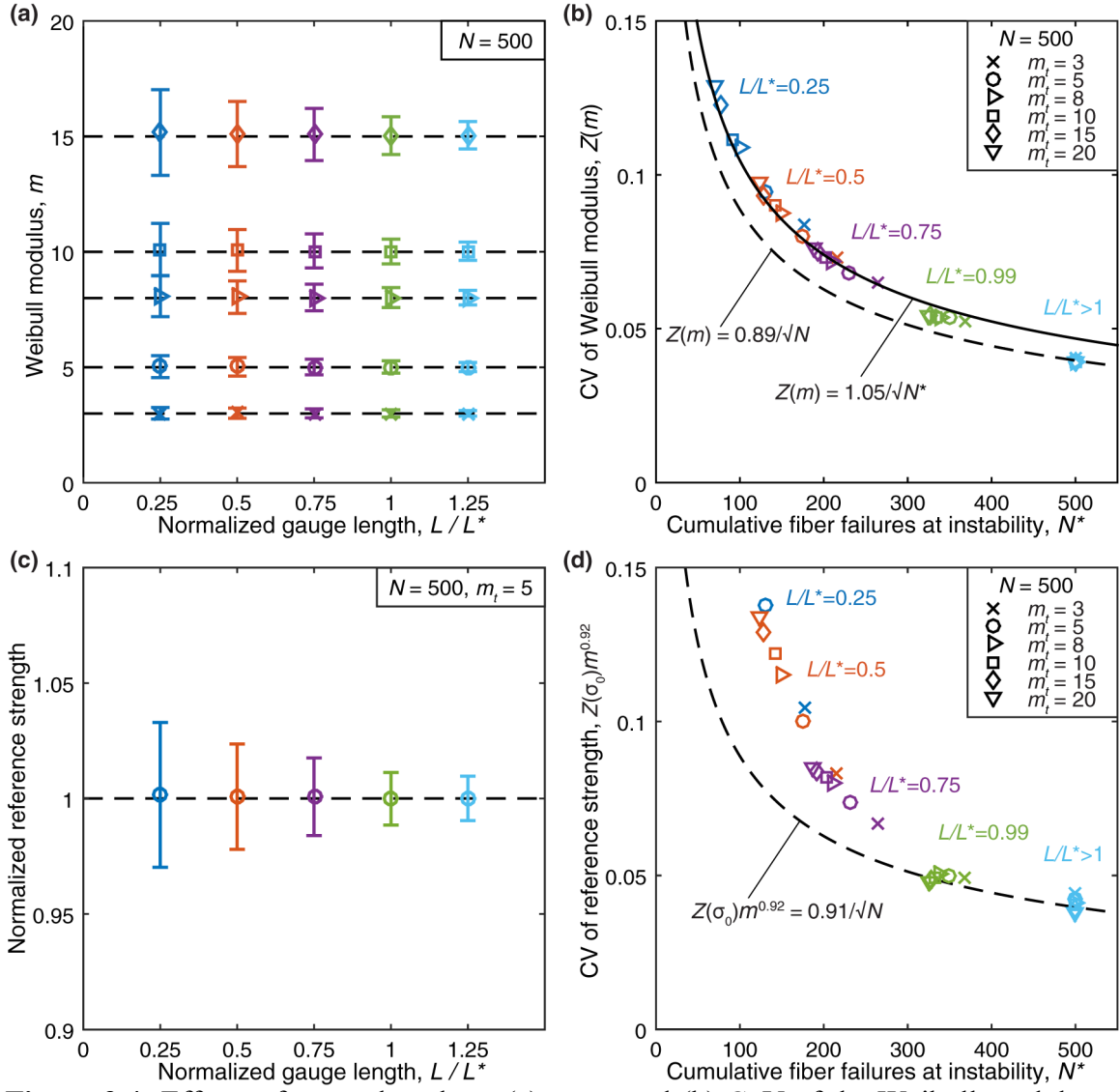


Figure 3.4: Effects of gauge length on (a) mean and (b) CoV of the Weibull modulus, and (c) mean and (d) CoV of the reference strength. In (a) and (c), error bars represent one standard deviation. In (b), the solid line is a fit of the MCS data. In (b) and (d), dashed lines are the fits for $\tilde{L} > 1$ (from Figure 3.3). Symbols are MCS results, interpreted using the LSF method.

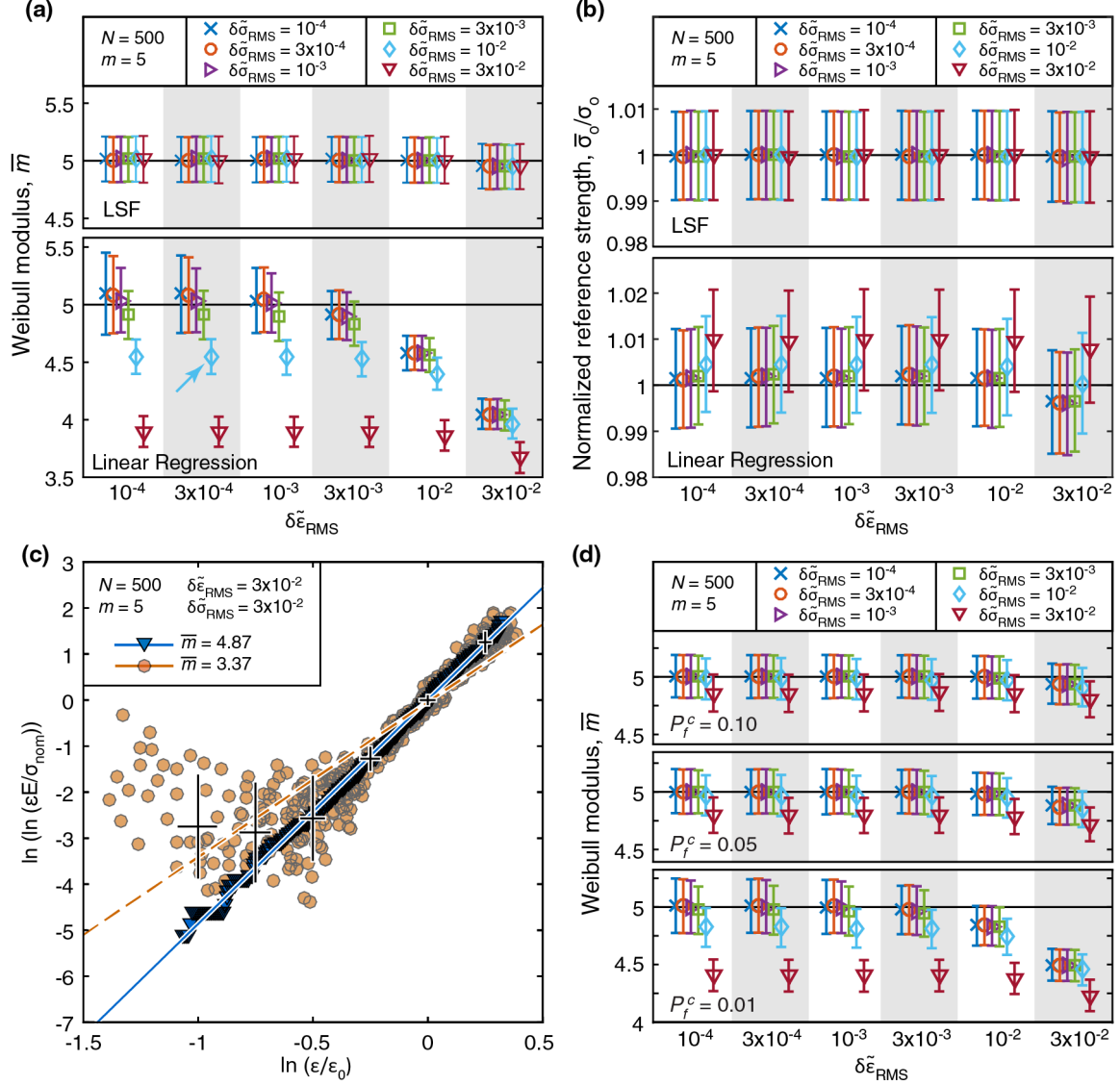


Figure 3.5: Effects of experimental error on (a) apparent Weibull modulus and (b) normalized reference strength, obtained by linear regression and LSF methods applied to the MCS results. (c) A Weibull plot generated from a MCS. Triangles are data without error and fit by the solid (blue) line. Circles are the same data with the inclusion of errors, with magnitudes given in the inset. The dashed (orange) line is the fit to this data. Black crosses represent error bars for this data. (d) Effects of a cut-off failure probability, P_f^c , on the inferred Weibull modulus from the linear regression method. The arrow in (a) corresponds approximately to the error values obtained in the current experimental study.

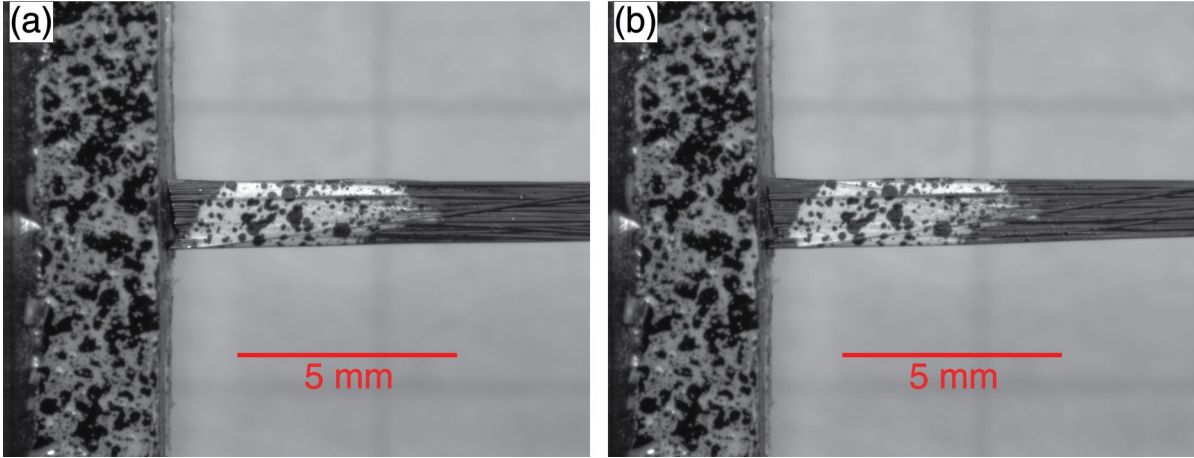


Figure 3.6: Speckle pattern on the end of a tow: (a) before and (b) after tensile testing.

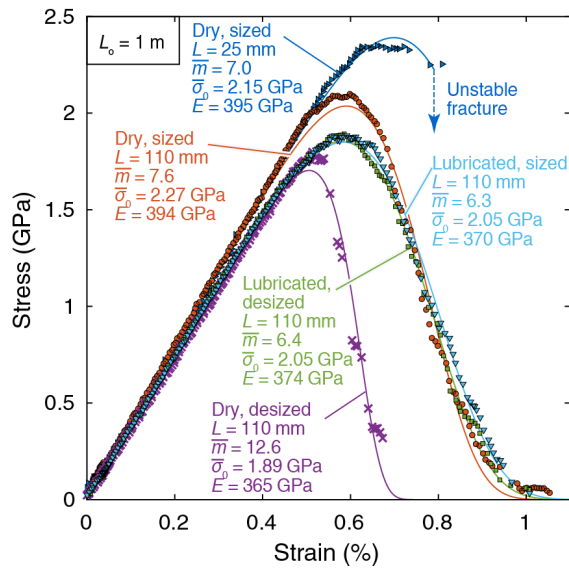


Figure 3.7: Representative test results showing effects of gauge length, sizing and lubrication on measured stress-strain curves. Data points are from experimental measurements and solid lines are from LSFs of Eqn. (3.2).

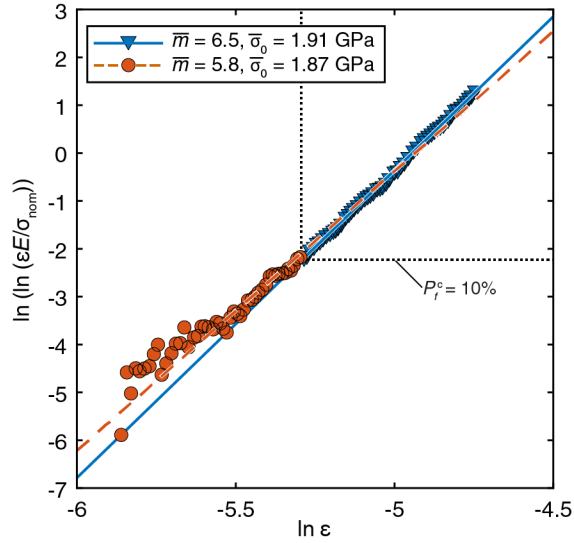


Figure 3.8: Weibull plot from measurements on a lubricated fiber bundle. The dashed (orange) line is the fit to all data points whereas the solid (blue) line is the fit over the range of failure probabilities $P_f > P_f^c = 0.10$. Blue triangles are data above the cutoff and orange circles are data below the cutoff.

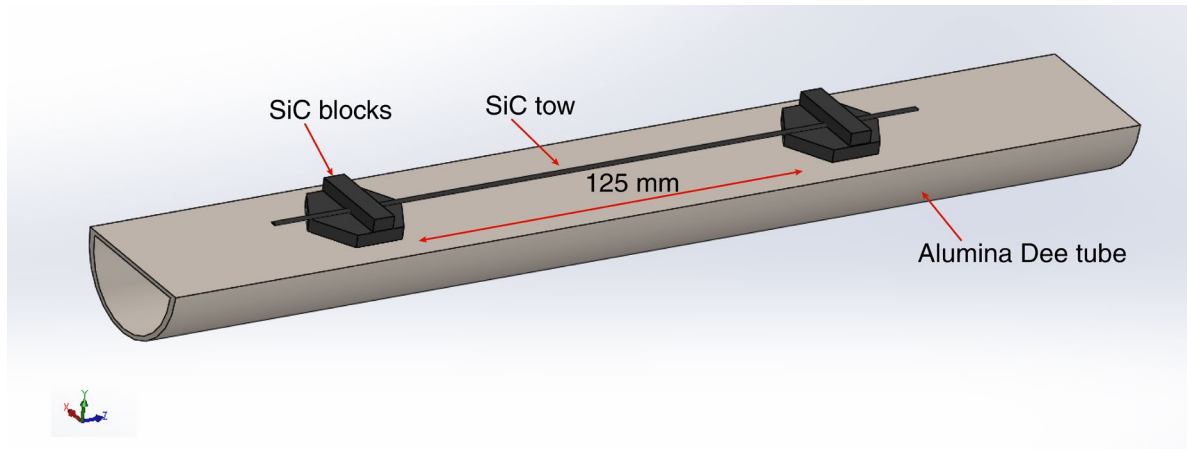


Figure 3.A1: Furnace setup with the gauge length section of the tow suspended above the alumina Dee tube.

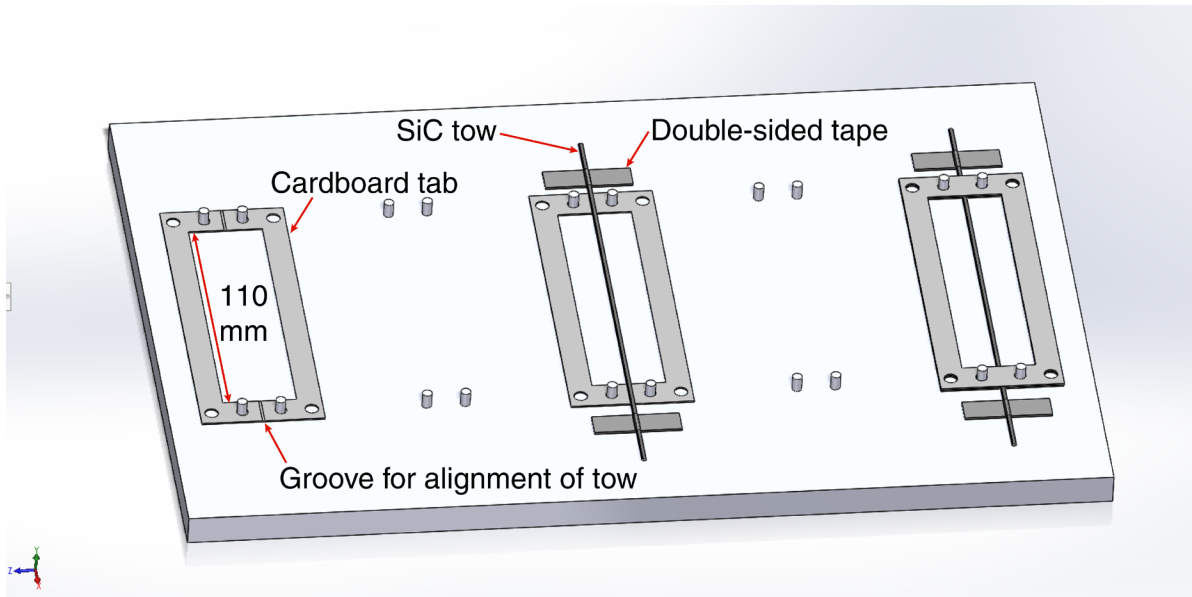
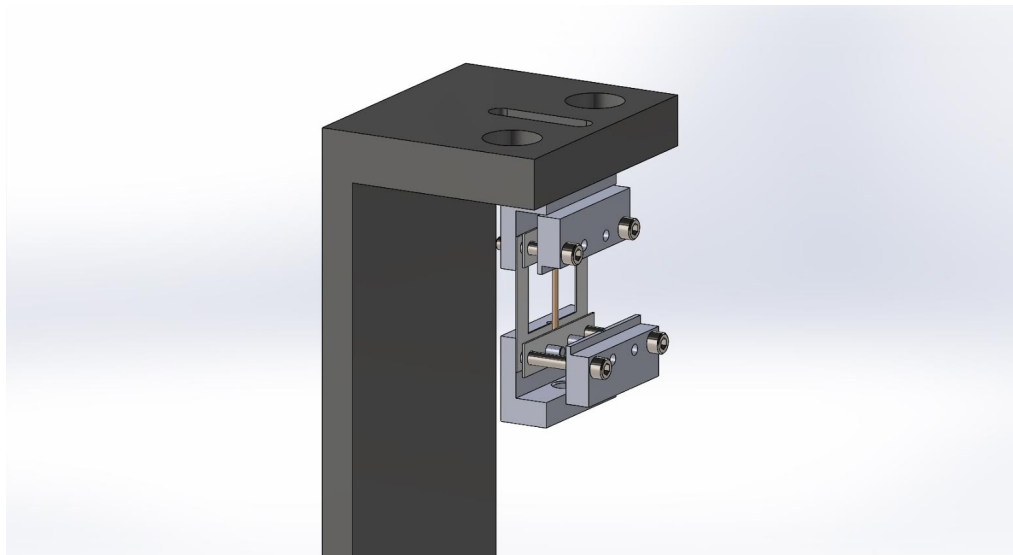
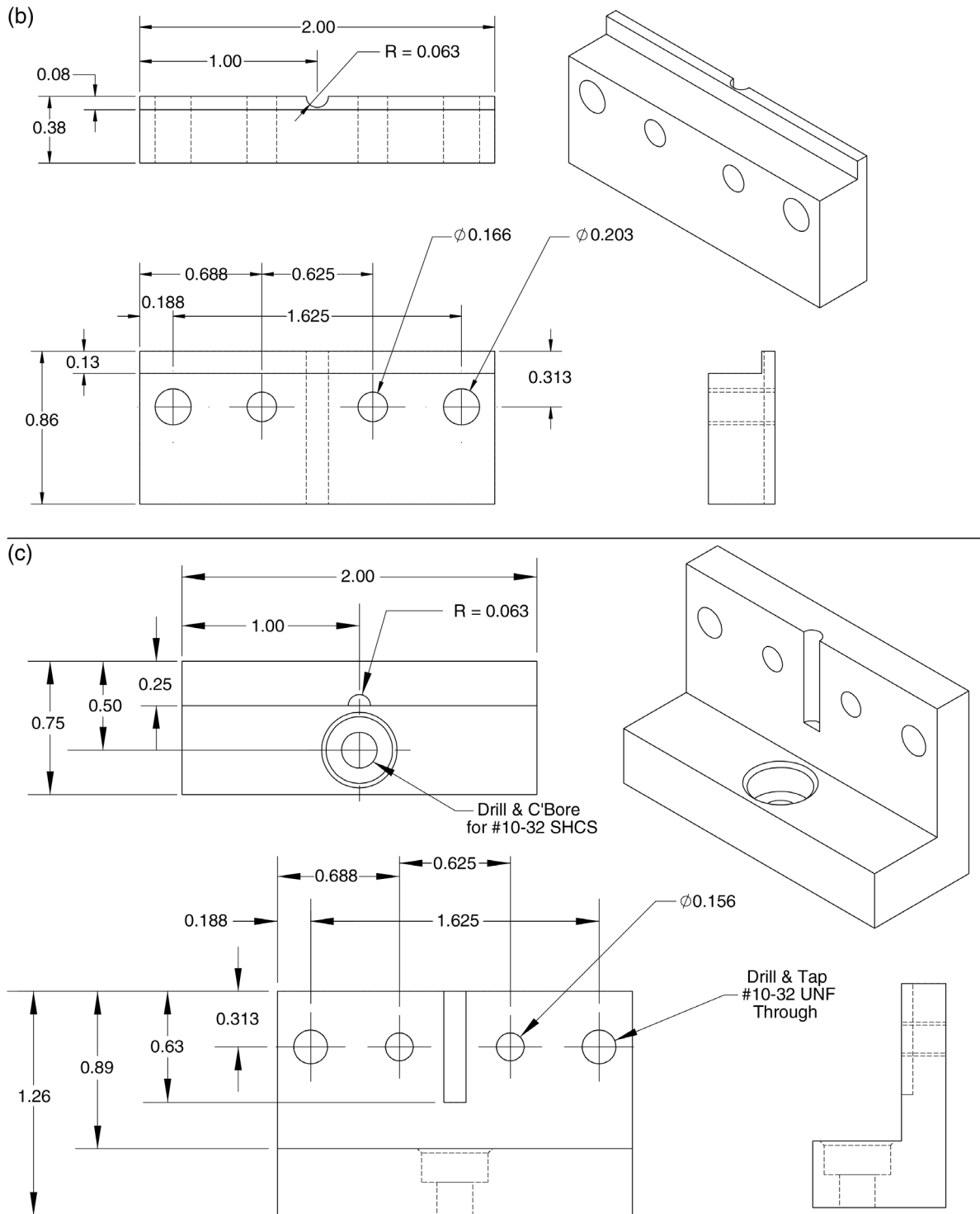


Figure 3.A2: Mounting plate with pins for alignment, showing the steps for mounting.

(a)





Dimensions are in inches

Figure 3.A3: (a) Perspective view of tensile testing fixture and (b, c) designs for clamp base and clamp plate.

Chapter 4

Weibull parameters obtained from dependence of fiber strength on fiber length and area[§]

Abstract

Weibull strength parameters of ceramic fibers can be inferred from variations in strength with fiber diameter or gauge length. The goal of the present chapter is to provide a critical assessment of the efficacy of these methods. The issues are addressed using theorems in regression analysis and uncertainty propagation as well as Monte Carlo simulations. The results show that, when Weibull moduli are obtained from strength variations with fiber area, inordinately large sample sizes (>1,000) are required to achieve reliable results. In contrast, Weibull moduli can be accurately estimated from the dependence of average fiber strength on gauge length for a modest sample size at each of two gauge lengths, provided the gauge length range is sufficiently large. The dependence of strengths of bundles containing many (ca. 500) fibers on gauge length yields yet more reliable results. The results are used to assess the fidelity of Weibull moduli obtained from these methods and provide guidance for preferred test methods.

[§] The content of this chapter has previously appeared in the Journal of the American Ceramic Society (**Evan Benjamin Callaway** and Frank W. Zok, “Weibull parameters obtained from dependence of fiber strength on fiber length and area,” *J. Am. Ceram. Soc.*, **101** [10] 4719–4731 (2018)). It is reproduced here with the permission of John Wiley and Sons.

4.1 Introduction

Relationships between stress, failure probability and volume have been studied extensively for a wide variety of high strength fibers, including SiC¹⁻⁹, alumina^{2, 10, 11}, carbon¹²⁻¹⁴, sapphire¹ and glass¹⁵. The overarching goal has been to characterize the strength distribution of a unit volume of material in terms of a small number of material properties (usually the Weibull modulus and the corresponding reference stress). In principle, when combined with weakest link fracture theory, the properties can be used to determine failure probabilities of fibers of different volumes. They can also be used to predict the behavior of collections of fibers stressed simultaneously, either in the form of a dry bundle or as a bundle embedded within a matrix (in a fiber composite).

Historically, the characteristics of fiber strength distributions have been determined using one of three approaches (Figure 4.1): (1) measuring strengths of many individual fibers, all with the same (nominal) gauge length and cross-sectional area, and fitting the results with a proposed distribution function that is consistent with weakest-link scaling laws; (2) measuring the stress-strain response of bundles (or tows) containing many fibers and fitting the measurements to that predicted from the proposed distribution; or (3) measuring strengths of fibers with varying length or area and inferring the parameter values from the sensitivity of strength to length or area. In principle, provided the proposed distribution accurately represents fiber strengths, all test methods should yield the same results.

In a number of previous studies, Weibull parameters obtained from these methods were found to be inconsistent with one another. The conclusion reached in some of these studies was that the fiber strength does not follow a Weibull distribution and thus an

alternative distribution function is required.^{1, 2} However, the assessments that differences in Weibull parameters are sufficiently large to warrant these conclusions have almost always been subjective.^{1, 2} Only rarely have they been made on the basis of statistical analyses that account for biases in mean value estimates and random errors.¹⁴ Even under the best circumstances the Weibull parameters obtained from a series of strength measurements exhibit significant uncertainty. For example, if 20 fiber strength measurements are made following the ASTM test standard, the 90% confidence interval on the point estimate of the Weibull modulus m obtained from the maximum likelihood method^{16, 17} is $(0.79-1.45)m$: a range that spans almost a factor of 2. As we show in due course, the range of m values inferred from length- or area-dependent strength data may be considerably broader, dependent largely on the range of the independent variable (length or area) probed by the experiments and the number of tested fibers.

The present chapter addresses specifically the fidelity of Weibull parameters inferred from measured sensitivities of strength to fiber length and fiber area, with a focus on effects of random errors. An analytical framework based on theorems in regression analysis and uncertainty propagation is developed and its veracity is assessed by exhaustive Monte Carlo simulations (MCS). Supporting experimental results from fiber bundle tests are also presented.

The chapter is organized in the following way. Methods of determining Weibull parameters are reviewed in Section 4.2. Analytical solutions for uncertainties in the parameter values are summarized in Section 4.3 (with details and derivations compiled in Appendix 4.A.1-3). Then, in Section 4.4, the analytical results are assessed through MCS. In Section 4.5 experimental results from bundle tests are presented and compared with the

analytical solutions and MCS. Finally, in Section 4.6, the results are used to assess the fidelity of Weibull moduli reported in the literature and to establish guidelines on preferred test methods and test parameters.

4.2 Determination of Weibull parameters

Tensile strengths of cylindrical fibers, each with area A and length L and with flaws distributed randomly throughout the fiber volume, can be described by the weakest link Weibull distribution:

$$P_f = 1 - \exp\left\{-\left(AL/A_oL_o\right)\left(\sigma/\sigma_o\right)^m\right\} \quad (4.1)$$

where P_f is the cumulative failure probability; L_o and A_o are reference values of length and area; σ is tensile stress; σ_o is the reference stress; and m is the Weibull modulus. The Weibull parameters σ_o and m can be determined in several ways (illustrated in Figure 4.1).

1. *Strength distribution measurement:* Standard practices call for the Weibull parameters to be determined from a series of strength measurements on fibers with (nominally) fixed length and area and then fitting the data using the maximum likelihood (ML) method.^{16, 18} (Although now superseded by the ML method, linear regression analysis of “Weibull plots”, in the form $\ln(-\ln(1-P_f))$ vs. $\ln \sigma$, continues to be used).
2. *Bundle response:* The stress-strain response of a parallel assembly of fibers, as found in a bundle (or tow), is measured and the results are fit to the function predicted from a Weibull strength distribution, namely

$$\sigma_{nom} = \varepsilon E_f \exp \left[- (L/L_o) (\varepsilon E_f / \sigma_o)^m \right] \quad (4.2)$$

where σ_{nom} is the nominal stress (computed on the basis of the entire bundle area).

3. *Volume-dependent strength*: Variations in strength with fiber volume are measured in one of three ways.

(i) Individual fibers with nominally equivalent areas are tested at two or more distinct gauge lengths. The Weibull parameters are then determined from the dependence of *mean* strength $\bar{\sigma}$ on gauge length. For a Weibull distribution, the predicted mean strength is¹⁹ $\bar{\sigma}/\sigma_o = (AL/A_oL_o)^{-1/m} \Gamma[1+1/m]$ where Γ is the gamma function.

Analyses of test data are performed on a logarithmic form of this result, notably:

$$\ln(\bar{\sigma}/\sigma_o) = (-1/m) \ln(AL/A_oL_o) + \ln(\Gamma(1+1/m)) \quad (4.3)$$

The Weibull modulus and reference strength are obtained from a linear regression fit of $\ln \bar{\sigma}$ vs. $\ln L$.

(ii) Individual fibers of the same gauge length but varying area are tested. Since area is a continuous, uncontrolled variable, only individual estimates of strength are obtained at each value of A . Therefore linear regression is performed on $\ln \sigma$ (not $\ln \bar{\sigma}$) vs. $\ln A$ to infer m and σ_o .

(iii) Fiber bundle strengths are measured at two or more distinct gauge lengths. When the number of fibers in a bundle is sufficiently large, the predicted bundle strength σ_B is given by²⁰ $\sigma_B/\sigma_o = (meL/L_o)^{-1/m}$ where e is the base of the natural logarithm (≈ 2.718). In logarithmic form, this becomes:

$$\ln \sigma_B/\sigma_o = (-1/m)(1 + \ln L/L_o + \ln m) \quad (4.4)$$

Linear regression of $\ln \sigma_B$ vs. $\ln L$ yields m and σ_0 .

The main goal of the remainder of this study is to provide a framework for assessment of methods (i) – (iii). Comparisons are also made with results stemming from the other test methods (in 1 and 2).

4.3 Distributions in Weibull parameters: Analytical results

Distributions in Weibull parameters obtained from a set of strength data are derived from established statistical methods. In many cases of practical interest, distributions are normal and can be conveniently represented by an expected or mean value and a coefficient of variation (CoV). In others, distributions are non-normal and hence cannot be represented by the same metrics. The nature of the distributions of inferred values of m and σ_0 are described in detail in the Appendix; the key analytical results are presented here. (A complete list of variables is in Table 4.1).

Linear regression analysis of strength vs. area or length (in logarithmic form) yields estimates of $1/m$. The distribution of $1/m$ is normal (Figure 4.2a). From the area-dependence of strength, the CoV of $1/m_A$ (m_A being the Weibull modulus obtained from this method) is $Z(1/m_A) \approx 1.28/Z(A)\sqrt{N}$ (Eqn. (4.A4)) where $Z(A)$ is the CoV of fiber area and N is the number of tested fibers. Provided $Z(1/m)$ is sufficiently small (≤ 0.2 , as we show later), error propagation analysis gives $Z(m) \approx Z(1/m)$. Otherwise, for larger values of $Z(1/m)$, the distribution of m is non-normal (see Eqns. (4.A12) and (4.A13)) and, typically, $Z(m) \gg Z(1/m)$. Moreover, the expected value of m is undefined, because the integral of the product of the probability density of m and m itself is non-convergent. Consequently, the

median and mode (Eqns. (4.A16) and (4.A17)) are used as point estimates of m . These results are plotted in Figures 4.3a-c.

The implications of this analysis become evident upon computing some typical values. If $Z(A) = 0.2$ (representative of SiC fibers²¹) and $N = 30$, $Z(1/m_A) \approx 1.2$; $Z(m_A)$ is even greater. The conclusion is that any estimate of m_A obtained from such data would be essentially meaningless.

Useful insights into the fidelity of Weibull parameters obtained from the length-dependence of strength are obtained through analyses of test results in which only two gauge lengths, denoted L_1 and L_2 , are employed. Here, $Z(1/m_L) = m_t \sqrt{2} Z(\sigma_{PE}) / |\ln \lambda|$ (Eqns. (4.A6) and (4.A7)) where $\lambda = L_1/L_2$ and σ_{PE} is a point estimate of strength: either the average strength $\bar{\sigma}$ (for individual tested fibers) or the bundle strength σ_B (for fiber bundles). In both cases, σ_{PE} is approximately normally distributed. The CoV of $\bar{\sigma}$ and σ_B are given by $Z(\bar{\sigma}) \approx m_t^{-0.92} / \sqrt{N}$ (N being the number of individual fibers tested at each of the two gauge lengths)^{19, 22} and $Z(\sigma_B) \approx 1 / \sqrt{m_t N}$ (N being the number of fibers within each of the two bundles)^{20, 23}. Combining these results yields $Z(m_L) \approx Z(1/m_L) = m_t^{0.08} \sqrt{2} / \sqrt{N} |\ln \lambda|$ (Eqn. (4.A6)) for individual fiber tests and $Z(m_L) \approx Z(1/m_L) = \sqrt{2m_t} / \sqrt{N} |\ln \lambda|$ (Eqn. (4.A7)) for fiber bundles, both valid for $Z(1/m_L) \leq 0.2$.

Subsequent MCS results show that, when more than two gauge lengths are employed, the linear regression fit is heavily influenced by the two extreme points (*i.e.* at the smallest and greatest gauge lengths). Consequently, the preceding results, with λ

reinterpreted as the ratio of minimum to maximum length, provide remarkably good estimates of $Z(1/m_L)$ and in turn $Z(m_L)$.

These results have practical implications. Although the dependence of $Z(m_L)$ on m_L for individual fiber tests is weak ($m^{0.08} \approx 1$) while that for bundle tests is relatively strong ($m^{1/2} \approx 2-3$), the dependence on N is the same in both cases ($1/\sqrt{N}$). Moreover, since a typical fiber bundle may contain 500 fibers ($1/\sqrt{N} \approx 0.04$) while the number of individual fibers tested may be 30 ($1/\sqrt{N} \approx 0.2$), the results from two bundle tests would have lower variation in m , by a factor of about 2, relative to that obtained from a total of 60 individual fiber tests. In this context, fiber bundle tests are preferred over individual fiber tests.

An alternative method of obtaining Weibull parameters involves measurement of the entire stress-strain response of a fiber bundle and fitting the result with Eqn. (4.2). Here $Z(m) = 0.89/\sqrt{N}$.²¹ Comparison of this result with Eqn. (4.A7) reveals that, when λ is sufficiently small, *i.e.*, $\ll 1$, the method based on gauge length dependence of bundle strength is preferred over fitting of the stress-strain response. Setting the CoVs of the Weibull moduli equal to one another yields a critical gauge length ratio given by $\lambda^* = e^{-1.59\sqrt{m}}$. For typical values of m (5–10), $\lambda^* \approx 0.03-0.01$. Otherwise, when $\lambda > \lambda^*$, the gauge length method yields results that are inferior to those from the fit of stress-strain curves (though possibly still acceptable).

The distribution in reference strength is obtained in a similar way. The reference strength obtained from the area-dependence of strength is $\sigma_{0,A} = e^{\beta+\gamma/m}$ (Eqn. (4.A19))

where γ is the Euler–Mascheroni constant (≈ 0.577) and β is the y-intercept from linear regression. The expected value and CoV of $\sigma_{0,A}$ are $E(\sigma_{0,A}) \approx \sigma_{0,t} e^{\pi^2/12m_t^2N}$ (Eqn. (4.A22)) and $Z(\sigma_{0,A}) \approx \pi/m\sqrt{6N}$ (Eqn. (4.A24)). A similar CoV is obtained from the standard test method, based on a series of strength measurements of nominally equivalent fibers and fitting the data by the maximum likelihood method: $Z(\sigma_{0,ML}) \approx 1.05/(m_t\sqrt{N})$. For $N = 30$ and $m_t = 5$, the two methods yield $Z(\sigma_{0,ML}) \approx 0.04$ and $Z(\sigma_{0,A}) \approx 0.05$. The distribution of reference strength obtained from length-dependence $\sigma_{0,L}$ follows a similar form: $Z(\sigma_{0,L}) \approx m_t^{-0.92}/\sqrt{N}$. The estimates of both $\sigma_{0,A}$ and $\sigma_{0,L}$ are only weakly affected by m and can be estimated accurately from a relatively small sample size.

4.4 Distributions in Weibull parameters: Monte Carlo simulations

4.4.1 Numerical procedures

MCS of single filament tests and fiber bundle tests were performed to probe the combined effects of sample size and distributions in fiber strength, fiber area and gauge length on the inferred Weibull parameters. Three scenarios were considered: (i) tests on single filaments with varying area at a constant gauge length, (ii) tests on single filaments with constant area at two or more gauge lengths, and (iii) tests on fiber bundles at two or more gauge lengths. The Weibull parameters were obtained from linear regression analysis of data presented in the logarithmic format in Eqns. (4.3) and (4.4).

Operationally, MCS is performed in the following way. Two sets of N random numbers between 0 and 1 are generated for each gauge length: one set each representing the

cumulative probability of fiber area, A/\bar{A} , and fiber strength, σ/σ_0 . Fiber areas and fiber strengths are taken to follow normal and Weibull distributions, respectively. Simulations on fiber bundles are performed by progressively increasing the applied strain in increments of $\Delta\varepsilon E_f/\sigma_0 = 2 \cdot 10^{-3}$ (E_f being fiber Young's modulus) until all fibers have failed. At each simulation step, the applied strain is compared to the fracture strain of each surviving fiber. Fractured fibers are assigned an area of 0. The load and nominal stress are computed from the strain, the intact fiber area and the fiber Young's modulus.

The ranges of parameter values in these simulations were $10 \leq N \leq 10,000$, $3 \leq m_t \leq 20$, $0 \leq Z(A) \leq 0.3$ and $0.25 \leq L/L_0 \leq 4$. Ranges of m_t and $Z(A)$ encompass those relevant to structural ceramic fibers of interest. Each set of simulations was performed 100,000 times.

4.4.2 MCS results

Results from the first set of MCS, probing the Weibull parameters obtained from the area-dependence of strength, along with analytical solutions from Section 4.3 and the Appendix, are plotted in Figures 4.2 and 4.3a,d. The MCS results agree exceptionally well with the analytical solutions over the entire parameter range, with one exception: the solution for $Z(m_A)$ breaks down once $Z(m_A) \geq 0.2$ or, equivalently, $Z(A)\sqrt{N} \leq 6$ (Figure 4.3d). In this domain, an increasing fraction of $1/m_A$ values begin to approach zero and thus m_A approaches $\pm\infty$. Thus, the mean and CoV of m_A tend towards $\pm\infty$ and Eqn. (4.A4) is no longer valid. In all cases the average reference strength is equal to the true value and is unaffected by negative values of m_A .

The second and third sets of MCS examined the gauge length dependence of individual fiber strengths and of fiber bundle strengths, respectively (Figures 4.3b,c,e,f and 4.4). For cases in which only two gauge lengths are used (Figure 4.3b,c,e,f), the MCS results again agree exceptionally well with the analytical solutions over the entire parameter range with the exception that the solution for $Z(m_L)$ breaks down once $Z(m_L) \geq 0.2$. Specifically, the median and mode of m_L agree with Eqns. (4.A16) and (4.A17) (Figure 4.3b-c) while $Z(1/m_L)$ and $Z(m_L)$ follow Eqn. (4.A7) (Figure 4.3e-f).

When more than two gauge lengths are used, the MCS results for $Z(1/m_L)$ and $Z(m_L)$ are almost the same as those obtained when using only the two extreme gauge lengths. Consequently, the results from multiple gauge lengths fall in line with the predictions of Eqn. (4.A7), with λ interpreted as the ratio of smallest and greatest gauge lengths (shown by solid black lines in Figure 4.4). Once again the analytical solution for $Z(m_L)$ breaks down once $Z(1/m_L) > 0.2$ (Figure 4.4).

4.5 Experimental measurements on SiC fiber bundles

The utility of the preceding results was illustrated through fiber bundle tests on Hi-Nicalon™ Type S NOx fibers. Each bundle contained 500 fibers. All bundles were from the same fiber lot. Bundles were tested at two gauge lengths: 25 mm and 110 mm. The area variation of these fibers is $Z(A) = 0.21^{22}$. Bundles were desized in boiling de-ionized water²⁴ and lubricated with a low-viscosity oil prior to testing in order to mitigate inter-fiber friction and associated coordinated fiber failure²⁵. Additional details of the testing procedure are presented elsewhere.²¹ Four tests were performed at each of the two gauge lengths.

Stress-strain curves for bundles with 110 mm gauge length are shown in Figure 4.5a. A key feature of these curves is the linearity in the initial portions, indicating minimal fiber misalignment.²⁶

The measured bundle strengths (Figure 4.5b) were fit to Eqn. (4.4), yielding $m_L = 6.1$ and $\sigma_{0,L} = 2.04$ GPa ($L_o = 1$ m). To obtain the variations in these parameters, values of m_L and $\sigma_{0,L}$ were computed from each pair of strength values at the two gauge lengths (a total of 16 pairs). The corresponding CoVs are $Z(m_L) = 0.13$ and $Z(\sigma_{0,L}) = 0.030$. Similar results are obtained from Eqn. (4.A7): $Z(m_L) = 0.12$ and $Z(\sigma_{0,L}) = 0.022$.

Additional comparisons were made between the preceding values of m_L and $\sigma_{0,L}$ and their CoVs with those obtained from a previous study on the same fibers.²¹ In the latter, Weibull parameters were obtained from least squares fits (LSF) of the predicted stress-strain response of a fiber bundle (Eqn. (4.2)) to measured stress-strain curves. The fits yielded $m_{LSF} = 6.4 \pm 0.3$ ($Z(m_{LSF}) = 0.051$) and $\sigma_{0,LSF} = 1.98 \pm 0.06$ GPa ($Z(\sigma_{0,LSF}) = 0.031$). The uncertainty in the experimental Weibull modulus agrees with that expected from MCS and the analytical solutions ($Z(m_{LSF}) = 0.040$). The Weibull parameters from the two methods fall within one standard deviation of their respective means. Moreover, the CoV of the Weibull modulus from the gauge length method is about twice that from the fit of the stress-strain curves (although both are deemed acceptably small). This, too, is borne out by theory.

The conclusions drawn from these comparisons are twofold. First, differences in Weibull parameters obtained from the two test methods are not statistically significant; the Weibull distribution appears to provide a consistent description of fiber strength. Second, the uncertainty in m obtained from fitting stress-strain curves is significantly lower (by a factor >2) than that from the gauge-length dependent fiber bundle strength. This result is consistent with the gauge length ratio employed in the present experiments ($\lambda = 0.23$) and the critical ratio below which the gauge-length dependent method is predicted to yield superior results ($\lambda^* = 0.02$ for $m = 6$).

4.6 Discussion

The key analytical solutions developed here and elsewhere^{21, 22} are summarized in Figure 4.1. The results are couched in terms of the minimum number of test fibers needed to attain a prescribed precision level on the Weibull modulus. If selection were based solely on minimizing random errors with the smallest total number of tests, the preferred method would usually be one based on a fit of tensile stress-strain curves; a single (instrumented) test on a bundle containing 500 fibers would yield results comparable to 500 individual fiber tests (following the standard method). The gauge length-dependent bundle strength may yield comparable results, provided the gauge length ratio is sufficiently small. The standard method of strength measurements and the method based on gauge-length dependence of mean fiber strength would require more tests to achieve the same goal. Finally, for area variations typical of commercial high-temperature structural fibers, the area-dependent fiber strength method requires an inordinately large number of tests.

In practice, the selection of a test method would include consideration of the efforts required to execute the tests as well as related measurement errors. For instance, in measuring the strengths of individual fibers, the area of each tested fiber should be measured; for small diameter fibers, the errors in such measurements are not insignificant. (Reliance on mean fiber area introduces systematic errors that skew the Weibull moduli to anomalously low values.^{22, 27, 28}) With respect to fiber bundle tests, precautions must be taken to ensure that all fibers are straight and uniformly loaded, that interfiber coupling is mitigated through use of sizing or low viscosity oil, and that fibers within the bundles exhibit minimal amounts of weld lines. Additionally, it requires high-precision strain measurement (typically $<10^{-4}$).

The large errors inherent to the method based on area-dependent strength and the skewing of the Weibull modulus distribution to anomalously low values have been vividly demonstrated in a number of previous experimental studies. For example, for Nextel™ fibers, measured values of m_A/m_{WP} ranged from 0.20 to 0.56.¹⁰ Similar studies on carbon fibers yielded comparable results: $m_A/m_{WP} \approx 0.2$.^{12, 13} For the test parameters used in those studies ($N = 50$ and $Z(A) = 0.1$), the present analysis suggests that the median Weibull modulus would be $m_{A,med}/m_t \approx 0.4$ and that the uncertainty in m would exceed m itself. Other data, on Tyranno™ fibers, have shown similarly large discrepancies in m , though in the opposite sense: $m_{WP} = 5.0$ whereas $m_A = 36$.⁵ As a practical matter, the method based on area-dependent strength has minimal value and should be avoided.

Discrepancies in Weibull moduli obtained from the various methods have been previously interpreted as a breakdown of the Weibull function in describing strength

distributions, without due consideration of the statistical significance of differences in measured values and systematic errors introduced by inadequate sample size.^{10, 12–15, 29} These interpretations have not only fueled misconceptions about the utility of the Weibull distribution but have also led to a number of proposed alternative distribution functions that violate the underlying weakest-link scaling principles.³⁰ In this regard, understanding the role of errors in the inferred Weibull parameters is crucial.

As a further application, we use the theory to assess reported Weibull moduli of three different Nextel™ oxide fibers using two methods: (i) the standard method of strength measurements on fibers of the same size combined with linear fits of Weibull plots and (ii) the method based on gauge-length dependence of mean strength. Reported Weibull moduli of Nextel™ 610, 650, and 720 fibers from the standard method were $m_{WP} = 10.1, 6.8$ and 7.6 , respectively; the corresponding results from the gauge length method were $m_L = 9.7, 7.3$ and 7.1 .¹¹ In each of these cases, m_L is within 7% of m_{WP} . Our MCS results for the same test conditions ($N = 10$ and $L_S = [25, 125, 254]$ mm, where L_S represents the set of gauge lengths) yield a median value $m_{L,med}$ within 0.5% of m_t and a CoV of $Z(1/m) = 0.22$. On this basis, we conclude that there is negligible systematic error in m from gauge length dependence and that the correlations between the inferred Weibull moduli from the two methods employed in the experiments are surprisingly good (with relative differences being only about 1/3 of the predicted CoV).

Finally, regarding the two methods based on gauge length dependence, we present the analytical results in Figure 4.1 as contours of fixed $Z(m)$ over a range of m values, in coordinates of λ and N ; results for mean fiber strengths and bundle strengths are in Figures 4.6a and b, respectively. Experimental data on a number of fiber types from previous

studies are also plotted as discrete points. Based on comparisons of the calculated curves with the experimental points, we infer that the uncertainties in some cases (bottom right corner) are small ($Z(m_L) < 0.1$) whereas others would have relatively large (and perhaps unacceptable) uncertainty levels ($Z(m_L) \geq 0.2$). As a whole, results from bundle strengths (in Figure 4.6b) are more reliable; the data points consistently reside in the domain $Z(m_L) < 0.1$ (some well below this value). The latter result is a consequence of the very large number of fibers that are probed in a single bundle test. As an additional issue, assessments of the fidelity of the measurements would need to account for systematic and/or measurement errors associated with test execution.

4.7 Summary and conclusions

Analytical solutions have been developed for distributions in Weibull parameters obtained from area- or length-dependent strengths. The solutions have been verified through exhaustive MCS and fiber bundle tests. In summary, the key results are:

- (i) Estimates of Weibull moduli obtained from fiber strength variations with fiber *area* are biased toward erroneously low values and have extraordinarily large uncertainties. For fiber area variations typical of commercially-available fibers, an inordinately large number of tests would be required to obtain reasonable estimates of the Weibull modulus.
- (ii) Accurate estimates of Weibull moduli can be obtained from the length-dependence of *mean fiber strength*, provided both the gauge length range and the number of tested fibers at each gauge length are sufficiently large. Analytical solutions for the

random uncertainty in the Weibull modulus presented here facilitate assessment of the validity of test data and guide selection of test parameters.

- (iii) Improved estimates of Weibull modulus can be obtained from the gauge-length dependence of *fiber bundle strength*. For bundles containing 500 fibers and specimen gauge lengths with ratio $\lambda < 0.25$, the CoV of the Weibull modulus is typically < 0.2 .
- (iv) Yet more reliable results for m are usually obtained from a LSF of the bundle stress-strain response. The method based on gauge-length dependent bundle strength becomes superior only when the gauge length ratio falls in the domain $\lambda < 0.01 - 0.03$ (dependent on m).
- (v) Test results on fiber bundles presented here and elsewhere²¹ support the use of the two-parameter Weibull distribution to describe the strength of Hi-Nicalon™ Type S NOx fibers.

Acknowledgements

This work was supported by the Pratt & Whitney Center of Excellence in Composites at the University of California, Santa Barbara.

4.A Appendix: Random errors of regression analysis

4.A.1 *Generic results*

Linear regression of a dependent variable, Y , on a single independent variable, X , takes the form $Y = \alpha X + \beta$, where α and β are constants. If X and Y are approximately normally distributed, the standard deviations, $S(\alpha)$ and $S(\beta)$, of the constants are:³¹

$$S(\alpha) = \sqrt{\frac{S^2(X)S^2(Y) - \text{cov}^2(X, Y)}{(n-2)S^4(X)}} \quad (4.A1)$$

$$S(\beta) = \sqrt{\left(\frac{1}{S^2(X)} + \frac{\bar{X}^2}{S^4(X)}\right) \left(\frac{S^2(X)S^2(Y) - \text{cov}^2(X, Y)}{(n-2)S^4(X)}\right)} \quad (4.A2)$$

where n is sample size; $S(X)$ and $S(Y)$ are standard deviations of X and Y ; \bar{X} and \bar{Y} are average values; and $\text{cov}(X, Y)$ is the covariance of X and Y , which is related to the other quantities by $\text{cov}(X, Y) = \alpha S^2(X)$.³¹ Furthermore, the fitting parameter β is given by $\beta = \bar{Y} - \alpha \bar{X}$.³¹

4.A.2 Application to the Weibull modulus

The preceding results can be re-cast in terms of the regression analyses used to obtain Weibull moduli via Eqns. (4.3) and (4.4). When the analysis is based on the area-dependence of strength, the uncertainty of $1/m_A$ (in Eqn. (4.3)) is obtained by setting $Y = \ln \sigma$ and $X = \ln A/A_o$ in Eqn. (4.A1), yielding:

$$S(1/m) = \sqrt{\frac{S^2(\ln A/A_o)S^2(\ln \sigma) - \text{cov}^2(\ln A/A_o, \ln \sigma)}{(N-2)S^4(\ln A/A_o)}} \quad (4.A3)$$

Eqn. (4.A3) is simplified by taking $N-2 \approx N$ and assuming that fiber area follows a normal distribution. Since the standard deviation of the logarithm of a normally-distributed variable (*i.e.* A) does not have an exact analytical solution, we approximate it by its CoV, defined as $Z(A) = S(A)/\bar{A}$ (\bar{A} being the average area). This approximation is adequate provided $Z(A)$ is small. In contrast, the standard deviation of a variable (*e.g.* strength) that follows a

Weibull distribution is exact; it is $S(\ln \sigma) = \pi / (m_t \sqrt{6})$ (solved in *Mathematica*). The covariance in turn is $\text{cov}(\ln(A/A_o), \ln \sigma) = \alpha Z^2(A/A_o)$. Combining these results and recognizing that, typically, $\pi^2/6 \gg Z^2(A)$, the CoV of $1/m_A$ becomes:

$$Z(1/m_A) = \pi / Z(A) \sqrt{6N} \quad (4.A4)$$

Error propagation analysis gives $Z(m_A) = Z(1/m_A)$, provided $Z(1/m_A) < 0.2$.

For the gauge length dependence of strength, general analytical solutions for $Z(1/m_L)$ are not available as the number of gauge lengths (n in Eqn. (4.A1)) is typically small (ca. 2–4) and the gauge lengths are a set of discrete values (unlike the continuous variable A). However, in cases in which there are *exactly* two gauge lengths, $Z(1/m)$ can be obtained from application of standard error propagation analysis to Eqns. (4.3) or (4.4). From Eqns. (4.3) and (4.4), $Y = \ln \sigma_{PE}$. The point estimate of strength σ_{PE} is approximately normally distributed so that $S(\ln \sigma_{PE}) \approx Z(\sigma_{PE})$. The standard error of the mean strength $\bar{\sigma}$ is estimated by $Z(\bar{\sigma}) = Z(\sigma) / \sqrt{N}$ where $Z(\sigma) = m_t^{-0.92}$ (accurate to within $\pm 2\%$ for $2 \leq m_t \leq 20^{22}$) and thus $Z(\bar{\sigma}) = m_t^{-0.92} / \sqrt{N}$. Similarly, $Z(\sigma_B)$ is also a function of only m_t and N :^{20, 23}

$$Z(\sigma_B) = \sqrt{(e^{-1/m_t} - 1) / N} \approx (m_t N)^{-0.5} \quad (4.A5)$$

for $m_t \gg 1$. This yields:

$$Z(1/m_L) = m_t^{0.08} \sqrt{2} / \sqrt{N} |\ln(\lambda)| \quad (4.A6)$$

$$Z(1/m_L) = \sqrt{2m_t} / \sqrt{N} |\ln(\lambda)| \quad (4.A7)$$

for single filament tests and fiber bundle tests, respectively. Here again we take $Z(m_L) \approx Z(1/m_L)$ when $Z(1/m_L)$ is small.

As previously noted, the preceding results (Eqns. (4.A4), (4.A6), and (4.A7)) are only valid when the spread in $-1/m$ is small. Otherwise, there is a progressively increasing probability of positive values of $-1/m$, in which case the inferred Weibull modulus is negative. (This feature is evident in Fig. 4.2a.) Furthermore, as $-1/m$ approaches zero, m tends towards $\pm\infty$. Since $-1/m$ is approximately normally distributed, an analytical solution for the distribution of m can be readily obtained from the distribution of $-1/m$. The distribution of m only depends on a shape parameter and a scale parameter for which we use $Z(1/m)$ and m_t , respectively. The cumulative distribution function (CDF) of $1/m$, denoted $F(1/m)$, and the probability density, $f(1/m)$, expressed in terms of $Z(1/m)$ and m_t are:

$$F(1/m) = \left(1 + \operatorname{erf}\left[\frac{(1 - m_t/m)/Z(1/m)}{\sqrt{2}}\right]\right)/2 \quad (4.A8)$$

$$f(1/m) = \frac{\partial F(1/m)}{\partial(1/m)} = \frac{m_t \exp\left[-(1 - m_t/m)^2 / 2Z^2(1/m)\right]}{Z(1/m)\sqrt{2\pi}} \quad (4.A9)$$

From Eqn. (4.A8), the probability P of $m < 0$ is:

$$P(m < 0) = \left(1 + \operatorname{erf}\left[-1/Z(1/m)\sqrt{2}\right]\right)/2 \quad (4.A10)$$

For small $Z(1/m)$, $P(m < 0) \approx 0$ and the CDFs of both m and $1/m$ are given by:

$$F(m) = F(1/m) = \left(1 + \operatorname{erf}\left[\frac{(1 - m_t/m)/Z(1/m)}{\sqrt{2}}\right]\right)/2 \quad (4.A11)$$

Otherwise, for finite values of $P(m < 0)$, $F(m)$ is a two-piece function: one each for positive and negative values of m . In general they are:

$$F(m) = \begin{cases} F(1/m) + P(m < 0), & m > 0 \\ F(1/m) + P(m < 0) - 1, & m < 0 \end{cases} \quad (4.A12)$$

while the corresponding probability density is:

$$f(m) = \frac{\partial F(m)}{\partial m} = \frac{m_t \exp\left[-(1 - m_t/m)^2 / 2Z^2(1/m)\right]}{m^2 Z(1/m) \sqrt{2\pi}} \quad (4.A13)$$

Eqn. (4.A13) is plotted in Figure 4.2b for $m_t = 10$, $Z(A) = 0.1$ and $N = 10-10,000$. For $N \leq 250$, a significant fraction of m values are negative, causing a shift of the median and the mode of m to lower values, less than m_t .

In principle, the preceding results should lead to solutions for the expected value, $E(m)$, and variance, $S^2(m)$, defined as:

$$E(m) = \int_{-\infty}^{\infty} mf(m) dm \quad (4.A14)$$

$$S^2(m) = \int_{-\infty}^{\infty} (m - E(m))^2 f(m) dm \quad (4.A15)$$

However, these integrals do not converge and hence both $E(m)$ and $S(m)$ are undefined.

Consequently, we use either the median, $m_{\text{med}} = m(F_m = 0.5)$, or the mode,

$m_{\text{mode}} = m(\partial f(m)/\partial m = 0)$, as point estimates of m . Following some algebraic

manipulation, the estimates become:

$$\frac{m_{\text{med}}}{m_t} = \left(1 + \sqrt{2}Z(1/m) \operatorname{erf}^{-1}\left[1 - \operatorname{erf}\left[1/Z(1/m)\sqrt{2}\right]\right]\right)^{-1} \quad (4.A16)$$

$$\frac{m_{\text{mode}}}{m_t} = \frac{-1 + \sqrt{1 + 8Z^2(1/m)}}{4Z^2(1/m)} \quad (4.A17)$$

4.A.3 Application to the reference strength

The distribution of reference strength is readily obtained analytically from the area dependence of strength. Here $Y = \ln \sigma$ and $\bar{Y} = \ln \sigma_{0,A} - (\gamma - Z^2(A)/2)/m$ where γ is the Euler–Mascheroni constant (≈ 0.577). Also, $X = \ln A/A_0$ and, assuming the fiber areas are normally distributed, $\bar{X} \approx -Z^2(A)/2$. Combining these results gives:

$$\beta = \bar{Y} - \alpha \bar{X} = \ln \sigma_{0,A} - \frac{\gamma}{m_A} \quad (4.A18)$$

and then solving for $\sigma_{0,A}$ gives:

$$\sigma_{0,A} = \exp(\beta + \gamma/m_A) \quad (4.A19)$$

Importantly, this (correct) result differs from that obtained by simply setting β equal to the last two terms in Eqn. (4.3).

The variance in β is obtained using approximations similar to those described for Eqn. (4.A3). Here Eqn. (4.A2) simplifies to $S(\beta) = \pi/m\sqrt{6N}$. The corresponding distribution of $\sigma_{0,A}$ is obtained in the same fashion as that for m . Namely, since β is normally distributed, the probability density and cumulative probability of $\sigma_{0,A}$ are:

$$f(\sigma_{0,A}) = \frac{m_t \sqrt{3N}}{\pi^{3/2} \sigma_{0,A}} \exp \left[\frac{-3m_t^2 N}{\pi^2} \ln^2 \sigma_{0,A}/\sigma_{0,t} \right] \quad (4.A20)$$

$$F(\sigma_{0,A}) = \frac{1}{2} + \frac{1}{2} \operatorname{erf} \left[\frac{m_t \sqrt{3N}}{\pi} \ln \sigma_{0,A}/\sigma_{0,t} \right] \quad (4.A21)$$

while the mean, variance and CoV of $\sigma_{0,A}$ are:

$$E(\sigma_{0,A}) = \int_0^\infty \sigma_{0,A} f(\sigma_{0,A}) d\sigma_{0,A} = \sigma_{0,t} e^{\pi^2/12m_t^2 N} \quad (4.A22)$$

$$\begin{aligned}
S^2(\sigma_{0,A}) &= \int_0^\infty (\sigma_{0,A} - E(\sigma_{0,A}))^2 f(\sigma_{0,A}) d\sigma_{0,A} \\
&= \sigma_{0,t}^2 \left(e^{\pi^2/3m_t^2N} - e^{\pi^2/6m_t^2N} \right)
\end{aligned} \tag{4.A23}$$

$$Z(\sigma_{0,A}) = \sqrt{e^{\pi^2/6m_t^2N} - 1} \approx \pi/m_t \sqrt{6N} \tag{4.A24}$$

The approximation in Eqn. (4.A24) is based on the assumption that the argument of the exponential term is $\ll 1$ (accurate for realistic combinations of m_t and N).

For the length dependence of single fiber strengths, the reference strength depends strongly on β but only weakly on m :

$$\sigma_{0,L} = \exp(\beta)/\Gamma(1+1/m) \tag{4.A25}$$

When only two gauge lengths (L_2 and $L_1 = L_0$) are used, $\beta = \ln \bar{\sigma}_1$ where $\bar{\sigma}_1$ is the average strength at $L = L_1$. From error propagation, $Z(\sigma_{0,L}) \approx Z(\bar{\sigma}) = m_t^{-0.92}/\sqrt{N}$. Comparing this result to that of $Z(m)$ (Eqn. (4.A7)), it is evident that the uncertainty in the reference strength is significantly lower than that of the Weibull modulus ($Z(m)/Z(\sigma_0) = m_t \sqrt{2}/|\ln(\lambda)| \ll 1$). Furthermore, $Z(\sigma_{0,L}) \approx Z(\sigma_{0,A})$ for realistic values of m_t ($Z(\sigma_{0,L})/Z(\sigma_{0,A}) = m_t^{0.08} \sqrt{6}/\pi \approx 1$). A similar result is obtained for the length dependence of bundle strength.

References

- ¹ A.K. De and K.K. Phani, "Gauge Length Effect on the Strength of Silicon Carbide and Sapphire Filaments," *J. Compos. Mater.*, **24** [2] 220–232 (1990).
- ² K. Goda and H. Fukunaga, "The evaluation of the strength distribution of silicon carbide and alumina fibres by a multi-modal Weibull distribution," *J. Mater. Sci.*, **21**

- [12] 4475–4480 (1986).
- 3 H.F. Wu and L.L. Wu, “Strength variability and size effect of Nicalon fibre bundles,”
J. Mater. Sci., **29** [16] 4232–4237 (1994).
- 4 T. Morimoto, S. Nakagawa, and S. Ogihara, “Bias in the Weibull strength estimation
of a SiC fiber for the small gauge length case,” *JSME International J.*, **48** [4] 194–198
(2005).
- 5 T. Morimoto, K. Yamamoto, and S. Ogihara, “Dependence of Weibull parameters on
the diameter and the internal defects of Tyranno ZMI fiber in the strength analysis,”
Adv. Compos. Mater., **16** [3] 245–258 (2007).
- 6 G. Simon and A.R. Bunsell, “Mechanical and structural characterization of the
Nicalon silicon carbide fibre,” *J. Mater. Sci.*, **19** [11] 3649–3657 (1984).
- 7 Y.T. Zhu, W.R. Blumenthal, S.T. Taylor, T.C. Lowe, and B. Zhou, “Analysis of Size
Dependence of Ceramic Fiber and Whisker Strength,” *J. Am. Ceram. Soc.*, **80** [6]
1447–1452 (1997).
- 8 S.T. Taylor, Y.T. Zhu, W.R. Blumenthal, M.G. Stout, D.P. Butt, and T.C. Lowe,
“Characterization of Nicalon fibres with varying diameters Part I Strength and
fracture studies,” *J. Mater. Sci.*, **33** [6] 1465–1473 (1998).
- 9 Y.T. Zhu, S.T. Taylor, M.G. Stout, D.P. Butt, W.R. Blumenthal, and T.C. Lowe,
“Characterization of Nicalon fibres with varying diameters Part II Modified Weibull
distribution,” *J. Mater. Sci.*, **33** [6] 1475–1480 (1998).
- 10 D.M. Wilson, “Statistical tensile strength of Nextel™ 610 and Nextel™ 720 fibres,”
J. Mater. Sci., **32** [10] 2535–2542 (1997).
- 11 D.M. Wilson and L.R. Visser, “High performance oxide fibers for metal and ceramic

- composites,” *Compos. - Part A Appl. Sci. Manuf.*, **32** [8] 1143–1153 (2001).
- ¹² W. Yu and J. Yao, “Tensile strength and its variation of PAN-based carbon fibers. I. Statistical distribution and volume dependence,” *J. Appl. Polym. Sci.*, **101** [5] 3175–3182 (2006).
- ¹³ T. Tagawa and T. Miyata, “Size effect on tensile strength of carbon fibers,” *Mater. Sci. Eng. A*, **238** [2] 336–342 (1997).
- ¹⁴ K. Naito, J.M. Yang, Y. Tanaka, and Y. Kagawa, “The effect of gauge length on tensile strength and Weibull modulus of polyacrylonitrile (PAN)- and pitch-based carbon fibers,” *J. Mater. Sci.*, **47** [2] 632–642 (2012).
- ¹⁵ J. Andersons, R. Joffe, M. Hojo, and S. Ochiai, “Glass fibre strength distribution determined by common experimental methods,” *Compos. Sci. Technol.*, **62** [1] 131–145 (2002).
- ¹⁶ ASTM C1239-13, “Standard Practice for Reporting Uniaxial Strength Data and Estimating Weibull Distribution Parameters for Advanced Ceramics,” (2013).
- ¹⁷ EN 843-5, “Advanced technical ceramics. Mechanical properties of monolithic ceramics at room temperature. Statistical analysis,” (2006).
- ¹⁸ ASTM C1557-14, “Standard Test Method for Tensile Strength and Young’s Modulus of Fibers,” (2014).
- ¹⁹ W. Weibull, “A statistical theory of the strength of materials,” *R. Swedish Inst. Eng. Res.*, **151** 1–45 (1939).
- ²⁰ H.E. Daniels, “The Statistical Theory of the Strength of Bundles of Threads. I,” *Proc. R. Soc. A Math. Phys. Eng. Sci.*, **183** [995] 405–435 (1945).
- ²¹ E.B. Callaway and F.W. Zok, “Strengths of ceramic fiber bundles: Theory and

- practice,” *J. Am. Ceram. Soc.*, **100** [11] 5306–5317 (2017).
- 22 E.B. Callaway and F.W. Zok, “Accurate determination of fiber strength distributions,” *J. Am. Ceram. Soc.*, **100** [3] 1202–1211 (2017).
- 23 V. Calard and J. Lamon, “Failure of fiber bundles,” *Compos. Sci. Technol.*, **64** [5] 701–710 (2004).
- 24 R.S. Hay and R.J. Chater, “Oxidation kinetics strength of Hi-Nicalon TM -S SiC fiber after oxidation in dry and wet air,” *J. Am. Ceram. Soc.*, **100** [9] 4110–4130 (2017).
- 25 R. Hill and E.U. Okoroafor, “Weibull statistics of fibre bundle failure using mechanical and acoustic emission testing: the influence of interfibre friction,” *Composites*, **26** [10] 699–705 (1995).
- 26 S.L. Phoenix, “Probabilistic Strength Analysis of Fibre Bundle Structures,” *Fibre Sci. Technol.*, **7** [1] 15–31 (1974).
- 27 E. Lara-Curzio and C.M. Russ, “On the relationship between the parameters of the distributions of fiber diameters, breaking loads, and fiber strengths,” *J. Mater. Sci. Lett.*, **18** [24] 2041–2044 (1999).
- 28 T.A. Parthasarathy, “Extraction of Weibull parameters of fiber strength from means and standard deviations of failure loads and fiber diameters,” *J. Am. Ceram. Soc.*, **84** [3] 588–592 (2001).
- 29 D.M. Kotchick, R.C. Hink, and R.E. Tressler, “Gauge Length and Surface Damage Effects on the Strength Distributions of Silicon Carbide and Sapphire Filaments,” *J. Compos. Mater.*, **9** [4] 327–336 (1975).
- 30 F.W. Zok, “On weakest link theory and Weibull statistics,” *J. Am. Ceram. Soc.*, **100** [4] 1265–1268 (2017).

- 31 F. Acton, *Analysis of Straight-Line Data*. Dover, New York, 1966.
- 32 A.S. Watson and R.L. Smith, “An examination of statistical theories for fibrous material in the light of experimental data,” *J. Mater. Sci.*, **20** [9] 3260–3270 (1985).
- 33 M. R’Mili, T. Bouchaour, and P. Merle, “Estimation of Weibull parameters from loose-bundle tests,” *Compos. Sci. Technol.*, **56** [7] 831–834 (1996).
- 34 K.G. Dassios, M. Steen, and C. Filiou, “Mechanical properties of alumina Nextel™ 720 fibres at room and elevated temperatures: Tensile bundle testing,” *Mater. Sci. Eng. A*, **349** [1] 63–72 (2003).

Table 4.1: List of variables

α Slope from linear regression	L_s Set of gauge lengths
β y-intercept from linear regression	m Weibull modulus
Γ Gamma function	n Sample size
γ Euler–Mascheroni constant (≈ 0.577)	N Number of fibers tested
λ Gauge length ratio	$P(x > a)$ Probability of random variable $x > a$
σ Stress/strength	P_f Probability of failure
$\bar{\sigma}$ Average strength	$S(x)$ Standard deviation of x
σ_0 Reference strength	$Z(x)$ Coefficient of variation of x
σ_B Bundle strength	
σ_{PE} Point estimate of strength	<i>Subscripts for m and σ</i>
A Fiber area	A Estimate from area method
A_0 Reference area	L Estimate from gauge length method
E_f Fiber Young’s modulus	med Median value
$E(x)$ Expected value of x	mode Mode of values
erf Error function	ML Estimate from maximum likelihood method
erf^{-1} Inverse error function	t True Weibull parameter
$f(x)$ Probability density function of x	WP Estimate from linear regression of Weibull plot
$F(x)$ Cumulative distribution function of x	
L Fiber length	
L_0 Reference length	

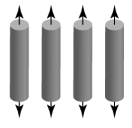
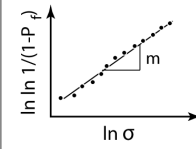

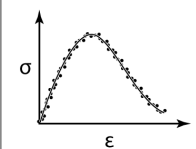
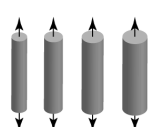
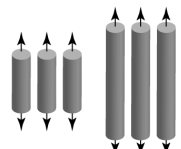
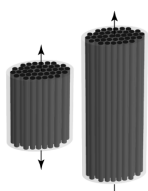
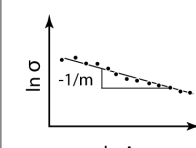
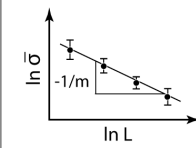
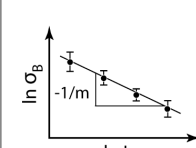
NATURE OF TEST	MEASUREMENTS	GUIDELINES FOR TEST DESIGN	
		GENERAL	TYPICAL
<p>1. Strength distribution</p>  <p>Individual fibers Constant A, L Strengths, $\sigma_1, \sigma_2, \dots$</p>		$N \geq 0.6 / Z^2(m)$	$N \geq 60$ ($Z(m) \leq 0.1$) $N \geq 15$ ($Z(m) \leq 0.2$)
<p>2. Bundle response</p>  <p>Fiber bundle Constant A, L Response $\sigma(\epsilon)$</p>		$N \geq 0.6 / Z^2(m)$	$N \geq 60$ ($Z(m) \leq 0.1$) $N \geq 15$ ($Z(m) \leq 0.2$)
<p>3. Volume-dependent strength</p>  <p>Individual fibers Constant L, varying A Strengths, $\sigma(A_1), \sigma(A_2), \dots$</p>  <p>Individual fibers Constant A, varying L Mean strengths, $\bar{\sigma}(L_1), \bar{\sigma}(L_2), \dots$</p>  <p>Fiber bundles Constant A, varying L Bundle strengths, $\sigma_B(L_1), \sigma_B(L_2), \dots$</p>	  	$N \geq 1.6 / (Z(m) Z(A))^2$ $N \geq 2m^{0.16} / (Z(m) \ln \lambda)^2$ $N \geq 2m / (Z(m) \ln \lambda)^2$	$N \geq 1,000$ ($Z(A) = 0.2$) $N \geq 4,000$ ($Z(A) = 0.1$) both for $Z(m) \leq 0.2$ $N \geq 135$ ($Z(m) \leq 0.1, \lambda = 0.25$) $N \geq 50$ ($Z(m) \leq 0.1, \lambda = 0.1$) $N \geq 35$ ($Z(m) \leq 0.2, \lambda = 0.25$) $N \geq 620$ ($Z(m) \leq 0.1, \lambda = 0.25$) $N \geq 230$ ($Z(m) \leq 0.1, \lambda = 0.1$) $N \geq 160$ ($Z(m) \leq 0.2, \lambda = 0.25$) all for $m = 6$

Figure 4.1: Schematics of test methods to determine Weibull parameters (in two left columns) and guidelines for selecting test parameters that yield acceptable random error.

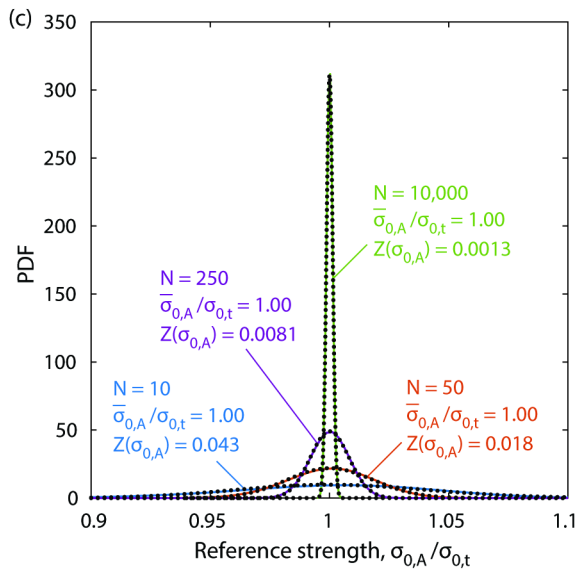
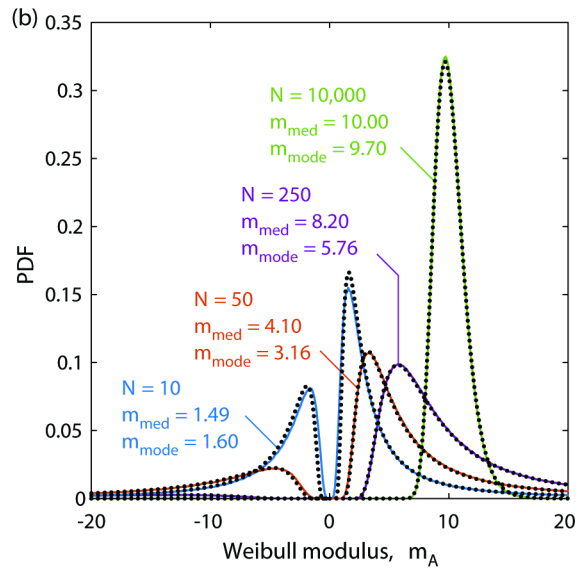
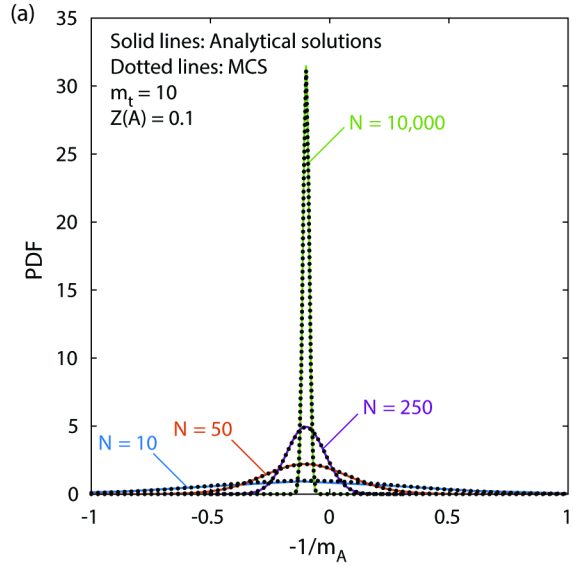


Figure 4.2: Comparisons of analytical solutions (solid lines) and MCS results (dotted lines) for distributions of (a) $-1/m_A$, (b) m_A and (c) $\sigma_{0,A}$, obtained from variations in strength with area. The true Weibull modulus is $m_t = 10$ and the CoV of fiber area is $Z(A) = 0.1$.

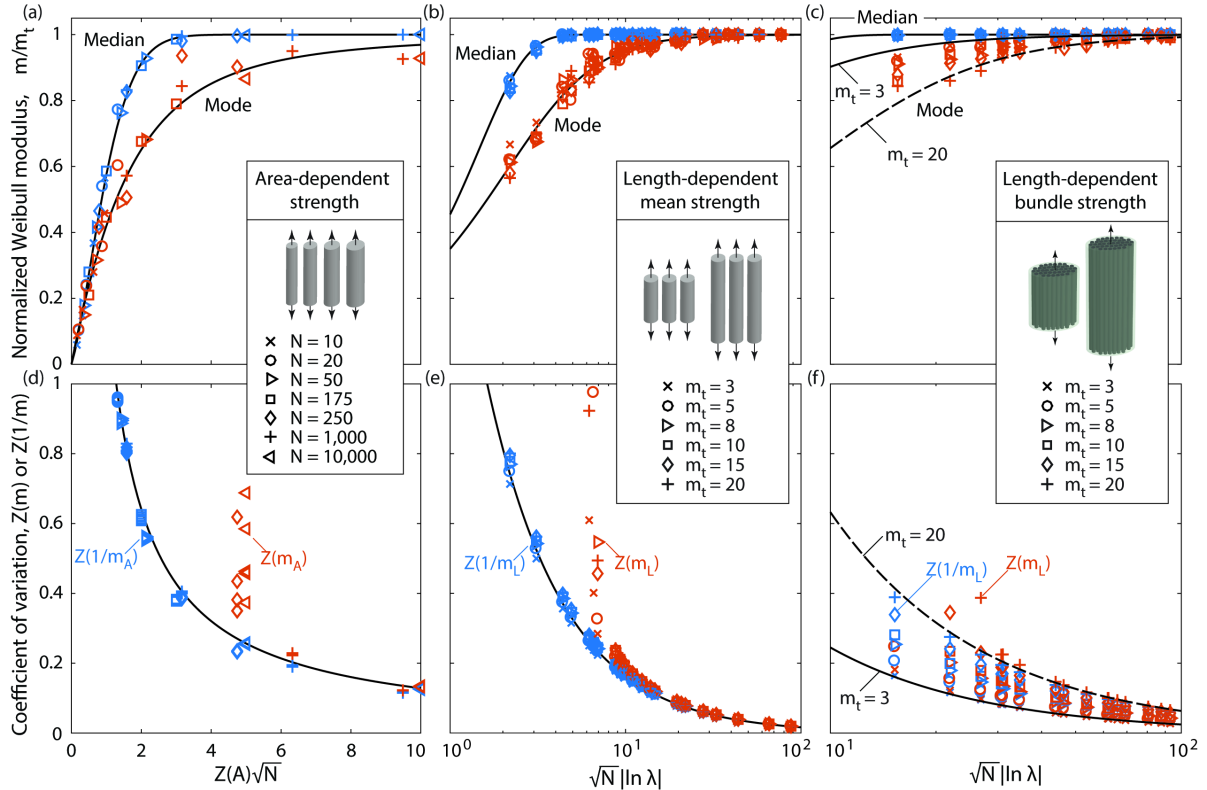


Figure 4.3: MCS results (symbols) and analytical solutions (lines) for median, mode and CoV of m obtained from (a, d) area-dependence of mean strength; (b, e) length-dependence of mean strength; and (c, f) length-dependence of fiber bundle strength. Correlations between $Z(1/m)$ and $Z(m)$ in (d-f) break down once $Z(1/m) > 0.2$. Unless otherwise noted, $m_t = 10$ for the lines representing analytical solutions.

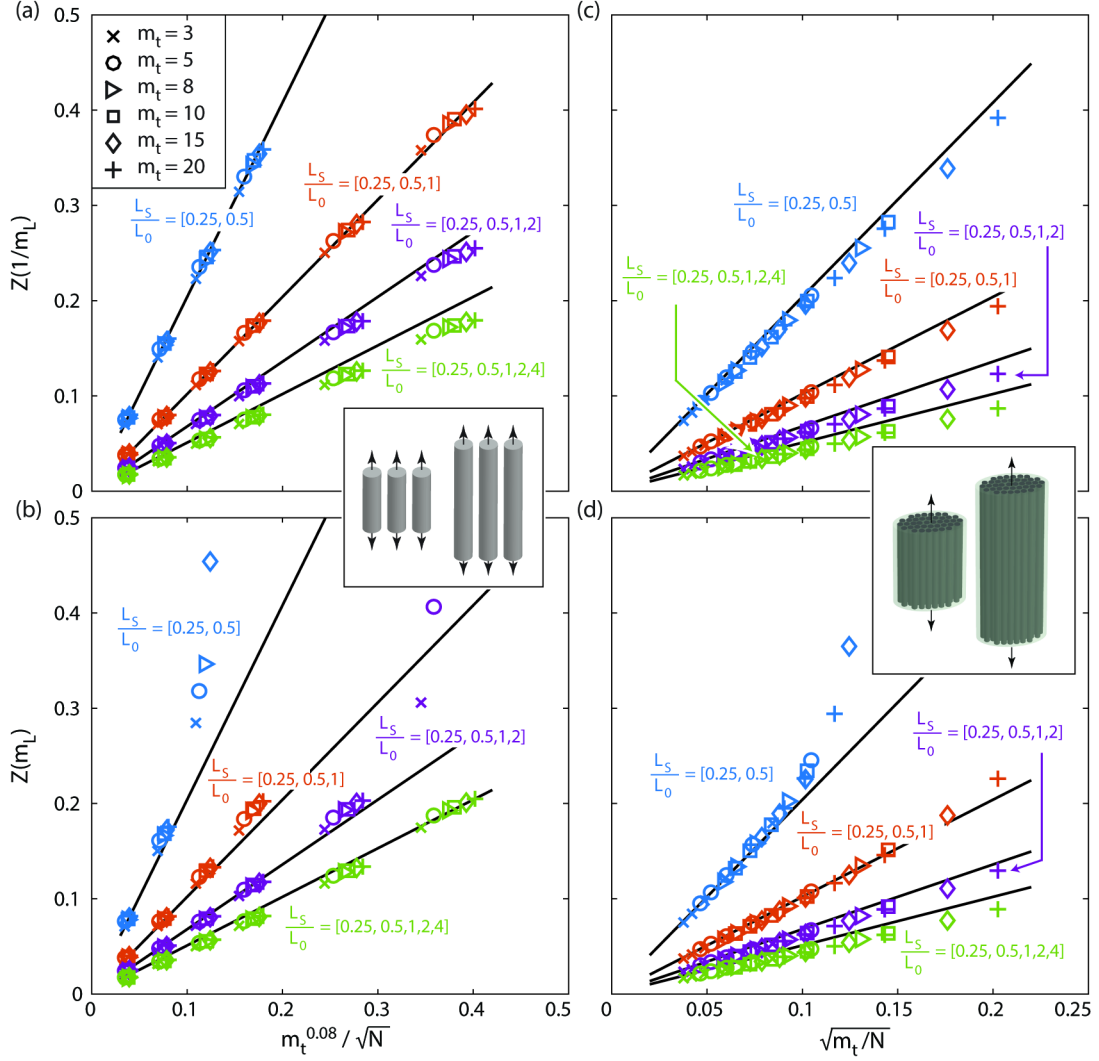


Figure 4.4: MCS results for $Z(1/m_L)$ and $Z(m_L)$ obtained from gauge-length dependence of (a,b) mean fiber strength and (c,d) fiber bundle strength. Four sets of gauge lengths are used for each simulation. Solid black lines are predictions of Eqns. (4.A6) and (4.A7). Eqns. (4.A6) and (4.A7) and the MCS begin to diverge once $Z(m_L) > 0.2$.

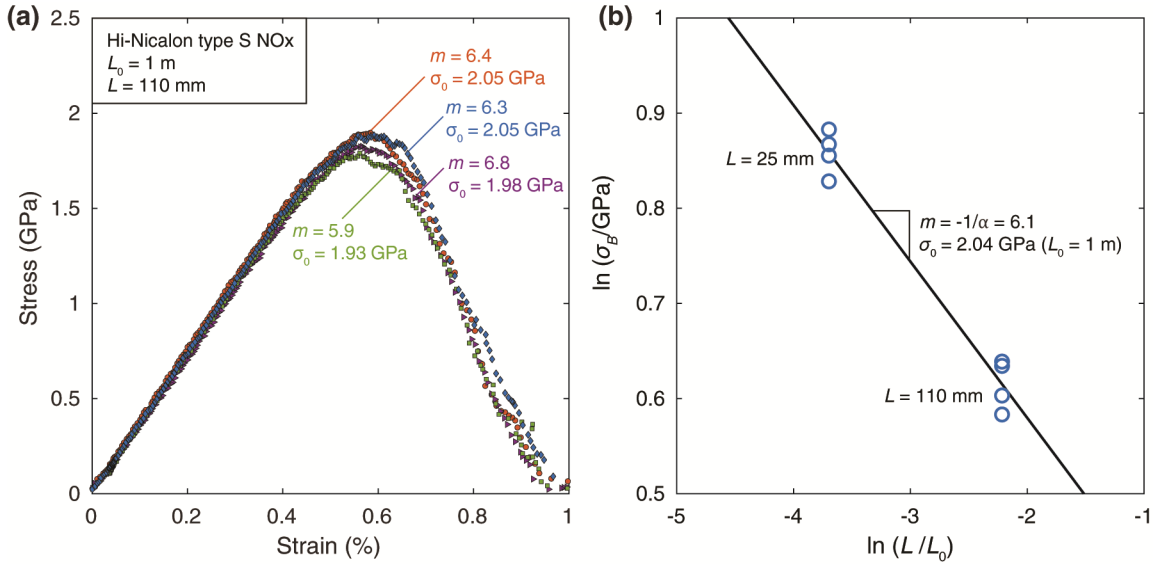


Figure 4.5: (a) Experimental stress-strain response for fiber bundles. (b) Weibull parameters obtained from measured bundle strengths at two gauge lengths.

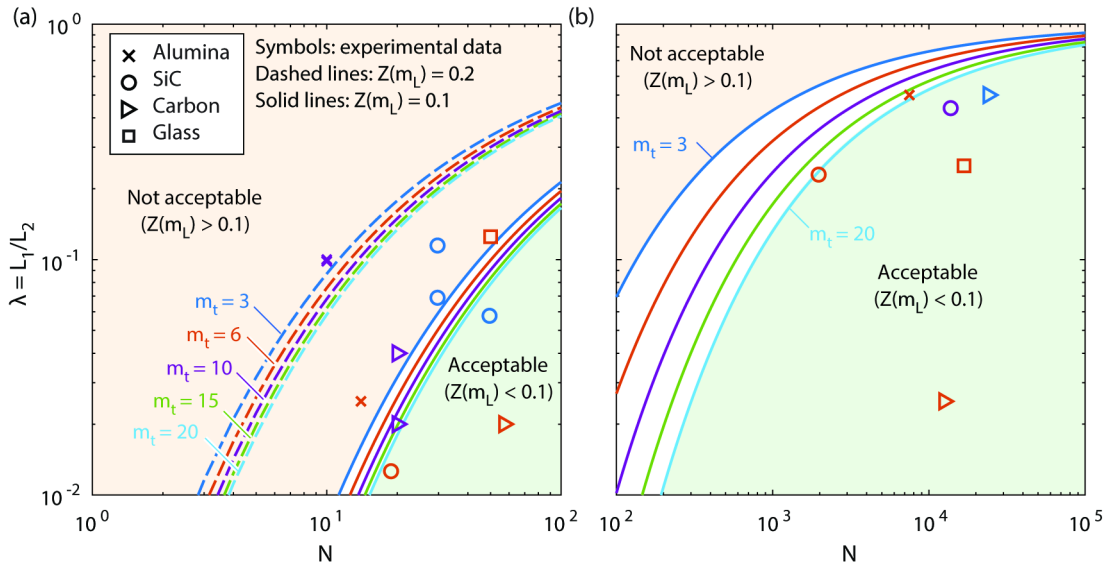


Figure 4.6: Uncertainty of Weibull moduli obtained from (a) single fiber tests^{3, 6, 10, 11, 14, 15, 29, 32} and (b) fiber bundle tests^{3, 15, 32–34}. Solid lines represent constant values of $Z(m_L)$ (0.1) for a wide range of Weibull moduli ($m_t = 3 - 20$). Points lying below the lines are deemed acceptable in that $Z(m_L)$ is less than the prescribed value (0.1). Also shown for reference in (a) are lines corresponding to $Z(m_L) = 0.2$. N in (b) represents the total number of fibers tested at each gauge length (*i.e.* the product of the number of fibers per tow and the number of bundles tested).

Chapter 5

Deformation, rupture, and sliding of fiber coatings in ceramic composites[‡]

Abstract

We examine the mechanics of shear deformation, rupture and frictional sliding of fiber coatings in ceramic composites through a combination of experiments, modeling and computational simulations. The work includes fiber push-in tests in several prototypical SiC-SiC composites with BN coatings on the fibers, using an established model of brittle interface fracture and subsequent sliding to interpret the data. The test results reveal two distinct behaviors: one in which a crack appears to form suddenly within the coating or at one of the interfaces with neighboring phases, followed by interface sliding (in accord with the established model), and another in which yielding of the BN occurs first, followed by rupture and sliding. Deficiencies in the existing brittle interface model are addressed through extensions of the model that account for coating plasticity prior to rupture. An analytical model based on shear lag analysis is developed and validated by finite element calculations and subsequently used in the interpretation of the test data. The work provides a new framework for interpreting fiber push-in results, including ways to ascertain the mechanism that governs the stress for push-in initiation and for extracting pertinent coating properties. It

[‡] The content of this chapter has been accepted for publication in the Journal of the Mechanics and Physics of Solids (**Evan Benjamin Callaway**, Paul Christodoulou, Frank W. Zok, “Deformation, rupture and sliding of fiber coatings in ceramic composites,” *J. Mech. Phys. Solids*, **132** (2019)). It is reproduced here with the permission of Elsevier.

also highlights the important role of plasticity in the design and performance of fiber coatings for ceramic composites.

5.1 Introduction

Mechanical performance of fiber-reinforced ceramic-matrix composites (CMCs) is critically dependent on the properties of interfaces between the fibers and the matrix. To exploit the full potential of high-strength fibers within CMCs, the fibers must be mechanically decoupled from the matrix. Otherwise, if the interface is excessively strong, cracks in the matrix penetrate into the fibers rather than deflecting into the interface. In practice, this behavior is enabled by fiber coatings that are either intrinsically weak or bond weakly to the fibers or the matrix.

In the context of SiC-SiC composites – the ones of most interest for use in gas turbine applications¹⁻⁶ – only two types of coatings have been developed to any significant extent. The first is based on pyrolytic C produced by chemical vapor deposition (CVD). Although their mechanical properties are nearly ideal in the as-deposited state, C coatings are intrinsically unstable in oxidizing environments at even moderate temperatures. Consequently, their potential use in long-term applications in oxidizing environments has been essentially abandoned.

The second coating type is BN. BN exhibits a number of attractive attributes. It is more resistant than C to oxidation in oxygen-containing environments. When in the hexagonal crystal form with the basal planes aligned parallel to the fiber surface, BN exhibits low resistance to shear deformation (especially in comparison to that of other refractory ceramics). But attaining these characteristics consistently is challenging. BN produced by CVD can take numerous forms with varying levels of crystallinity and alignment of basal planes in the preferred orientation. Additionally, its properties appear to depend on the nature of the surfaces on which it is deposited, on the precursor gases, and on

the temperatures, pressures and times used for deposition.^{4, 7–11} In addition to these sensitivities, which themselves are poorly understood, control of the deposition processes to achieve the desired properties remains somewhat of an artform. Furthermore, properties of BN produced in bulk form may differ from those of thin (ca 0.1–0.5 μm) BN coatings on SiC fibers. Therefore, to be most useful, coating properties should be measured *in situ* within composites of interest, not on bulk materials.

Fiber push-in, performed using an instrumented nanoindenter, is the premiere diagnostic tool for probing interface and coating properties in CMCs, especially under loadings that reflect those experienced during matrix cracking and fiber bridging.^{12, 13} The standard model for interpreting push-in measurements assumes that fiber coatings – when present but very thin – can be represented by two-dimensional interfaces, characterized by a toughness, Γ , and a sliding stress, τ_s , *but without capacity for elastic or plastic deformation*. From shear lag analysis and energy considerations, the load–displacement responses from push-in tests can be readily related to Γ and τ_s , among other properties (Young’s moduli, fiber radius, etc.).¹⁴

Here we examine the mechanics of shear deformation, rupture and frictional sliding of coated fibers in ceramic matrices. Experimental results from fiber push-in tests on several representative SiC/SiC composites with BN coatings on the fibers reveal that, in some cases, the push-in response is not fully consistent with that predicted by the standard model. Instead, they suggest a domain in which coatings *yield* before undergoing rupture and sliding. Accordingly, we develop and present a new model based on shear lag analysis, extending the standard model. The new model considers three behavioral domains: (i) purely-elastic loading of fiber, coating and surrounding matrix, (ii) coating yielding, and (iii)

coating rupture followed by frictional sliding. In the latter domain, crack growth is resisted by a Dugdale-like zone with two characteristic strengths: one dictated by yield and the other by frictional sliding. Notwithstanding its evident deficiencies in capturing yielding of the coating, the standard model remains useful in its description of both Γ and τ_s . One of the goals of the present work is to expound on the meaning of Γ in terms of elastic-plastic rupture. But the mere recognition that coating failure may involve local plasticity prior to rupture has important implications in the understanding of crack deflection and fiber bridging in CMCs during tensile loading, as discussed later.

The chapter proceeds in the following way. Section 5.2 begins with a synopsis of the basic mechanics of fiber push-in based on the standard model of interface rupture and sliding. This is followed by descriptions of test protocols, methods of data analysis used to infer interface properties, and experimental results interpreted in accordance with the standard model. An extended analytical model that accounts for elasticity and plasticity within the coating prior to coating rupture and supporting finite element analyses are presented in Section 5.3. The experimental results are then re-examined in the light of the new model, in Section 5.4. We speculate on the nature of the mechanisms operating during the push-in process in Section 5.5. Finally, the implications of the findings in composite design and composite properties are discussed briefly in Section 5.6.

5.2 Basic mechanics, test methods, and experimental measurements

5.2.1 The standard model

In the standard model of fiber push-in, illustrated in Figure 5.1A, coatings are represented as rigid-brittle interphases. A mechanics analysis of push-in was first presented by Marshall

and Oliver.^{14, 15} The push-in response is obtained from a shear lag analysis of the spatial domain within which sliding occurs and an energy balance analysis of incremental growth of a fully-developed interface crack. Being 1D in nature, the model neglects radial gradients in fiber strain. When the sliding resistance τ_s is constant along the crack surface (the case considered by Marshall and Oliver), the axial fiber strain decreases linearly into the composite, at a rate of $d(\sigma_f/E_f)/d(z/R_f) = 2\tau_s/E_f$, where σ_f is the average fiber stress at depth z below the surface, E_f is the fiber Young's modulus, and R_f is fiber radius. The crack tip resides at a depth $z = c$; at this point, the axial fiber strain undergoes essentially a discontinuity, from $\sigma_f/E_f = 2(\Gamma/R_f E_f)^{1/2}$ just behind the crack tip to 0 just ahead of it. The critical load F_r and corresponding fiber stress on the top fiber surface $\bar{\sigma}_{f,r}$ to generate a crack with $c \gg R_f$ (assuming negligible residual stress) are given by:

$$\frac{\bar{\sigma}_{f,r}}{E_f} \equiv \frac{F_r}{\pi R_f^2 E_f} = 2 \sqrt{\frac{\Gamma}{R_f E_f}} \quad (5.1)$$

Thereafter, the inelastic displacement on the top fiber surface due to sliding is

$$\frac{u_{in}}{R_f} = \frac{\bar{\sigma}_f^2}{4E_f \tau_s} - \frac{\Gamma}{\tau_s R_f} \quad (5.2)$$

where $\bar{\sigma}_f \equiv F/\pi R_f^2$. Upon subsequent unloading-reloading, hysteresis loops develop, with width Δ described by

$$\frac{\Delta}{R_f} = \left[\frac{\Delta_s}{R_f} \right] \left[\frac{\bar{\sigma}_f}{\bar{\sigma}_{f, \max}} \right] \left[1 - \frac{\bar{\sigma}_f}{\bar{\sigma}_{f, \max}} \right] \quad (5.3)$$

where $\bar{\sigma}_{f, \max}$ is the maximum axial fiber stress (at $z=0$ at the load maximum) and $\Delta_s/R_f \equiv \bar{\sigma}_{f, \max}^2/4\tau_s E_f$.^{16, 17} Eqn. (5.3) is valid when the *cyclic* sliding distance is less than the slip distance at peak load; when unloading is performed to zero load, this condition is satisfied for $\bar{\sigma}_{f, \max} \geq 2\bar{\sigma}_{f, r}$.^{14, 16}

Hutchinson and Jensen extended this analysis to fiber bridging of matrix cracks in CMCs loaded in tension parallel to the fiber direction, taking into account elastic anisotropy of the constituents, thermal misfit strains, and both constant sliding stress and Coulomb-like descriptions of sliding.¹⁸ For conditions examined by Marshall and Oliver, Hutchinson and Jensen recover the same results[§].

It warrants repeating that the preceding models assume that the interface crack is long compared to the fiber diameter and therefore its initiation from small putative flaws in the most-heavily stressed regions is neglected. A related tacit assumption is that axial fiber stress gradients are small over lengths comparable to the fiber diameter; therefore, stresses developed in the early stages of loading (being highly localized in the near-surface regions) are not accurately predicted. One consequence is that, when $\Gamma \approx 0$, the models predict that sliding begins essentially at the *onset* of loading (Eqn. (5.2)). Recognizing this limitation, Marshall and Oliver proceeded to estimate the shear stress at the fiber-matrix interface in the near-surface region. For this purpose they used Mindlin's solution for the stress field around a point force acting on an elastic half-space.¹⁹ The shear stress distribution along a cylindrical surface defined by $r = R_f$ is given by

[§] The one minor difference is that, in Hutchinson and Jensen's analysis, the plane strain modulus emerges in place of the Young's modulus. This arises because the calculations are based on stress intensity factors and the conversions to energy release rates assume plane-strain loading.

$$\frac{\tau}{\bar{\sigma}_f} = \frac{3(z/R_f)^2}{2\left(1+(z/R_f)^2\right)^{5/2}} \quad (5.4)$$

Its maximum value is $\tau/\bar{\sigma}_f \approx 0.28$ and occurs at a depth $z/R_f \approx 0.82$. Marshall and Oliver used this result to rationalize the finite load needed to initiate sliding in cases where C coatings were very weakly bonded to SiC fibers and the interface toughness was essentially zero.

One of the subtle lessons from Marshall and Oliver's work is the recognition that, in order for interface rupture and sliding to occur, the loading conditions must simultaneously satisfy *both* the energetics of interface crack growth *and* the stresses needed for sliding; interface rupture cannot occur without shear sliding and sliding cannot occur without interface rupture. Therefore the greater of the two conditions (couched in terms of critical fiber stresses) for interface rupture and for interface sliding dictates the onset of both. A corollary is that fiber push-in tests cannot immediately discriminate between the two conditions governing the onset of rupture and sliding. This dilemma is addressed in the present study.

5.2.2 Test methods

Push-in tests were performed on SiC/SiC composites using an instrumented nanoindenter (iMicro Nanoindenter, Nanomechanics, Inc.) equipped with a 10 μm -radius spheroconical indenter, the latter selected to mitigate plastic indentation of the fiber. The load was cycled to progressively increasing peak loads, between 100 mN and 400 mN in 100 mN increments, at a rate of 100 mN/s. Two load-unload cycles were performed to each peak load. In cases where the indenter came into contact with the matrix (an event marked by a

sharp increase in stiffness, typically at displacements greater than 2 μm), data in the post-contact domain were neglected. Additionally, to ensure a cyclic sliding distance less than the slip distance at peak load, only loops for which $\bar{\sigma}_{f,\text{max}} \geq 2\bar{\sigma}_{f,r}$ were used in calculating sliding stresses. Surface profiles of a number of pushed-in fibers were subsequently obtained by confocal microscopy. These measurements confirmed that the indentations were essentially purely elastic, with residual indentation depths of <10 nm (see example in Figure 5.2). Typically about 30–40 fibers were tested in each specimen.

Test results are reported for four materials systems, all with coatings of hexagonal BN on the fibers: (i) a 3D woven composite of Tyranno ZMITM fibers in a SiC matrix, produced by a combination of chemical vapor deposition, slurry infiltration, and precursor impregnation and pyrolysis (PIP)²⁰; (ii) a unidirectional minicomposite of Tyranno ZMITM fibers in a CVI SiC matrix, (iii) a unidirectional minicomposite of Hi-Nicalon Type STM (HNS) fibers in a CVI SiC matrix, and (iv) a 2D woven composite with Hi-NicalonTM fibers in a SiCN PIP-derived matrix²¹ (known by the trade name S200-H). The fiber radii, measured on polished cross-sections through the composites, were 6.4 ± 0.6 μm for the ZMI 3D composite, 6.6 ± 0.7 μm for the ZMI minicomposite, 6.9 ± 0.5 μm for the HNS minicomposite, and 7.6 ± 1.1 μm for S200-H. Typically, larger diameter fibers were selected for push-in tests, to prevent the indenter tip from contacting the matrix. Thicknesses of the BN coatings varied between 100 and 500 nm. No correlation between fiber radius or coating thickness and interfacial properties was observed. Micrographs of each are shown in Figure 5.2. A typical confocal microscope image of a pushed-in fiber is also shown.

5.2.3 Data analysis

In the first round of analysis, interface properties were obtained from the push-in data using Marshall and Oliver's brittle fracture model. Operationally, the total measured fiber displacement u_f^o is partitioned into three components: (i) the elastic displacement u_H associated with the indenter-fiber contact (assumed to be Hertzian), (ii) the additional elastic displacement u_{el} due to shear deformation of the coating and the surrounding matrix, and (iii) the inelastic displacement u_{in} due to sliding at the fiber-matrix interface.

Prior to interface rupture, $u_{in} = 0$ and thus the total fiber displacement is

$$u_f^o = u_H + u_{el} = c_1 F^{2/3} + c_2 F \quad (5.5)$$

where c_1 and c_2 are constants that depend on geometry and elastic properties of the constituents. This result can be re-expressed as

$$u_f^o / F = c_1 F^{-1/3} + c_2 \quad (5.6)$$

Thus, in this (purely-elastic) domain, the secant compliance u_f^o / F is predicted to vary linearly with $F^{-1/3}$ (Figure 5.3). This linearity is lost once rupture occurs.

As we show in the subsequent section, the transition from elastic to inelastic deformation generally occurs in one of two ways: (i) with a rapid increase in u_f^o / F almost immediately after linearity in u_f^o / F vs. $F^{-1/3}$ is lost (as illustrated by the numerical results in Figure 5.3) or (ii) with progressive deviation from linearity in u_f^o / F vs. $F^{-1/3}$ prior to attainment of the minimum. In the present interpretation of the data, the interface rupture load, F_r , is taken to be that at the *minimum compliance*. This selection is motivated by the desire to automate analysis of large data sets. (The implications of this selection are discussed later.) In turn, F_r is used to compute the toughness Γ from Eqn. (5.1) while the

sliding stress τ_s is computed by fitting variations in loop width with load during reload-unload cycles, in accordance with Eqn. (5.3).¹⁶ The preceding methods for obtaining Γ and τ_s are de-coupled from one another in the sense that Γ is obtained solely from the forward loading curve whereas τ_s is obtained solely from subsequent loading-unloading hysteresis loops (independent of the forward loading curve).

5.2.4 *Experimental results*

Typical load-displacement curves including unloading-reloading loops for each of the four materials are shown in Figure 5.4. Sliding stresses obtained from successive cycles after interface failure are consistent with one another, within about 10% (Figure 5.5). Distributions in sliding stress (represented by cumulative distribution functions, CDF, in Figure 5.6A) show pronounced differences between the four materials tested, by as much as a factor of 4.

Transitions from elastic to inelastic deformation are illustrated by plots of u_f^o/F vs. $F^{-1/3}$ (Figure 5.7). As noted, the transition can occur with the minimum in compliance almost immediately after linearity in u_f^o/F vs. $F^{-1/3}$ is lost or with some deviation from linearity prior to the minimum. In the ZMI minicomposite and the S200H composite, the transition is largely of the former kind, reflecting brittle coating rupture; in contrast, that in the HNS minicomposite and the ZMI 3D composite is of the latter kind, reflecting non-brittle rupture. The resulting distributions in coating toughness (obtained from the load at minimum compliance) show wide variations among the four materials, by as much as a factor of 10 (Figure 5.6B).

Additional insights into the elastic/inelastic transition are obtained by computing and plotting variations in load with *inelastic* displacement, u_{in} . The latter is obtained by performing a linear fit of the data in Figure 5.7 in the linear domain (to obtain the constants c_1 and c_2) and subsequently subtracting the Hertzian and elastic displacement, $c_1 F^{2/3} + c_2 F$, from the total displacement u_f^o at each load level. Typical results for each of the four materials are shown in Figure 5.8. Two features are particularly noteworthy. First, in cases in which the transition to sliding occurs through a relatively abrupt change in compliance, the load-inelastic displacement curve appears consistent with the prediction of the standard brittle fracture model. (It should be noted that the response in the sliding regime is computed using the sliding stress inferred from the subsequent hysteresis loops, not the forward loading data shown in the figure.) In other cases, a distinct change in slope is obtained near the load corresponding to minimum compliance. Here, although the response at higher loads is consistent with the prediction of the standard model, the inferred critical load occurs at a finite (and significant) inelastic displacement (ca. 50–100 nm). Additionally, the response between the onset of push-in and the transition load is *not* consistent with the model prediction. Indeed, these results motivate re-examination of the standard brittle fracture model and development of a new model of elastic-plastic coating deformation and rupture.

5.3. Elastic-plastic deformation and rupture of fiber coatings

5.3.1 Analytical model

We present a model based on shear lag analysis of push-in of a coated fiber embedded in a cylindrical matrix jacket. The problem is shown schematically in Figure 5.1B. Fibers and matrix are assumed elastic (without residual stress) whereas the coating is taken to be

elastic, perfectly-plastic. A uniform compressive stress $\bar{\sigma}_f$ is applied to the top (external) fiber surface^{**}. As usual in analyses of this type, axial fiber strains are assumed to be uniform within each transverse plane but can vary with depth, z . The coating thickness h is taken to be small in relation to the fiber radius so that the shear stress in the coating is uniform and only varies with depth. The analysis is presented in three steps: the first for the case where the coating is purely elastic, the second where the coating is elastic-plastic, and the third where the coating has ruptured and frictional sliding ensues.

Elastic coating: Hooke's law for the fiber gives:

$$\frac{\partial u_f(z)}{\partial z} = \varepsilon_f = \frac{\sigma_f(z)}{E_f} \quad (5.7)$$

Mechanical equilibrium via shear lag is established by:

$$\frac{\partial \sigma_f(z)}{\partial z} = \frac{-2\tau_c(z)}{R_f} \quad (5.8)$$

where τ_c is the shear stress in the coating. Differentiating with respect to z and re-arranging gives:

$$\frac{\partial \tau_c(z)}{\partial z} = \frac{-R_f}{2} \frac{\partial^2 \sigma_f(z)}{\partial z^2} \quad (5.9)$$

Similarly, elasticity of the matrix and radial compatibility yields:

$$\frac{\partial u_m(z)}{\partial r} = \frac{\tau_c(z)R_f}{rG_m}, \quad r > R_f + h \quad (5.10)$$

^{**} Because of the assumed loading, the displacement on the top fiber surface has contributions from linear-elastic and inelastic deformation, but not the Hertzian contribution found in experimental measurements.

where G_m is the matrix shear modulus. Integrating Eqn. (5.10) gives the displacement at the matrix-coating interface:

$$u_1(z) = \int_{R_f+h}^{R_o} \frac{\tau_c(z)R_f}{rG_m} dr = \frac{\tau_c(z)R_f}{G_m} \ln\left(\frac{R_o}{R_f+h}\right) \quad (5.11)$$

where R_o is a cut-off radius; although R_o must be selected somewhat arbitrarily, its value has little consequence in the computed displacement because of the weak (logarithmic) dependence in Eqn. (5.11). (This feature is common in cases where concentrated loads are applied onto a half-space and the stress fields exhibit a $1/r$ singularity.²²) The shear displacement across the coating is:

$$u_1(z) - u_2(z) = \frac{-\tau_c(z)h}{G_c} \quad (5.12)$$

where $u_2(z)$ is the axial displacement at the fiber-coating interface and G_c is the coating shear modulus. Substituting Eqn. (5.11) into Eqn. (5.12) gives:

$$u_2(z) = \frac{\tau_c(z)h}{G_c} + \frac{\tau_c(z)R_f}{G_m} \ln\left(\frac{R_o}{R_f+h}\right) \quad (5.13)$$

Combining Eqns. (5.7), (5.9) and (5.13) yields the governing differential equation:

$$\sigma_f(z) + \eta^2 R_f^2 \frac{\partial^2 \sigma_f(z)}{\partial z^2} = 0 \quad (5.14)$$

where

$$\eta^2 \equiv \frac{E_f}{2} \left(\frac{h}{R_f G_c} + \frac{1}{G_m} \ln\left(\frac{R_o}{R_f+h}\right) \right) \quad (5.15)$$

Here η is a non-dimensional parameter that incorporates geometric and elastic properties of the constituents.

For the appropriate boundary conditions ($\sigma_f = \bar{\sigma}_f = F/\pi R_f^2$ at $z = 0$ and $\sigma_f = 0$ at $z = \infty$), the solution to Eqn. (5.14) is:

$$\frac{\sigma_f(z)}{\bar{\sigma}_f} = \exp\left(\frac{-z}{\eta R_f}\right) \quad (5.16)$$

which, combined with Eqn. (5.8), yields the shear stress distribution:

$$\frac{\tau_c(z)}{E_f} = \frac{\bar{\sigma}_f}{2\eta E_f} \exp\left(\frac{-z}{\eta R_f}\right) \quad (5.17)$$

From Eqns. (5.7) and (5.16), the macroscopic elastic response becomes:

$$\frac{u_f}{R_f} = \int_0^\infty \frac{\sigma_f(z)}{R_f E_f} dz = \frac{\eta \bar{\sigma}_f}{E_f} \quad (5.18)$$

where u_f is the non-Hertzian displacement. Together, Eqns. (5.16)–(5.18) are the first set of key results. They remain valid when coatings are absent (*i.e.* $h = 0$).

Elastic-plastic coating: Yielding begins when the maximum shear stress in the coating (at $z = 0$) reaches the shear yield strength τ_y of the coating. From Eqn. (5.17), this occurs at a stress $\bar{\sigma}_{f,y}/E_f = 2\eta\tau_y/E_f$. Thereafter, the plastic zone spreads into the composite interior to a depth L_p . The shear stress in the coating then follows a piecewise function of z ; it is equal to τ_y over $0 \leq z \leq L_p$ and to that in the elastic field over $L_p \leq z \leq \infty$. Setting the elastic shear stress equal to τ_y , the length of the plastic zone becomes $L_p/R_f = \bar{\sigma}_f/2\tau_y - \eta$.

The fiber stress also follows a piecewise function:

$$\frac{\sigma_f(z)}{E_f} = \begin{cases} \frac{\bar{\sigma}_f}{E_f} - \frac{2\tau_y z}{E_f R_f} & 0 \leq z \leq L_p \\ \frac{\sigma_f^{el}(z - z_o)}{E_f} & L_p \leq z \leq \infty \end{cases} \quad (5.19)$$

Here σ_f^{el} represents the elastic stress field in the fiber (Eqn. (16)) and z_o is a spatial shift in the elastic field, given by $z_o = L_p - L_\tau$, where L_τ is defined as the depth at which the shear stress of the elastic field equals τ_y . Using Eqn. (5.17), this depth is:

$$\frac{L_\tau}{R_f} = \eta \ln \left(\frac{\bar{\sigma}_f}{2\eta\tau_y} \right) \quad (5.20)$$

The shift z_o in Eqn. (5.19) ensures that $\sigma_f(z)$, $\partial\sigma_f(z)/\partial z$, and $\tau_c(z)$ are continuous at $z = L_p$ (at the transition from elastic to plastic deformation). The top-surface fiber displacement is then obtained by integrating Eqn. (5.19):

$$\frac{u_f}{R_f} = \frac{\bar{\sigma}_f^2}{4E_f\tau_y} + \frac{\tau_y\eta^2}{E_f} \quad (5.21)$$

The first and second terms on the right side are the plastic and elastic displacement components, respectively. This is the second key result of the analysis.

Coating rupture and frictional sliding: Once the coating ruptures and frictional sliding ensues (for $\bar{\sigma}_f > \bar{\sigma}_{f,r}$), the response is

$$\frac{u_f}{R_f} = \frac{\bar{\sigma}_f^2}{4E_f\tau_s} - \frac{\Gamma}{R_f\tau_s} + \frac{u_{f,r}}{R_f} \quad (5.22)$$

where $u_{f,r}$ is the displacement at the onset of coating rupture, given b

$$\frac{u_{f,r}}{R_f} = \frac{\Gamma}{R_f\tau_y} + \frac{\eta^2\tau_y}{E_f} \quad (5.23)$$

Eqns. (5.22) and (5.23) are the third key result.

With the assumptions used here – that the coating is elastic, perfectly-plastic and that sliding after rupture is resisted by a constant shear stress – the process in the post-rupture domain reaches a pseudo-steady-state in the sense that the elastic and plastic zones simply extend along the interface in an unchanged fashion while the frictional zone trails behind^{††}. As a result, the present model (especially Eqns. (5.22) and (5.23)) can be reinterpreted in terms of the standard brittle fracture model (Eqn. (5.2)) via an effective coating toughness $\Gamma_{eff} = \tau_y u_c$ where u_c is the critical *inelastic* shear displacement for coating rupture. It can be readily shown from Eqn. (5.23) that u_c and $u_{f,r}$ are related by $u_c/R_f = u_{f,r}/R_f - \eta^2 \tau_y / E_f$, differing only by the elastic term $\eta^2 \tau_y / E_f$.

5.3.2 *Finite element analysis*

To assess the analytical model, finite element (FE) simulations were performed on an axisymmetric model of a coated fiber within a cylindrical matrix jacket. Displacement at the bottom of the composite was fixed and a uniformly-distributed load was applied to the top surface of the fiber, progressively increasing from 0 to 3 GPa. The fiber radius (6 μm) and the thickness of the matrix jacket (100 μm) were fixed in all simulations. The coating thickness was selected to be either 0.1, 0.3, or 0.6 μm (a range that reflects BN coatings in composites of interest). The height of the composite was taken to be 20 times the outer radius of the matrix jacket. The width of the elements in the radial direction was $R_f/12$ in both the fiber and the matrix; in the coating, the element width was taken to be $h/3$.

^{††} The process is not a true steady state because the frictional zone continues to grow and hence the stress required to sustain the process increases with time.

Element heights were graded, from a minimum of $R_f/3000$ μm at the top surface, increasing by a factor of 1.004 in successive element layers going downwards. The total number of elements was $>400,000$ in all cases. These selections were based on a preliminary mesh-sensitivity study.

Elastic properties of the fiber and the matrix were taken to be the same: Young's modulus of 300 GPa and Poisson's ratio of 0.2. The Young's modulus of the coating E_c was taken as either 10, 30, or 50 GPa, its Poisson's ratio was set at 0.2, and its shear yield strength τ_y was either 10, 30, or 90 MPa. (The coating properties fall in the range reported for hexagonal BN, e.g. $E = 17 - 103$ GPa, $\nu = 0.22$, and flexural strength of about 20-100 MPa.²³⁻²⁵) The coating material was taken to be elastic-perfectly plastic with an equivalent (Mises) yield strength of $\sigma_y = \sqrt{3}\tau_y$.

The FE results are presented in terms of three non-dimensional independent variables: coating thickness, h/R_f (0.0167–0.10), coating modulus, E_c/E_f (0.033–0.167), and coating yield stress, τ_y/E_f ($3.3 \times 10^{-5} - 3 \times 10^{-4}$). The computed parameters are: top surface fiber displacement, u_f/R_f , top-surface fiber stress, $\bar{\sigma}_f/E_f$, coating shear stress, τ_c/E_f , and plastic zone length, L_p/R_f . Reported axial fiber displacements are with respect to the axial displacement of the outer edge of the matrix jacket. (The radial distance from the center to the outer edge of the matrix jacket is equivalent to the cut-off radius in the analytical model. Therefore, in the FEA simulations, $R_o/(R_f + h) \approx 17$.)

5.3.3 Assessment of analytical model

The analytical predictions agree remarkably well with the FEA results. In the elastic domain, distributions of coating shear stress $\tau_c/\bar{\sigma}_f$ are only weakly dependent on the thickness and the modulus of the coating (Figure 5.9). Here the analytical results are shown for two values of cut-off radius: $R_o/(R_f + h) = 10$ and 20, spanning that employed in the FEA (17). The peak values of shear stress $\tau_{\max}/\bar{\sigma}_f$ from FEA and the analytical model agree with one another to within about 10% and, collectively, fall in the range of about 0.2–0.3. By comparison, the Mindlin solution for a point force on an elastic half-space (employed by Marshall and Oliver) yields a peak $\tau_{\max}/\bar{\sigma}_f = 0.28$. The latter is close to that obtained from FEA for cases in which the coating is thin and stiff ($\tau_{\max}/\bar{\sigma}_f \approx 0.30$). The shear stress decays approximately exponentially with distance from the free surface, decreasing from its peak by a factor of about 3 at $z/R_f = 2$.

The push-in responses, couched in terms of $\bar{\sigma}_f/E_f$ vs. u_f/R_f , show particularly good agreement both in the elastic domain and after coating yielding (Figure 5.10). The evolution of plastic zone length is also captured well (Figure 5.11). The plastic zone length is predicted from the model to be $L_p/R_f = (\bar{\sigma}_f/E_f)/(2\tau_y/E_f) - \eta$; it exhibits an inverse dependence on the coating yield stress and only a weak sensitivity to coating properties (through η).

5.3.4 Initiation of inelastic fiber push-in

The preceding analysis reveals three possible scenarios with respect to the onset of inelastic deformation during push-in, predicated on three assumptions: (i) that frictional sliding cannot occur without interface rupture; (ii) that interface rupture cannot occur without frictional sliding; and (iii) that yielding cannot occur once rupture and frictional sliding have begun. The three scenarios follow.

- (i) When $\bar{\sigma}_{f,sl} < \bar{\sigma}_{f,r} < \bar{\sigma}_{f,y}$, a fully-developed interface crack is formed at stress $\bar{\sigma}_{f,r}$; at this point, the frictional sliding condition is met. Yielding does not occur.
- (ii) When, instead, $\bar{\sigma}_{f,r} < \bar{\sigma}_{f,sl} < \bar{\sigma}_{f,y}$, sliding begins at stress $\bar{\sigma}_{f,sl}$; at this point, the rupture condition is met. Again, yielding does not occur. (This is the case obtained by Marshall and Oliver for cases of weakly-bonded C coatings on SiC fibers.)
- (iii) Finally, when $\bar{\sigma}_{f,sl} < \bar{\sigma}_{f,y} < \bar{\sigma}_{f,r}$, coating yielding begins at stress $\bar{\sigma}_{f,y}$; coating rupture and frictional sliding then begin at $\bar{\sigma}_{f,r}$.

These scenarios can be depicted using three non-dimensional parameters that emerge from the analysis: $\eta\tau_s/E_f$, representing the sliding stress; $\Gamma/R_f E_f$, representing the toughness; and τ_y/τ_s , representing the coating yield stress. A map showing $\eta\tau_s/E_f$ vs. $\Gamma/R_f E_f$ for $\tau_y/\tau_s = 3$ is presented in Figure 5.12. The two boundaries between the three domains are obtained by setting $\bar{\sigma}_{f,r} = \bar{\sigma}_{f,sl}$ and (separately) $\bar{\sigma}_{f,r} = \bar{\sigma}_{f,y}$. The former boundary is defined by $\eta\tau_s/E_f = \sqrt{\Gamma/R_f E_f}$ and the latter by $\eta\tau_s/E_f = (\tau_s/\tau_y)\sqrt{\Gamma/R_f E_f}$. The map also shows contours of constant critical fiber stress to initiate push-in in each of the three domains: $\bar{\sigma}_f/E_f = 2\eta\tau_s/E_f$ for sliding, $\bar{\sigma}_f/E_f = 2\sqrt{\Gamma/R_f E_f}$ for rupture, and

$\bar{\sigma}_f/E_f = (2\eta\tau_s/E_f)(\tau_y/\tau_s)$ for yielding. When $\tau_y > \tau_s$, these contours (shown as dashed grey lines) follow a characteristic stair-step pattern. As τ_y decreases and approaches τ_s , the rupture-controlled domain shrinks and the stresses in the sliding- and yielding-controlled domains get closer to one another. Eventually, once $\tau_y \leq \tau_s$, both the sliding- and the rupture-controlled domains vanish and the behavior over the entire space is controlled by yielding.

One of the implications of this analysis is that the mechanism controlling the onset of fiber push-in cannot be discerned solely from the critical stress. To ascertain the controlling mechanism, other features of the push-in response must be considered. For example, in the yield-controlled domain, the inelastic response exhibits two distinct parts: the first governed by the yield stress and the second by the sliding stress (the latter being lower than the former). This feature is unique to this combination of mechanisms. When yielding is not involved, discriminating between sliding- and rupture-controlled push-in can be made by comparing $\eta\tau_s/E_f$ with $\sqrt{\Gamma/R_f E_f}$; when $\eta\tau_s/E_f < \sqrt{\Gamma/R_f E_f}$, push-in is rupture-controlled and, when $\eta\tau_s/E_f > \sqrt{\Gamma/R_f E_f}$, push-in is sliding-controlled.

5.4 Re-examination of experimental data

The experimental push-in data are re-examined in the light of the new model, with three goals in mind: (i) to determine the coating yield strengths (in cases where yielding precedes rupture); (ii) to ascertain the mechanism controlling the onset of inelastic displacement; and (iii) to assess the accuracy of toughness values inferred from the standard model.

To begin, it is useful to examine the variation in the square of the load F^2 with the non-Hertzian fiber displacement ($u_f = u_f^o - c_1 F^{2/3}$). The model predicts two behavioral types: (i) when rupture precedes yielding, the relationship between F^2 and displacement is linear within the inelastic domain (in accordance with Eqn. (5.21)) and (ii) when yielding precedes rupture and sliding, two linear domains are obtained, the first associated with yielding and the second with rupture and sliding (Eqns. (5.21) and (5.22)). Representative results for both cases are plotted in Figure 5.13. Linear regression analyses of results in this form yield τ_y (when relevant) and Γ .^{‡‡} Pertinent characteristics of the property distributions are summarized in Table 5.1.

Comparisons of Γ values obtained from the two methods (Figure 5.14) show that, for cases where yielding does not occur, Γ values are within about $\pm 0.3 \text{ J/m}^2$ of one another in more than 85% of all cases. In a small number of cases, the inferred Γ values are over-predicted by a large margin. These are obtained when the compliance minimum occurs well after rupture; they are characteristic of combinations of very low Γ and very high τ_s . When, instead, yielding precedes rupture, Γ values from the two methods usually differ by somewhat greater amounts; in these cases, the brittle fracture model generally leads to Γ values that are somewhat lower than those from the elastic-plastic model. Here the compliance minimum is obtained before coating rupture (often near the onset of coating yielding) and thus the rupture load is under-estimated. Additionally, Γ is essentially the same as $\tau_y u_c$ (Figure 5.15). (Further analysis and discussion of the limitations of the

^{‡‡} Linear regression analysis can also be used to compute τ_s , thereby providing a check on the value obtained from subsequent loop width measurements. We find that the two values are essentially the same (within about 10%) for all cases considered here.

compliance minimum method for estimating the rupture load are presented in Appendix 5.A)

Correlations between property values obtained from the elastic-plastic model, couched in terms of the non-dimensional parameters $\Gamma/R_f E_f$, $\eta\tau_s/E_f$ and $\eta\tau_y/E_f$, are shown in Figure 5.16. Also shown in the figure is the boundary above which the onset of push-in is controlled by sliding; below it, either yielding or rupture dominate. We find that, in all cases studied here, either yielding or rupture control the onset of push-in. Moreover, $\eta\tau_s/E_f$ appears to be approximately proportional to $\sqrt{\Gamma/R_f E_f}$ (with relatively strong correlation). A least-squares fit of $\eta\tau_s/E_f$ and $\sqrt{\Gamma/R_f E_f}$ in Figure 5.16A yields a Pearson correlation coefficient of $r(\tau_s, \Gamma) = 0.70$ ($p=10^{-39}$). The correlation with yield stress is lower but still significant ($r(\tau_y, \Gamma) = 0.43$, $p=0.0016$). As expected the yield stresses are greater than the sliding stresses in all cases (Figure 5.17). Also, a weak linear correlation is observed between yield stress and sliding stress ($r(\tau_y, \tau_s) = 0.42$, $p=0.0017$). The origin of these correlations is not presently understood.

5.5 Discussion

Direct observations of the mechanisms associated with yielding, rupture and sliding present significant experimental challenges; these have not yet been pursued. In light of this shortcoming, we speculate on the nature of the mechanisms operating during the push-in process. We base the arguments on four key findings from the push-in tests.

(i) When yielding precedes rupture, the push-in response is characterized by two *distinct* domains, each fully consistent with that predicted assuming a constant shear

resistance (either yielding or sliding), with appropriate displacement shifts to account for elastic displacement and for finite toughness (via Eqns. (5.21)–(5.23)). One inference is that the response is not due to mechanisms associated with *progressive* coating evolution (e.g. fretting of coating asperities). The fact that the inferred resistances are independent of applied load (e.g. Figure 5.5) further suggests that radial expansion of the fiber and the associated normal pressure at the interface play an insignificant role. Thus, in the frictional sliding domain, the assumption that the sliding stress is constant (and does not follow a Coulomb-like law) is indeed a good one.

(ii) The amount of inelastic displacement at the transition (at the onset of coating rupture) is typically 50–100 nm. Therefore, at the top surface, where the coating strain is greatest, the shear strain, calculated assuming uniform deformation through the coating and taking a representative coating thickness of 200 nm, is roughly 0.25–0.5. If the deformation were distributed nonuniformly, in localized bands within the coating, the local strain that would be needed to obtain the measured displacements would be even greater (probably $\gg 1$). Mechanisms associated with microcracking would not be expected to provide strains of this magnitude.

(iii) The inferred sliding stresses for all four materials fall in the range of about 10–25 MPa (Table 5.1). These values are in accord with those reported previously on minicomposites with BN-coated SiC fibers, obtained from *tensile* hysteresis loops (15 ± 10 MPa²⁶ and 31 MPa²⁷ for Hi-NicalonTM fibers, 11 MPa²⁷ for Hi-Nicalon STM fibers, and 11 MPa²⁷ for Tyranno ZMITM fibers). This, again, supports the assumption of a sliding stress that is independent of normal stress.

(iv) The inferred shear yield strengths for both the ZMI 3D composite and the HNS minicomposite are typically about 60 MPa (Table 5.1). Although seemingly low in the context of engineering ceramics, this value appears to fall in line with reported hardness values for hexagonal BN. Because of the difficulty of sintering bulk BN, consolidation is usually achieved through the use of very high pressures and temperatures and with significant amounts of sintering additives (e.g. boria) to accelerate the process. The result is that the purity of the consolidated BN and the amount of residual porosity vary significantly; mechanical properties similarly vary over a wide range. In one notable study, pure BN had been consolidated to about 97% of theoretical density by hot isostatic pressing without additives.²⁸ The reported Knoop hardness of this material was $H \approx 280$ MPa. Treating the BN as a Mises-like material, the inferred shear yield strength is about $H/5 \approx 55$ MPa. This value is remarkably close (perhaps fortuitously close) to the values obtained from our push-in tests (about 60 MPa). The implication is that the plastic deformation mechanisms operative during push-in are likely the same as those beneath an indenter during hardness testing. Furthermore, in light of the fact that coating deformation during push-in is essentially fully constrained by the adjacent (stiff) fibers and matrix, the capability of the material to undergo plastic deformation is not unexpected. (Under other loading states, e.g. bending or tension, strengths are low and the amount of plasticity is negligible.)

5.6 Summary and conclusions

In summary, the present work provides a new framework for interpreting results from fiber push-in tests including ways to ascertain the mechanism that governs the onset of push-in and the pertinent mechanical properties. The framework builds on the seminal work of

Marshall and Oliver¹⁴ on fiber push-in in systems with brittle interfaces, with integration, most importantly, of coating plasticity. Its utility has been demonstrated through analyses of experimental data on several prototypical composite systems.

Selection of the critical load for coating rupture as that at the point of minimum compliance appears to be a useful (though inexact) procedure. The procedure becomes increasingly inaccurate in two scenarios. (i) When yielding precedes rupture and sliding, the critical load and the toughness are usually under-estimated somewhat. The errors in toughness are typically less than 30%, though in few cases they can be as high as 50%. (ii) When rupture and sliding occur without yielding, the inferred toughness from the compliance minimum usually agrees well with the true value. Exceptions arise for low toughness values, where the compliance minimum occurs well after rupture and the inferred toughness may be in error by a factor of 3 or more. Therefore, although the selection of the load at the compliance minimum is convenient for automation of calculations of toughness from large data sets and the results are reasonably accurate in most cases, some caution should be exercised in following this protocol without considering the origin of the minimum. Some additional guidelines on this front are provided in Appendix 5A.

The present model of coating deformation, rupture and sliding is analogous to the Dugdale model for localized plasticity ahead of a notch in a thin metal sheet under mode I loading. In the latter, the effective toughness is $\sigma_y \delta_o$ where σ_y is the material tensile yield strength and δ_o is the critical normal displacement for rupture. In the push-in problem, when yielding precedes rupture, the effective coating toughness is $\Gamma = \tau_y u_c$. The present model differs from the Dugdale model mainly in that, once the coating ruptures, the crack surfaces are *not* traction-free but rather continue to resist sliding, albeit at a reduced level of shear

stress. In this context, the present model can be viewed as a *two-zone* Dugdale-like shear model with two characteristic strengths: one dictated by yield and the other by frictional sliding.

Finally, the recognition that coating yielding may precede rupture is itself a significant finding. Yielding is preferable to brittle rupture in that it naturally mitigates the high stresses otherwise present at the tip of a matrix crack when a ceramic composite is loaded in tension. Additionally, coating yielding may reduce accessibility of oxidants within matrix cracks to the fibers (relative to that when interface fracture occurs), potentially increasing composite lifetime. Absent yielding and neglecting elastic mismatch, the established condition for crack deflection is $\Gamma < \Gamma_f/4$ where Γ_f is fiber toughness.²⁹ Since the fibers of interest have low toughness (typically 5–15 J/m²), this condition places rather severe constraints on the allowable coating toughness. If, on the other hand, large-scale coating yielding precedes rupture, coating toughness becomes almost irrelevant to the discussion regarding crack deflection vs. crack penetration. Indeed, a nearly-infinite toughness would be acceptable, provided it were achieved through a large critical displacement and not through an excessively high yield strength. These findings suggest that, in the future, a greater focus of materials design efforts should be on tailoring the yield strength of coatings, not just their toughness.

Acknowledgements

This work was supported by the Pratt & Whitney Center of Excellence in Composites and the IHI Turbine Materials Research Center, both at the University of California, Santa Barbara.

5.A Appendix: Determination of critical rupture load from compliance

measurements

Here we examine the selection of the load at the compliance minimum as the critical load for coating rupture. The selection assumes that the minimum is obtained when the compliance associated with elastic-plastic coating deformation coincides with the compliance in the post-rupture domain. This assumption neglects two possibilities: that the minimum point inherent to coating deformation (without rupture) might occur at a load *lower* than that at the intersection point or that the compliance may continue to decrease after rupture has initiated. Numerical results for both scenarios are presented in Figure 5.A1; the corresponding analyses follow.

In the domain in which the coating is elastic-plastic (but has not yet ruptured), the compliance (from Eqns. (5.5) and (5.21)) is given by

$$\frac{u_f^o}{F} = \frac{c_1}{F^{1/3}} + c_2 + \frac{F}{4\pi^2 R_f^3 E_f \tau_y} + \frac{\eta^2 \tau_y R_f}{F E_f} \quad (5.A1)$$

where $c_1 = 3^{2/3}/2^{4/3} R_{tip}^{1/3} E_*^{2/3}$ for a spheroconical tip of radius R_{tip} and the reduced modulus, E_* , is defined by $1/E_* = (1-\nu_f^2)/E_f + (1-\nu_{tip}^2)/E_{tip}$.³⁰ For realistic property values, the last term on the right side of Eqn. (5.A1) is negligible compared with the others. Differentiating the remainder with respect to F and setting the result equal to zero yields the force F_1 at the compliance minimum

$$F_1 = \left(\frac{4\pi^2 R_f^3 E_f \tau_y c_1}{3} \right)^{3/4} \quad (5.A2)$$

Once rupture has occurred, the compliance (from Eqns. (5.5), (5.22) and (5.23)) becomes

$$\frac{u_f^o}{F} = \frac{c_1}{F^{1/3}} + c_2 + \frac{F}{4\pi^2 R_f^3 E_f \tau_s} + \frac{1}{F} \left[\frac{\Gamma}{\tau_y} - \frac{\Gamma}{\tau_s} + \frac{\eta^2 \tau_y R_f}{E_f} \right] \quad (5.A3)$$

Setting the compliances in (A1) and (A3) equal to one another yields the load F_2 at the intersection point

$$F_2 = 2\pi \sqrt{E_f \Gamma R_f^3} \quad (5.A4)$$

In order for the minimum compliance method to be valid, $F_2 < F_1$, which, from Eqns. (5.A2) and (5.A4), yields the condition:

$$\Gamma < \Gamma_1^* \approx \left(c_1^3 R_f^3 \tau_y^3 E_f \right)^{1/2} \quad (5.A5)$$

Numerical results for $\Gamma < \Gamma_1^*$, $\Gamma > \Gamma_1^*$, and $\Gamma \approx \Gamma_1^*$ are shown in Figure 5.A1A. The results in Figure 5.14B show that, for high toughness values (especially for the ZMI 3D composite), the minimum compliance method *underestimates* the true toughness. The errors arise because the condition in Eqn. (5.A5) is not met.

When coating rupture occurs without yielding, the compliance (from Eqns. (5.5) and (5.22)) is given by

$$\frac{u_f^o}{F} = \frac{c_1}{F^{1/3}} + c_2 + \frac{F}{4\pi^2 R_f^3 E_f \tau_s} - \frac{\Gamma}{F \tau_s} \quad (5.A6)$$

Differentiating Eqn. (5.A6) with respect to F and setting the result equal to zero yields the force F_1 at the compliance minimum:

$$F_1 = \sqrt{\frac{2^{11/3} c_1^2 \tau_s^2 \left(\pi^2 R_f^3 E_f \right)^{5/3}}{27 c_3 \Gamma^{1/3}} + \frac{2^{7/3} c_1 c_3 \tau_s \Gamma^{1/3} \left(\pi^2 R_f^3 E_f \right)^{4/3}}{3} - 4\pi^2 R_f^3 E_f \Gamma} \quad (5.A7)$$

where $c_3 = \left(-1 + \sqrt{1 - 16\pi^2 R_f^3 E_f c_1^3 \tau_s^3 / 729\Gamma^2}\right)^{1/3}$. In this case, in order for the minimum compliance method to be valid, $F_1 < F_2$, which, from Eqns. (5.A7) and (5.A4), yields the condition:

$$\Gamma > \Gamma_2^* \approx 0.43 \left(c_1^3 R_f^3 \tau_s^3 E_f\right)^{1/2} \quad (5.A8)$$

Numerical results for $\Gamma < \Gamma_2^*$, $\Gamma > \Gamma_2^*$, and $\Gamma \approx \Gamma_2^*$ are shown in Figure 5.A1B. The outliers on Figure 5.14A represent cases in which the condition in Eqn. (5.A8) is not satisfied and hence the toughness from the minimum compliance method *overestimates* the true value.³¹

References

- ¹ F.W. Zok, “Ceramic-matrix composites enable revolutionary gains in turbine engine efficiency,” *Am. Ceram. Soc. Bull.*, **95** [5] 22–28 (2016).
- ² R.R. Naslain, “SiC-matrix composites: nonbrittle ceramics for thermo-structural applicaion,” *Eng. Ceram. Curr. Status Futur. Prospect.*, **2** [2] 75–84 (2005).
- ³ R.R. Naslain, “Design, preparation and properties of non-oxide CMCs for application in engines and nuclear reactors: an overview,” *Compos. Sci. Technol.*, **64** [2] 155–170 (2004).
- ⁴ J.I. Eldridge, N.P. Bansal, and R.T. Bhatt, “The evolution of interfacial sliding stresses during cyclic push-in testing C- and BN-coated Hi-Nicalon fiber-reinforced CMCs;” p. Volume 19, Issue 3 in *22nd Annu. Conf. Compos. Adv. Ceram. Mater. Struct. A Ceram. Eng. Sci. Proc.* Edited by D. Bray. John Wiley & Sons, Inc., Hoboken, NJ, 2008.

- 5 G.N. Morscher, G. Ojard, R. Miller, Y. Gowayed, U. Santhosh, J. Ahmad, and R. John, "Tensile creep and fatigue of Sylramic-iBN melt-infiltrated SiC matrix composites: Retained properties, damage development, and failure mechanisms," *Compos. Sci. Technol.*, **68** [15–16] 3305–3313 (2008).
- 6 J.A. DiCarlo, H.M. Yun, G.N. Morscher, and R.T. Bhatt, "SiC/SiC composites for 1200C and above;" in *Handb. Ceram. Compos.* Edited by N.P. Bansal. Springer, 2010.
- 7 S. Le Gallet, G. Chollon, F. Rebillat, A. Guette, X. Bourrat, R. Naslain, M. Couzi, and J.L. Bruneel, "Microstructural and microtextural investigations of boron nitride deposited from BCl₃–NH₃–H₂ gas mixtures," *J. Eur. Ceram. Soc.*, **24** 33–44 (2004).
- 8 E.O. Einset, N.-B. Patibandla, and K.L. Luthra, "Processing Conditions for Boron Nitride Coatings in Fiber Bundles via Chemical Vapor Deposition," *J. Am. Ceram. Soc.*, **77** [12] 3081–3086 (1994).
- 9 E.K. Nyutu and S.L. Suib, "Experimental design in the deposition of BN interface coatings on SiC fibers by chemical vapor deposition," *Surf. Coatings Technol.*, **201** [6] 2741–2748 (2006).
- 10 G.N. Morscher, D.R. Bryant, and R.E. Tressler, "Environmental Durability of BN-Based Interphases (For SiCf/SiCm Composites) in H₂O Containing Atmospheres at Intermediate Temperatures," *Ceram. Eng. Sci. Proc.*, **18** [3] 252–534 (1997).
- 11 A.W. Moore, H. Sayir, S.C. Fanner, and G.N. Morscher, "Improved Interface Coatings for SiC Fibers in Ceramic Composites," *Ceram. Eng. Sci. Proc.*, **16** [4] 409–416 (1995).
- 12 W.A. Curtin, "Theory of mechanical properties of ceramic-matrix composites," *J.*

- Am. Ceram. Soc.*, **74** [11] 2837–2845 (1991).
- ¹³ A.G. Evans and F.W. Zok, “The physics and mechanics of fibre-reinforced brittle matrix composites,” *J. Mater. Sci.*, **29** [15] 3857–3896 (1994).
- ¹⁴ D.B. Marshall and W.C. Oliver, “Measurement of interfacial mechanical properties in fiber-reinforced ceramic composites,” *J. Am. Ceram. Soc.*, **70** [8] 542–548 (1987).
- ¹⁵ D.B. Marshall, “An Indentation Method for Measuring Matrix-Fiber Frictional Stresses in Ceramic Composites t,” *J. Am. Ceram. Soc.*, **67** [12] 259–260 (1984).
- ¹⁶ J.H. Weaver, J. Rannou, M.A. Mattoni, and F.W. Zok, “Interface properties in a porous-matrix oxide composite,” *J. Am. Ceram. Soc.*, **89** [9] 2869–2873 (2006).
- ¹⁷ F.W. Zok, “Developments in oxide fiber composites,” *J. Am. Ceram. Soc.*, **89** [11] 3309–3324 (2006).
- ¹⁸ J.W. Hutchinson and H.M. Jensen, “Models of fiber debonding and pullout in brittle composites with friction,” *Mech. Mater.*, **9** [2] 139–163 (1990).
- ¹⁹ R.D. Mindlin, “Force at a Point in the Interior of a Semi-Infinite Solid,” *Physics (College. Park. Md.)*, **7** 195–202 (1936).
- ²⁰ F.W. Zok, P.T. Maxwell, K. Kawanishi, and E.B. Callaway, “Degradation of a SiC-SiC Composite in Water Vapor Environments,” *Submiss.*, (2019).
- ²¹ D.L. Poerschke, M.N. Rossol, and F.W. Zok, “Intermediate Temperature Internal Oxidation of a SiC / SiCN Composite with a Polymer-Derived Matrix,” *J. Am. Ceram. Soc.*, **99** [9] 3120–3128 (2016).
- ²² K.L. Johnson, *Contact Mechanics*, 9th ed. Cambridge University Press, Cambridge, UK, 2003.
- ²³ Y. Gowayed, G. Ojard, R. Miller, U. Santhosh, J. Ahmad, and R. John, “Correlation

- of elastic properties of melt infiltrated SiC / SiC composites to in situ properties of constituent phases,” *Compos. Sci. Technol.*, **70** [3] 435–441 (2010).
- ²⁴ *Precision Ceramics Boron Nitride*, (n.d.).
- ²⁵ *Boron Nitride (BN) - Properties and Information on Boron Nitride*, (n.d.).
- ²⁶ G.N. Morscher and J. Martinez-Fernandez, “Fiber effects on minicomposite mechanical properties for several silicon carbide fiber-chemically vapor-infiltrated silicon carbide matrix systems,” *J. Am. Ceram. Soc.*, **82** [1] 145–155 (1999).
- ²⁷ A.S. Almansour, E. Maillet, S. Ramasamy, and G.N. Morscher, “Effect of fiber content on single tow SiC minicomposite mechanical and damage properties using acoustic emission,” *J. Eur. Ceram. Soc.*, **35** [13] 3389–3399 (2015).
- ²⁸ A. Lipp, K.A. Schwetz, and K. Hunold, “Hexagonal boron nitride: Fabrication, properties and applications,” *J. Eur. Ceram. Soc.*, **5** [1] 3–9 (1989).
- ²⁹ M.-Y. He and J.W. Hutchinson, “Crack deflection at the interface between dissimilar materials,” *Int. J. Solids Struct.*, **25** [9] 1053–1067 (1989).
- ³⁰ A.C. Fischer-Cripps, *Nanoindentation*. Springer-Verlag, New York, 2002.
- ³¹ C.Y. Hui, S.L. Phoenix, M. Ibnabdeljalil, and R.L. Smith, “An exact closed form solution for fragmentation of Weibull fibers in a single filament composite with applications to fiber-reinforced ceramics,” *J. Mech. Phys. Solids*, **43** [10] 1551–1585 (1995).

Table 5.1: Summary of distributions of interface properties

	ZMI 3D			ZMI mini		HNS mini			S200-H	
	Γ (J/m ²)	τ_s (MPa)	τ_y (MPa)	Γ (J/m ²)	τ_s (MPa)	Γ (J/m ²)	τ_s (MPa)	τ_y (MPa)	Γ (J/m ²)	τ_s (MPa)
Mean	6.3	24	59	0.53	9.5	3.7	30	66	3.1	17
Median	6.4	23	60	0.16	6.7	3.6	28	55	2.8	12
Standard deviation	2.4	8.6	20	1.2	9.9	1.2	7.9	40	2.3	12
Skew	0.64	0.40	0.26	4.3	3.4	0.90	0.77	1.6	0.89	1.7
Interquartile range	3.3	11	21	0.32	7.4	1.3	7.6	41	2.6	9.8

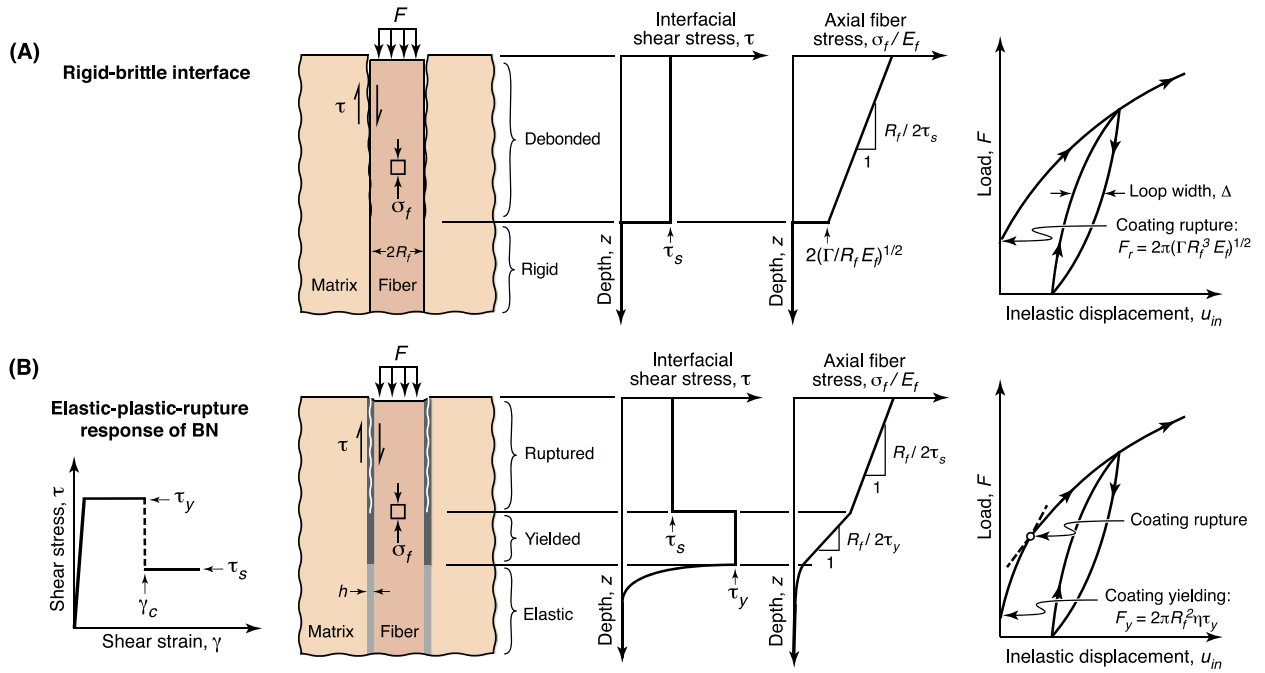


Figure 5.1: (A) The brittle fracture model of interface rupture and sliding during push-in assumes that the sliding stress is constant along the crack surface and that the axial fiber stress decreases linearly into the composite depth. These stress distributions are manifested in the macroscopic response shown on the right. (B) In some cases, push-in response is more accurately represented by a two-zone Dugdale-like model for the crack wake processes, accompanied by a small and largely-insignificant crack-front elastic field.

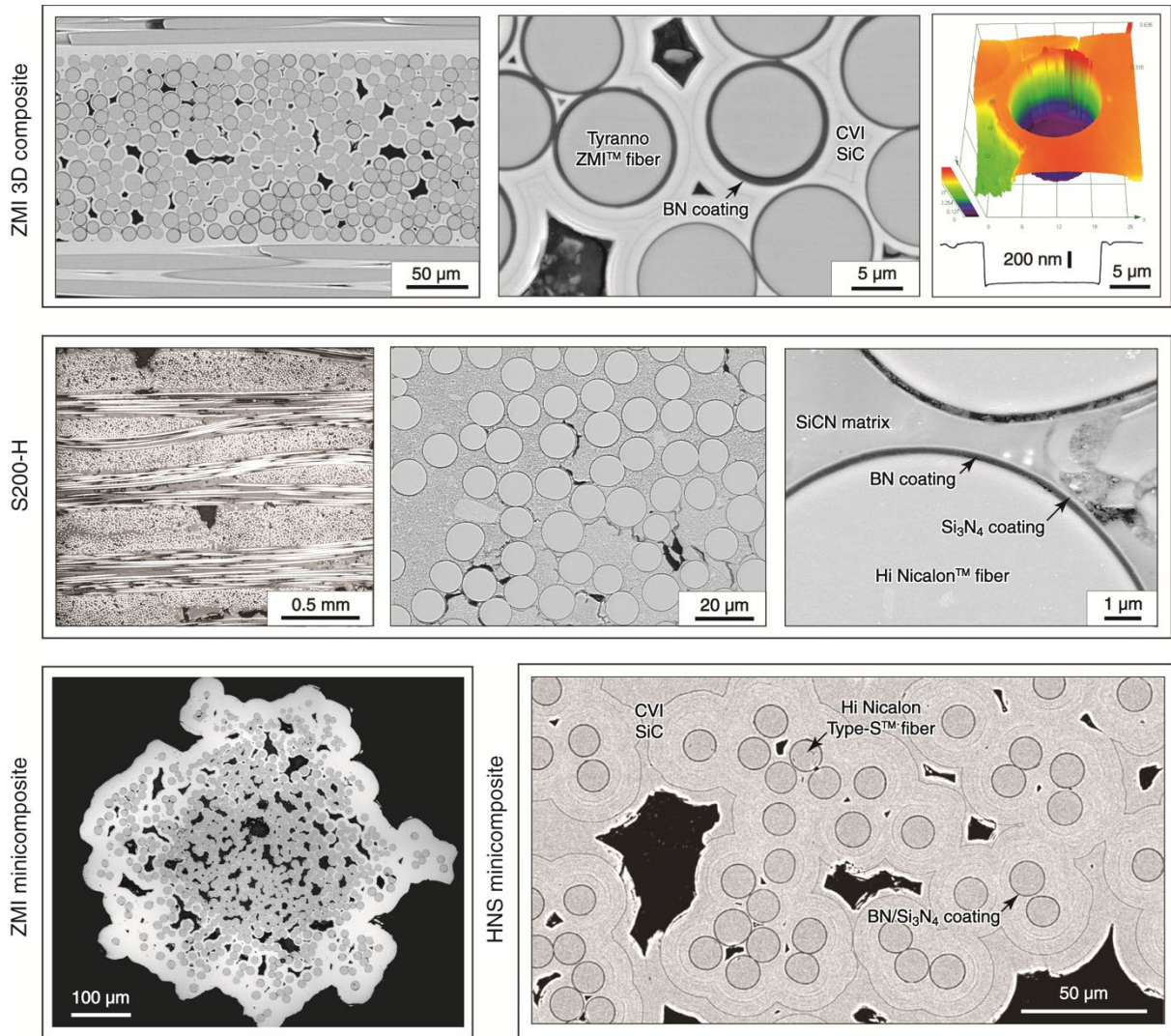


Figure 5.2: The experimental study addresses coating deformation, rupture and sliding in several prototypical composite materials from various manufacturers and based on different fiber types. The collection of micrographs here depicts the nature of the composite microstructures. Additionally, the image in the top right corner shows a confocal microscope image of a pushed-in fiber and a line scan of the depth of the top surface of the fiber (peak load = 400 mN).

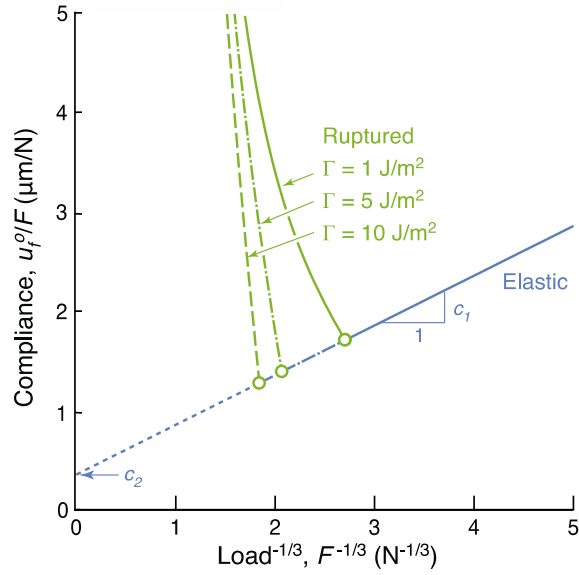


Figure 5.3: Computed compliance from Eqns. (5.1), (5.2), and (5.6) with representative fiber and coating properties, demonstrating the onset of rupture at the minimum compliance, indicated by open circles. ($c_1 = 0.5 \mu\text{m}/\text{N}^{2/3}$, $R_f = 6 \mu\text{m}$, $E_f = 300 \text{ GPa}$, $\tau_s = 20 \text{ MPa}$)

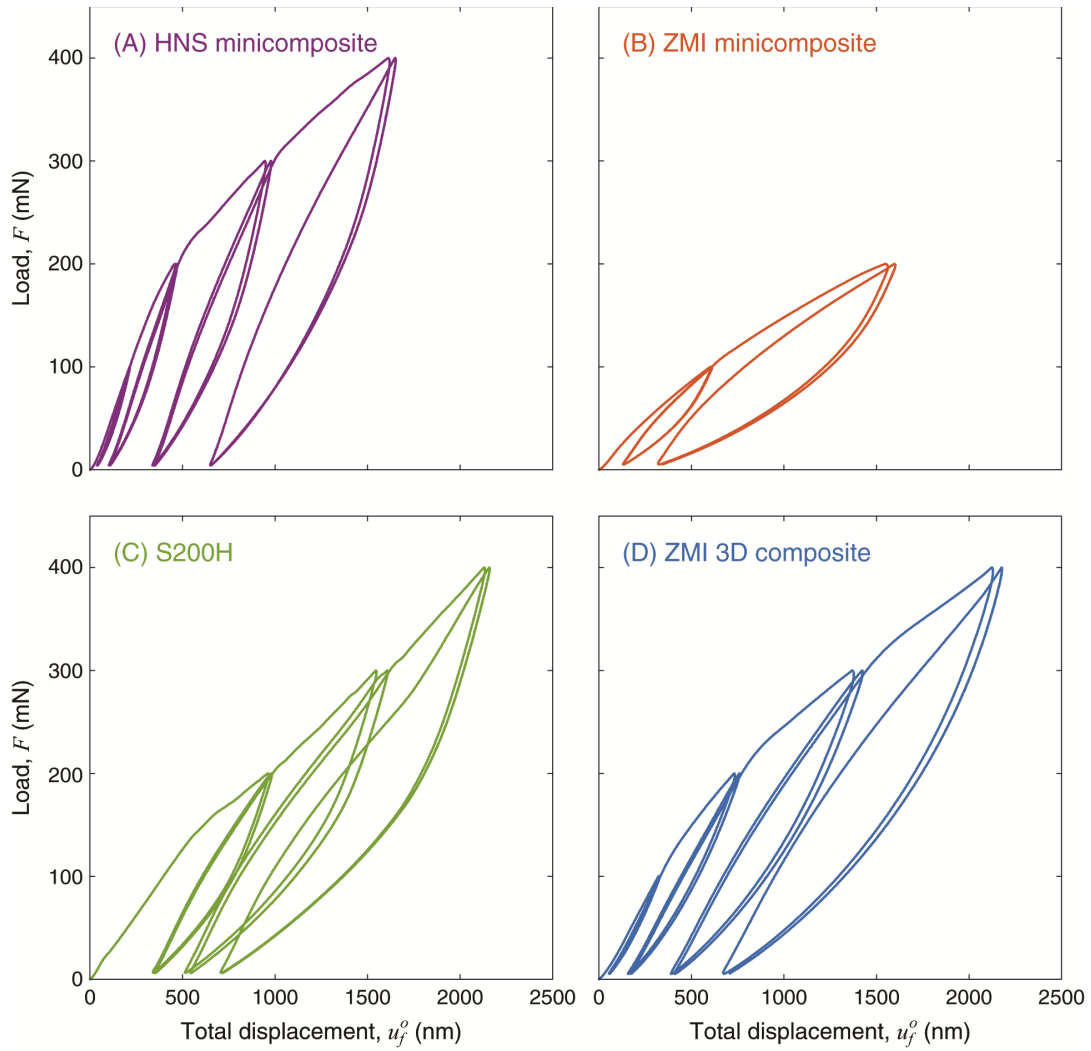


Figure 5.4: Representative load-displacement curves during push-in show qualitatively varying responses among the four composite materials.

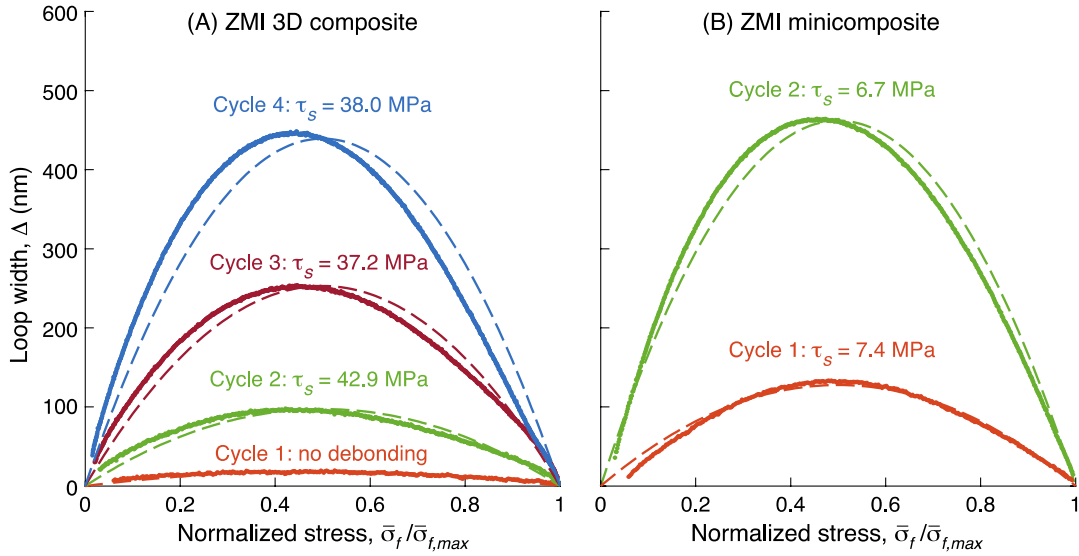


Figure 5.5: Variations in loop width with load are used to infer the sliding stress, in accordance with Eqn. (5.3). Solid lines are experimental measurements while dashed lines are model fits. The sliding stress appears to be consistent between cycles at progressively increasing peak load. Similar results are obtained in the other two composite materials.

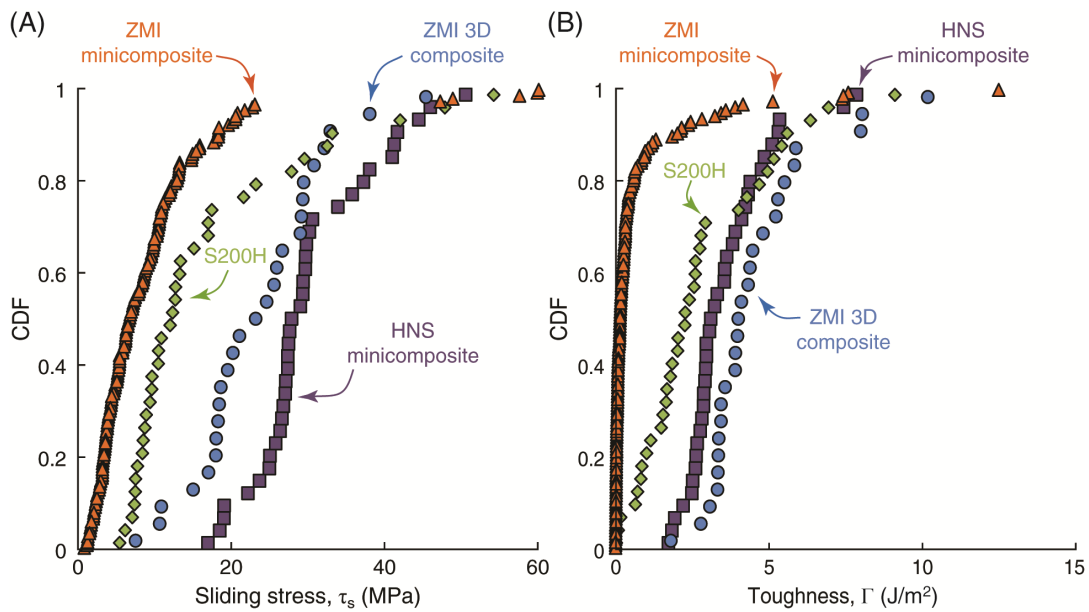


Figure 5.6: Distributions of sliding stress and interface toughness for the four material systems using the standard brittle fracture interpretation of the push-in response, showing large (4- to 10-fold) differences among materials. (Each reported sliding stress is the average from all valid unload-reload cycles in an individual push-in test.)

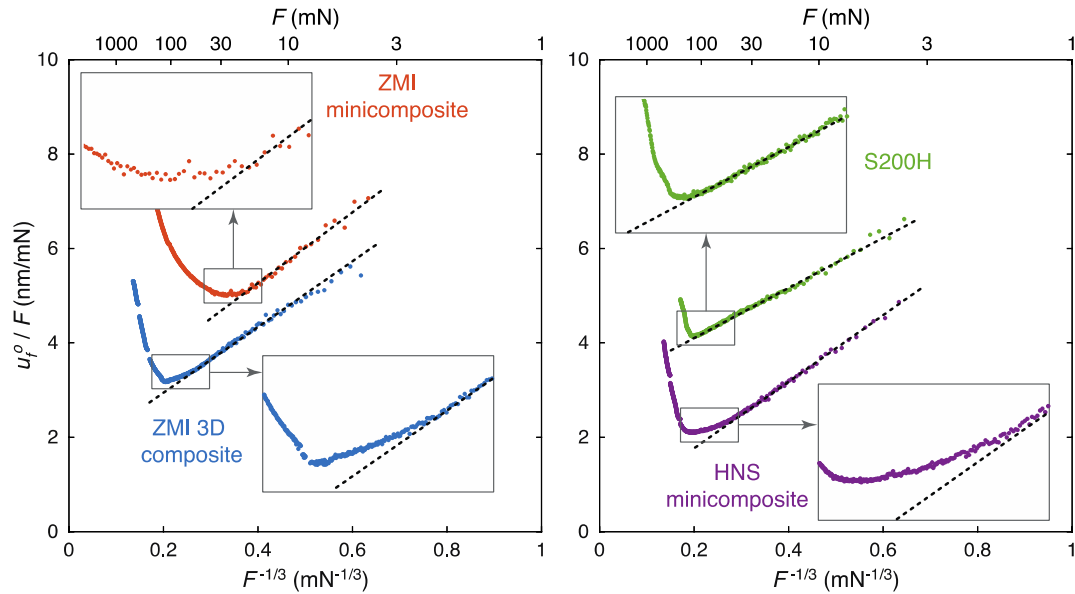


Figure 5.7: During push-in at low loads, the compliance u_f^o/F varies linearly with $F^{-1/3}$. The upturn in compliance at higher loads (*i.e.* lower values of $F^{-1/3}$) may arise from a combination of coating yielding, interface rupture, and/or sliding.

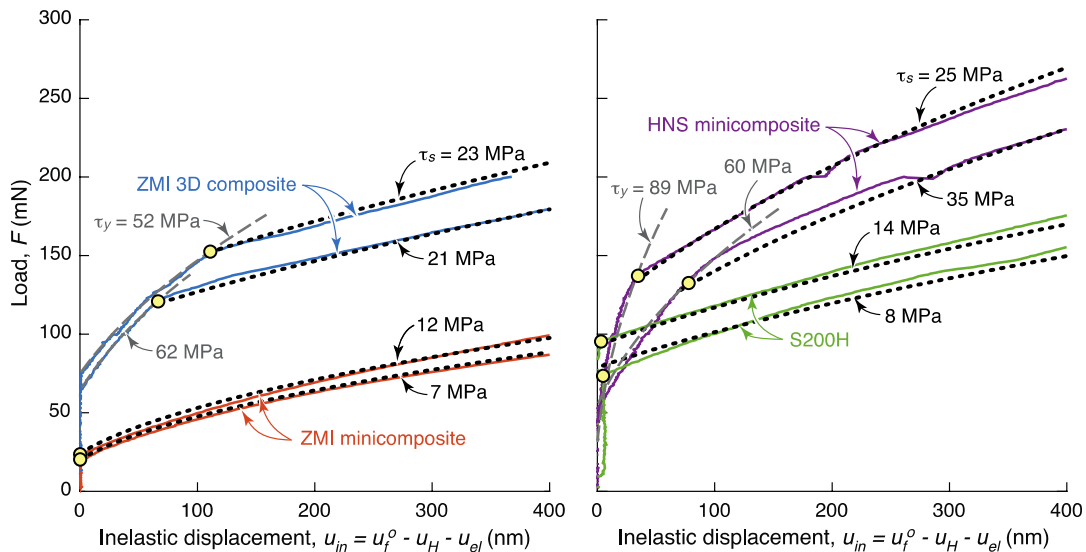


Figure 5.8: Representative curves of load vs. inelastic displacement for the four composite materials exemplify the two types of behavior. Gray dashed lines for the ZMI 3D composite and the HNS minicomposite are fits to the plastic domain (Eqn. (5.21)), from which τ_y is obtained; black dotted lines are computed from Eqn. (5.22), with known τ_s and Γ from loop width and compliance measurements, respectively. Circles represent points at which rupture begins. The corresponding loads are used to obtain toughness. Inelastic displacements at these points represent the critical rupture displacement, u_c , for cases in which yielding precedes rupture.

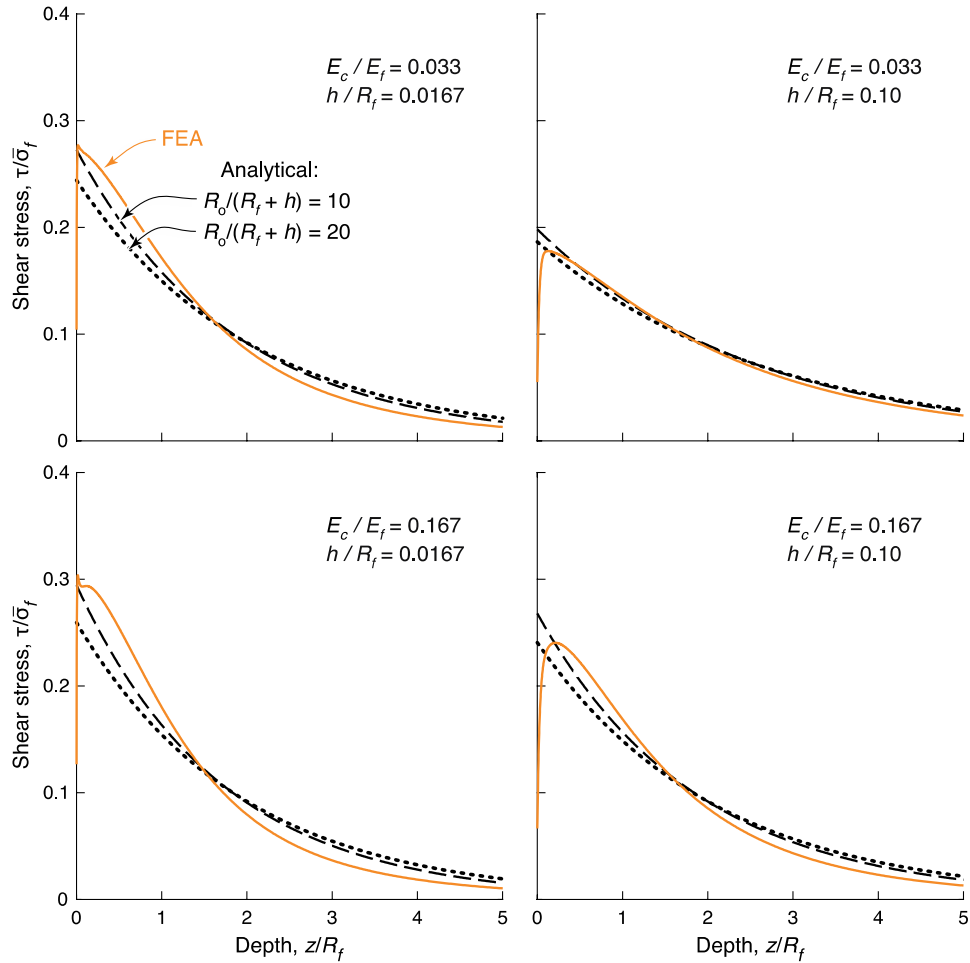


Figure 5.9: Shear stress distributions within the coatings from FEA agree well with those from the analytical model. Here the comparisons are made for the extreme values of coating thickness and modulus considered in the FEA study. The cut-off radii in the analytical model ($R_o/(R_f + h) = 10$ and 20) were selected to fall on either side of the one in the FEA ($R_o/(R_f + h) \approx 17$), though their selection has little effect on the results.

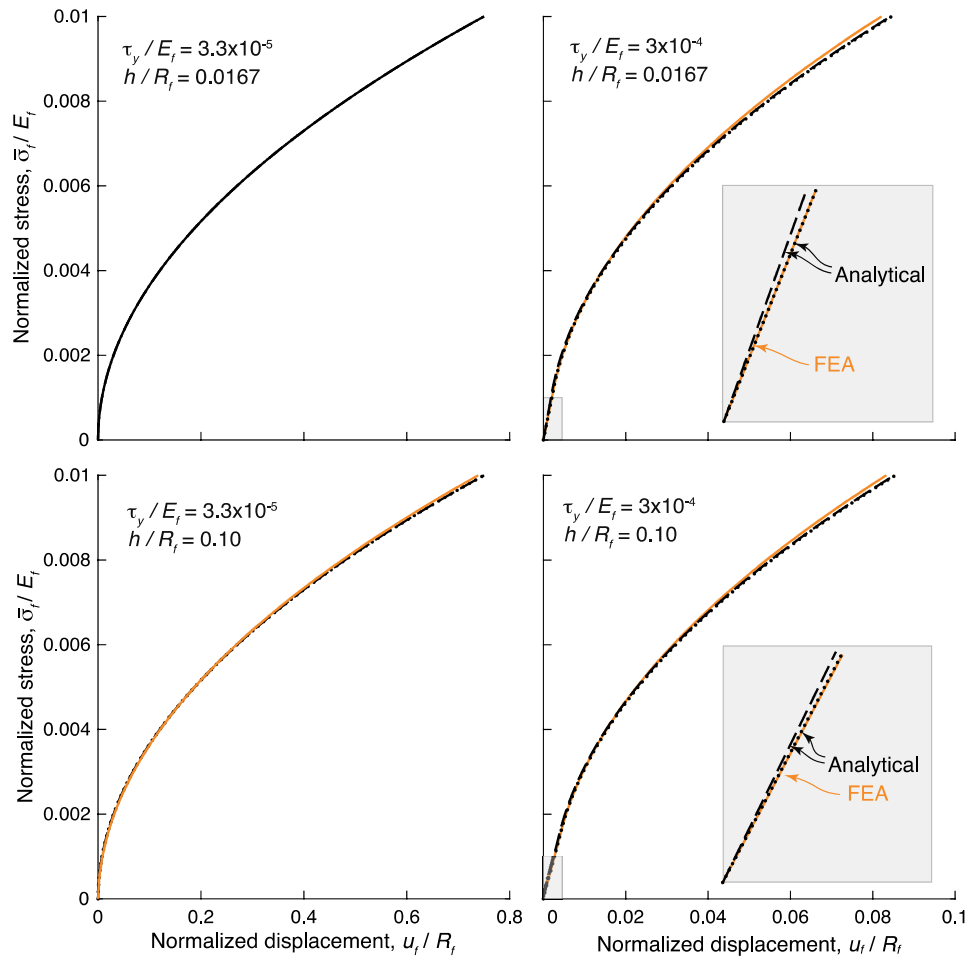


Figure 5.10. Push-in responses in the elastic and plastic domains from FEA and from the analytical model are virtually identical for all cases considered. Dashed and dotted black lines are computed for cut-off radii, $R_o / (R_f + h)$, of 10 and 20, respectively (as in Figure 5.8).

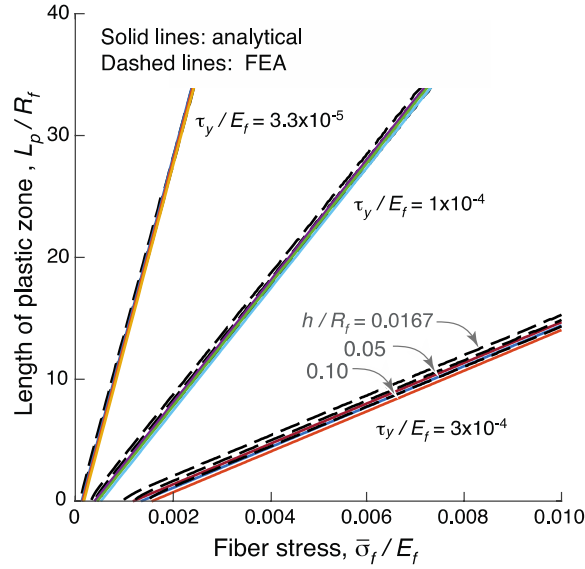


Figure 5.11: Plastic zone length within the coating increases linearly with applied stress at a rate dictated largely by the coating yield strength; it is insensitive to the coating thickness. FE and analytical results are almost coincident with one another.

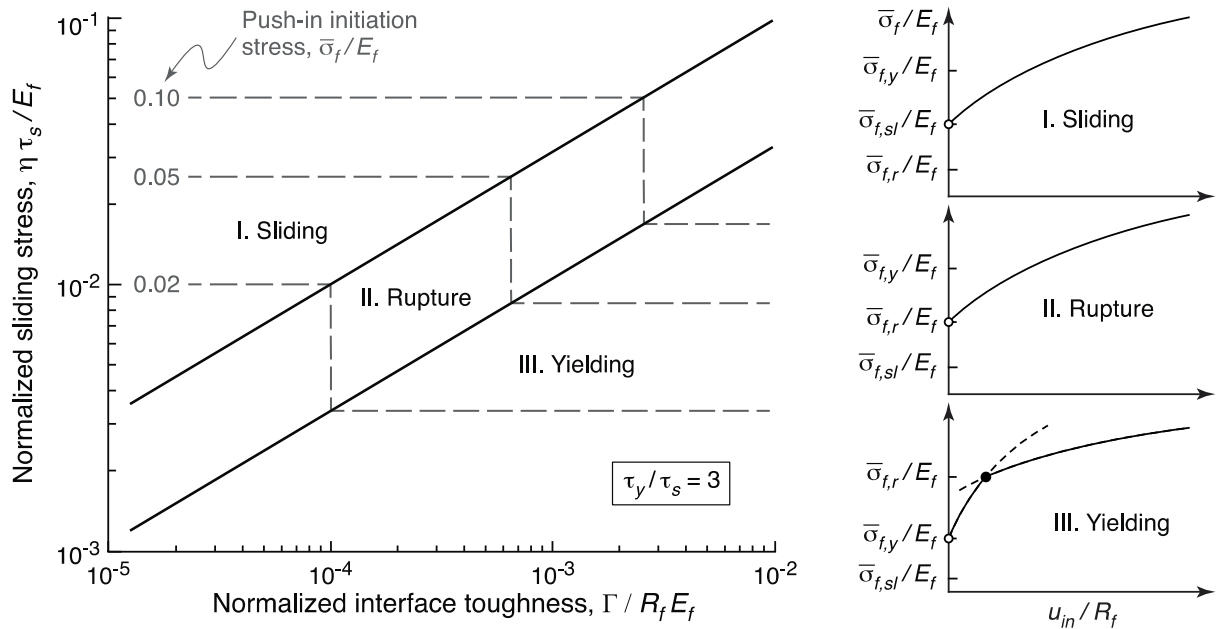


Figure 5.12: Domains in which initiation of fiber push-in is governed by frictional sliding, coating rupture or coating yielding are mapped in terms of three non-dimensional parameters. Expected push-in responses and relative values of the three initiation stresses are plotted schematically on the right. Open circles represent the onset of push-in while the filled circle is the point of coating rupture after yielding.

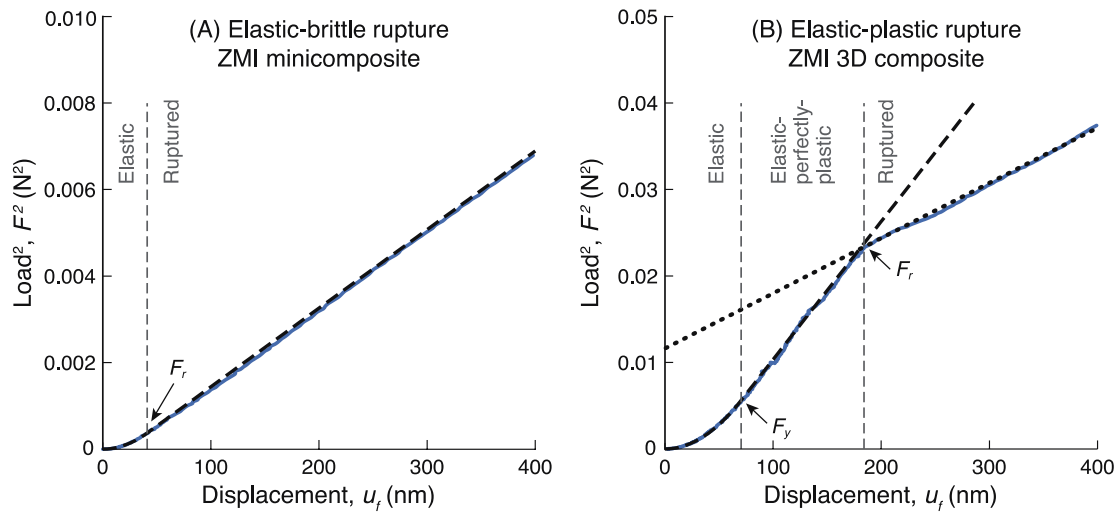


Figure 5.13: Two examples of variations in F^2 with non-Hertzian fiber displacement, illustrating the two behavioral types: (A) a single linear domain, indicating rupture and sliding without yielding; and (B) two linear domains, the first associated with yielding and the second with rupture and sliding. Solid blue lines are experimental data. Dashed and dotted black lines represent fits to Eqns. (5.21) and (5.22) to obtain τ_y and Γ .

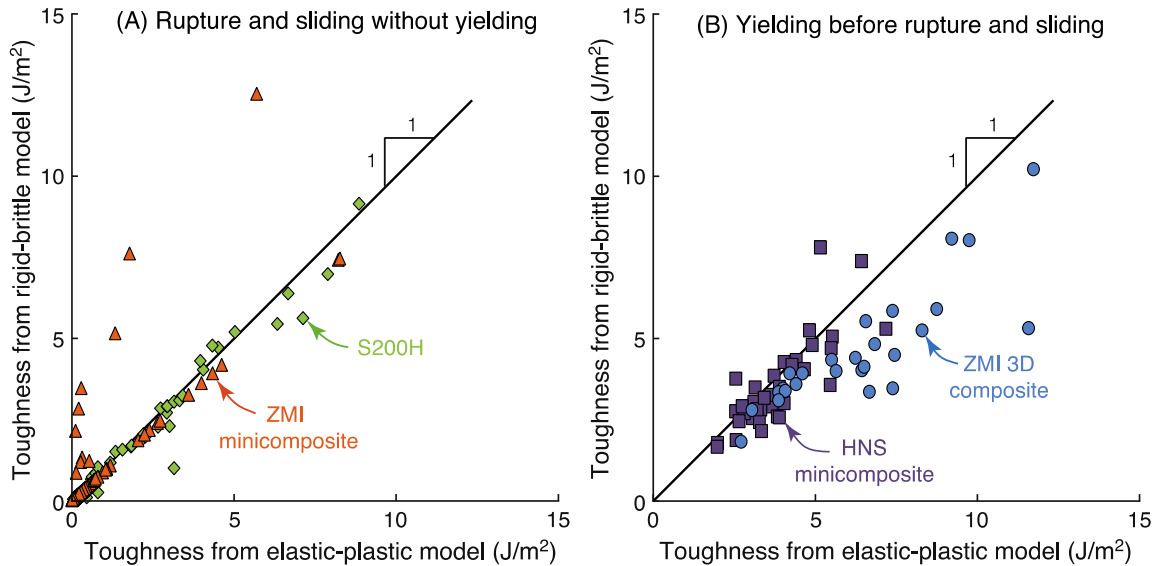


Figure 5.14: (A) Toughness values obtained from the standard brittle fracture model correlate quite well with those from the new model when rupture and sliding occur without yielding. (B) When yielding precedes rupture, the brittle fracture model produces toughnesses that generally underestimate the true values.

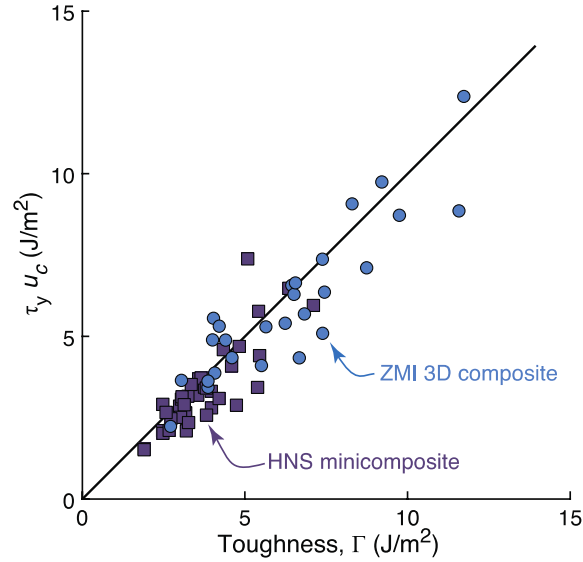


Figure 5.15: Γ tracks linearly with $\tau_y u_c$ for materials in which yielding precedes rupture.

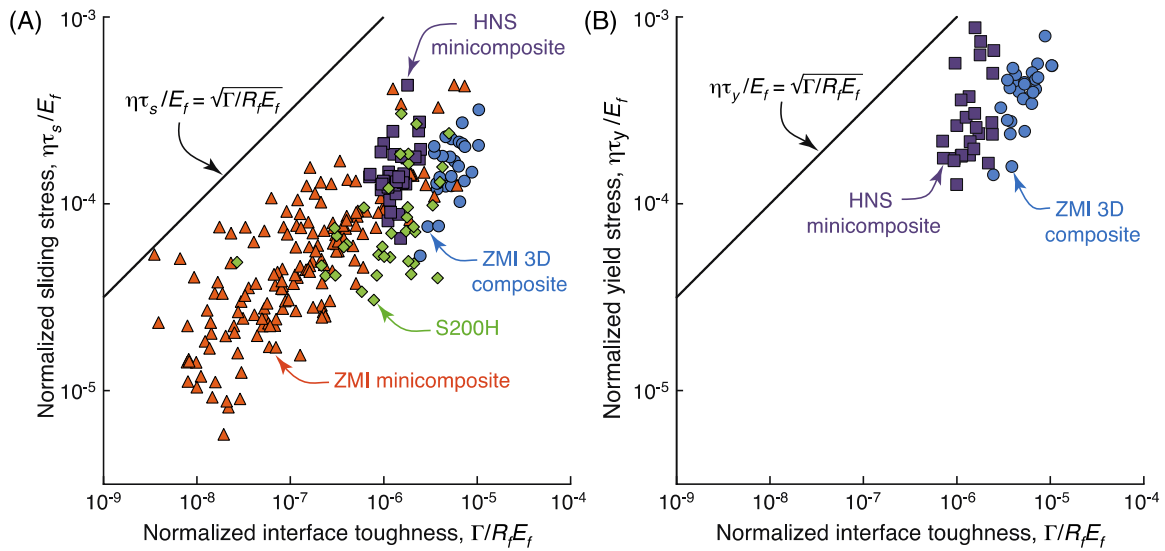


Figure 5.16: (A) Sliding stress and toughness appear to be strongly correlated; a least squares fit of the data to a power law yields a correlation coefficient $r(\tau_s, \Gamma) = 0.70$ ($p=10^{-39}$). (B) Yield stress shows a weaker correlation with toughness, though the range of values obtained experimentally is considerably smaller. Here the correlation coefficient of a power law fit is only $r(\tau_y, \Gamma) = 0.43$ ($p=0.0016$).

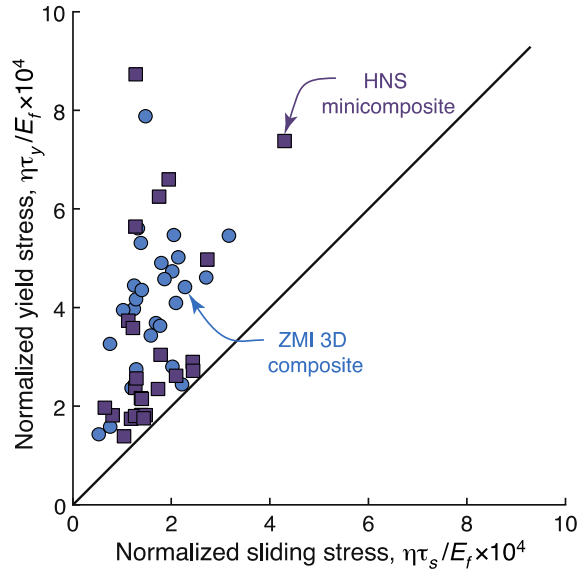


Figure 5.17: Normalized yield and sliding stresses for cases in which yielding precedes rupture. As expected, the yield stress is greater than the sliding stress in all cases. Linear regression analysis yields a correlation coefficient $r(\tau_y, \tau_s) = 0.42$, ($p=0.0017$) indicating a weak correlation.

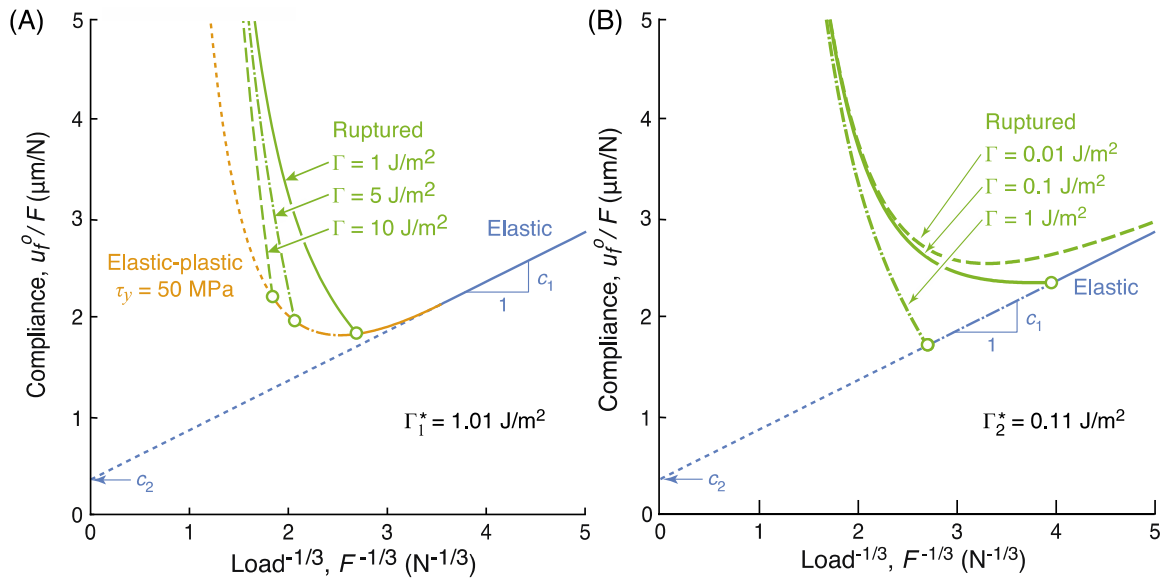


Figure 5.A1: Calculated compliance curves for representative fiber and coating properties showing that, (A) for high values of Γ , the rupture load may exceed that at the compliance minimum, and (B) for low values of Γ , the rupture load may be lower than that at the compliance minimum. Open circles denote points at which rupture begins. ($c_1 = 0.5 \mu\text{m}/\text{N}^{2/3}$, $R_f = 6 \mu\text{m}$, $E_f = 300 \text{ GPa}$, $\tau_s = 20 \text{ MPa}$)

Chapter 6

Tensile response of unidirectional ceramic minicomposites

Abstract

Mechanical response of ceramic matrix composites is critically dependent on properties of fibers and fiber coatings. In the present study, we examine effects of these and other constituent properties on the tensile response of unidirectionally-reinforced composites through a combination of Monte Carlo simulations of fragmentation, adaptations of existing theories of fiber fracture, and complementary experimental measurements. The results show that, contrary to prevailing theories, the process of fiber fragmentation does not go to completion. At low stresses (before the maximum), fibers break essentially randomly throughout the bundle; but, at the stress maximum, all additional breaks are localized to regions adjacent to the fracture plane. Therefore, the resulting distributions in pullout length and strength of pulled-out fibers do not match predictions from existing theory. Although the stress-strain response associated with concurrent fragmentation of matrix and fibers can be readily predicted through adaptations of existing fragmentation models, accurate prediction of the point of instability requires consideration of the *local* response of fibers in the most heavily strained regions (within matrix crack planes). The response in the latter regions leads to instability at stresses and strains that are lower than those obtained from the *average* stress-strain response. In cases of practical interest, the failure stress and strain vary considerably with fiber volume fraction, especially when the matrix strength distribution is broad, and the full potential of the fibers is not realized.

6.1. Introduction

Tensile tests on unidirectional SiC/SiC minicomposites are commonly used to extract basic mechanical properties, especially those governed by fibers and fiber coatings.¹⁻⁸ Minicomposites typically consist of a single tow of 500-1600 fibers, BN or C coatings on the fibers, and a matrix made by chemical vapor infiltration (CVI), melt infiltration (MI), or polymer impregnation and pyrolysis (PIP). In principle, because of the simple configuration of fibers and matrix, properties of minicomposites are easier to interpret relative to multidirectional laminates. The present chapter addresses issues associated with this interpretation.

The natural starting point for interpretation of tensile tests is the suite of micromechanics models for unidirectional ceramic composites developed over the past several decades. These models describe onset and evolution of matrix cracking⁹⁻¹³, interfacial debonding and sliding adjacent to matrix cracks¹⁴⁻¹⁶, fiber fragmentation^{17,18}, pullout of broken fiber fragments^{17,19,20}, and fiber strength distributions inferred from fracture mirrors¹⁷. For the models to be tractable, fibers are assumed to be straight, aligned, and uniformly arranged; the matrix is treated as a uniform, fully-dense phase that fills all space between fibers; and the matrix and fibers are assumed to be coupled mechanically via frictionally-sliding interfaces. In most treatments, most constituent properties, including elastic moduli, fracture toughnesses and interfacial sliding resistance, are taken to be deterministic; fiber strength, in contrast, is assumed to be stochastic and to follow a Weibull distribution. A further tacit assumption is that the number of fibers in the composite and the composite length are sufficiently large so that the composite can be treated essentially as an infinite body.

In practice, SiC/SiC minicomposites may exhibit features that do not conform to the preceding assumptions, especially with regard to the matrix. In cases in which the fiber volume fraction is high, the matrix tends to be present as cylindrical jackets around individual fibers. This yields a collection of fiber/matrix clusters connected internally by matrix but with individual clusters isolated from others in the composite. At the other end of the spectrum, where the fiber volume fraction is low, complete densification may be preceded by formation of a contiguous matrix jacket around the tow periphery, precluding further ingress of precursor gases into the tow interior.

Despite some of the processing shortcomings, the tensile properties of minicomposites in which the matrix phase is largely contiguous resemble those of fully-densified unidirectional ceramic composites.^{15,21} Representative stress-strain curves are shown in Figure 6.1. Notable features in each include a high matrix cracking stress, inelasticity due to matrix cracking and interfacial debonding and sliding, and a high failure strain ($\geq 0.5\%$). This is the response type of interest here. (When the minicomposite comprises numerous isolated clusters of matrix and fibers, transfer of load between clusters is poor, strains are potentially distributed non-uniformly, and the measured tensile response exhibits large variability.^{1,5} These provide little insight into the mechanics issues of interest.) In the present study, micromechanical models of unidirectional ceramic composites are combined with Monte Carlo simulations in order to glean new insights into the tensile properties of minicomposites especially as they pertain to prediction of fracture. The chapter proceeds with a presentation of the relevant mechanics, including both established models as well as extensions or adaptations needed to interpret the current results. This is followed by a description of the Monte Carlo simulation methods and presentation of simulation results.

The latter address effects of fiber volume fraction, fiber properties, and matrix properties on fiber and matrix fragmentation, localization, and fiber pullout. Finally, aspects of the predictions are assessed through comparisons with experimental measurements on one specific composite system.

6.2 Mechanics of tensile response of unidirectional composites

6.2.1 Overview

The inelastic response of unidirectional composites under tensile loading proceeds in the following way. Matrix cracking marks the onset of non-linearity. Provided the coatings and/or interfaces are sufficiently weak, matrix cracks deflect into the interface region, leading to debonding and sliding of fibers past the matrix. If the fiber volume fraction is sufficiently high, fibers spanning the matrix crack survive. Upon further loading, additional matrix cracks form, each bridged initially by largely-intact fibers and each spanning across the entire composite cross-section. As the strain is increased further, fibers begin to break, with the broken ends of the fibers being re-loaded via frictional sliding. Softening due to progressive fiber fragmentation competes with further elastic loading of intact fiber segments, eventually reaching a point at which the tangent modulus goes to zero. This marks the onset of localization and fracture.

The nature of the fracture processes is illustrated schematically in Figures 6.2A and B. In essence, it involves *two concurrent fragmentation processes*: one of the matrix and one of the fibers. The degree to which these processes interact determines the conditions at which localization occurs. The present chapter focuses largely on these interactions.

6.2.2 Onset of matrix cracking

The onset of initial matrix cracking may depend on the size distribution of pre-existing matrix flaws and/or the effects of fiber bridging during crack growth. Two limiting scenarios capture the important features.

- (i) When flaws are abundant, sufficiently long, and entirely bridged by fibers, the crack tip energy release rate is independent of crack length. Provided interfacial toughness Γ_i is small, the stress required to extend such a flaw into a fully-developed steady-state crack is given by:^{9,10}

$$\sigma_{mc}^* = \left(\frac{6E_c^2 E_f f^2 \tau_s \Gamma_m}{E_m^2 (1-f) R_f} \right)^{1/3} \quad (6.1)$$

where f is the fiber volume fraction, R_f is the fiber radius, Γ_m is the matrix toughness, τ_s is the interfacial sliding resistance, E_m and E_f are the matrix and fiber Young's moduli, and E_c is the longitudinal composite Young's modulus, $E_c = fE_f + (1-f)E_m$. (A complete list of variables is in Table 6.1.) The critical crack length at which steady-state conditions are attained is given approximately by $a_o \approx 4\Gamma_m (1-f)E_c / \sigma_{mc}^*{}^2$.¹² For typical property values ($f = 0.5$, $E_m = E_f = 400$ GPa, $R_f = 6 \mu\text{m}$, $\tau_s = 10$ MPa, $\Gamma_m = 10$ J/m²), $\sigma_{mc}^* = 270$ MPa and $a_o = 100 \mu\text{m}$. As the density of fully-developed cracks increases, the driving force for activating additional flaws in the intervening matrix segments diminishes, eventually falling below a critical level at which the crack density reaches saturation.

- (ii) When, instead, flaws are very short – say, comparable to the size of matrix pockets between neighboring fibers – effects of bridging are unimportant; the composite stress

required to activate these flaws scales with the inverse root of the flaw size in accordance with a modulus-corrected Griffith relation: $\sigma_{mc} = (E_c/E_m) \sqrt{E_m \Gamma_m / \pi a}$. In this domain, the evolution of matrix cracks is governed by the distribution of matrix flaws and the matrix toughness, *independent of fiber and interface properties*. After the first matrix crack forms, the stress in the matrix near the crack increases linearly over a distance equal to the slip length: $l_m = (1-f) R_f \sigma_m / 2f \tau_s$. Additional matrix cracks may form subsequently, at distances greater than $\pm l_m$ from the first.

Studies on SiC/SiC minicomposites made by CVI suggest that, when the matrix phase is largely contiguous, matrix cracking is controlled by activation of *short unbridged* flaws. This conclusion is inferred from the observation that matrix cracking usually begins at high stresses (about 500 MPa, as evident in Figure 6.1), well above the predicted steady-state values. It is further supported by the knowledge that the matrix, being made by CVI, is of high quality and is unlikely to contain flaws with lengths approaching a_o . On this basis, we assume in the following Monte Carlo simulations that matrix cracking is indeed dictated by activation of short flaws and that the flaw population is described by Weibull statistics.

6.2.3 *Fragmentation and rupture*

Theoretical analyses of fiber fragmentation and the corresponding stress-strain response, all based on one-dimensional shear lag, have been presented by Curtin¹⁷, Hui¹⁸, Phoenix²² and others. The form of axial strain distributions in the constituent phases during matrix cracking and fiber fracture are illustrated in Figures 6.2C-E. The analyses are predicated on four key assumptions: (i) that load previously carried by a broken fiber is shed equally to all other fibers in the plane of the break (the global load sharing condition); (ii) the number of fibers

is essentially infinite, (iii) stress on intact fiber segments is the same everywhere, independent of breaks in neighboring fibers; and (iv) stress borne by the matrix is negligible compared to that in the fibers which, in turn, leads to fiber strain distributions represented by the dotted lines in Figures 6.2C-E. Under these conditions, each fiber behaves as though it were embedded alone in a large strain-to-failure matrix; this is the notional *single fiber composite* (SFC) model.

In reality, when multiple fibers break, the average stress on the intact fiber segments is not the same in all fiber volume elements¹⁷. When the number of fibers is finite, planes with randomly higher percentages of intact fibers experience a lower intact fiber stress than planes with fewer intact fibers. Although these variations are small over most of the loading history, they do become important in cases where the matrix is capable of supporting significant stress and when the number of fibers is small. The latter effects are explored here in detail.

A useful approximate analytical solution for the *in situ* fiber bundle response (based largely but not exclusively on the work of Curtin¹⁷) is derived in the following way. The stress within intact fiber segments is simply $\sigma_f^i = \varepsilon_t E_f$ where ε_t is the axial composite strain. Adjacent to a fiber break, within a distance equal to the slip length $l_f = R_f \sigma_f^i / 2\tau_s$, the stress is $\sigma_f^{sf} = 2\tau_s z / R_f$ with $z = 0$ being the location of the break. Provided the slip zones of adjacent breaks do not overlap, the average fiber stress in the domain $-l_f \leq z \leq l_f$ is $\bar{\sigma}_f^{sf} = \varepsilon_t E_f / 2$ and thus the average fiber stress over the entire gauge length (including both intact and slipped segments) is²³

$$\bar{\sigma}_f = \varepsilon_t E_f (1 - P_s) / 2 + \varepsilon E_f P_s \quad (6.2)$$

where P_s is the survival probability of a fiber of length $2l_f$ (*i.e.* the fractional length of intact fiber), given by:

$$P_s = \exp \left[- \left(2l_f / L_o \right) \left(\sigma_f^i / \sigma_{o,f} \right)^{m_f} \right] \quad (6.3)$$

Here L_o is the reference length, m_f is the fiber Weibull modulus, and $\sigma_{o,f}$ is the fiber reference strength. This result can be re-expressed in terms of a characteristic *in situ* fiber strength $\sigma_{c,f}$:

$$P_s = \exp \left[- \left(\sigma_f^i / \sigma_{c,f} \right)^{m_f+1} \right] = \exp \left[- \left(\varepsilon_t / \varepsilon_{c,f} \right)^{m_f+1} \right] \quad (6.4)$$

where $\varepsilon_{c,f} = \sigma_{c,f} / E_f$ and¹⁷

$$\sigma_{c,f} / \sigma_{o,f} = \left(L_o / R_f \right)^{1/(m_f+1)} \left(\tau_s / \sigma_{o,f} \right)^{1/(m_f+1)} \quad (6.5)$$

These results are valid when the gauge length is greater than a characteristic value, δ_c , given by:

$$\delta_c / R_f = \left(L_o / R_f \right)^{1/(m_f+1)} \left(\sigma_{o,f} / \tau_s \right)^{m_f/(m_f+1)} \quad (6.6)$$

From Eqns. (6.2) and (6.4), the predicted stress-strain response up to the load maximum is:

$$\bar{\sigma}_f / \sigma_{c,f} = \left(\varepsilon_t / 2\varepsilon_{c,f} \right) \left(1 + \exp \left[- \left(\varepsilon_t / \varepsilon_{c,f} \right)^{m_f+1} \right] \right) \quad (6.7)$$

Maximizing Eqn. (6.7) yields the fiber bundle failure strain:

$$\varepsilon_b / \varepsilon_{c,f} = \left(\alpha - \text{ProductLog} \left[-\alpha \exp \{ \alpha \} \right] \right)^\alpha \quad (6.8)$$

where $\alpha \equiv 1/(m_f + 1)$ and $\text{ProductLog}[z]$ is the principal solution for w in $z = w \exp w$. The corresponding bundle strength is obtained by substituting Eqn. (6.8) into (6.7).

The results in Eqns. (6.7) and (6.8) differ slightly from Curtin's solution. In the latter, the exponential term in Eqn. (6.7) is approximated by the first two terms in a Taylor series. Although this approximation is good for $(\varepsilon_t/\varepsilon_{c,f})^{m_f+1} \ll 1$, it begins to break down near the load maximum. It is therefore not able (nor was it intended) to accurately capture the post-peak softening.

An exact solution to the fiber fragmentation problem, based on the same set of assumptions but accounting for interactions between adjacent breaks, was developed by Hui. While the closed form solution originally presented by Hui for the normalized average *in situ* fiber stress ($S_f \equiv \bar{\sigma}_f/\sigma_{c,f}$) vs. normalized intact fiber strain ($\Delta_f \equiv \varepsilon_f^i/\varepsilon_{c,f}$)* response is rather unwieldy, the evolution of the tangent modulus is more manageable (though it still requires numerical integration). It is given by:

$$\frac{dS_f}{d\Delta_f} = m_f \left(\frac{1}{m_f} - 1 + 2\Delta_f^{-1-m_f} \left(1 - \exp\left[\frac{-\Delta_f^{m_f+1}}{2} \right] \right) - \frac{\Delta_f^{m_f+1}}{4} \right) \exp\left[\frac{-\Delta_f^{m_f+1} - 2m_f \left(\gamma + \Gamma\left(0, \Delta_f^{m_f+1}/2\right) + \ln\left(\Delta_f^{m_f+1}/2\right) \right)}{m_f + 1} \right] \quad (6.9)$$

where γ is the Euler–Mascheroni constant (≈ 0.577), $\Gamma(a,b) \equiv \int_b^\infty t^{a-1} \exp(-t) dt$ is the incomplete gamma function.

* Taking fiber response to be linear-elastic to failure, $\sigma_f/\sigma_{c,f} = \varepsilon_f E_f/\sigma_{c,f} = \varepsilon_f/\varepsilon_{c,f}$. As such, S_f and Δ_f in the SFC problem are not, strictly, stress and strain, respectively. Indeed, Hui et al.¹⁸ refer to Δ_f as a normalized stress. The key distinction between the two quantities is that S_f is an *average* value over the entire length of fiber and Δ_f is the value in *intact* regions. Only upon extending the SFC exact solution to unidirectional composite response does it necessitate defining S_f as the *in situ* bundle stress and Δ_f as the total strain.¹⁸

Comparisons of the stress-strain responses from Eqn. (6.7), Curtin's solution, and Hui's exact result are plotted on Figure 6.3. Because P_s remains high up to the load maximum (0.7–0.9 for $m_f = 5$ –20), the fractional length of overlapping slip zones remains small and, therefore, Eqn. (6.7) nearly-perfectly matches the exact solution up to the load maximum (Figure 6.3). Arguably, since a unidirectional composite loaded in tension cannot exploit the response in the post load-maximum domain, Eqn. (6.7) adequately captures the measurable and useful domain of the fiber bundle response. Its main advantage over the exact solution is its simple form; the need to numerically integrate Eqn. (6.9) makes the exact solution burdensome, especially in fitting and interpreting experimental data. Notwithstanding, the exact solution (with the post-peak softening) becomes essential in modeling the *matrix* response, as follows.

In parallel with fiber fragmentation, the matrix undergoes an analogous fragmentation process. Here the problem can be viewed as a single long matrix element embedded in a sea of frictionally-coupled supporting fibers: conceptually identical to the SFC model used to analyze fiber fragmentation. As a result, the preceding solutions for fiber fragmentation can be adapted to matrix fragmentation by simply reversing the assignment of matrix and fiber properties, e.g. fiber volume fraction becomes matrix volume fraction, and vice versa. But, because matrix fragmentation usually goes to completion well before the fiber bundle ruptures, the post-peak domain of the matrix response (as described by Hui's exact solution) becomes important in properly modeling the composite response; Eqn. (6.7) is not sufficient. The utility and limitations of the analytical models in describing the behaviors obtained from Monte Carlo simulations and experimental results are addressed in due course.

6.2.4 Length and strength of pulled-out fibers

Analysis of a SFC in a large strain-to-failure matrix leads to the terminal distribution of fragment lengths (assuming the fragmentation process can indeed go to completion) and, in turn, to the distribution in fiber pullout lengths that would be observed on the composite fracture surface. In this case the computed mean pullout length is $\bar{L}_p/\delta_c = \lambda_1(m_f)/4$ ¹⁷ where $\lambda_1(m_f)$ is weakly dependent on m_f and near unity for structural ceramic fibers of interest. If, instead, the breaks are confined to a region adjacent to a *single matrix crack* (SMC), the mean pullout length is significantly smaller: $\bar{L}_p/\delta_c = \lambda_2(m_f)/4$ ^{19,20} where

$$\lambda_2(m_f) = 2\Gamma\left[\frac{(m_f + 2)}{(m_f + 1)}\right] / (m_f + 1)^{m_f/(m_f + 1)} \approx 0.3 - 0.5 \quad (6.10)$$

and $\Gamma(\)$ is the gamma function.

In both models, the strength of pulled-out fibers follows a Weibull distribution similar to but not identical to the true fiber strength distribution;²⁴ appropriate correction factors (ranging from about 0.8 to 1.1) have been computed by Curtin.^{17,24} In some cases, these results can be used in conjunction with experimental measurements of fiber fracture mirrors²⁵ to ascertain the *in situ* fiber properties and to identify differences with those of pristine fibers. But, as we find through the Monte Carlo simulations, neither of the two idealizations – from the SFC or the SMC models – leads to an accurate representation of the distributions in pullout length or strength of pulled-out fibers.

6.3 Monte Carlo simulations: Methods, results, and analyses

6.3.1 Simulation methods

Extensive Monte Carlo (MC) simulations of tensile loading of unidirectional composites were performed. The goal was to ascertain the combined effects of fiber volume fraction and fiber and matrix properties on global composite response, fiber fragmentation, localization, fiber pullout length distribution, and strength distribution of pulled-out fibers. In all cases, fibers are assumed to be frictionally coupled to the surrounding matrix via a sliding stress τ_s , the matrix is taken to be rigid in shear (enabling perfect global load sharing), and the interface toughness is assumed to be zero (assumptions commonly used in analyses of this kind^{17,18}). Scenarios in which the axial load-bearing capacity of the matrix is either zero or of finite value are both considered.

The number N of fibers in the model was varied from 500 (typical of that found in an individual tow) to 5000, and the fiber volume fraction f was varied from 0.01 to 0.5. Each fiber is segmented into lengths of $L_o = R_f$ (L_o being the Weibull reference length) and each segment is assigned a unique, random strength $\sigma/\sigma_{o,f}$ from a Weibull distribution with prescribed Weibull modulus m_f (from 5 to 20). When present, the matrix is also segmented in lengths of $L_o = R_f$ and assigned random strengths with Weibull parameters $m_m = 5$ or 20 and $\sigma_{o,m}/\sigma_{o,f} = 0.05, 0.10$ or 0.15. (A matrix is unnecessary when its axial strength is zero.) Matrix cracking is assumed to be controlled by intrinsic matrix flaws combined with matrix toughness, and that fiber bridging does not affect cracking stresses. The sliding stress is set to $\tau_s/\sigma_{o,f} = 0.002$ (of the same order as that in typical composites). Recognizing that the composite response is independent of gauge length for $L > \delta_c$, the composite gauge length was set to either $5\delta_c$ or $10\delta_c$. For example, for $m_f = 5$, $\delta_c/R_f = 177$ (from Eqn.

(6.6)); therefore, for a gauge length $10 \delta_c$, each fiber consists of 1770 segments, each of length $L_o = R_f$.

With the constituent properties and geometry set, the simulations are run by progressively increasing the applied load by increments sufficient to cause one additional fiber break or matrix crack. The stress adjacent to a break is increased linearly over the pertinent slip length (l_f for fibers and l_m for the matrix). To ensure that the total load within each plane perpendicular to the loading direction is maintained equal to the current applied load, a load drop associated with a fiber break or a matrix crack is spread uniformly over all intact segments in the same plane. Computationally, a force balance loop is used to redistribute the load to the i intact segments at fixed applied load. Load redistribution following a single cracking event may cause an additional break at the same applied load; when this occurs, the force balance loop again redistributes the load, now amongst the remaining $i-1$ intact segments. Once equilibrium is established and no further breaks are possible, the applied load is increased to that required to cause yet another break (in the matrix or the fibers). The process repeats until there exists a plane in which there are no intact segments. At that point, the simulation ends. The simulations were repeated up to 1000 times, to ascertain the statistical variations in the inferred properties.

The MCS results are analyzed to address three specific issues: (i) the interpretation of distributions in length and strength of pulled-out fibers; (ii) the *in situ* fiber properties, obtained from an analysis of the stress-strain response, following a procedure described below, and (iii) the critical fiber volume fraction needed to exploit the fiber capabilities. They are also used (in Section 6.4) to assess an analytical model for the point of localization.

6.3.2 Stress-strain response, fiber fragmentation, and rupture

When the number of fibers is very high and the matrix strength is zero, the simulated stress-strain response follows the exact SFC solution with nearly-perfect agreement up to the load maximum. A representative simulation result, for $N = 5000$, $m_f = 5$, and $L = 10 \delta_c = 1770 L_o$, is plotted in Figure 6.4A (dotted line). In this case, the composite strength and corresponding strain are 99.7% and 96.0% of the respective values obtained from the exact SFC solution. When the number of fibers is reduced to $N = 500$, strengths and failure strains exhibit some (but small) variability; their average values fall slightly below (but still very close to) the exact SFC results. The stress-strain curves are plotted on Figure 6.4A and the key numerical results are summarized in the inset table. From 1000 simulations, the coefficients of variation (CoV) Z on strength and failure strain are found to be described well by $Z(\sigma_b) = 0.38/m_f^{0.47} \sqrt{N}$ and $Z(\varepsilon_b) = 1.3/m_f^{0.68} \sqrt{N}$, respectively.

The fiber fragmentation process also follows that of the SFC model when the matrix has no strength, but only in the pre-peak loading domain. At low loads, fiber breaks are essentially non-interacting; the load shed from a single broken fiber leads to only a very small stress increase within intact fibers and only rarely causes additional fiber breaks. In this domain, fiber fractures are random and therefore P_s follows Eqn. (6.4) and is essentially uniform along the composite length (e.g. purple and green lines in Figure 6.5A). As the load approaches the maximum, fiber interactions become significant, for two reasons: (i) there are fewer intact fibers with which to share the load from a broken fiber, and (ii) the stress on intact fibers approaches the mode of the strength distribution and thus a larger number of fibers is likely to break over a narrow range of applied load. Although the mean value of P_s

along the composite length remains consistent with Eqn. (6.4), P_s becomes increasingly non-uniform as the load approaches its maximum. This is because regions with slightly lower-than-average fiber strength have fewer intact fibers and, in turn, the intact fibers must carry a slightly higher-than-average stress, leading to additional local fiber breaks. The wavelength of these fluctuations is comparable to the characteristic transfer length δ_c .

The magnitude of these fluctuations, characterized by the CoV of P_f , increases as the process proceeds and as P_f rises, at a rate that scales with m_f (Figure 6.6A). For $N=5000$, the CoV of P_f is initially roughly proportional to P_f , up to a CoV of about 0.08, beyond which it rises rapidly as failure becomes imminent. Nevertheless, these non-uniformities have only a small effect on the point of localization. When $N=500$, the CoV of P_f follows a similar increasing trend with P_f but at a rate that is about 3 times that for $N=5000$ (also in Figure 6.6A). This is consistent with the expected $1/\sqrt{N}$ scaling, i.e. $\sqrt{5000/500} \approx 3$. As $N \rightarrow \infty$, these fluctuations would likely vanish and failure would occur at the load maximum of the exact solution.

In the final loading step (at the load maximum), the first additional fiber break typically occurs in one of the “valleys” of low P_s (located at about $z/\delta_c = 3$ in the example in Figure 6.5A). This event triggers a cascade of additional fiber breaks, all occurring within $\pm\delta_c/2$ of the eventual fracture plane. The fragmentation process at the peak load is analogous to the SMC problem analyzed by Sutcu¹⁹ and by Thouless²⁰, with the exception that many of the weak fibers have already broken and therefore do not participate in the final sequence of fracture events. Therefore, there are two distinct domains in the fiber fragmentation process: one, at low loads, where fibers break in a nearly-random fashion (in

accordance with the SFC exact solution) and a second, at the load maximum, where fibers break in a more localized manner and the fibers break at higher stresses. This is reflected in the two strength populations shown in Figure 6.7A.

When the matrix has finite but low strength ($\sigma_{o,m}/\sigma_{o,f} = 1/20$), the matrix strength distribution is narrow ($m_m = 20$), and the fiber content is moderately high ($f = 0.3$), matrix cracking occurs over a narrow range of stress and matrix crack saturation is attained before a significant fraction of fibers have broken (Figure 6.8). (For the example in Figure 6.8, $P_s = 0.997$ for the fibers at matrix crack saturation). Once the matrix crack density has saturated, the stress profile in the matrix remains unchanged for the remainder of the simulation. The response in this domain is dictated largely by the fibers and is essentially the same as that without a matrix, with three exceptions. First, the composite stress at a prescribed strain is elevated by an amount equal to the average matrix stress, $\bar{\sigma}_m$. Second, in addition to short-range fluctuations caused by the presence of matrix cracks, with P_s exhibiting local minima at the matrix crack locations (Figure 6.5B), the magnitude of the long-range fluctuations in P_s is increased significantly. This is manifested in an increase in the CoV of P_f , by as much as a factor of 3–4 relative to that in the absence of a matrix (Figure 6.6B). Third, fiber breaks are clustered near matrix cracks which correspond to local maxima in fiber strain. This type of fiber fragmentation behavior has been observed experimentally in *in situ* X-ray microtomography of minicomposite tensile tests.³ One consequence of these differences is that fiber bundle failure occurs at somewhat lower stress and strain; for the case shown in Figure 6.8, the bundle strength and failure strain are 94.7% and 86.5% of their respective values obtained from the exact SFC solution.

The eventual fracture plane corresponds approximately with the location along the gauge length where the average matrix stress is lowest and hence the fiber stress is greatest. This trend is demonstrated in Figure 6.9. Here the variation in P_s within the matrix crack planes after the penultimate load increment is plotted against a moving-average matrix stress, calculated over a sliding window of length δ_c . Composite fracture typically occurs at or adjacent to the matrix crack at which the moving-average matrix stress is lowest. When the matrix strength is greater or the fiber volume fraction is lower, the loading domain between the end of matrix cracking and the onset of appreciable fiber fracture narrows. This produces greater fiber strain fluctuations near the maximum and therefore a further reduction in the *in situ* bundle strength and failure strain. These effects are explored further in Section 6.3.5.

6.3.3 Lengths and strengths of pulled-out fibers

The two domains of fiber fragmentation lead to complex distributions in pullout length. The probability density distributions (PDFs) from the MCS and from both the SFC and the SMC models for $m_f=5$ and 15 are shown in Figure 6.10. Fibers that break before the load maximum exhibit a pullout distribution that follows that from the SFC model; fibers that break at the load maximum, instead, exhibit a pullout distribution that more closely follows that computed from the SMC problem. The total pullout length distribution from the simulations falls between those of the two limiting cases. Similar results are seen in simulations with finite matrix strength (Figure 6.11).

The strength distributions of pulled-out fibers also exhibit two domains, manifested in two essentially-linear segments on a Weibull plot (Figure 6.12). The first, at low stresses,

corresponds to fibers broken prior to the load maximum while the second, at high stresses, corresponds to fiber breaks *at* the load maximum. While the Weibull parameters inferred from the first domain are consistent with the true fiber strength distribution, the second domain is characterized by a reduced apparent Weibull modulus. (For reasons not presently understood, the apparent Weibull modulus in the second domain appears to be consistently 40% of the true value of m_f over the range $5 \leq m_f \leq 20$.)

As a whole, the strength does not follow a Weibull distribution (even in an approximate sense) and therefore fitting the distribution to a Weibull function would not yield meaningful results. Additionally, the use of fracture mirrors to compute the *in situ* fiber strength distribution is not likely to be useful without an exhaustive accompanying analysis. This shortcoming, in turn, motivates the procedure described in the following section.

6.3.4 Determining *in situ* fiber strength distributions

An alternative approach to determining the *in situ* fiber strength distribution involves analysis of stress-strain curves. The procedure is outlined first for the case in which the matrix has no axial strength. Combining Eqns. (6.2) and (6.4) and rearranging yields

$$P_s = 2\bar{\sigma}_f / \varepsilon_t E_f - 1 = \exp \left[- \left(\varepsilon_t / \varepsilon_{c,f} \right)^{m_f + 1} \right] \quad (6.11)$$

The *in situ* Weibull parameters can therefore be obtained from a Weibull-like plot of $\ln \left\{ -\ln \left[2\bar{\sigma}_f / \varepsilon_t E_f - 1 \right] \right\}$ vs. $\ln \varepsilon_t$. In this form, the relationship is linear with slope $m_f + 1$.

When the matrix has finite strength, the preceding method can be readily adapted, provided matrix cracking is complete before appreciable fiber fracture occurs. This is done by

determining the average matrix stress from a linear regression analysis of the stress-strain response in the linear domain between the end of matrix cracking and the onset of fiber fracture. The average fiber stress is then computed from the difference of the composite stress and the average (post crack saturation) matrix stress, within the domain in which matrix cracking is complete. (The utility of this method becomes questionable when matrix cracking and fiber fracture overlap over a significant strain range.)

To assess this method, 1000 MC simulations were run for $m_f = 5, 10, 15,$ or $20, N = 500$ and $L = 5 \delta_c$. Stress-strain curves and corresponding Weibull plots are shown in Figures 6.4A and B, respectively. Linear regression analyses of the latter plots yield distributions in *in situ* Weibull parameters summarized on Figure 6.13. CoVs are typically less than 10%. For $m_f = 5, Z(m_f) = 1.0/\sqrt{N}$. (By comparison, the corresponding CoVs from single fiber tests and fiber bundle tests are $Z(m_f) = 0.77/\sqrt{N}$ and $Z(m_f) = 0.89/\sqrt{N}$, respectively.)^{30,31}

6.3.5 Tough-to-brittle transition

The preceding analyses are predicated on the assumption that the fiber bundle can support the entire load in the plane of a matrix crack. To satisfy this condition, the fiber volume-weighted bundle strength must be greater than the matrix cracking stress:

$$f\sigma_b > \sigma_{mc} = \varepsilon_{mc}E_c = \varepsilon_{mc}(fE_f + (1-f)E_m) \quad (6.12)$$

where the bundle strength is given by Eqns. (6.7) and (6.8) and ε_{mc} is taken (initially) to be deterministic. Solving the inequality in Eqn. (6.12) for f yields a critical fiber volume fraction f_c necessary to attain large composite strain and the theoretical bundle strength:

$$f_c = \varepsilon_{mc} E_m / (\sigma_B + \varepsilon_{mc} (E_m - E_f)) \quad (6.13)$$

For a composite with very low fiber fraction ($f < f_c$), composite failure occurs when the first matrix crack forms. High failure strain can only be obtained when $f > f_c$.

To probe this tough-to-brittle transition, MC simulations were run for (i) $\sigma_{o,m} / \sigma_{o,f} = 0.05$ and $m_m = 20$, and (ii) $\sigma_{o,m} / \sigma_{o,f} = 0.15$ and $m_m = 5$, with f varying from 0.01 to 0.5 and with $N = 500$ and $L = 5\delta_c$. 50 simulations were run for each case. Using the average matrix failure strain $\bar{\sigma}_m(L, m_m, \sigma_{o,m}) / E_m$ as the cracking strain ε_{mc} in Eqn. (6.13) yields a critical volume fraction $f_c \approx 0.14$ for both scenarios. Representative stress-strain curves are plotted on Figure 6.14 while the bundle strengths and failure strains are summarized in Figure 6.15.

The breadth of the transition is affected by the breadth of the matrix strength distribution. For $m_m = 20$, matrix cracking occurs over a narrow strain range and only minor differences are observed between simulations. For $f \leq 0.10$, composite rupture occurs immediately after the first matrix crack is formed, at a strain $\varepsilon_t / \varepsilon_{c,f} = 0.095 \pm 0.005$. By comparison, the expected value for matrix strain to failure for the prescribed Weibull parameters and gauge length is $\varepsilon_t / \varepsilon_{c,f} = 0.093$. The transition from brittle to tough response begins at $f = 0.11$, where composite failure occurs after the third matrix crack has formed. Matrix crack saturation is first achieved at $f = 0.13$ (which coincides closely with the analytical estimate of f_c). Over the range $f = 0.10$ to 0.13, σ_b rises rapidly, from 13% to 84% of the theoretical value (Figure 6.15A). For lower values of m_m , matrix cracking occurs over a broader strain range and thus the tough-to-brittle transition is broader as well

(Figure 6.15B). Here fiber volume fractions of $f \geq 2f_c$ are needed to get close to the theoretical fracture properties. For example, at $f = 0.30$, σ_b and ε_b are 89% and 81% of their respective theoretical values.

6.4 Exact closed-form solution for unidirectional composite response

Here we seek an analytical solution for the global stress-strain response of a composite during *concurrent fragmentation* of the two phases. In general, the composite stress is given by the volume-weighted average of the stresses in the fibers and in the matrix, each computed *at the same composite strain*. Because the fibers are contiguous along the loading direction, the average intact fiber strain Δ_f is nearly identical to the composite strain up to composite rupture. In contrast, since the matrix is not contiguous, its intact strain Δ_m differs from Δ_f (Δ_m does not account for displacement due to matrix crack opening). The challenge therefore is to combine the two fragmentation solutions on the basis of a common strain metric. In the following analysis, we use $\Delta_m \equiv \varepsilon_a / \varepsilon_{c,m}$ as that strain metric where $\varepsilon_a \equiv \sigma_a / E_c$ is the strain in planes with notionally intact fibers and matrix. σ_a is the applied composite stress (Figure 6.2). In the initial linear elastic domain, $\varepsilon_a = \varepsilon_t$ where ε_t is the total composite strain. Upon the onset of matrix cracking, $\varepsilon_a < \varepsilon_t$ as ε_a does not account for additional displacement due to matrix crack opening. Analogously, $\Delta_f = \varepsilon_t / \varepsilon_{c,f}$ before any fibers have broken and $\Delta_f < \varepsilon_t / \varepsilon_{c,f}$ after the first fiber breaks. However, $\Delta_f \approx \varepsilon_t / \varepsilon_{c,f}$ up to composite rupture because (a) the increase in strain resulting from an individual fiber break is small and (b) most fibers remain intact up to composite rupture. The composite response can therefore be written formally as

$$S_t(\Delta_f(\Delta_m))\sigma_{c,f} = fS_f(\Delta_f(\Delta_m))\sigma_{c,f} + (1-f)S_m(\Delta_m)\sigma_{c,m} \quad (6.14)$$

Determination of the two stresses, S_f and S_m , and the relationship $\Delta_f(\Delta_m)$ follows.

As demonstrated earlier, Hui's solution for the *fiber* response, $S_f(\Delta_f)$, obtained by integration of Eqn. (6.9), agrees remarkably well with the results from the MC simulations (Figure 6.4A).[†] The same solution can be adapted to *matrix* fragmentation by simply reversing the assignment of matrix and fiber properties in Eqn. (6.9). Re-casting the solution in terms relating to the matrix, the characteristic matrix stress becomes³²

$$\frac{\sigma_{c,m}}{\sigma_{o,m}} = \left(\frac{f}{(1-f)} \frac{L_o}{R_f} \frac{\tau_s}{\sigma_o} \right)^{1/(m_m+1)} \quad (6.15)$$

Eqn. (6.15) is the same as Eqn. (6.5) except for the fiber volume fraction term. Combining this with Eqn. (6.9) (with matrix and fiber re-interpreted accordingly) and integrating yields $S_m(\Delta_m) \equiv \int_0^{\Delta_m} g(x, m_m) dx$. Here $g(x, m) \equiv dS/dx$ and is given by Eqn. (6.9), expressed in terms of the dummy variable x :

$$g(x, m) = m \left(\frac{1}{m} - 1 + 2x^{-1-m} \left(1 - \exp \left[\frac{-x^{m+1}}{2} \right] \right) - \frac{x^{m+1}}{4} \right) \exp \left[\frac{-x^{m+1} - 2m \left(\gamma + \Gamma \left(0, x^{m+1}/2 \right) + \ln \left(x^{m+1}/2 \right) \right)}{m+1} \right] \cdot \quad (6.16)$$

[†] Arguably, the analytical approximation in Eqn. (6.7) would be sufficient to obtain $S_f(\Delta_f)$ up to the point of fiber bundle rupture. But, because matrix fragmentation usually goes to completion before fiber bundle fracture, the complete fragmentation solution is needed to capture the *matrix* response $S_m(\Delta_m)$; Eqn. (6.7) is not adequate.

This numerical result, obtained by integration of $g(x, m_m)$, agrees with results from the MC simulations (Figure 6.16). The relationship $\Delta_f(\Delta_m)$ is derived from a standard shear lag analysis (see Appendix); the pertinent parameters are indicated in the inset of Figure 6.2C. The result is

$$\Delta_f(\Delta_m) = \frac{\sigma_{c,m}}{f\sigma_{c,f}} \left[(f-1)S_m(\Delta_m) + \frac{\Delta_m E_c}{E_m} \right] \quad (6.17)$$

The overall composite response is then

$$\begin{aligned} S_t(\Delta_f(\Delta_m)) &= fS_f(\Delta_f(\Delta_m)) + ((1-f)\sigma_{c,m}/\sigma_{c,f})S_m(\Delta_m) \\ &= f \int_0^{\Delta_f(\Delta_m)} g(x, m_f) dx + ((1-f)\sigma_{c,m}/\sigma_{c,f}) \int_0^{\Delta_m} g(x, m_m) dx \end{aligned} \quad (6.18)$$

Evaluation of $S_t(\Delta_f)$ requires numerical integration.

Eqn. (6.18) is a key result of this work; it relates the constituent properties to the global stress-strain response of the composite. Its utility is demonstrated through comparison of the computed stress-strain response with that obtained from the MC simulations. One such example, for realistic matrix and fiber properties, is shown in Figure 6.8. The agreement is excellent. Other case studies (not presented here) show equally good agreement.

Although the preceding model is able to capture the stress-strain response when both the matrix and the fibers undergo fragmentation, it does not shed light on why the bundle strengths and failure strains from MCS generally fall below the theoretical values, especially when a matrix with finite strength is present. The theoretical values derive from an instability condition of the form $dS_f/d\Delta_f = 0$, where, to emphasize, S_f is the average fiber stress and Δ_f is the average strain in intact fiber segments. Since this condition is based on

average stresses and strains (neglecting axial variations in these quantities), it only accurately predicts the failure point in cases where the matrix has no strength and hence the fiber strain is uniform; it invariably overestimates the strengths and failure strains when a matrix is present. This deficiency is remediated in the following way.

Composite rupture is an extreme value phenomenon. As such, the point of rupture can be couched in terms of a *local* instability: one in which the stress-strain response in the most critically stressed cross-section passes through a stress maximum. The most critically stressed sections are naturally those of the matrix cracks, where the load is carried solely by the fibers. Denoting the fiber strain in the matrix crack Δ_f^{\max} and the corresponding *in situ* bundle stress (for a strain of Δ_f^{\max}) $S_f^{\max}(\Delta_f^{\max}) \equiv \int_0^{\Delta_f^{\max}} g(x, m_f) dx$, the instability condition becomes $dS_f^{\max}/d\Delta_f^{\max} = 0$. From shear lag, the maximum fiber strain is:

$$\Delta_f^{\max}(\Delta_m) = \frac{\Delta_m \varepsilon_{c,m} E_c}{f \varepsilon_{c,f} E_f} \quad (6.19)$$

Δ_f^{\max} depends only on elastic and geometric properties and applied stress (independent of matrix crack density, matrix strength and fiber strength). Importantly, Eqn. (6.19) remains valid during the softening portion of matrix response, where matrix slip zones overlap.

From the fragmentation model, the instability condition is written explicitly as

$$dS_f^{\max}/d\Delta_f^{\max} \equiv g(\Delta_f^{\max}, m_f) = 0 \quad (6.20)$$

Solving Eqn. (6.20) for Δ_m yields the critical intact matrix strain Δ_m^* required for composite rupture. The corresponding global rupture strain, *in situ* bundle strength, and composite

strength are $\Delta_f^* = \Delta_f(\Delta_m^*)$ (from Eqn. (6.17)), $S_f^* = S_f(\Delta_f^*)$, and $S_t^* = S_t(\Delta_f^*)$ (from Eqn. (6.18)), respectively.

The function $S_f^{\max}(\Delta_f^{\max}(\Delta_f))$ is plotted on Figure 6.8, using constituent properties corresponding to those of the MC simulation also shown on that figure. This function exhibits a maximum at a composite strain that is essentially identical to that from the MC simulation. Additionally, applying this solution to composites with a range of fiber volume fractions yields a failure envelope of the type shown in Figure 6.14 and trends in failure stress and strain plotted in Figure 6.15. Once again, the predicted failure points agree well with those from the simulations. The main differences are obtained at very low f and are attributable to the finite number of fibers and finite gauge length in the simulations. (Both are tacitly assumed to be infinite in the analytical model.) For instance, the strength and failure strain from the numerical solution approach zero as $f \rightarrow 0$, because the strength of a matrix material of infinite length is zero. In contrast, in the MC simulations, it is closer to the average matrix strength for the prescribed gauge length, in this case $L = 5\delta_c$.

Elastic modulus mismatch between fibers and matrix (thus far neglected) also plays a role in the tough-to-brittle transition. Computed variations in strength and failure strain with fiber volume fraction for $E_m/E_f = 3, 1$ and $1/3$ are shown in Figures 6.15C and D. The main effect of the mismatch, obtained when $E_m/E_f < 1$, is to broaden the transition zone (in terms of f). The specific calculations for $E_m/E_f = 1/3$ and $m_m = 5$ (Figure 6.15D) indicate that the theoretical strengths and failure strains would probably not be attainable in composites with realistic fiber volume fractions.

6.5 Experimental study

6.5.1 Materials and measurements

Tensile tests were conducted on several minicomposites, each comprising a single tow of 400 BN-coated Tyranno ZMITM fibers with a CVI SiC matrix. A representative polished cross-section is shown in Figure 6.17A. The average fiber volume fraction, obtained by image analysis, is $f = 0.27$. The specimen gauge length was 25 mm. Strains were measured by digital image correlation (DIC) using one camera with the entire gauge length in the field of view. A fine speckle pattern was applied with spray paint onto the minicomposites at the very ends of the gauge section. The results are presented in terms of a nominal stress, defined as $\sigma_{nom} \equiv F/A_b = \sigma_a/f$, where F is force, A_b is the cross-sectional area of the fiber bundle and σ_a is the applied composite stress.

Measurements on the minicomposites were augmented by property measurements on the fibers and the interfaces. Fiber properties were obtained from instrumented fiber bundle tests on both coated and uncoated fibers at a gauge length, L , of 110 mm.³¹ The Young's modulus and Weibull parameters were computed from a least-squares fit of the Weibull function to the measured stress-strain curves (Figure 6.18A), following procedures described elsewhere.³¹ The average fiber Young's modulus obtained from these tests is $E_f = 171 \pm 7$ GPa. The Weibull parameters are summarized in Table 6.2. Apparently the application of BN coatings reduces the fiber strength by about 25%. This is likely due to the high temperature typically used in BN deposition ($\sim 1400^\circ\text{C}$)^{5,6}; by comparison the reported strength retention temperature for these fibers is 1300°C .³³ Bundle strengths were also measured at several other gauge lengths, ranging from 5 to 305 mm. The gauge-length

dependence of bundle strength³⁴ was used to confirm the Weibull parameters obtained from fits of the stress-strain curves at $L = 110$ mm (Figure 6.18B).

The interface sliding stress and toughness were obtained from fiber push-in tests.³⁵ Means and standard deviations in these properties are given in Table 6.3. In subsequent analysis, the sliding stress τ_s is taken to be 7 MPa: the median value from about 150 push-in tests.³⁵ The interface toughness is taken to be 0; at stresses at which fibers begin to break, the entire interface has been debonded as a result of matrix cracking.

A representative tensile test result for a minicomposite is shown in Figure 6.19A. The curve displays four domains of response: (i) linear-elastic deformation at low strains; (ii) non-linear deformation due to matrix cracking, over the strain range 0.055–0.65%; (iii) linear response dominated by fibers over the strain range 0.7–0.9%, with a tangent modulus ($E_{nom}^{mcs} = 176$ GPa, superscript *mcs* denoting matrix crack saturation) that is essentially the same as the fiber modulus obtained from fiber bundle tests; and (iv) slightly-nonlinear response with progressive reduction in tangent modulus during fiber fragmentation, up to a failure strain of about 1.3%. One notable feature of the latter part of the curve is that the tangent modulus at the onset of fracture (shown in inset) is about $0.5 E_f$: well above the value (0) used as the basis of fracture prediction in the models of Hui and of Curtin. The *in situ* fiber bundle response, obtained by subtracting the average nominal matrix stress $\bar{\sigma}_{m,nom}^{mcs} = 0.60$ GPa from the composite stress in the post crack saturation domain, is also shown in Figure 6.19A (orange curve).

Subsequent examinations of broken test specimens reveal a range of pullout lengths (Figure 6.17B), with a median value $L_p^{med} = 190 \pm 110$ μm (obtained from measurements on

127 fibers), and periodic matrix cracking (Figure 6.17C), with an average spacing $\bar{x} = 380 \pm 270 \mu\text{m}$ (obtained from measurements on 32 cracks).

6.5.2 Analysis of test results

Preliminary analyses of the test data are used to assess the critical fiber volume fraction f_c and the nature of flaws controlling matrix cracking in the present composite. From Eqn. (6.13), and using the property values $\varepsilon_{mc} = 0.055\%$, $\sigma_b = 2.2 \text{ GPa}$, $E_m = 400 \text{ GPa}$, and $E_f = 175 \text{ GPa}$, f_c is estimated to be 0.10: well below $f = 0.27$. With regard to matrix cracking, the predicted composite stress for extension of a steady-state, fully-bridged matrix crack (from Eqn. (6.1), assuming a matrix toughness $\Gamma_m = 10 \text{ J/m}^2$) is about 90 MPa. By comparison, the measured (true) composite stress at the onset of cracking is 190 MPa. The large difference in these stresses re-affirms the assumption that matrix cracking is governed by activation of small matrix flaws and that bridging effects do not play a role.

The stress-strain curves are analyzed in the following way. First, the *in situ* fiber Weibull parameters, m_f^* and $\sigma_{o,f}^*$, are obtained from a Weibull-like plot of $\ln(-\ln P_s)$ vs $\ln \varepsilon_t$ (as described in Section 6.3.4); here the predicted slope is $m_f^* + 1$ and the intercept is $-(m_f^* + 1) \ln \varepsilon_{c,f}$ (Figure 6.19B). From three minicomposite tensile tests, the average *in situ* Weibull parameters are $m_f^* = 5.6 \pm 0.1$ and $\sigma_{o,f}^* = 1.04 \pm 0.09$ for $L_o = 1$. Next, with the *in situ* fiber properties and the interface sliding stress in hand, the composite stress-strain curves are fit, using Eqn. (6.18), to obtain the matrix Weibull parameters. Because of the complexity of the numerical integration, fitting is done manually, rather than with a formal least-squared fitting procedure. Nonetheless, the fitting yields curves that closely match the

measured ones (Figure 6.20). From analyses of three tests, the matrix Weibull parameters are found to be $m_m = 7, 8,$ and $6,$ and $\sigma_{o,m} = 120, 160,$ and 90 MPa (for $L_o = 1$ m and $A_o = \bar{A}_m = 0.30$ mm², where \bar{A}_m is the average cross-sectional area of the matrix). For a gauge length of $L = 25$ mm, the three sets of matrix Weibull parameters correspond to an average failure strain of $\bar{\varepsilon}_m = 0.048, 0.060,$ and 0.039% . Non-linearity in minicomposite response occurs at $0.055, 0.067,$ and 0.041% , respectively. Agreement is excellent.

Also shown in Figure 6.20 is the computed *in situ* fiber bundle response (solid line) and the *predicted* point of fracture, the latter obtained from the point at which the local fiber bundle response undergoes instability. The correlation between the computed and measured stress-strain curves is unsurprising: the measured curve having been used to infer the fiber properties that go into the model. More remarkably, however, prediction of fracture (and this *is* truly a prediction) proves to be exceptionally accurate. When, instead, the fiber Weibull parameters are taken to be those obtained from tensile tests on coated fiber bundles (dashed-dotted lines in Figure 6.19A), both the fracture stress and strain are over-predicted by about 1/3. The possible origins of these differences are discussed in the next section.

As a final assessment of the model predictions, the measured median pullout length, normalized by $\delta_c = 1.9$ mm (Eqn. (6.6)), is $L_p^{med} / \delta_c = 0.10 \pm 0.06$. By comparison, that from the MC simulations for $m_f = 5$ is $L_p^{med} / \delta_c = 0.12$: essentially the same as the measured value. If, instead, results from the SFC model were used, the predicted pullout length would be $L_p^{med} / \delta_c = 0.22$, while those from the SMC model would yield $L_p^{med} / \delta_c = 0.08$.

6.5.3 Discussion

Analysis of the tensile stress-strain response of ceramic minicomposites can yield vital information about the properties of the constituents as well as the nature of load transfer between the constituents. It can also provide an assessment of the extent to which fiber properties are altered as a result of the composite fabrication process. Ideally, properties of coated fibers would be retained and load transfer between constituent elements in the composite would follow global load sharing characteristics. When ideal conditions are present, confirmation would be obtained from agreement between predicted and measured stress-strain curves, including fracture stress and strain. Otherwise, because of the coupled effects of fiber properties and load sharing characteristics on the tensile response, elucidating the origins of discrepancies between experiment and theory can be challenging.

In the composite studied here, the *in situ* fiber Weibull properties inferred from tests on the minicomposites yield fracture predictions that are remarkably accurate. (Similarly remarkable agreement is obtained between the fracture predictions and the fracture properties obtained from the MC simulations.) The outstanding discrepancy is between the inferred *in situ* fiber properties and those measured directly on coated fiber bundles: the latter yielding somewhat higher predicted fracture stresses and strains within the composites. The discrepancy might arise in one of two possible ways.

First, properties of the fibers may be degraded by the elevated temperature exposure during matrix formation (in this case via CVI). Although processing details of the present composites are not known, we surmise, based on processing details reported elsewhere, that CVI deposition of SiC, typically done at temperatures of about 1000°C³⁶, would not cause fiber strength degradation from thermal effects alone. (As noted earlier, the strength

retention temperature of the fibers is 1300°C). Second, because of incomplete densification, especially in the composite interior, the load transfer characteristics are likely not ideal. That is, fiber clusters on the composite interior – being physically separated from the more heavily-densified regions around the composite periphery – are unable to share load with other composite elements as they would otherwise if the matrix were fully dense and contiguous throughout. As a result, the full potential of the fiber bundle may not be realized in composite properties.

6.6 Conclusions

We have examined the mechanics of the tensile response of unidirectional fiber-reinforced ceramic composites through a combination of Monte Carlo simulations of fragmentation, adaptations of existing theories of fiber fracture, and complementary experimental measurements. Despite being a problem seemingly solved long ago, several nuanced features with important practical implications have been identified. The key conclusions follow.

- (i) Contrary to the single fiber composite (SFC) model, the process of fiber fragmentation cannot go to completion in unidirectional composites under uniaxial tension. At low stresses (before the maximum), fibers break essentially randomly throughout the bundle; but, at the stress maximum, all additional breaks are localized to regions adjacent to the fracture plane over a length δ_c . Therefore, the resulting pullout length distribution does not match predictions from either the SFC or SMC models. The distribution of strength of pulled-out fibers is similarly inconsistent with existing model predictions. When presented as a Weibull plot, the

latter distribution is bilinear. An important consequence is that measured distributions in length and strength of pulled-out fibers cannot be interpreted using either the SFC or SMC models and are therefore of limited utility without a more detailed accompanying analysis.

- (ii) An alternative method, based on analysis of the composite response following matrix crack saturation, is more effective in inferring the *in situ* fiber properties, without relying on data obtained from examinations of fracture surfaces. The method is straightforward when matrix cracking goes to completion before significant fiber fracture has occurred, a condition often satisfied in typical minicomposites. Otherwise, the concurrent fragmentation analysis presented in Section 6.4 could be employed to infer the matrix and fiber strength characteristics simultaneously.
- (iii) Although the stress-strain response associated with concurrent fragmentation of matrix and fibers can be readily described by adaptations of existing fragmentation models, accurate prediction of the point of instability requires consideration of the *local* response of fibers in the most heavily strained regions (within matrix crack planes). The fiber bundle response in the latter regions leads to instability at stresses and strains that are lower than those obtained from the *average* stress-strain response. In this context, contrary to conventional wisdom, the matrix plays an important role in fiber bundle fracture.
- (iv) Although a critical fiber volume fraction for achieving high failure strain can be estimated assuming fiber and matrix strengths to be deterministic, the transition in failure strain when the constituent strengths are stochastic is inherently more

gradual, especially when the matrix strength distribution is broad. In cases of practical interest, the theoretical strength and failure strain may not be attained until the fiber fraction exceeds twice the critical value. This result has important implications in the interpretation of experimental test data on ceramic minicomposites. For example, in cases where the microstructure appears reasonably uniform and the fiber fraction is moderately high, the ultimate properties may fall short of expectations based on existing theories, potentially leading to erroneous inferences about the *in situ* properties of the fibers and/or the interfaces.

Acknowledgements

This work was supported by the Pratt & Whitney Center of Excellence in Composites and the IHI Turbine Materials Research Center, both at the University of California, Santa Barbara.

6.A Appendix: Derivation of $\Delta_f(\Delta_m)$

Here we present a derivation of the relationship between strain in intact fiber segments Δ_f (with normalization based on the characteristic *fiber* strain $\varepsilon_{c,f}$) and strain in intact matrix segments Δ_m (with normalization based on the characteristic *matrix* strain $\varepsilon_{c,m}$) in unidirectional minicomposites. Prior to matrix cracking, the axial strain is uniform along the length and therefore $\Delta_f = \Delta_m \varepsilon_{c,m} / \varepsilon_{c,f}$. With formation of the first matrix crack, the intact fiber strain is no longer uniform over the entire gauge length (Figure 6.2C). Within the

matrix slip zone, load previously carried by the matrix is shed to the fibers. The local intact fiber strain therefore increases ($\Delta_f > \Delta_m \varepsilon_{c,m} / \varepsilon_{c,f}$). Outside the matrix slip zone, the intact matrix strain is uniform and the relation $\Delta_f = \Delta_m \varepsilon_{c,m} / \varepsilon_{c,f}$ is maintained. Δ_f is therefore given by the volume-weighted average of fiber strain in the intact matrix regions and average fiber strain in slipped matrix regions:

$$\Delta_f(\Delta_m) = P_{s,m} \Delta_m \frac{\varepsilon_{c,m}}{\varepsilon_{c,f}} + (1 - P_{s,m}) \frac{\bar{\varepsilon}_f^{sm}}{\varepsilon_{c,f}} \quad (6.A1)$$

where $P_{s,m}$ is the survival probability of the matrix and $\bar{\varepsilon}_f^{sm}$ is the average fiber strain in the slipped regions. From considerations of mechanical equilibrium, $\bar{\varepsilon}_f^{sm}$ can be couched in terms of Δ_m and the average matrix strain, $\bar{\varepsilon}_m^{sm}$, in slipped matrix regions via:

$$\bar{\varepsilon}_f^{sm} = \Delta_m \frac{\varepsilon_{c,m}}{f} \frac{E_c}{E_f} - \left(\frac{1-f}{f} \right) \frac{E_m}{E_f} \bar{\varepsilon}_m^{sm} \quad (6.A2)$$

The first term in Eqn. (6.A2) is Δ_f^{\max} in Eqn. (6.20). For a linear-elastic matrix,

$\bar{\varepsilon}_m^{sm} = \bar{S}_m^{sm} \sigma_{c,m} / E_m$ where \bar{S}_m^{sm} is the average matrix stress in the slipped matrix regions.

Similarly to Eqn. (6.A1), the normalized matrix stress S_m can be expressed as the sum of the volume-weighted stress in the intact matrix regions and average stress in slipped matrix regions:

$$S_m = P_{s,m} \Delta_m + (1 - P_{s,m}) \bar{S}_m^{sm} \quad (6.A3)$$

Solving Eqn. (6.A3) for \bar{S}_m^{sm} and substituting the result into Eqn. (6. A2) and then (6. A1) yields

$$\Delta_f(\Delta_m) = \frac{\sigma_{c,m}}{f \sigma_{c,f}} \left[(f-1) S_m(\Delta_m) + \frac{\Delta_m E_c}{E_m} \right] \quad (6.A4)$$

where $S_m(\Delta_m) \equiv \int_0^{\Delta_m} g(x, m_m) dx$ and $g(x, m_m)$ is given by Eqn. (6.16). Evaluation of $S_m(\Delta_m)$ and therefore $\Delta_f(\Delta_m)$ require numerical integration.

References

1. Almansour AS, Maillet E, Ramasamy S, Morscher GN. Effect of fiber content on single tow SiC minicomposite mechanical and damage properties using acoustic emission. *J Eur Ceram Soc.* 2015;35(13):3389–99.
2. Buet E, Sauder C, Sornin D, Poissonnet S, Rouzaud J, Vix-guterl C. Influence of surface fibre properties and textural organization of a pyrocarbon interphase on the interfacial shear stress of SiC / SiC minicomposites reinforced with Hi-Nicalon S and Tyranno SA3 fibres. *J Eur Ceram Soc.* 2014;34(2):179–88.
3. Chateau C, Gélébart L, Bornert M, Crépin J, Boller E, Sauder C, et al. In situ X-ray microtomography characterization of damage in SiC f / SiC minicomposites. *Compos Sci Technol.* 2011;71(6):916–24.
4. Martínez-Fernández J, Morscher GN. Room and elevated temperature tensile properties of single tow Hi-Nicalon, carbon interphase, CVI SiC matrix minicomposites. *J Eur Ceram Soc.* 2000;20(14–15):2627–36.
5. Morscher GN. Tensile stress rupture of SiCf/SiCm minicomposites with carbon and boron nitride interphases at elevated temperatures in air. *J Am Ceram Soc.* 1997;42(8):2029–42.
6. Morscher GN, Martinez-Fernandez J. Fiber effects on minicomposite mechanical properties for several silicon carbide fiber-chemically vapor-infiltrated dilicon carbide matrix systems. *J Am Ceram Soc.* 1999;82(1):145–55.

7. Rebillat F, Guette A, Espitalier L, Debieuvre C, Naslain R. Oxidation resistance of SiC/SiC micro and minicomposites with a highly crystallised BN interphase. *J Eur Ceram Soc.* 1998;18(13):1809–19.
8. Sauder C, Brusson A, Lamon J. Influence of interface characteristics on the mechanical properties of Hi-Nicalon type-S or Tyranno-SA3 fiber-reinforced SiC/SiC minicomposites. *Int J Appl Ceram Technol.* 2010;7(3):291–303.
9. Aveston J, Kelly A. Theory of multiple fracture of fibrous composites. *J Mater Sci.* 1973;8(3):352–62.
10. Hutchinson JW, Budiansky B, Evans AG. Matrix fracture in fiber-reinforced ceramics. *J Mech Phys Solids.* 1986;34(2):167–89.
11. Marshall DB, Cox BN, Evans AG. The mechanics of matrix cracking in brittle-matrix fiber composites. *Acta Metall.* 1985;33(11):2013–21.
12. Spearing SM, Zok FW. Stochastic aspects of matrix cracking in brittle matrix composites. *J Eng Mater Technol.* 1993;115(3):314–8.
13. Yang XF, Knowles KM. The one-dimensional car parking problem and its application to the distribution of spacings between matrix cracks in unidirectional fiber-reinforced brittle materials. *J Am Ceram Soc.* 1992;75(1):141–7.
14. Hutchinson JW, Jensen HM. Models of fiber debonding and pullout in brittle composites with friction. *Mech Mater.* 1990;9(2):139–63.
15. Domergue J-M, Vagaggini E, Evans AG. Relationships between hysteresis measurements and the constituent properties of ceramic matrix composites: II, Experimental studies on unidirectional materials. *J Am Ceram Soc.* 1995;78(10):2721–31.

16. Vagaggini E, Domergue J-MM, Evans AG. Relationships between hysteresis measurements and the constituent properties of ceramic matrix composites: I, Theory. *J Am Ceram Soc.* 1995;78(10):2709–20.
17. Curtin WA. Theory of mechanical properties of ceramic-matrix composites. *J Am Ceram Soc.* 1991;74(11):2837–45.
18. Hui CY, Phoenix SL, Ibnabdeljalil M, Smith RL. An exact closed form solution for fragmentation of Weibull fibers in a single filament composite with applications to fiber-reinforced ceramics. *J Mech Phys Solids.* 1995;43(10):1551–85.
19. Sutcu M. Weibull statistics applied to fiber failure in ceramic composites and work of fracture. *Acta Metall.* 1989;37(2):651–61.
20. Thouless MD, Evans AG. Effects of pull-out on the mechanical properties of ceramic-matrix composites. *Acta Metall.* 1988;36(3):517–22.
21. Cady C, Heredia FE, Evans AG. In-Plane Mechanical Properties. *J Am Ceram Soc.* 1995;78(8):2065–78.
22. Phoenix SL. Probabilistic Strength Analysis of Fibre Bundle Structures. *Fibre Sci Technol.* 1974;7(1):15–31.
23. Zok FW. Fracture and Fatigue of Continuous Fiber-reinforced Metal Matrix Composites. In: Kelly A, Zweben C, editors. *Comprehensive Composite Materials.* Pergamon; 2000. p. 189–220.
24. Curtin WA. In Situ Fiber Strengths in Ceramic-Matrix Composites from Fracture Mirrors. *J Am Ceram Soc.* 1994;77(4):1075–8.
25. Thouless MD, Sbaizero O, Sigl LS, Evans AG. Effect of interface mechanical properties on pullout in a SiC-fiber-reinforced lithium aluminum silicate glass-

- ceramic. *J Am Ceram Soc.* 1989;72(4):525–32.
26. Davies IJ, Ishikawa T, Shibuya M, Hirokawa T. Fibre strength parameters measured in situ for ceramic-matrix composites tested at elevated temperature in vacuum and in air. *Compos Sci Technol.* 1999;59(6 SPEC. SEC.):801–11.
 27. Davies IJ, Ishikawa T, Shibuya M, Hirokawa T, Gotoh J. Fibre and interfacial properties measured in situ for a 3D woven SiC/SiC-based composite with glass sealant. *Compos Part A Appl Sci Manuf.* 1999;30(4):587–91.
 28. Cao HC, Bischoff E, Ruhle M, Evans AG, Marshall DB, Brennan JJ. Effect of Interfaces on the Properties of Fiber-Reinforced Ceramics. *J Am Ceram Soc.* 1990;73(6):1691–9.
 29. Poerschke DL, Rossol MN, Zok FW. Intermediate temperature oxidative strength degradation of a SiC / SiNC composite with a polymer-derived matrix. *J Am Ceram Soc.* 2017;1606–17.
 30. Callaway EB, Zok FW. Accurate determination of fiber strength distributions. *J Am Ceram Soc.* 2017;100(3):1202–11.
 31. Callaway EB, Zok FW. Strengths of ceramic fiber bundles: Theory and practice. *J Am Ceram Soc.* 2017;100(11):5306–5317.
 32. Curtin WA. Multiple matrix cracking in brittle matrix composites. *Acta Metall Mater.* 1993;41(5):1369–77.
 33. Ichikawa H. Polymer-derived ceramic fibers. *Annu Rev Mater Res.* 2016;(46):335–56.
 34. Callaway EB, Zok FW. Weibull parameters obtained from dependence of fiber strength on fiber length and area. *J Am Ceram Soc.* 2018;101(10):4719–31.

35. Callaway EB, Christodoulou P, Zok FW. Deformation, Rupture, and Sliding of Fiber Coatings in Ceramic Composites. Submiss.
36. Dicarlo JA. Advances in SiC/SiC composites for aero-propulsion. In: Bansal NP, Lamon J, editors. Ceramic matrix composites: Materials, modeling, technology, and applications. Wiley; 2014. p. 217–35.

Table 6.1: List of variables

<p>A_b Area of bundle a Flaw size a_o Critical crack length E Elastic modulus F Force f Fiber volume fraction f_c Critical fiber volume fraction L Gauge length L_p Pullout length l Slip length m Weibull modulus N Number of fibers P_f Probability of failure P_s Probability of survival R_f Fiber radius $S \equiv \bar{\sigma}/\sigma_c$ Normalized average stress S^* Normalized strength S_f^{\max} Normalized fiber stress for a strain of Δ_f^{\max} x Matrix crack spacing z Position $Z(x)$ Coefficient of variation x</p>	<p>$\alpha \equiv 1/(m_f + 1)$ $\Gamma(\)$ Gamma function Γ_i Interfacial toughness Γ_m Matrix toughness γ Euler–Mascheroni constant (≈ 0.577) $\Delta \equiv \varepsilon^i/\varepsilon_c$ Normalized intact strain Δ^* Normalized rupture strain Δ_f^{\max} Normalized fiber strain in matrix crack planes δ_c Characteristic length ε Strain ε_a Applied strain in intact regions ε_b Bundle rupture strain ε_c Characteristic strain ε_{\max} Strain at maximum stress from Hui’s solution ε_{mc} Matrix cracking strain λ_1, λ_2 Pullout lengths prefactors</p>	<p>σ Stress σ_a Applied composite stress σ_b Bundle strength σ_c Characteristic strength σ_{\max} Maximum stress from Hui’s solution σ_{mc} Matrix cracking stress $\sigma_{nom} \equiv F/A_b$ Nominal stress τ_s Sliding resistance</p> <p>Recurring subscripts: o Weibull reference value f Fiber property m Matrix property t Total composite value</p> <p>Recurring superscripts: i Value in intact fiber or matrix region mcs Value after matrix crack saturation med Median value sf Value in slipped fiber region sm Value in slipped matrix region \bar{y} Average value of y</p>
--	--	--

Table 6.2: Summary of fiber properties

	Tyranno ZMI™			
	Uncoated		BN-coated	
	m_f	$\sigma_{o,f}$ (GPa)	m_f	$\sigma_{o,f}$ (GPa)
Mean	5.2	1.66	4.2	1.14
St. Dev.	0.55	0.12	0.44	0.10
CoV	0.11	0.074	0.11	0.089

Table 6.3: Summary of interface properties

	Tyranno ZMI™ minicomposite	
	Γ_i (J/m ²)	τ_s (MPa)
Mean	0.53	9.5
Median	0.16	6.7
Standard deviation	1.2	9.9
Skew	4.3	3.4
Interquartile range	0.32	7.4

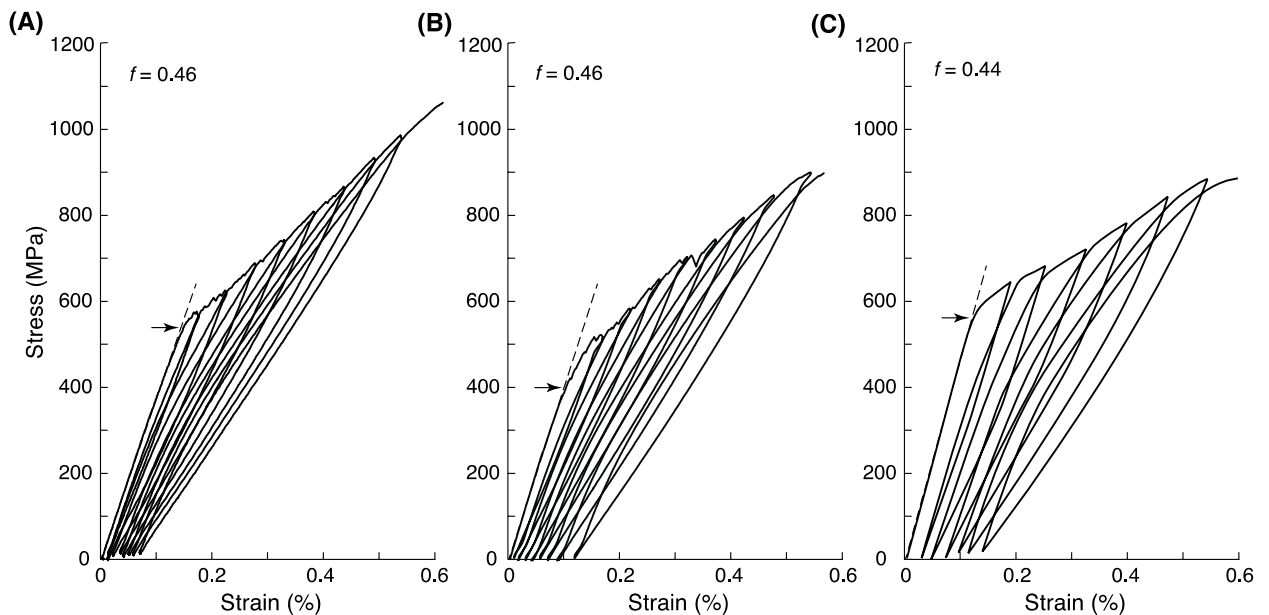


Figure 6.1: Representative tensile stress-strain curves for SiC/SiC minicomposites show the onset of matrix cracking at strains of about 0.10–0.12% and stresses of 400–550 MPa, followed by extensive inelasticity and hysteresis upon unloading and reloading. All composites comprise Hi Nicalon Type-S fibers, pyrolytic C coatings on the fibers, and CVD SiC matrices. Arrows indicate onset of matrix cracking. (Results adapted from Buet *et al.* (A, B)² and Sauder *et al.* (C)⁸).

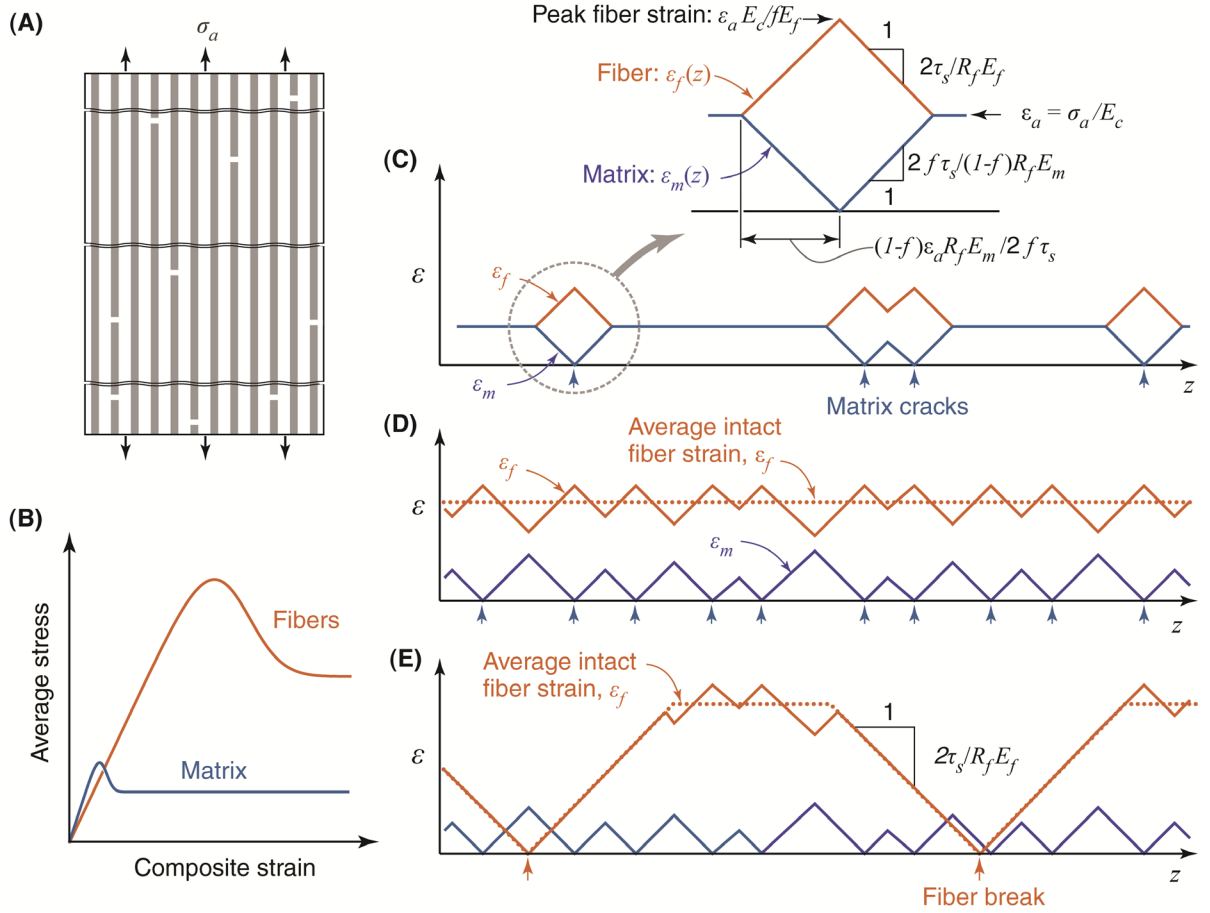


Figure 6.2: (A) Concurrent fragmentation of fibers and matrix during tensile loading leads to (B) rising and falling parts of average stress-strain curves within the constituents as well as plateau values once fragmentation in the respective phase is complete. (C–E) Evolution of axial strains in individual fibers and matrix with progressively increasing applied stress, showing: (C) strain elevations in fibers within matrix crack planes and overlap of slip zones adjacent to two closely-spaced cracks; (D) saturation in matrix crack density; and (E) slip around two fiber breaks. Dotted lines indicate the fiber strain distributions used by Curtin, Hui and others in the development of fiber fragmentation models (neglecting fluctuations due to matrix cracks).

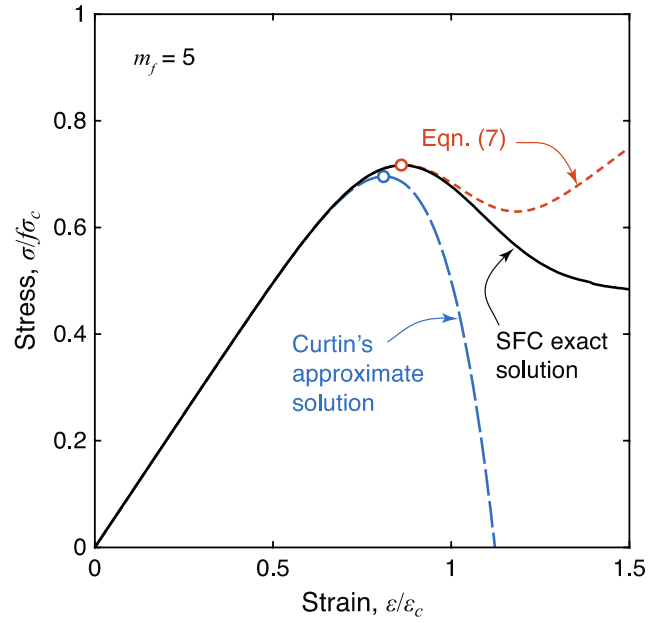


Figure 6.3: The analytical solution in Eqn. (6.7) accurately replicates the exact solution up to and slightly beyond the peak load. Curtin's approximate solution works reasonably well before the load maximum. Comparisons of results for other Weibull moduli lead to the same conclusions.

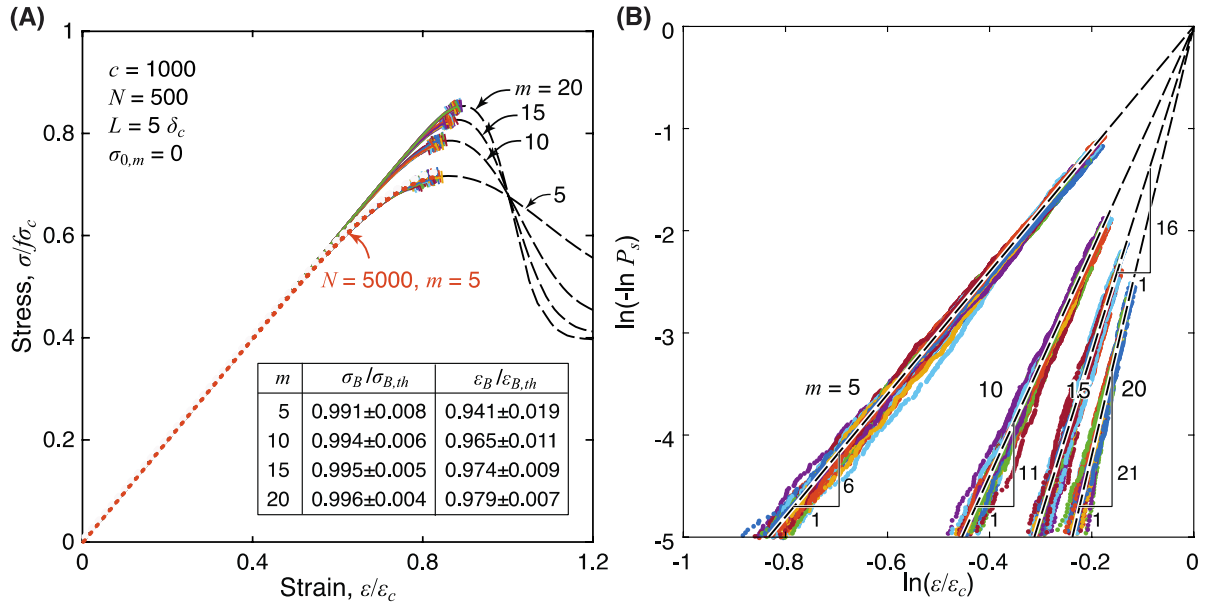


Figure 6.4: (A) MC simulations of a minicomposite with 500 fibers and no matrix reveal narrow distributions in bundle strength and failure strain, and means falling slightly below theoretical limits, $\sigma_{B,th}$ and $\varepsilon_{B,th}$. Hash marks indicate terminal points of the simulations. The stress-strain response from Hui's fragmentation model agrees very well with the simulations, with the exception of the rupture condition. (B) *In situ* fiber Weibull parameters are obtained from composite stress-strain data using a Weibull-like plot. Dashed lines correspond to the input Weibull parameters.

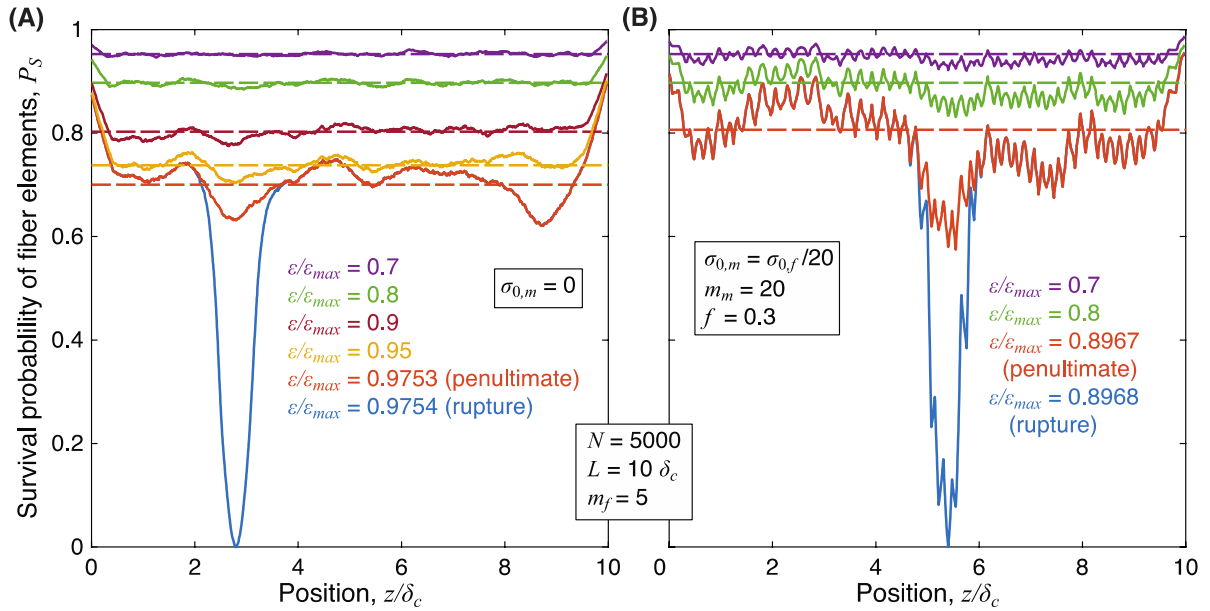


Figure 6.5: (A) In the absence of a matrix, survival probability of fiber segments in each plane remains quite uniform along the composite length up to strains of 90% of Hui's predicted failure strain, ϵ_{max} . Long-range periodic fluctuations become evident for higher strains. (B) When a matrix is present, long-range fluctuations are enhanced and are augmented by short-range fluctuations dictated by matrix crack spacing. Dashed lines in both (A) and (B) are predicted averages from Eqn. (6.4).

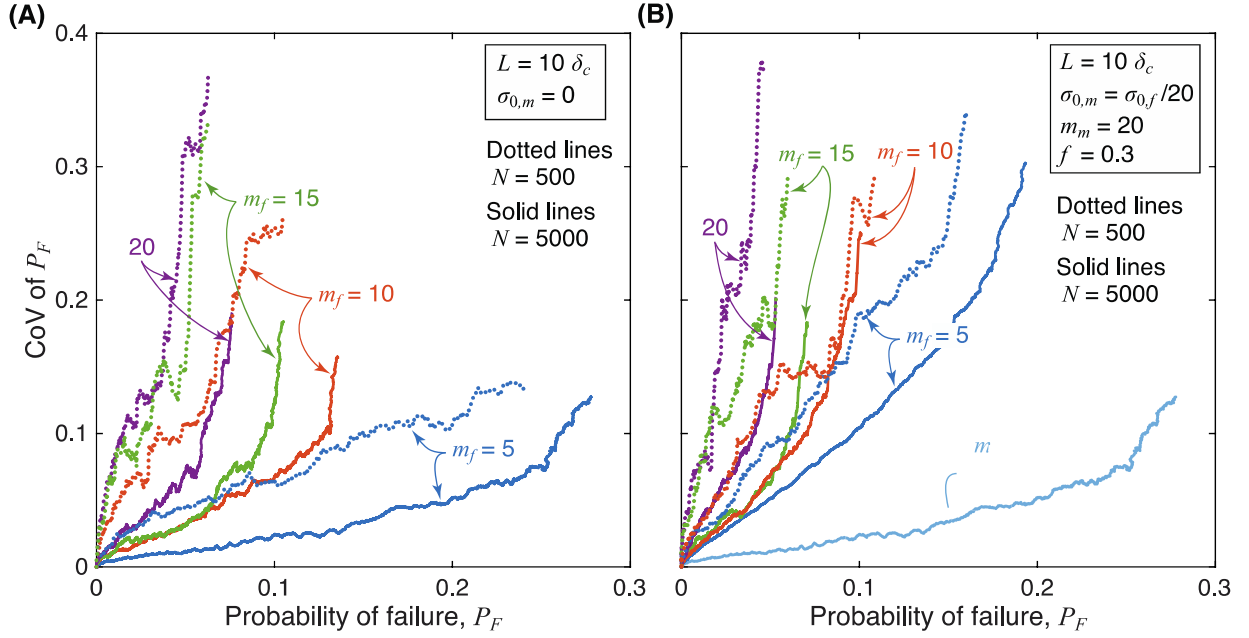


Figure 6.6: Fluctuations in P_f , characterized by the CoV of P_f , increase with m_f and with P_f . The effects are exacerbated as the number of fibers is reduced (by a factor of about $1/\sqrt{N}$). The presence of a matrix (in (B)) has an even stronger effect. The latter is evident upon comparison of the two curves for $m_f = 5$ in (B): solid blue line for the case where the matrix is present and pale blue line for the case where there the matrix is absent (from (A)).

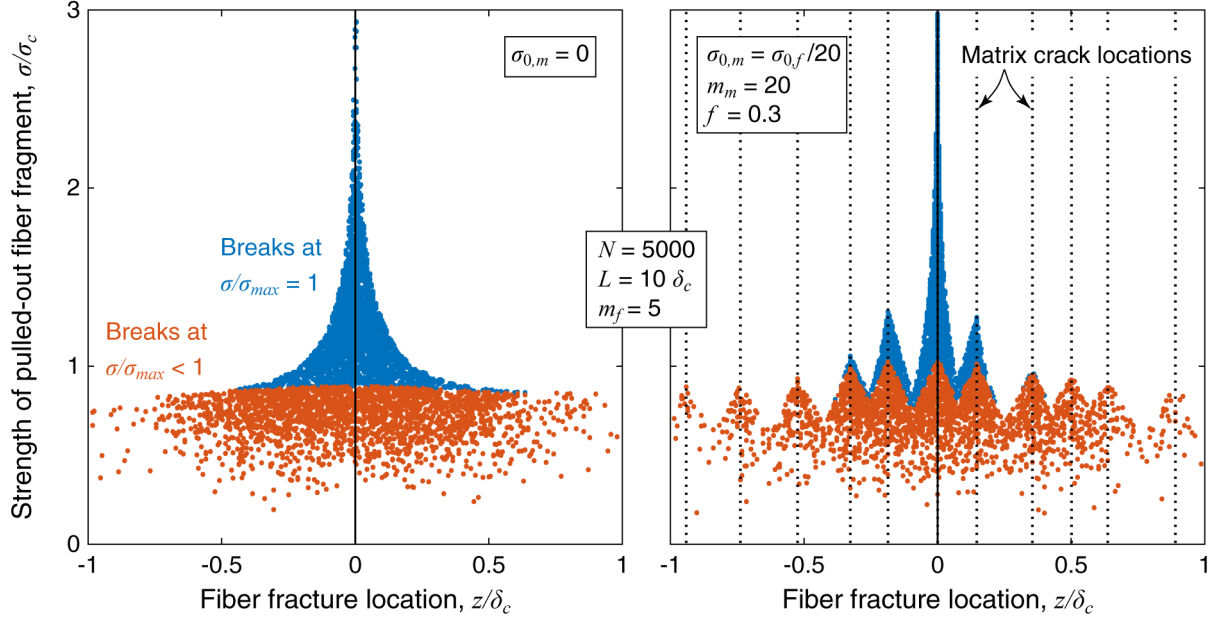


Figure 6.7: (A) In the absence of a matrix, fiber breaks that occur before the peak stress are broadly distributed around the eventual fracture plane; those occurring *at* the peak stress are more localized and involve stronger fibers. (B) When matrix cracks are present, the breaks are preferentially located at the crack locations both before and at the peak stress.

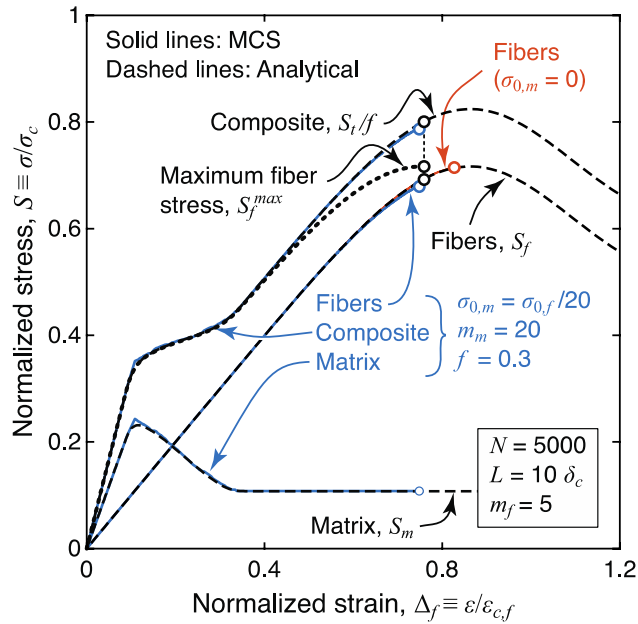


Figure 6.8: Stress-strain curves for composite with moderately high fiber volume fraction (0.3) and the corresponding contributions from the fibers, S_f , and from the matrix, S_m . Solid lines are from MC simulations; dashed lines are from the analytical models; and dotted line represents the maximum fiber stress-strain response (within the matrix crack planes), $S_f^{\max}(\Delta_f^{\max})$, based on Eqns. (6.19) and (6.20).

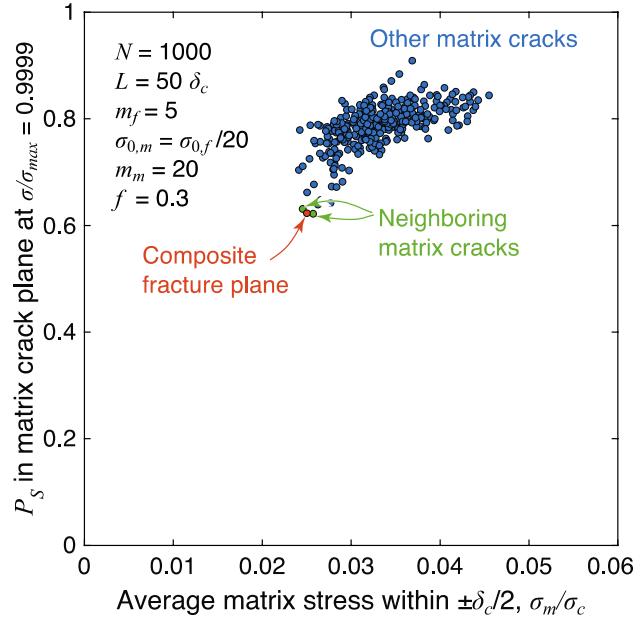


Figure 6.9: Composite fracture tends to occur along or near planes where the local average matrix stress after matrix crack saturation is lowest and hence the fiber survival probability is also lowest. Here σ_{max} is the maximum stress of Hui's exact solution.

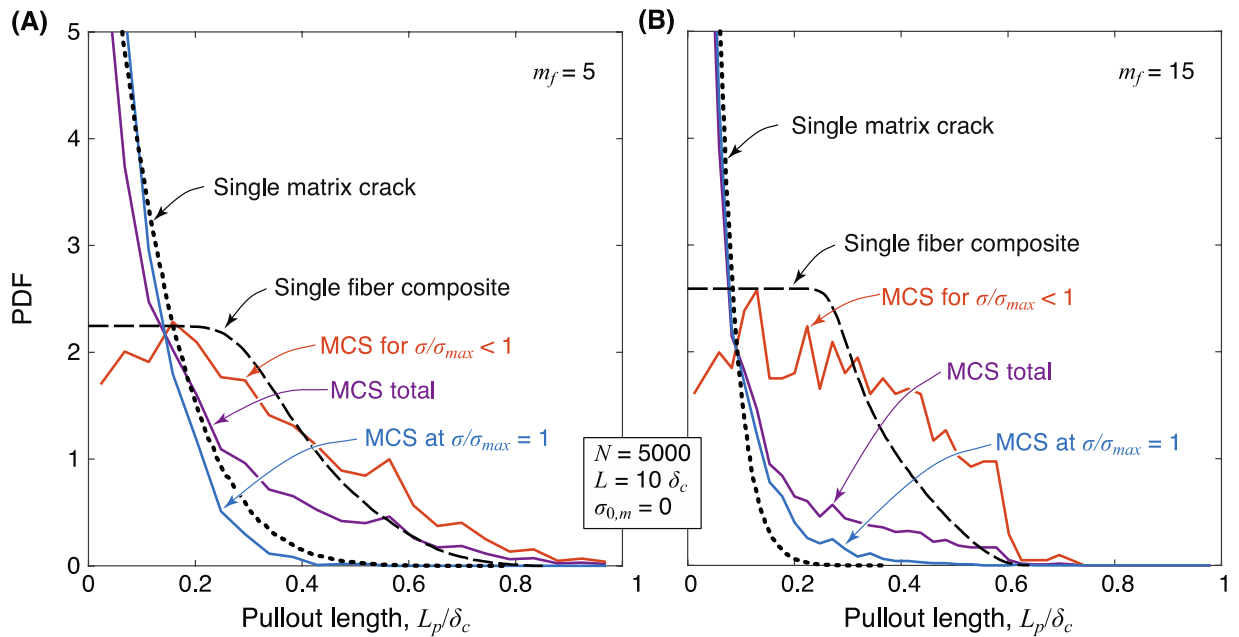


Figure 6.10: Probability distributions of pullout lengths from MCS show that, for fibers broken before the peak stress, the distributions are roughly consistent with the analysis from the SFC model. In contrast, for fibers broken *at* the peak stress, the distributions are more closely aligned with that from the SMC model. When the two parts are combined, the resulting (total) distributions do not follow either one of the two models.

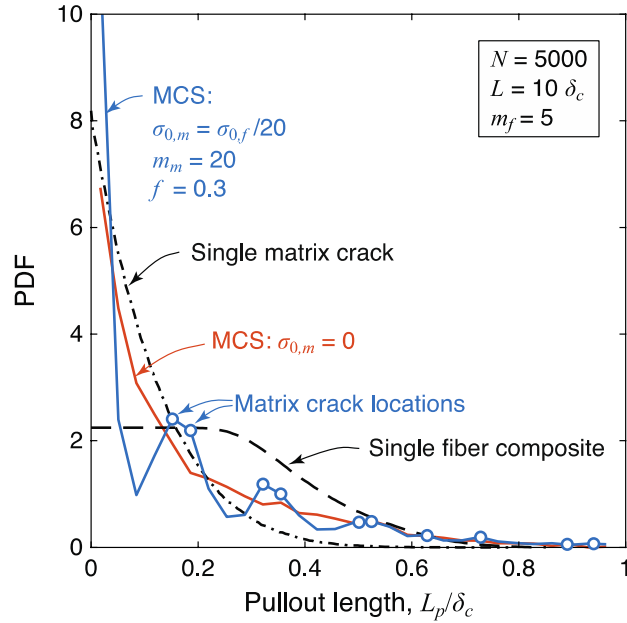


Figure 6.11: When matrix cracks are present, the pullout length distribution exhibits small local peaks at matrix crack locations, although the overall trend is similar to that obtained without a matrix.

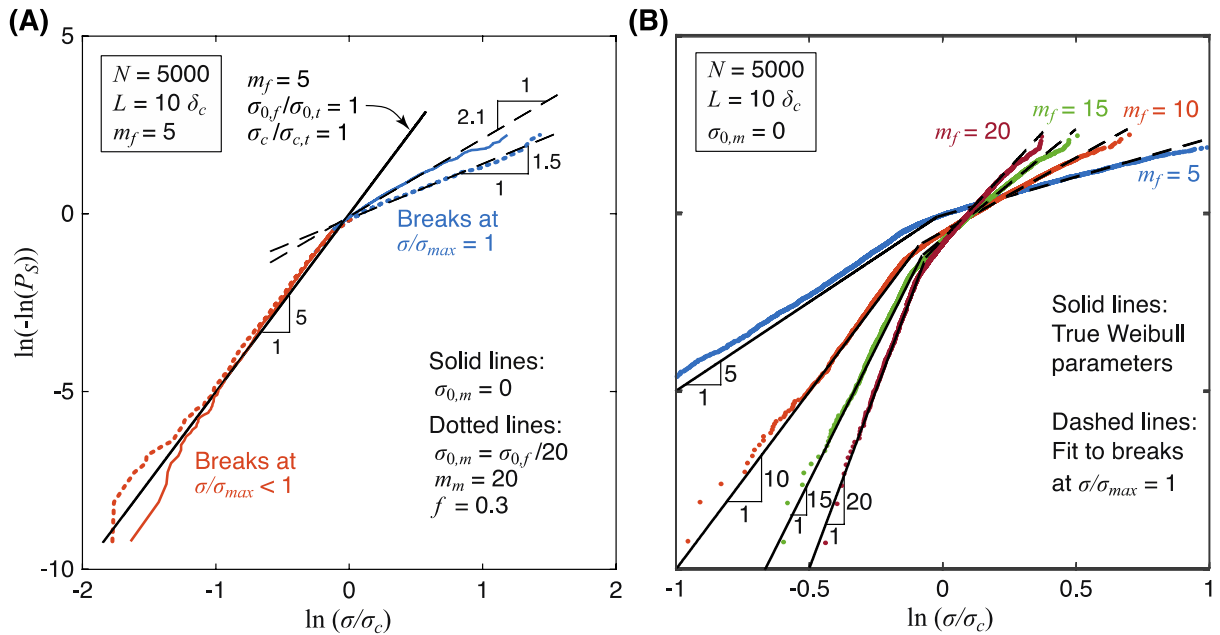


Figure 6.12: (A) Strength distributions of pulled-out fibers both with and without a matrix present are bilinear on a Weibull plot. Strengths at the low end of distributions are consistent with the true fiber strength distribution; those at the high end are biased by the localized nature of the final fiber fracture sequence. Similar distributions are obtained both with and without a matrix present. (B) Changes in Weibull modulus are reflected in changes in the slopes of the strength distributions of pulled-out fibers, although the overall bilinear trend is maintained.

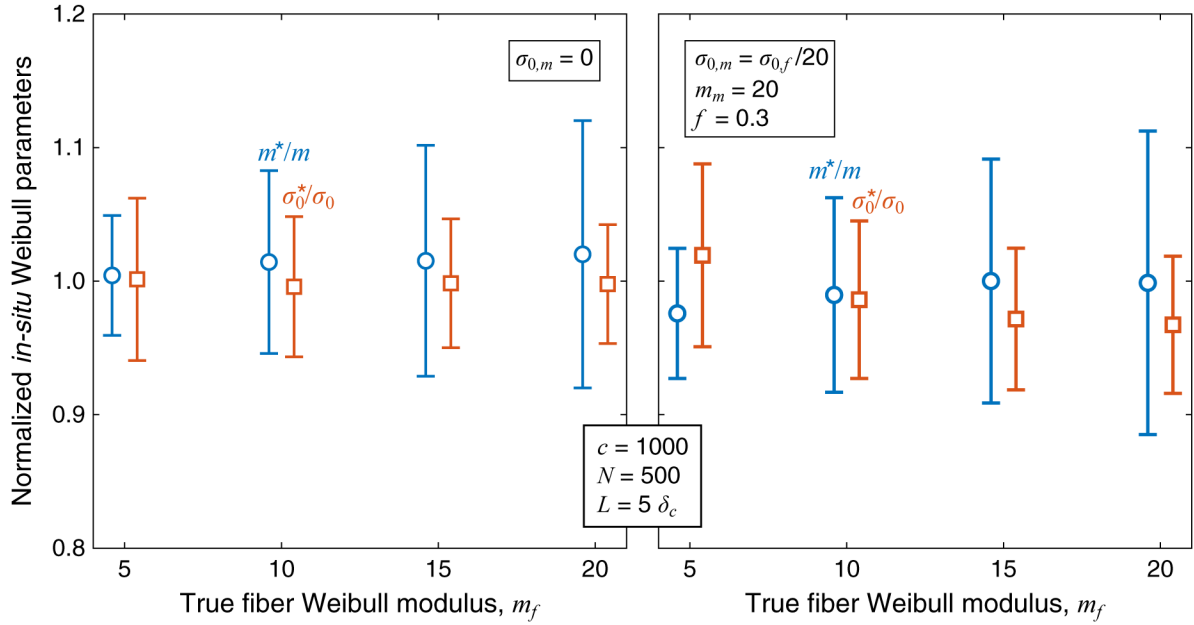


Figure 6.13: Mean values of *in situ* Weibull parameters (symbols), obtained from MC simulations and the Weibull-like plots in Figure 6.4, for minicomposites with 500 fibers lie within about 2–3% of their true values. Their coefficients of variation (error bars) are typically 5–10%.

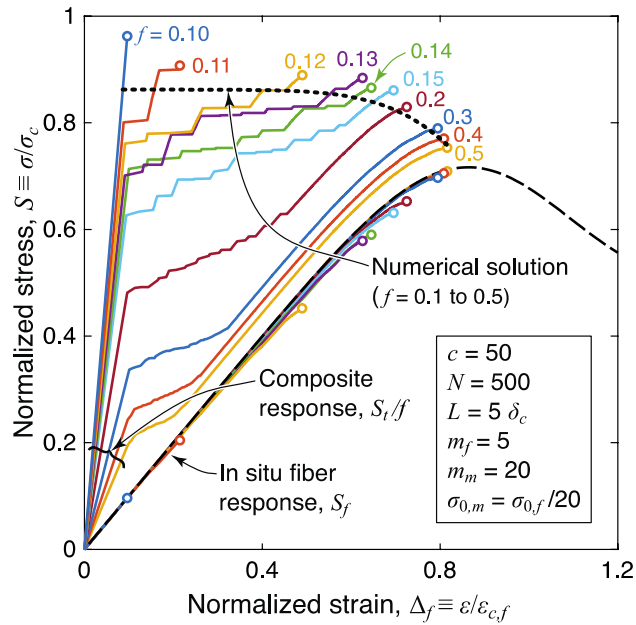


Figure 6.14: The *in situ* fiber bundle response depends sensitively on f , especially in the domain $f \leq f_c$. Solid lines are from MCS; dashed line is from analytical solution, and dotted line is failure locus predicted by Eqn. (6.20).

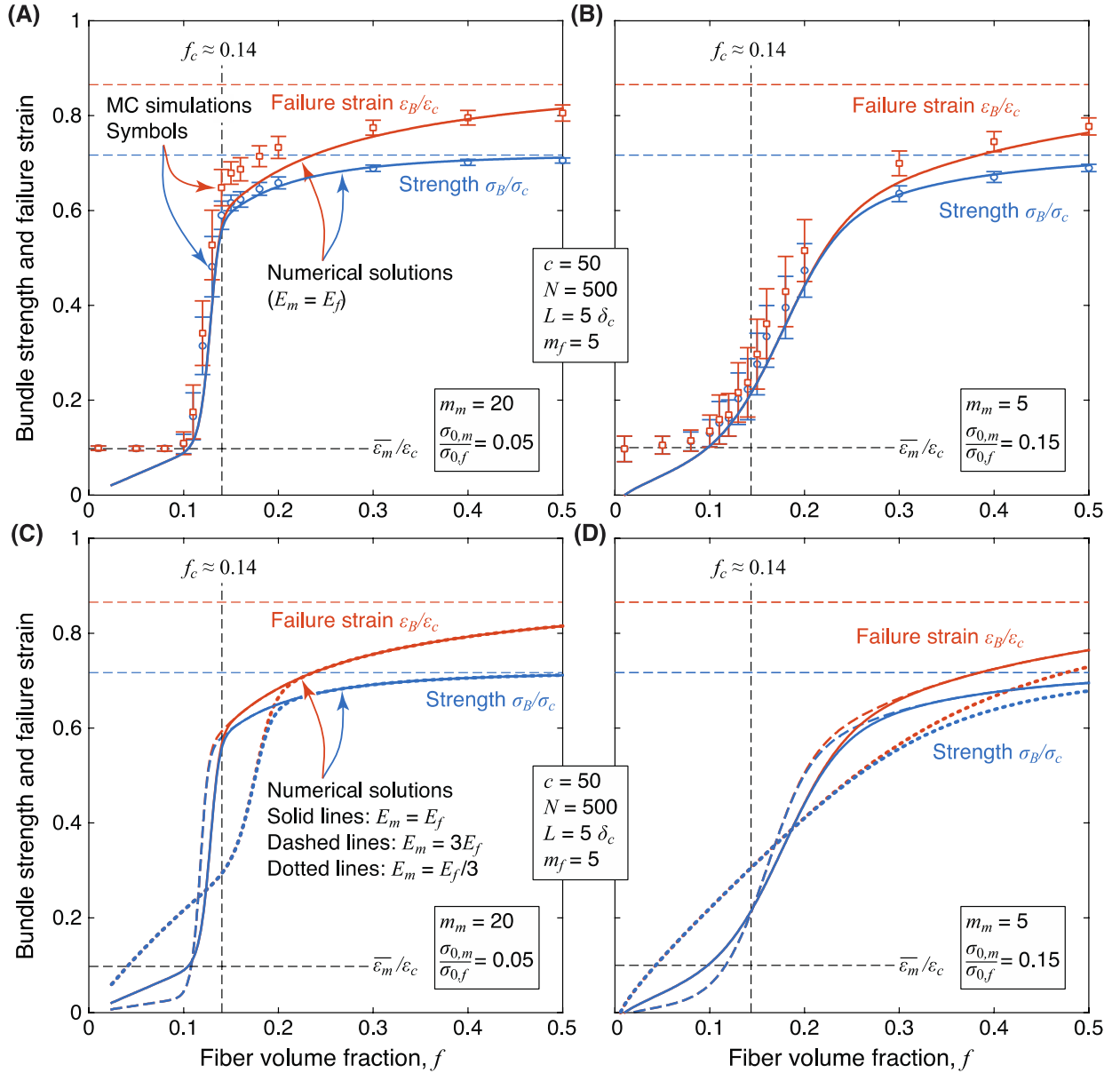


Figure 6.15: Fiber volume fraction plays a crucial role in extracting the full potential from the fiber bundle. (A) When the matrix Weibull modulus is high (20), the transition from tough-to-brittle behavior occurs over a narrow strain range. (B) When it is low (5), the transition is broader and the fiber volume fraction needed to get close to the theoretical values increases. (C, D) Effects of elastic mismatch are small when the matrix is stiffer than the fiber; the effects become more significant when the matrix is more compliant than the fiber. Symbols in (A) and (B) are mean values from 50 MC simulations with error bars representing one standard deviation. Blue and orange curves are from analytical solutions. Horizontal dashed blue and orange lines are the theoretical upper bounds for *in situ* bundle strength and failure strain, respectively (from the maximum of Hui’s exact solution). MC simulations and analytical solutions asymptotically approach the upper bounds in the limit of $f \rightarrow 1$.

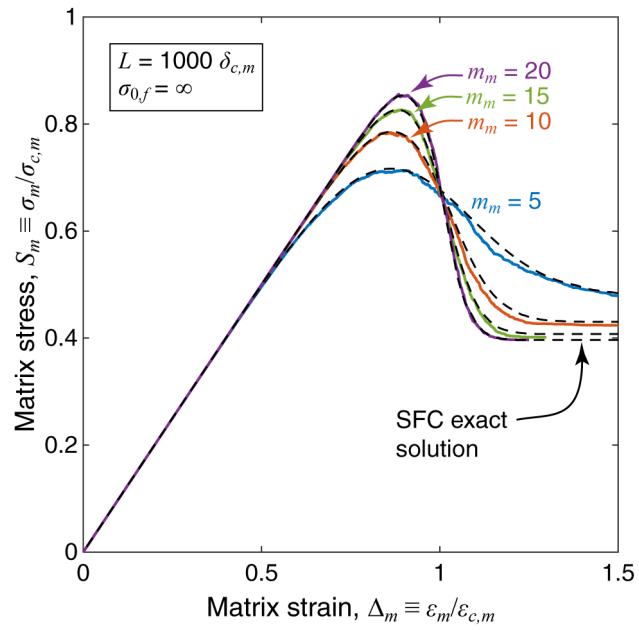


Figure 6.16: *In situ* matrix response from MC simulations (solid lines) follows that of the exact fragmentation solution (dashed lines).

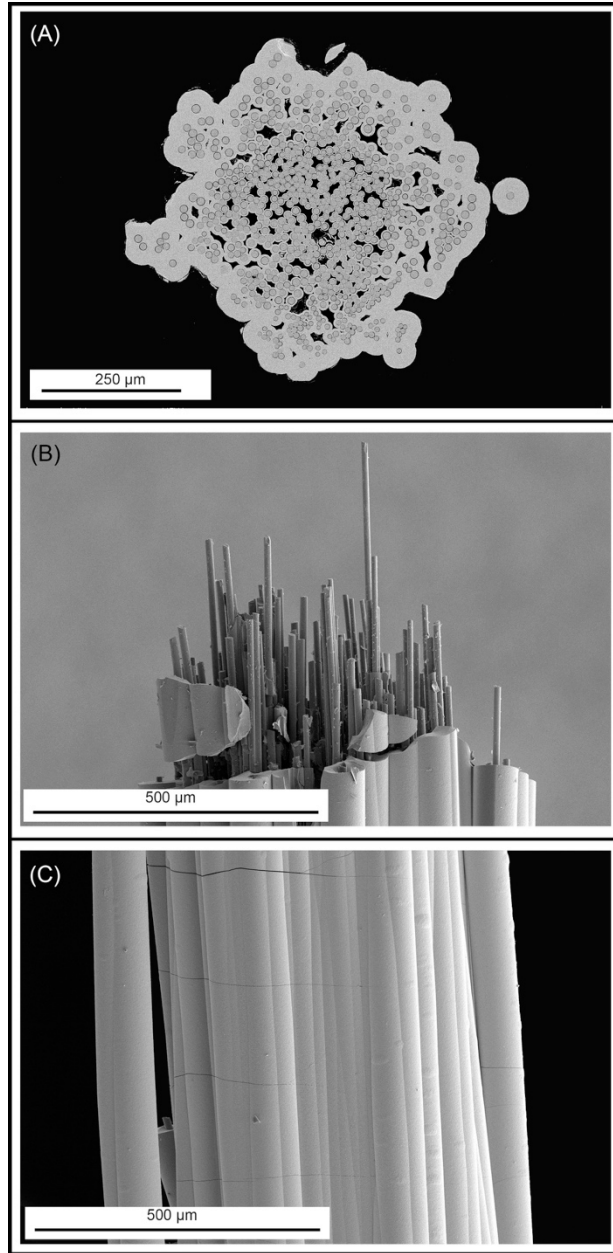


Figure 6.17: (A) Representative cross-section through a minicomposite of Tyranno ZMI™ fibers in CVI SiC matrix. (B, C) Significant fiber pullout and matrix cracking are evident after testing.

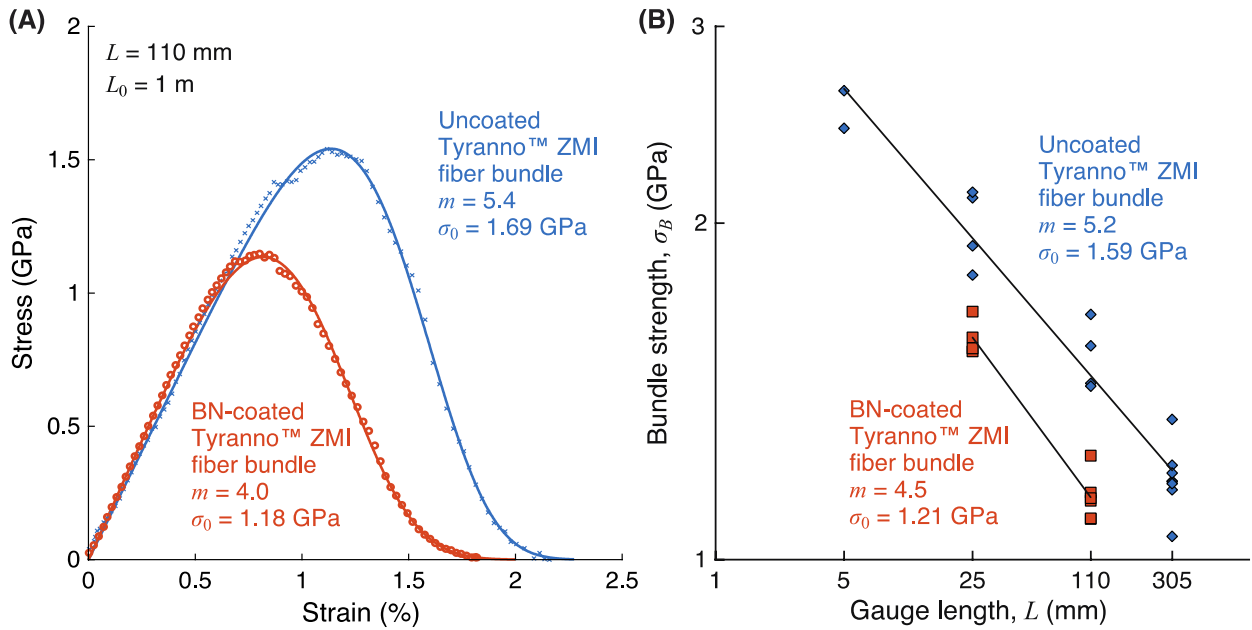


Figure 6.18: (A) Representative fiber bundle test results showing a drop in fiber strength after coating with BN. Solid lines are the least squares fit to the data from which the Weibull parameters are obtained. (B) Logarithmic plot showing the effect of gauge length on bundle strength. Weibull parameters are obtained from a linear regression of the data in log-log coordinates.³⁴

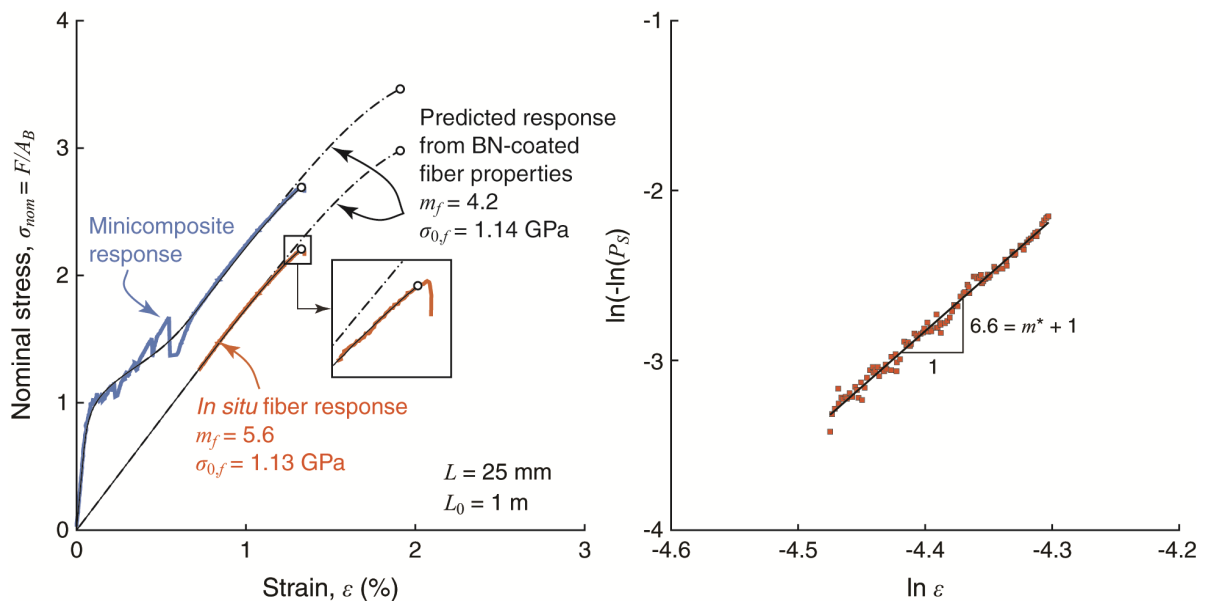


Figure 6.19: (A) Representative minicomposite response, showing the total composite nominal stress-strain response (in blue), the *in situ* fiber bundle response (in orange), and the predicted *in situ* fiber response based on properties of coated fibers. (B) Weibull-like plot is used to determine the *in situ* fiber Weibull parameters.

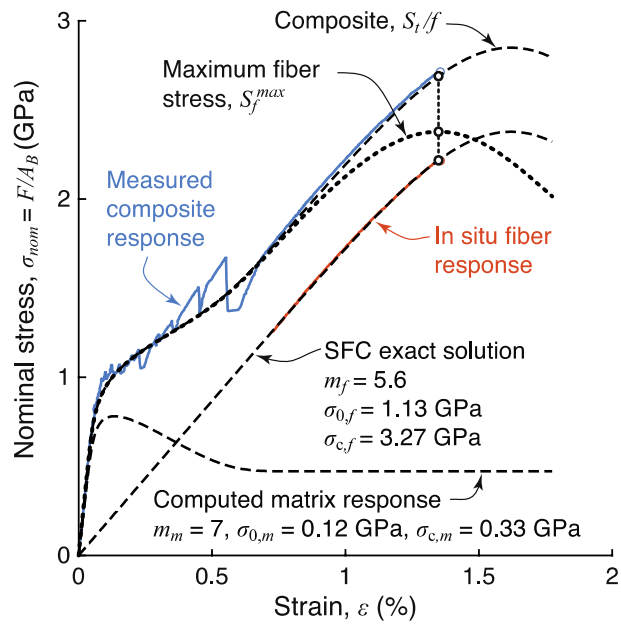


Figure 6.20: Stress-strain curves with fits from Eqns. (6.9), (6.18), and (6.20).

Chapter 7

Conclusions and recommendations

7.1 General conclusions and impact

In this study, experimental and simulation methods, analysis techniques, and micromechanical models for characterizing properties of unidirectional CMCs and their constituents were developed. The work provides a foundation for obtaining properties with high fidelity and an improved understanding of how constituent properties affect composite response. These are necessary not only for assessing properties of as-processed materials but also as a baseline for future studies of in-service material degradation.

Although obtaining constituent properties from tests of the kind employed here – fiber bundle tests, push-in tests, and minicomposite tensile tests – has been common practice, methods for rigorous analysis of test data has been lacking. This is due in part to the absence of accepted test standards. As a result, analysis techniques have often been *ad hoc* in nature and have lacked the statistical analyses needed to assess their fidelity. One consequence is that works from various sources cannot be compared reliably.

The work described in Chapters 2-4 addressed these issues in the context of fiber Weibull parameters obtained from tests on either individual filaments or fiber bundles. Experimental methods employed to obtain these parameters are selected in part by two competing considerations: having a sufficiently large sample size to fit to a Weibull distribution and completing the tests in a timely manner. In general, random errors on Weibull parameters scale with $1/\sqrt{N}$ where N is the number of fibers tested. For testing of single filaments, the minimum value of N that has been employed in the past is typically

30; thus, $1/\sqrt{N} \approx 0.2$. The same scaling holds for tests of fiber bundles.* The total number of fibers tested from even a few bundle tests readily exceeds 1000 and thus random errors are exceedingly small ($1/\sqrt{1000} = 0.03$). Even the most exhaustive study using single filament tests would not approach a sample size equal to the number of fibers in one bundle.

In some respects, bundle tests are more complicated than single filament tests. Bundle tests require careful handling of tows to maintain alignment of the constituent fibers during mounting into tabs and into the test machine. They also require use of high-resolution strain measurement, which can be readily accomplished using modern digital image correlation techniques. (Strain measurement is unnecessary in measuring strengths of individual filaments.) Additionally, to capture the entire bundle response, including the post-peak softening, the bundle gauge length must be sufficiently long to prevent instability at or near the load maximum. The critical length is governed by a combination of the stiffness of the load train and the stiffness of the fiber bundle. Finally, to prevent coordinated fiber fracture stemming from inter-fiber friction, bundles must be lubricated. When these issues are properly addressed, bundle tests provide the most accurate means for obtaining fiber Weibull parameters.

In cases where tests are performed on individual fibers, some forethought should be directed at the need for measuring fiber areas and hence obtaining the true (rather than nominal) fiber strengths. When variations in fiber area are small relative to variations in fiber strength, the systematic errors introduced in the inferred Weibull moduli can be

* In tensile testing of bundles with high fidelity strain measurement, strain to failure, in essence, is measured for each individual fiber within the bundle. Conveniently, strain to failure is largely independent of fiber area. Neither small variations in fiber area nor the nature of flaws (surface vs. bulk) have a significant impact on the Weibull parameters obtained from a least-squares fit of the bundle stress-strain response.

corrected using analysis methods presented here. Cut-offs for acceptable limits on fiber area variations were established so that the coefficient of variation (CoV) in the corrected Weibull modulus falls below a critical value, here taken to be 0.2. But even with these corrections, the CoV of the Weibull modulus is higher than that obtained from the distribution of true strength (which requires measurement of individual fiber areas). With estimates of CoVs of fiber area and nominal fiber strength, the analytical framework can be used to estimate the minimum number of tests that would yield sufficiently high-fidelity results without having to resort to measuring individual fiber areas. Whether the additional effort required to measure individual fiber areas is offset by the reduced number of required tests can then be assessed.

Even when variations in fiber area are large relative to variations in fiber strength, accurate estimates of Weibull parameters can be obtained from the length-dependence of mean nominal (or true) fiber strength. Although the nominal strength distribution is broader than the true strength distribution (*i.e.* lower inferred Weibull modulus), point estimates of strength (*e.g.* mean strength, Weibull reference strength, fiber bundle strength, *etc.*) are largely unaffected by systematic errors stemming from nominal strength measurements. Mean *nominal* fiber strength is equal to mean *true* fiber strength (although the standard deviation of mean nominal strength is greater than that of mean true strength.) The analytical framework facilitates assessment of the validity of test data and guides selection of test parameters (sample size and range of gauge lengths). Once again, this would allow one to assess up front whether the additional effort required to measure individual fiber areas would be offset by the reduced number of required tests.

Estimates of Weibull parameters obtained from length-dependent strength can be improved by testing of fiber bundles (rather than single filaments) at two or more distinct gauge lengths. Once again, random errors scale with inverse root of sample size, which readily exceeds 1000 from a few bundle tests at each gauge length. However, a least-squares fit of bundle stress-strain response usually yields more accurate estimates of Weibull parameters than that from a fit of bundle strength vs. gauge length. The ratio of maximum to minimum gauge length must be about 100 for a similar level of confidence. Such a large ratio is not usually practical.

Instead, length-dependence of bundle strength is best used to check whether Weibull parameters obtained from a fit of bundle stress-strain response at one gauge length accurately capture the expected gauge length effects. For constituent properties typical of SiC-SiC composites, the characteristic length, δ_c , (the length scale of interest in the *in situ* bundle) is about 1 mm. Conducting fiber bundle tests at a gauge length of 1 mm is not practical. The critical gauge length needed for capturing the entire bundle stress-strain response is often many tens of millimeters. Bundle strength is unaffected by post-peak instability; it can be accurately measured at gauge lengths less than the critical length. In this work, reported Weibull parameters were primarily obtained from least-squares fit of stress-strain response of bundle tests at a gauge length of $L = 110$ mm. For various batches of bare and coated TyrannoTM ZMI and Hi-NicalonTM type S fibers, Weibull parameters obtained from measured bundle strengths at gauge lengths ranging from 5 mm to 305 mm agree with those from least-squares fit at $L = 110$ mm. This result indicates that the gauge length effects are indeed captured by the Weibull distribution and that extrapolation to $L = \delta_c \approx 1$ mm is likely to be valid.

In principle, estimates of Weibull moduli can also be obtained from fiber strength variations with fiber area. However, these estimates are biased toward erroneously low values of Weibull moduli and have extraordinarily large uncertainties. For fiber area variations typical of commercially-available fibers ($Z(A) = 0.1 - 0.2$), an inordinately large number of single filament tests ($N > 1000$) is required to obtain reasonable estimates of the Weibull modulus. This method is not recommended.

The work described in Chapter 5 addressed issues in interpreting results from fiber push-in tests, including ways to ascertain the mechanism that governs the onset of push-in and the pertinent mechanical properties. A new mechanics framework that incorporates coating plasticity into the push-in analysis of Marshall and Oliver was developed.¹ Calculation of interface toughness from the load at the point of minimum compliance is readily automated, but this method can yield inaccurate results in certain scenarios. Some caution should therefore be exercised in following this protocol without considering the origin of the minimum.

Experimental evidence that coating yielding may precede rupture is a significant finding of this work. It has far-reaching implications for coating design. A coating with moderate yield strength and high critical displacement may be preferable to that with low toughness and no capacity for yielding. In the case of a brittle coating, three scenarios of crack deflection may occur: (i) adhesive failure at the fiber-coating interface (*i.e.* inner debonding), (ii) adhesive failure at the matrix-coating interface (*i.e.* outer debonding), or (iii) cohesive failure in the bulk of the coating. In all three scenarios, oxidant ingress through the matrix crack and into the coating crack would expose more surface area of coating to the oxidants. Recession rates would be greater than that for the case of an intact (or yielded)

coating with no pathway for rapid oxidant ingress into the coating. Additionally in scenario (i), rupture along the fiber-coating interface immediately exposes the fiber surface to oxidants within the matrix crack. Subsequent fiber degradation would occur more rapidly than in scenarios (ii) and (iii) in which the coating may provide some protection (at least initially) in preventing fiber oxidation. A greater focus of materials design efforts should be on tailoring the yield strength of coatings and not just their toughness.

The work described in Chapter 6 examined the mechanics of the tensile stress-strain response of unidirectional fiber-reinforced ceramic composites through a combination of adaptations of existing theories of fiber fracture, Monte Carlo (MC) simulations, and complementary experimental measurements. Analysis of this response yields vital information about the properties of the constituents as well as the nature of load transfer between the constituents. Importantly, the results indicate that traditional methods of inferring fiber Weibull parameters from measured distributions in length and strength of pulled-out fibers using existing models are likely to be unreliable and of limited utility. Alternatively, *in situ* fiber and matrix Weibull parameters can be obtained from the tensile stress-strain response using analysis procedures developed here.

Matrix volume fraction and distribution in matrix strength have important effects in composite rupture. Composite rupture stems from an instability in the *local* response of fibers in the most heavily strained regions (within matrix crack planes). For a matrix of finite strength, this instability occurs *before* the global tangent modulus goes to zero. As a result, previous analytical solutions overestimate *in situ* bundle strength.^{2, 3} At sufficiently low fiber volume fractions, composite response is brittle; fiber segments bridging the matrix crack cannot support the entire applied load at the onset of matrix cracking. In this scenario,

fibers fail predominately in or near the matrix crack plane. The tensile stress-strain response and fracture surface would therefore appear similar to those of composites with higher fiber volume fraction in combination with excessively high interface toughness. Fiber volume fraction must be sufficiently high to probe the true *in situ* bundle response and infer the *in situ* fiber Weibull parameters. Accurate micromechanical models capturing effects of all three constituents (fibers, matrix and interfaces) on tensile stress-strain response of unidirectional composites is critically important for properly analyzing experimental data.

7.2 Future work

Much of the work in this dissertation focused on developing improved methods and analysis techniques for obtaining constituent properties with high fidelity. The experimental work was largely foundational in nature. Results presented here were from tests on pristine fibers (both bare and coated) and pristine composites. The same techniques (fiber bundle tests, push-in tests, minicomposite tensile tests) could be used in future work to identify and quantify degradation mechanisms associated with thermochemical excursions. Studying degradation mechanisms from tests at a larger scale (say, at a component level or on a coupon) is an arduous task. Careful design of experiments on simplified geometries would allow one to systematically probe degradation mechanisms during processing and service.

Two sets of outstanding questions stem from push-in results in Chapter 5. First, why do coatings yield prior to rupture in some composite systems (or in some push-in tests within a given sample) but not in others, how does coating yielding preceding rupture affect composite response, and can the occurrence of coating yielding be used to improve the design of coatings? These questions are generally difficult to answer. Preliminary TEM

investigations were largely inconclusive in relating interface properties to coating microstructure. Property-microstructure-processing relationships for coatings will likely require extensive TEM work.

Second, what is the cause of the large variations in interface properties, how do these variations affect tensile stress-strain response in unidirectional composites, and how can the variations be reduced? As shown in Chapter 5, variations in interface properties are significant. In the four material systems tested, CoVs of sliding resistance range from 0.3 to 1.0. For reference, a typical fiber Weibull modulus of 5 corresponds to a CoV of fiber strength of 0.2. Interface toughness ranges from near zero to values exceeding fiber toughness. In addition, CoV of radius in commercial fibers ranges from 0.1 to 0.3. Quantifying effects of property variations experimentally would be difficult because each property could not be varied independently. Such effects could be readily studied using the MC simulations developed in Chapter 6. Simulating the tensile response of a unidirectional composite with a single matrix crack would be a simple starting point. Existing analytical models for cases of uniform interface properties would establish baseline properties against which the results from MC simulations could be compared.⁴⁻⁸ Coating yielding preceding rupture could also be readily incorporated into the MC simulations, to investigate effects of variations in coating yield strength on composite response.

Additionally, the MC simulations could be modified to investigate effects of BN coating recession on local *in situ* bundle response. For example, in cases where water vapor enters the composite through matrix cracks and reacts with the BN to cause volatilization, the simulations could be used to study the effects of progressive growth of the recession length and hence growth of fiber volume under high stress (where fibers are decoupled from

the matrix) on the fiber bundle strength. The expectation is that, at moderately high stresses (greater than that of the dry bundle strength for the given gauge length), composite rupture would occur once the recession length reached a critical value, even in the absence of fiber degradation. These results would establish a minimum in the strength loss associated with BN recession.

References

- ¹ D.B. Marshall and W.C. Oliver, "Measurement of interfacial mechanical properties in fiber-reinforced ceramic composites," *J. Am. Ceram. Soc.*, **70** [8] 542–548 (1987).
- ² W.A. Curtin, "Theory of mechanical properties of ceramic-matrix composites," *J. Am. Ceram. Soc.*, **74** [11] 2837–2845 (1991).
- ³ C.Y. Hui, S.L. Phoenix, M. Ibnabdeljalil, and R.L. Smith, "An exact closed form solution for fragmentation of Weibull fibers in a single filament composite with applications to fiber-reinforced ceramics," *J. Mech. Phys. Solids*, **43** [10] 1551–1585 (1995).
- ⁴ M.D. Thouless and A.G. Evans, "Effects of pull-out on the mechanical properties of ceramic-matrix composites," *Acta Metall.*, **36** [3] 517–522 (1988).
- ⁵ M. Sutcu, "Weibull statistics applied to fiber failure in ceramic composites and work of fracture," *Acta Metall.*, **37** [2] 651–661 (1989).
- ⁶ S.L. Phoenix, "Statistical issues in the fracture of brittle-matrix fibrous composites," *Compos. Sci. Technol.*, **48** [1–4] 65–80 (1993).
- ⁷ J.W. Hutchinson and H.M. Jensen, "Models of fiber debonding and pullout in brittle composites with friction," *Mech. Mater.*, **9** [2] 139–163 (1990).

- 8 D.B. Marshall, “Analysis of fiber debonding and sliding experiments in brittle matrix composites,” *Acta Metall. Mater.*, **40** [3] 427–441 (1992).